Computational insights into the unconfined flow of a non-Newtonian power-law fluid past counter-rotating circular cylinders

Lekhraj Malviya^a, Ram Prakash Bharti^{a,*}, Abhishek Kumar Lal^a

^aComplex Fluid Dynamics and Microfluidics (CFDM) Lab, Department of Chemical Engineering, Indian Institute of Technology Roorkee, Roorkee - 247667, Uttarakhand, India

Abstract

This study numerically examines the steady unconfined laminar flow of incompressible non-Newtonian power-law fluids past a pair of side-by-side counter-rotating circular cylinders using the finite element method. The cylinders simultaneously rotate at equal angular speeds in opposite directions, with the upper cylinder (UC) rotating clockwise and the lower cylinder (LC) counterclockwise. The numerical simulations are performed over wide parameter ranges: power-law index $(0.2 \le n \le 1.8)$, rotational rate $(0 \le \alpha \le 2)$, gap ratio $(0.2 \le G \le 1)$, and Reynolds number $(1 \le Re \le 40)$. The detailed influence of these flow parameters on key flow characteristics, including streamlines, surface pressure, centerline velocity, and individual as well as total drag and lift coefficients, is systematically analyzed. For stationary cylinders $(\alpha = 0)$, a twin-vortex structure forms in the wake, which progressively vanishes with increasing rotation $(\alpha = 2)$. The surface pressure coefficient attains its maximum values for shear-thickening fluids (n > 1) at higher rotational speeds, irrespective of the gap ratio. The total drag coefficient (C_D) decreases with increasing α and α , whereas the lift coefficient α exhibits a more intricate dependence on the flow parameters. The results provide fundamental insights into the interplay between rotation, non-Newtonian rheology, and geometric confinement in determining the hydrodynamic behavior of rotating cylinder systems.

Keywords: Rotating cylinders, Gap spacing, Drag and lift coefficient, Non-Newtonian fluids, Power-law index

1. Background

The flow over cylinders has been the classical problem in fluid mechanics over the century [1–10] due to the simplicity of the flow configuration, yet providing enormous flow features essential to a variety of practical industrial applications, including paper and pulp industries, heat exchanger, cooling tower arrays, nuclear reactors (fuel and control rods), chimney stacks, bridge piers, and offshore structures. The cylinders of different cross-sectional (e.g., circular and non-circular) shapes and sizes (equal or unequal

^{*}Corresponding author

diameter, length) can be arranged in various configurations (single, tandem, side-by-side, triangular, rectangular, and staggered arrangements) to represent the wide-ranging flow problems of industrial importance. Furthermore, the industrial applications involving cylindrical structures use a wide variety of fluids (e.g., polymer solutions, emulsions, suspensions, high molecular weight substances, paper and pulp suspensions, drilling mud, crude oil, and multiphase mixtures) displaying the non-Newtonian natures such as shear-dependent, viscoelastic, viscoplastic and time-dependent characteristics [11]. The rheological nature of wide-ranging shear-dependent fluids is typically expressed by the power-law constitutive model. However, to the best of our knowledge, the unconfined steady flow of incompressible power-law fluids across side-by-side rotating cylinders remains unexplored in the literature, despite signifying numerous practically applications. Therefore, this article aims to provide a novel contribution by examining the effects of rotational rate and gap ratio on the hydrodynamics of non-Newtonian power-law fluids flowing across two side-by-side rotating cylinders. It is, however, imperative to present the relevant literature to understand better the existing knowledge gaps for flow around circular cylinders and news results presented in this work.

Enormous knowledge framework comprehends various features of the flow over cylinders subjected to unconfined (and confined) Newtonian (and non-Newtonian) fluids, as presented in excellent reviews, articles, and books [1–10, 43–63]. For instance, Zdravkovich [2] has categorized the wake regime for laminar flow around a single stationary cylinder as steady unseparated wakes ($Re \le 5$), steady separated near-wake ($6 \le Re \le 30$), steady near-wake oscillation ($30 \le Re \le 60$), and unsteady periodic wakes ($Re \ge 60$). Various studies [10, 47, 50, 51, 55, 64–70] have extensively investigated unconfined non-Newtonian power-law fluid flow around a stationary cylinder for wide range of the Reynolds number (Re = 1 - 100) and power-law index (Re = 0.2 - 1.8). Furthermore, the flow regimes, in particular, the critical Reynolds numbers (Re_c and Re^c) indicating the range of Reynolds number ($Re_c \le Re \le Re^c$) for symmetrical wake formation around the cylinder, have been characterized numerically for power-law fluid (Re = 0.2 - 1.8) flow across an unconfined [65] and a channel-confined [71] cylinder. Few studies [55, 72, 73] have also numerically examined the vortex shedding characteristics of power-law flow over a cylinder. Recently, Mohanty et al. [63] have explored the roles of the solvent viscosity contribution and Deborah number (Re = 0.2 - 1.8) on the creeping flow of Oldroyd-B viscoelastic fluid over a channel confined

Table 1: Literature on the flow of Newtonian (n = 1) and non-Newtonian $(n \neq 1)$ fluids across a pair of the side-by-side stationary $(\alpha = 0)$ and rotating $(\alpha \neq 0)$ circular cylinders

[12] 0 0.5–3 100–200 1 N (FEM) [13] 0 i5 40–160 1 N (IBM) [14] 0 0.2–0.6 150–14300 1 E (LIF, PIV) [15] 0 0.1–2 30–100 1 N (SEM) [16] 0 0.3–1 20–80 1 N (VSFM) [17] 0 0.5–3 100, 300, 10 ⁴ 1 N (FVM) [18] 0 0.1–30 1–20 1 N (FVM) [19] 0 0.2–3 100 1 N (FVM) [19] 0 0.2–3 100 1 N (FVM) [20] 0 0.1–7 100 1 N (FVM) [21] 0 0.7, 1.8 50–70 1 N (DNS) [22] 0 0.5–3.5 500 1 N (FEM) [23] 0 0.2–4 20–160 1 N (FVM)	Source	α	G	Re	n	Technique	Remarks
$ \begin{array}{c ccccccccccccccccccccccccccccccccccc$	Present study	0 – 2	0.2 - 1	1 - 40	0.2-1.8	N (FEM)	Counter-rotating cylinders
$ \begin{bmatrix} 14 & 0 & 0.2-0.6 & 150-14300 & 1 & E (LIF, PIV) \\ [15] & 0 & 0.1-2 & 30-100 & 1 & N (SEM) \\ [16] & 0 & 0.3-1 & 20-80 & 1 & N (VSFM) \\ [17] & 0 & 0.5-3 & 100, 300, 10^4 & 1 & N (FVM) \\ [18] & 0 & 0.1-30 & 1-20 & 1 & N (FVM) \\ [19] & 0 & 0.2-3 & 100 & 1 & N (FEM) \\ [20] & 0 & 0.1-7 & 100 & 1 & N (FVM) \\ [21] & 0 & 0.7, 1.8 & 50-70 & 1 & N (DNS) \\ [22] & 0 & 0.5-3.5 & 500 & 1 & N (FVM) \\ [23] & 0 & 0.2-4 & 20-160 & 1 & N (FVM) \\ [24] & 0 & 0.2-1.7 & 3900 & 1 & N (LES, FVM) \\ [25] & 0 & 0.5-4 & 100 & 1 & N (LBM) \\ [26] & 0 & 0.5-3 & 5-40 & 1 & N (FVM) \\ [27-29] & \leq 2 & 0.2-3 & 100 & 1 & N (LBM) \\ [30] & 0-4 & 0.11 & 425-1130 & 1 & N (LBM) \\ [31] & 2 & 0.7-1.5 & 160-200 & 1 & N (LBM) \\ [33] & 0-5 & 1-5 & 100-200 & 1 & N (LBM) \\ [34] & 0-5 & 0.8-6.5 & 100-500 & 1 & E (PIV) \\ [35] & 0.5-1.25 & 0.1-3.5 & 100 & 1 & N (FVM) \\ [36] & 0-3 & 1 & 40-200 & 1 & N (FVM) \\ [37] & 0-4 & 0.5-2 & 200 & 1 & N (FVM) \\ [38] & 0-4 & 0.5-2 & 200 & 1 & N (FVM) \\ [39] & \leq 2 & 0.2-3 & 100 & 1 & N (FVM) \\ [39] & \leq 2 & 0.2-3 & 100 & 1 & N (FVM) \\ [39] & \leq 2 & 0.2-3 & 100 & 1 & N (FVM) \\ [39] & \leq 2 & 0.2-3 & 100 & 1 & N (FVM) \\ [39] & \leq 2 & 0.2-3 & 100 & 1 & N (FVM) \\ [39] & \leq 2 & 0.2-3 & 100 & 1 & N (FVM) \\ [39] & \leq 2 & 0.2-3 & 100 & 1 & N (FVM) \\ [39] & \leq 2 & 0.2-3 & 100 & 1 & N (FVM) \\ [40] & 0 & 0.5-3 & 1-40 & 0.4-1.8 & N (FVM) \\ [41] & 0 & 0.5 & 1-40 & 0.2-1.0 & N (FVM) \\ [41] & 0 & 0.5 & 1-40 & 0.2-1.0 & N (FVM) \\ [42] & 0 & 0.2-3 & 0.1-100 & 0.2-1.8 & N (FVM) \\ [42] & 0 & 0.2-3 & 0.1-100 & 0.2-1.8 & N (FVM) \\ [42] & 0 & 0.2-3 & 0.1-100 & 0.2-1.8 & N (FVM) \\ [42] & 0 & 0.2-3 & 0.1-100 & 0.2-1.8 & N (FVM) \\ [42] & 0 & 0.2-3 & 0.1-100 & 0.2-1.8 & N (FVM) \\ [42] & 0 & 0.2-3 & 0.1-100 & 0.2-1.8 & N (FVM) \\ [42] & 0 & 0.2-3 & 0.1-100 & 0.2-1.8 & N (FVM) \\ [42] & 0 & 0.2-3 & 0.1-100 & 0.2-1.8 & N (FVM) \\ [42] & 0 & 0.2-3 & 0.1-100 & 0.2-1.8 & N (FVM) \\ [42] & 0 & 0.2-3 & 0.1-100 & 0.2-1.8 & N (FVM) \\ [42] & 0 & 0.2-3 & 0.1-100 & 0.2-1.8 & N (FVM) \\ [42] & 0 & 0.2-3 & 0.1-100 & 0.2-1.8 & N (FVM) \\ [43] & 0.2-2 & 0.2-3 & 0.1-100 & 0.2-1.8$	[12]	0	0.5–3	100–200	1	N (FEM)	
$ \begin{bmatrix} 15 \\ 16 \\ 0 \\ 0 \\ 0.3-1 \\ 20-80 \\ 1 \\ N (VSFM) \\ 1 N (VSFM) \\ 1 N (FVM) \\ 1 B \\ 0 \\ 0.1-30 \\ 0.2-3 \\ 100 \\ 301 \\ 100 \\ 1 D \\ 1 $	[13]	0	i 5	40–160	1	N (IBM)	
$ \begin{bmatrix} 16 \\ 17 \\ 17 \\ 0 \\ 0.5-3 \\ 0.5-3 \\ 100,300,10^4 \\ 1 \\ 1 \\ N (FVM) \\ 1 \\ 18 \\ 0 \\ 0.1-30 \\ 1-20 \\ 1 \\ N (FVM) \\ 1 \\ 1 \\ 1 \\ 0 \\ 0.5-3.5 \\ 0.0 \\ 0.5-4 \\ 100 \\ 1 \\ 100 \\ 1 \\ 1 \\ 1 \\ 1 \\ 1 \\ 1$	[14]	0	0.2-0.6	150-14300	1	E (LIF, PIV)	
$ \begin{array}{c ccccccccccccccccccccccccccccccccccc$	[15]	0	0.1–2	30–100	1	N (SEM)	
[18] 0 0.1–30 1–20 1 N (FVM) [19] 0 0.2–3 100 1 N (FEM) [20] 0 0.1–7 100 1 N (FVM) [21] 0 0.7, 1.8 50–70 1 N (DNS) [22] 0 0.5–3.5 500 1 N (FVM) [23] 0 0.2–4 20–160 1 N (FVM) [24] 0 0.2–1.7 3900 1 N (LBM) [25] 0 0.5–4 100 1 N (LBM) [26] 0 0.5–3 5–40 1 N (FVM) [27–29] ≤ 2 0.2–3 100 1 N (LBM) Counter-rotating cylinders [30] 0–4 0.11 425–1130 1 N (LBM) Counter-rotating cylinders [31] 2 0.7–1.5 160–200 1 N (EBM) N (EPIV) [33] 0–5 1–5 100–200 1	[16]	0	0.3-1	20–80	1	N (VSFM)	
	[17]	0	0.5–3	100, 300, 10 ⁴	1	N (FVM)	
$ \begin{array}{c ccccccccccccccccccccccccccccccccccc$	[18]	0	0.1–30	1–20	1	N (FVM)	
	[19]	0	0.2–3	100	1	N (FEM)	
	[20]	0	0.1–7	100	1	N (FVM)	
	[21]	0	0.7, 1.8	50-70	1	N (DNS)	
	[22]	0	0.5–3.5	500	1	N (FEM)	
$ \begin{array}{c ccccccccccccccccccccccccccccccccccc$	[23]	0	0.2–4	20–160	1	N (FVM)	
$ \begin{array}{c ccccccccccccccccccccccccccccccccccc$	[24]	0	0.2-1.7	3900	1	N (LES, FVM)	Unequal sized cylinders; 3-D turbulent flow
$ \begin{array}{c ccccccccccccccccccccccccccccccccccc$	[25]	0	0.5–4	100	1	N (LBM)	
$ \begin{array}{c ccccccccccccccccccccccccccccccccccc$	[26]	0	0.5–3	5–40	1	N (FVM)	
	[27–29]	≤ 2	0.2–3	100	1	N (IBM)	Counter-rotating cylinders
	[30]	0–4	0.11	425–1130	1	N (LBM); E (PIV)	
	[31]	2	0.7–1.5	160–200	1	N (LBM)	
	[32]	0–2	0.2–3	100	1	N (LBM)	
	[33]	0–5	1–5	100-200	1	N (SDM); E (PIV)	
	[34]	0–5	0.8–6.5	100-500	1	E (PIV)	
	[35]	0.5–1.25	0.1–3.5	100	1	N (FVM)	
	[36]	0–3	1	40–200	1	N (FVM)	
[39] ≤ 2 0.2–3 100 1 N (FVM) Counter-rotating cylinders [40] 0 0.5–3 1–40 0.4–1.8 N (FVM) [41] 0 0.5 1–40 0.2–1.0 N (FVM) [42] 0 0.2–3 0.1–100 0.2–1.8 N (FVM)	[37]	0–4	0.5–2	200	1	N (FVM)	
[40] 0 0.5–3 1–40 0.4–1.8 N (FVM) [41] 0 0.5 1–40 0.2–1.0 N (FVM) [42] 0 0.2–3 0.1–100 0.2–1.8 N (FVM)	[38]	0–4	0.5–2	200	1	N (FVM)	
[41] 0 0.5 1-40 0.2-1.0 N (FVM) [42] 0 0.2-3 0.1-100 0.2-1.8 N (FVM)	[39]	≤ 2	0.2-3	100	1	N (FVM)	Counter-rotating cylinders
[42] 0 0.2–3 0.1–100 0.2–1.8 N (FVM)	[40]	0	0.5–3	1–40	0.4–1.8	N (FVM)	
	[41]	0	0.5	1–40	0.2–1.0	N (FVM)	
[43] 0 1.1–1.6 100 0.8–1.5 N (FVM)	[42]	0	0.2–3	0.1-100	0.2–1.8	N (FVM)	
	[43]	0	1.1–1.6	100	0.8–1.5	N (FVM)	

 $[\]rightarrow$ N (Numerical): FDM (finite difference method); FEM (finite element method); SEM (spectral element method); FVM (finite volume method); IBM (immersed boundary method); LBM (lattice Boltzmann method); SDM (spectral difference method); VSFM (vorticity - stream function method); \rightarrow E (Experimental): LIF (laser-induced fluorescence); PIV (particle image velocimetry); \rightarrow Re (Reynolds number); n (power-law index); G (gap ratio); α (rotational velocity)

circular cylinder. On the other hand, a few studies have numerically revealed negative drag and lift forces in the non-Newtonian flow characteristics of a rotating single circular cylinder $(0.2 \le n \le 1; 0 \le \alpha \le 6; 0.1 \le Re \le 40)$ [74, 75] and elliptical cylinder $(0.4 \le n \le 1.8; 1 \le \alpha \le 4; 5 \le Re \le 40; 0.1 \le e \le 0.7)$ [61].

Recently, Kumar et al. [76, 77] have used experimental (2D-PIV) and numerical (FEM) techniques to explore the friction stir welding (FSW) process wherein the welding tool of cylindrical shape rotates and translates in the direction of welding of the material sheets behaving as non-Newtonian fluids.

Furthermore, researchers have extensively explored the hydrodynamics of multiple cylinder configurations (such as tandem, staggered, or side-by-side) submerged in steady cross-flow and revealed complex flow phenomena influenced by the positioning of the cylinders, flow governing parameters and the nature of the fluid [10]. In addition to the flow governing parameters for a single cylinder, the gap spacing (G = h/D)between the surface of two cylinders is pivotal and causes significant changes in flow characteristics. Table 1 lists the relevant prior studies on the flow across the pair of the side-by-side arrangements of stationary $(\alpha = 0)$ and rotating $(\alpha \neq 0)$ cylinders. Further, several studies [25, 67, 68, 78–84], not listed in Table 1, have examined the cross-flow across a pair of tandem cylinders spanning over the wide ranges of flow governing parameters (Re, n, G, α). These studies (Table 1) have revealed complex flow features as a function of the parameters governing the flow around side-by-side circular cylinders. However, most of the existing studies have dealt with Newtonian (n = 1) fluid flow around a pair of side-by-side circular cylinders over the wide range of gap ratio (G), Reynolds number (Re), and rotational rate (α) . While few studies [40–43] deal with non-Newtonian ($n \ne 1$) fluid, they are limited to the stationary ($\alpha = 0$) cylinders; conversely, none of the literature has explored the combined influence of non-Newtonian fluids and rotational rate $(n \neq 1, \alpha \neq 0)$ for the flow around a pair of the side-by-side circular cylinders. Therefore, this study aims to explore the hydrodynamic characteristics of non-Newtonian power-law fluid flowing across a pair of counter-rotating circular cylinders arranged in an unconfined side-by-side configuration. The two-dimensional flow governing equations have been solved numerically using the finite element method spanning over the wide range of dimensionless conditions (Reynolds number, $1 \le Re \le 40$; power-law index, $0.2 \le n \le 1.8$; gap ratio, $0.2 \le G \le 1$; cylinder rotational rate, $0 \le \alpha \le 2$) to obtain the flow field and subsequent analysis of local and global flow characteristics, including streamline profiles, centerline velocity, pressure coefficients on the cylinder surface, and individual and total force coefficients.

2. Problem Description

Consider the two-dimensional steady incompressible flow across an unconfined pair of counter-rotating side-by-side circular cylinders, as sketched in Fig. 1. The cylinders of equal diameter (D) are arranged side by side and positioned vertically symmetric $(y = \pm s)$ about the horizontal mid-plane (y = 0) at a streamwise distance L_u (upstream length) from the inlet and L_d (downstream length) from the outlet, both measured to the center of cylinders. The spacing between the cylinders is h (surface-to-surface) and 2s (center-to-center), where s = (D + h)/2. The centers (x_c, y_c) of the upper cylinder (UC) and lower cylinder (LC) are located at (L_u, s) and $(L_u, -s)$, respectively. In addition, the position of any point on the surface of the cylinders is specified by the angle ϕ , measured clockwise from the mid-plane $(y = \pm s)$ through the center the cylinders. Accordingly, the front stagnation point (FSP) and the rear stagnation point (RSP) correspond to $\phi = 0$ and $\phi = \pi$, respectively, for both cylinders. Furthermore, the lateral boundaries are placed symmetrically at $y = \pm H/2$ about the mid-plane. The physical domain therefore spans an axial streamwise length L (= $L_u + L_d$) and a lateral height H, respectively. The gap ratio between cylinders is defined as G = h/D, and the wall blockage ratio as $\beta = D/H$. To represent the unconfined flow, the top and bottom boundaries are treated as imaginary $(\beta \to \infty)$, and the outlet is placed sufficiently far downstream

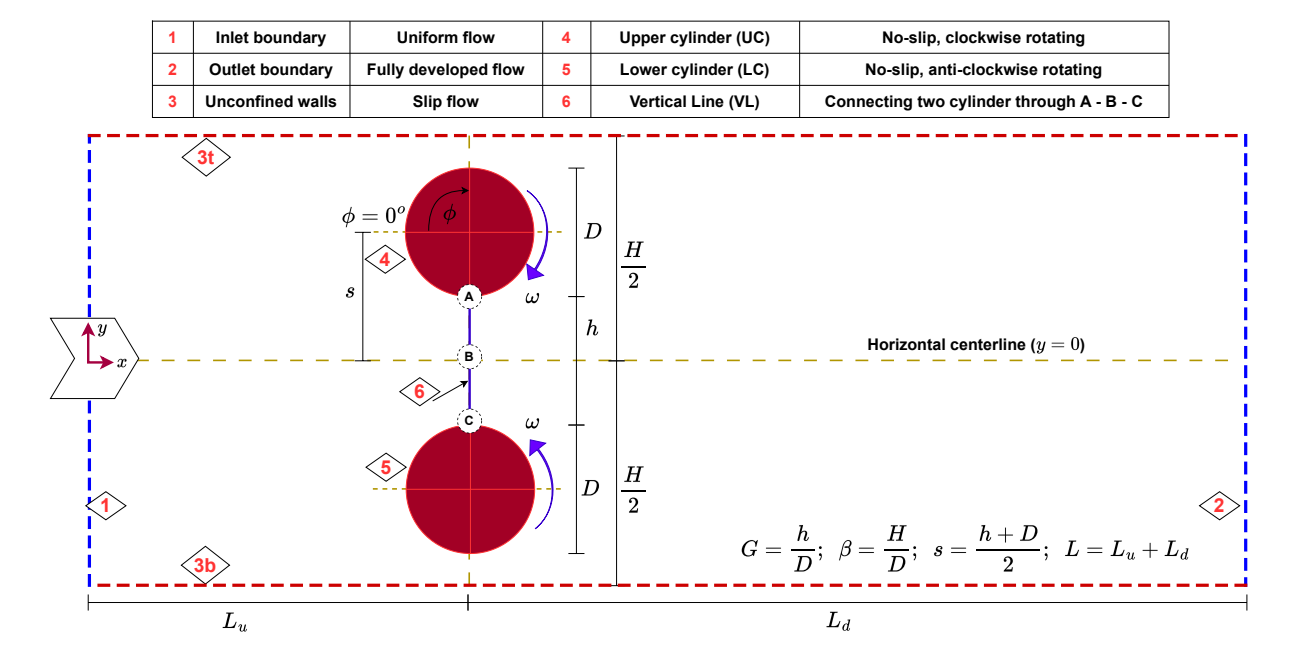


Figure 1: Schematic representation of an unconfined flow across a pair of side-by-side counter-rotating circular cylinders.

of the cylinders, allowing the flow to be fully developed before exiting. All length variables are measured in meters.

The streaming liquid, with uniform velocity (U_0 , m/s), approaches the counter-rotating cylinders, where the upper cylinder (UC) rotates clockwise and the lower cylinder (LC) counter-clockwise about their centers at a fixed angular velocity (ω , rad/s). The physical properties of the fluid, such as density (ρ , kg/m³) and viscosity (η , Pa·s), are assumed independent of temperature and pressure. Furthermore, the viscous behavior of the incompressible fluid is represented using the non-Newtonian power-law model [11, 85] as follows.

$$\eta = m(I_2/2)^{[(n-1)/2]} \tag{1}$$

$$I_2 = 2\left(\varepsilon_{xx}^2 + \varepsilon_{yy}^2 + \varepsilon_{xy}^2 + \varepsilon_{yx}^2\right); \qquad \varepsilon(U) = (1/2)\left[(\nabla U) + (\nabla U)^T\right]$$
 (2)

n < 1: shear-thinning; n = 1: Newtonian; n > 1: shear-thickening

where m is the flow consistency index (Pa·sⁿ), n is the flow behavior index (dimensionless), ε is the rate-of-strain tensor (s⁻¹), and I_2 is the second invariant of the strain-rate tensor (s⁻²).

The physical problem described above is governed by the steady incompressible Navier-Stokes (N-S) equations [42, 67, 68]. In this study, the field variables are non-dimensionalized using the characteristic scales U_0 , D, ρU_0^2 , $m(U_0/D)^{n-1}$, and $m(U_0/D)^n$ for velocity, length, pressure, viscosity, and shear stress, respectively. Consequently, the dimensionless parameters derived from the scaling of the field variables and equations are defined as follows.

$$\alpha = \frac{\omega(D/2)}{U_0}; \qquad Re = \frac{D^n U_0^{2-n} \rho}{m}; \qquad Re_\omega = \alpha^{(2-n)} Re; \tag{3}$$

Here, α , Re, and Re_{ω} denote the dimensionless rotational (angular) velocity of cylinders, the Reynolds number for power-law fluids, and the rotational Reynolds number of the cylinders, respectively. Henceforth, all equations and variables are expressed in dimensionless form unless stated otherwise.

Subsequently, the governing equations and boundary conditions in dimensionless form are presented as

follows.

$$\nabla \cdot \boldsymbol{U} = 0, \tag{4}$$

$$(\boldsymbol{U} \cdot \nabla)\boldsymbol{U} = -\nabla p + Re^{-1} (\nabla \cdot \boldsymbol{\tau}), \tag{5}$$

where, U, p, and τ denote the velocity vector (with components U_x and U_y in Cartesian coordinates), the isotropic pressure, and the deviatoric stress tensor, respectively. The stress tensor (τ) for an incompressible fluid is related to the rate-of-strain tensor (ε) as follows [11, 85].

$$\tau = 2\eta \varepsilon$$
 where $\eta = (I_2/2)^{(n-1)/2}$ (6)

Here, η denotes the viscosity of the power-law fluid (dimensionless form of Eq. 1), and ε is the rate-of-strain tensor (dimensionless form of Eq. 2).

The physically relevant boundary conditions (BCs) for the considered flow configuration (see Fig. 1) are specified as follows.

• BC 1 (inlet boundary): A uniform velocity field prescribed in the streamwise direction as follows.

$$U = (U_x, \ U_y) = (1, \ 0) \tag{7}$$

• BC 2 (outlet boundary): A homogeneous Neumann condition, representing fully developed flow at the outlet, is prescribed as follows.

$$\frac{\partial U_x}{\partial x} = 0;$$
 $\frac{\partial U_y}{\partial x} = 0;$ and $p = 0$ (8)

• BC 3 (top and bottom boundaries): To represent the unconfined flow, the top and bottom boundaries are treated as imaginary with no dissipation and are subject to a slip condition, as follows.

$$\frac{\partial U_x}{\partial y} = 0;$$
 and $U_y = 0$ (9)

BCs 4 and 5 (surface of the cylinders): A no-slip condition is imposed on the surfaces of the solid, impermeable cylinders, which rotate with a fixed rotational rate (α) about their axes in the clockwise (upper cylinder) and counter-clockwise (lower cylinder) directions, as follows:

$$U = (U_x, U_y) = \begin{cases} (-\alpha \sin \phi, +\alpha \cos \phi), & \text{for UC,} \\ (+\alpha \sin \phi, -\alpha \cos \phi), & \text{for LC} \end{cases}$$
 (10)

The governing equations (Eqs. 4–5), together with the boundary conditions (Eqs. 7–10), describe the flow field in terms of the primitive variables, namely the velocity (U) and pressure (p). Subsequently, the hydrodynamic characteristics such as streamlines, pressure coefficient, and drag and lift coefficients are evaluated following standard definitions [42, 68]. For completeness, the relevant fluid dynamic quantities are defined below.

The pressure coefficient (C_p) over the surface of the cylinders is obtained as follows:

$$C_p = \frac{(p - p_0)}{p_d}; \qquad p_d = \frac{1}{2}(\rho U_0^2)$$
 (11)

where, p, p_0 , and p_d denote the local pressure at an angular position ϕ on the cylinder surface and the reference pressure in the far-field region (i.e., at the outlet boundary, BC 2), dynamic pressure of the flow, respectively.

The force coefficients (C_i) , denoting the dimensionless hydrodynamic forces (F_i) , are defined as follows.

$$C_D = \frac{F_D}{p_d D} = C_{DP} + C_{DF}; \qquad C_L = \frac{F_L}{p_d D} = C_{LP} + C_{LF}$$
 (12)

where C_D and C_L denote the total drag and lift coefficients, respectively, corresponding to the total drag $(F_D = F_{DP} + F_{DF}, N/m)$ and lift $(F_L = F_{LP} + F_{LF}, N/m)$ forces per unit length of the cylinder. The pressure contributions to the drag and lift coefficients $(C_{DP} \text{ and } C_{LP})$ are expressed as follows.

$$C_{DP} = \frac{F_{DP}}{p_d D} = \int_S C_p n_x dS; \quad \text{and} \quad C_{LP} = \frac{F_{LP}}{p_d D} = \int_S C_p n_y dS$$
 (13)

where F_{DP} and F_{LP} denote the pressure components of the drag and lift forces, respectively, and S

represents the surface of the cylinders. Similarly, the viscous components of the drag and lift coefficients $(C_{DF} \text{ and } C_{LF})$ are expressed as follows.

$$C_{DF} = \frac{F_{DF}}{p_d D} = \frac{2^{n+1}}{Re} \int_{S} [(\boldsymbol{\tau} \cdot \mathbf{n}_s) \cdot \hat{\mathbf{i}}] \, dS = \frac{2^{n+1}}{Re} \int_{S} (\tau_{xx} n_x + \tau_{xy} n_y) \, dS, \tag{14}$$

$$C_{LF} = \frac{F_{LF}}{p_d D} = \frac{2^{n+1}}{Re} \int_{S} [(\boldsymbol{\tau} \cdot \mathbf{n}_s) \cdot \hat{\mathbf{j}}] \, dS = \frac{2^{n+1}}{Re} \int_{S} (\tau_{yx} n_x + \tau_{yy} n_y) \, dS, \tag{15}$$

where, F_{DF} and F_{LF} denote the frictional components of the drag and lift forces, respectively. The outward unit normal vector to the cylinder surface (\mathbf{n}_s) is defined as follows.

$$\mathbf{n}_{s} = \frac{x\mathbf{e}_{x} + y\mathbf{e}_{y}}{\sqrt{x^{2} + y^{2}}} = n_{x}\mathbf{e}_{x} + n_{y}\mathbf{e}_{y}$$
(16)

where \mathbf{e}_x , and \mathbf{e}_y denote the unit vectors along the x- and y-directions, respectively.

The numerical solution of the flow governing equations (Eqs. 4–10) is obtained to analyze the dynamics of local and global flow characteristics as functions of the dimensionless parameters (n, Re, α, G) . The following section presents the numerical methodology and the selection of parameters used to obtain the final results. It is reiterated that, hereafter, all quantities are expressed in dimensionless form unless otherwise stated.

3. Numerical approach and parameters

In this study, the flow governing equations (Eqs. 4 - 10) are solved numerically using the finite element method (FEM) based the commercial CFD solver COMSOL Multiphysics. The two-dimensional (2D) single-phase (spf) laminar flow module is employed to model the physical system, and the fluid viscosity is defined using a shear-dependent, inelastic, non-Newtonian power-law model.

The computational domain (Fig. 1) is discretized using a hybrid mesh of uniform triangular elements near the cylinder surfaces and non-uniform quadrilateral elements elsewhere. The mesh density gradually decreases away from the cylinders, and the grid is generated using integrated CAD geometry and mesh generation tools in COMSOL. The mesh near the cylinder surfaces has a uniform spacing of δ_r , with N_c points on the surface of each cylinder. The mesh is gradually stretched from δ_r near the cylinders to δ and

finally to Δ in the faraway from cylinders.

The discretized flow governing equations on the non-uniform grid result in a coupled set of simultaneous algebraic equations, which are solved using parallel direct linear solver (PARDISO) based on LU matrix factorization, combined with an automatic highly non-linear (Newton) method and a relative convergence criterion of 10^{-6} . The steady-state solutions yield the flow field (\mathbf{U}, p) as functions of the governing parameters (n, α , Re, G). All reported local and global flow quantities are rounded to four significant digits. A parametric sweep was performed over n and α sequentially to reduce computational effort.

Furthermore, the existing literature [42, 43, 47, 50–59, 61, 63, 67, 68, 86] has recognized that the sizes of the computational domain and mesh are critical numerical parameters for obtaining accurate and reliable results. In the case of unconfined flow, the computational domain is characterized by the upstream length (L_u) , downstream length (L_d) , and height (H), as illustrated in Fig. 1. In the present study, detailed investigations on domain and mesh independence have been carried out and are presented in Tables A.1–A.5 in Appendix A, to determine suitable values for the computational domain (L_u, L_d, H) and mesh resolution. Based on this comprehensive analysis and our previous experience, a computational domain of $L_u = 120$, $L_d = 300$, and H = 300, along with a non-uniform unstructured mesh $(G_2$ consisting of $N_c = 135$, $\delta_r - \delta - \Delta = 0.005 - 0.1 - 0.5$; refer to Table A.4 for details), has been adopted to obtain the final results discussed in the subsequent sections.

4. Results and Discussion

In this study, numerical simulations have been performed to examine the influence of the flow parameters, such as Reynolds number (Re), power-law index (n), rotational rate (α), and gap ratio (G), on the unconfined flow characteristics of a pair of counter-rotating circular cylinders submerged in a power-law fluid medium. The simulations cover a broad range of conditions: $Re = 1, 5, 10, 20, 40; 0.2 \le n \le 1.8$ (steps of 0.2, covering shear-thinning, Newtonian, and shear-thickening fluid behaviors); $0.2 \le G \le 1$ (steps of 0.2); and $0 \le \alpha \le 2$ (steps of 0.5). Prior to presenting the new findings, the accuracy and reliability of the present modeling and simulation methodology are verified by comparing the results with available data [13, 42] for limited benchmark cases.

Table 2 presents a comparison of the present and literature values of the force coefficients (C_D, C_L) and their

Table 2: Comparison of present and literature values of force coefficients (C_D, C_L) for a fixed condition (G = 1, Re = 40, n = 1). The δ denotes the relative deviation between the present and literature results.

Cylinder	Parameters	Present work	Panda [42]	Kang [13]		
UC	C_D	1.6836	1.7064	1.7000		
	(δ %)	_	(1.35)	(0.97)		
	C_L	0.3591	0.3665	0.3651		
	(δ %)	_	(2.06)	(1.67)		
LC	C_D	1.6835	1.7066	1.7000		
	(δ %)	_	(1.37)	(0.98)		
	C_L	-0.3594	-0.3658	-0.3706		
	(δ %)	_	(1.78)	(3.12)		

relative deviations (δ %) for a cylinder under the limiting condition (G = 1, Re = 40, n = 1). An analysis of Table 2 shows good agreement between the present and literature results, with maximum deviations of 1.35% for drag (C_D) and 3.12% for lift (C_L) coefficients. While the drag (C_D) deviations are nearly identical for UC and LC, the lift (C_L) deviation is slightly larger for LC. Similar deviations have been reported in the literature [42, 43, 47, 50–59, 61, 63, 67, 68, 86], attributed to differences in numerical methods (FEM, FVM, FDM, LBM), solvers, and mesh refinement levels. Therefore, the present results are considered reliable and accurate within an acceptable range of $\pm 1 - 2\%$ for design and engineering applications.

4.1. Detailed flow kinematics

The detailed insights into the flow kinematics are obtained by examining the streamline patterns, velocity fields, and pressure distributions in the following sections.

4.1.1. Streamline profiles

Figs. 2 and 3 show the normalized streamline, $\psi = (\psi^* - \psi^*_{min})/(\psi^*_{max} - \psi^*_{min})$, profiles as a function of the dimensionless parameters (Re, n, α , G). Each figure presents uniformly distributed streamlines, with sub-figures organized such that rows correspond to rotational rates (A, B, C for $\alpha = 0, 1, 2$) and columns correspond to power-law indices (1, 2, 3 for n = 0.2, 1, 1.8). The streamline profiles for other conditions are shown in Appendix D. The streamline profiles are symmetric about the mid-plane for all considered flow conditions (Re, n, α , G), owing to the symmetric placement of the counter-rotating side-by-side cylinders (see Fig. 1).

For stationary cylinders ($\alpha = 0$) at Re = 1, shear-thinning and Newtonian fluids ($n \le 1$) exhibit uniform flow

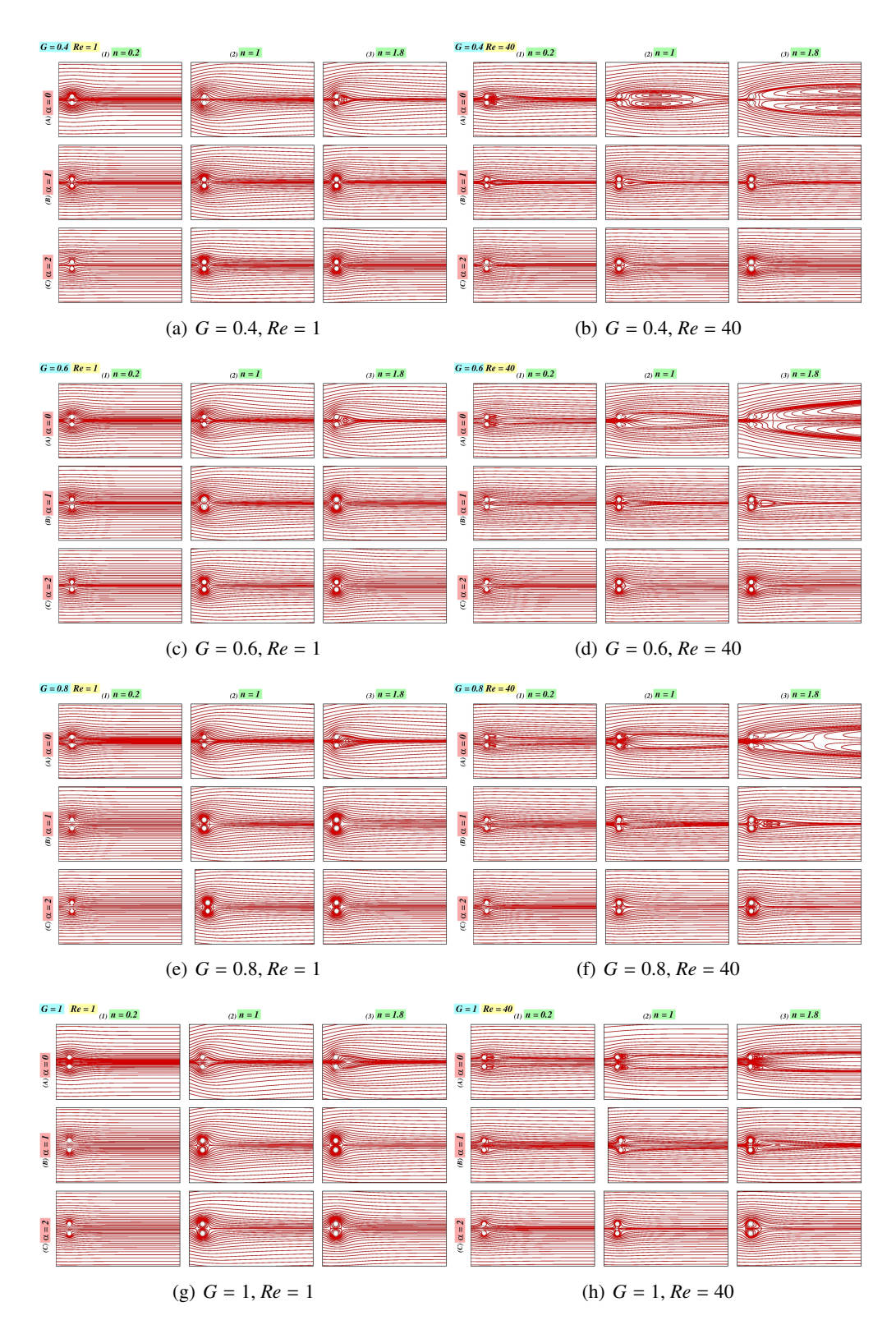


Figure 2: Influence of gap ratio $(0.4 \le G \le 1)$, power-law index $(0.2 \le n \le 1.8)$ and rotational rate $(0 \le \alpha \le 2)$ on the streamline profiles for the extreme values of Reynolds number (Re = 1, 40). The full-size images are included in Appendix D.

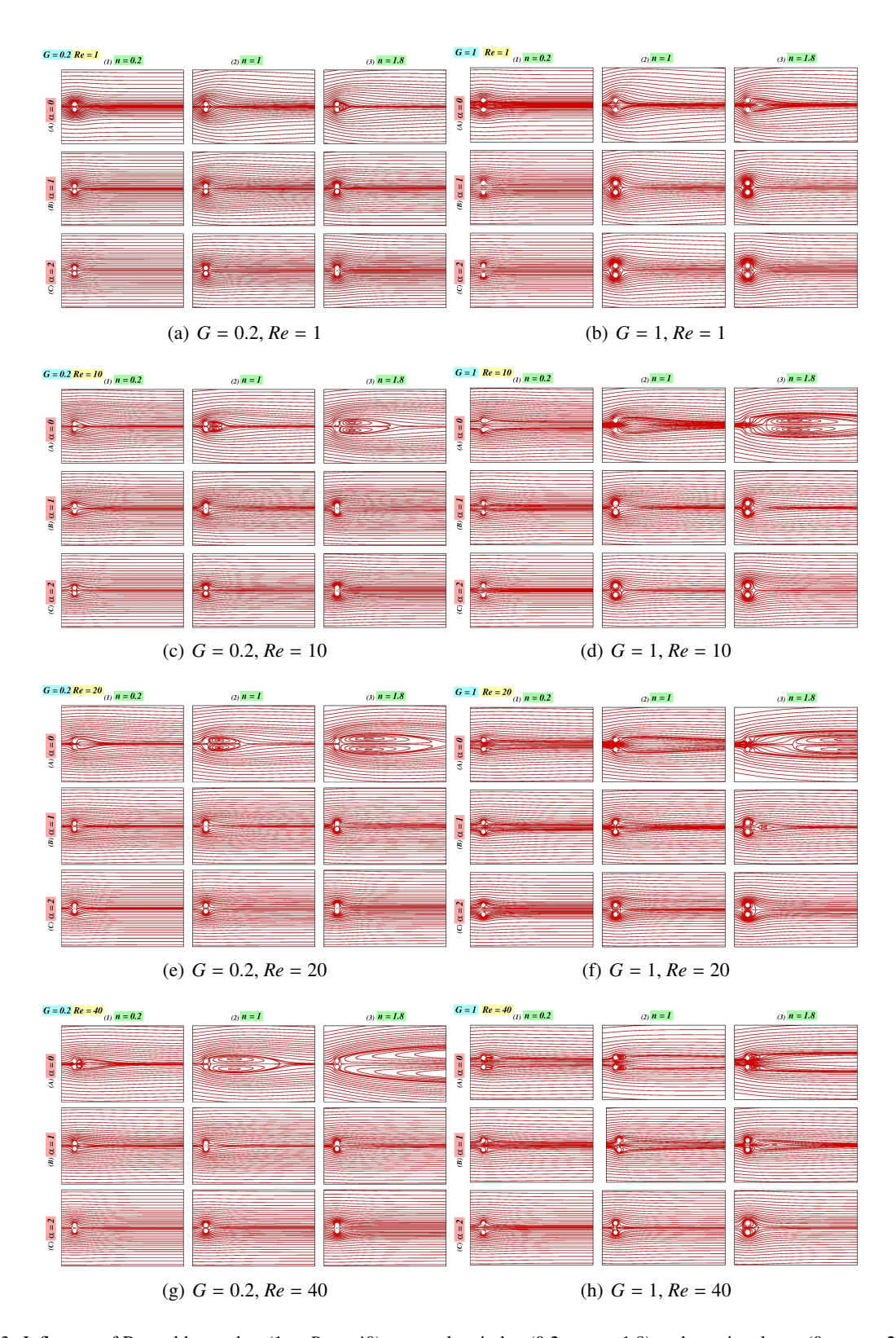


Figure 3: Influence of Reynolds number $(1 \le Re \le 40)$, power-law index $(0.2 \le n \le 1.8)$ and rotational rate $(0 \le \alpha \le 2)$ on the streamline profiles for the extreme values of gap ratio (G = 0.2, 1). The full-size images are included in Appendix D.

without separation for all gaps (G) (see panels A1-A2 in Figs. 2(a)-2(g)), consistent with previous studies [87]. In contrast, shear-thickening fluids (n > 1) show flow separation and the onset of wake formation at low gap ratios ($G \le 0.6$) (see panel A3 in Figs. 2(a) and 2(c)). For $G \le 0.6$, $Re \le 20$, and $n \ge 1$, the two stationary cylinders are hydrodynamically isolated and behave similarly to a single cylinder. At larger gaps ($G \ge 0.8$), a small residual bulge forms behind the cylinders due to the increased flow resistance of shear-thickening fluids, causing localized fluid accumulation (see panel A3 in Figs. 2(e) and 2(g)). The critical phenomena, such as vortex formation and vortex shedding, are suppressed between the cylinders due to their close proximity, an effect referred to as the "near-wall effect" [14].

For intermediate Reynolds number (Re = 10 and 20), wake formation occurs for Newtonian and shear-thickening fluids ($n \ge 1$), whereas no wake forms for shear-thinning fluids (n < 1) across all gap ratios (G) (see Figs. 3(c) and 3(e)). However, the wake disappears for Newtonian fluids (n = 1) at larger gaps ($G \ge 0.8$) (see panel A2 in Figs. D.9 and D.10). Broadly, wakes are generated by the shear layers of the upper and lower cylinders. As the gap widens, the interior shear layers interact within the gap. For small gaps, transitions between single and larger wakes increase momentum transfer. At $Re \ge 10$, increasing G from 0.2 to 0.6 produces symmetric single-body vortices downstream for $n \ge 1$, which grow and shift downstream. For larger gaps ($G \ge 0.8$), separated double-body wakes appear behind each cylinder for $n \le 1$ (panel A2 in Figs. 2(f) and 2(h)), slightly misaligned with the incoming flow due to gap size and cylinder interactions. Shear-thickening fluids, in contrast, exhibit symmetric vortex pairs behind the cylinders at $G \ge 0.8$ for $10 \le Re \le 20$.

At Re = 40, wake interference between the stationary cylinders is observed for shear-thinning fluids (n < 1) for G = 0.2 (panel A1 in Fig. 3(g)). The flow exhibits a distinct "double-body wake" structure characterized by two separated vortices behind each cylinder. The interacting shear layers promote the formation of a coherent "vortex array" in the wake region. A separated double-body wakes appear for n < 1 (at $G \ge 0.4$), for n = 1 (at $G \ge 0.8$), and for n > 1 (at G = 1), consistent with the literature [23]. Furthermore, a transition from double-body to delayed wake formation is observed for n > 1 (at G = 0.6 and 0.8) (panel A3 in Figs. 2(d) and 2(f)).

When the rotational rate increases from $\alpha=0$ to 2 at Re=1, the wake phenomenon disappears for shear-thinning fluids (n<1). Instead, a thin fluid layer forms around the cylinders (panels B and C in

Figs. 2(a)-2(g)), becoming more prominent with higher n and larger gap ratios (0.2 $\leq G \leq 1$). As α increases, vortex shedding is fully suppressed, leading to a steady, vortex-free flow [29]. This behavior is observed for $G \leq 0.6$ (at $Re \leq 20$) and for $G \geq 0.8$ (at $Re \leq 10$), where the cylinders are surrounded by increasingly thicker fluid layers with increasing G and G. Further, at G and G and G are a small residual bulge appears for Newtonian fluids at $G \leq 0.6$, becoming more pronounced as G increases. For $G \geq 0.8$, a residual bulge forms for G and G are a faint wake re-emerges behind both cylinders when G and G are a faint wake re-emerges behind both cylinders when G and G are a faint wake re-emerges behind both cylinders when G and G are a faint wake re-emerges behind both cylinders when G and G are a faint wake re-emerges behind both cylinders when G and G are a faint wake re-emerges behind both cylinders when G and G are a faint wake re-emerges behind both cylinders when G and G are a faint wake re-emerges behind both cylinders when G and G are a faint wake re-emerges behind both cylinders when G and G are a faint wake re-emerges behind both cylinders when G are a faint wake re-emerges behind both cylinders when G and G are a faint wake re-emerges behind both cylinders when G are a faint wake re-emerges behind both cylinders when G are a faint wake re-emerges behind both cylinders when G are a faint wake re-emerges behind both cylinders when G are a faint wake re-emerges behind both cylinders when G are a faint wake re-emerges behind both cylinders when G are a faint wake re-emerges behind both cylinders when G are a faint wake re-emerges behind both cylinders when G are a faint wake re-emerges behind both cylinders when G and G are a faint wake re-emerges behind both cylinders when G are a faint wake re-emerges behind both cylinders when G are a faint wake re-emerges behind both cylinders when G are a faint wak

4.1.2. Centerline velocity profiles

Fig. 4 illustrates the normalized streamwise velocity component (U_x) along the centerline $(x = L_u)$, measured along line 6 (connecting points A-B-C) in Fig. 1, between the two cylinders. The plots depict the distinct trends in the variation of U_x under different combinations of Reynolds number $(1 \le Re \le 40)$, power-law index $(0.2 \le n \le 1.8)$, rotational rate $(0 \le \alpha \le 2)$, and gap ratio $(0.2 \le G \le 1)$, where in each panel, Re and α vary along columns and rows, respectively. In general, the velocity profile exhibits a parabolic shape with maximum velocity at the mid-plane (y = 0), which becomes flatter (i.e., plug shapped) as Re, G, or α increase. The profiles remain symmetric about the mid-plane due to the symmetry of the geometrical configuration at all conditions. For low Reynolds numbers (Re = 1), the flow is dominated by viscous effects, resulting in smaller and more rounded velocity distributions, whereas at higher Reynolds numbers (Re = 40), the profiles become flatter and exhibit higher velocity magnitudes, indicating stronger inertial effects. As the power-law index (n) increases, the velocity magnitude rises, reflecting enhanced momentum transfer in shear-thickening fluids (n > 1), while shear-thinning fluids (n < 1) show suppressed velocities due to higher effective viscosity. The influence of cylinder rotation (α) is evident in the downward shift of velocity profiles and the expansion of negative velocity regions near the cylinder surfaces, particularly at higher Re, demonstrating the suppression of wake formation and the transition toward steady flow. Furthermore, increasing the gap ratio (G) broadens the flow passage and enhances the centerline velocity, as the interference between the cylinders weakens and the pressure drop

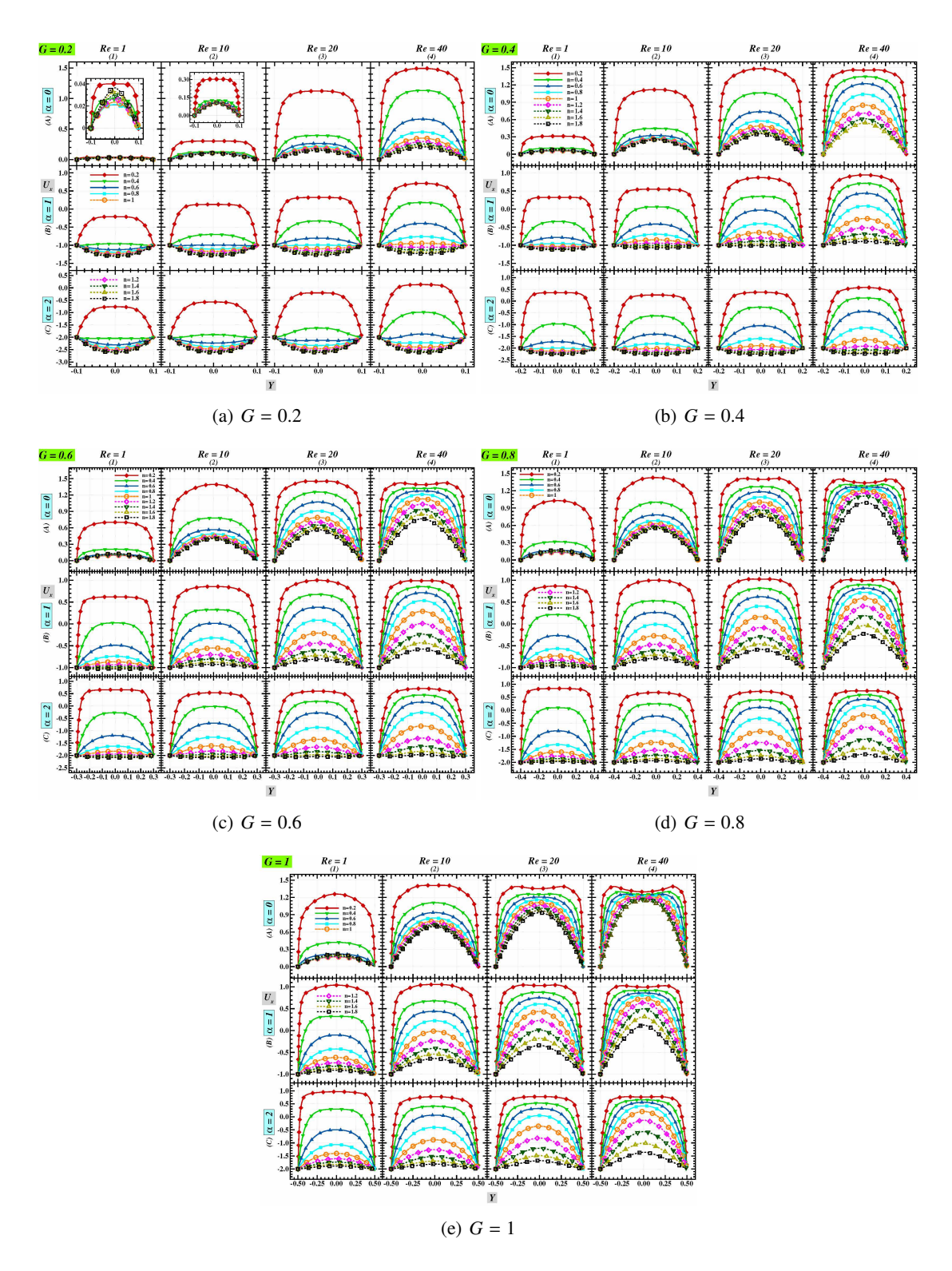


Figure 4: Centerline velocity profiles (U_x at line 6, Fig. 1) for different power-law indices (n) at various rotational rates (α in rows) and Reynolds numbers (Re in columns) for gap ratios G = 0.2 - 1. The full-size images are included in Appendix E.

across the gap decreases. Overall, the combined effects of inertia, non-Newtonian rheology, and cylinder rotation govern the shape and magnitude of the velocity profiles within the cylinders-gap region. Consistent with previous findings [13, 14, 23], closely spaced cylinders ($G \le 0.2$) exhibit weak interstitial flow characterized by reduced velocity and momentum. As G increases, the pressure in the gap decreases, leading to an enhancement of the streamwise velocity (U_x) with increasing Re.

The velocity (U_x) increases with increasing gap (G), Reynolds numbers (Re), and rotation rates (α) , indicating enhanced fluid acceleration and reduced inter-cylinder resistance, as shown in Fig. 4. However, for lower gap ratio $(G \le 0.4)$, the influence of the power-law index (n) becomes more complex due to strong shear interactions and geometric confinement between the cylinders (Figs. 4(a) and 4(b)). For all Re at smaller gaps (G < 0.6) (Fig. 4(a)) and for $Re \le 10$ at moderate gaps $(G \ge 0.6)$, see Figs. 4(c)–4(e), the maximum velocity $(U_{x,max})$ peak appears at the mid-plane (point B in Fig. 1) for all n and n indicating symmetric flow distribution dominated by viscous effects. In contrast, as the gap widens $(G \ge 0.6)$ and Re increases $(Re \ge 20)$ for slow rotations $(n \le 1)$ (refer panels A3-A4 and B3-B4 in Figs. 4(c)–4(e)), $U_{x,max}$ progressively shifts toward the surface of cylinders (i.e., towards points A and C), especially for shear-thinning (n < 1) fluids. This shift corresponds to the emergence of separated double wakes behind each cylinder, resulting in an inverse parabolic velocity distribution within the cylinders gap region, highlighting the growing dominance of inertial and non-Newtonian effects over viscous confinement at larger G and Re.

In shear-thinning fluids (n < 1), decreasing viscosity, with increasing shear rate, enhances flow acceleration in the gap between the cylinders, leading to the formation of separated double wakes and a noticeable shift of the maximum axial velocity ($U_{x,max}$) from the mid-plane toward the cylinders. As the rotational rate (α) increases, thin fluid layers form around the cylinders, which suppress wake formation and yield an inverse parabolic or concave velocity profile for Newtonian and shear-thickening fluids ($n \ge 1$) (see panels B and C in Figs. 4(a) - 4(c)). This effect becomes more prominent with increasing gap (G) and rotation (α). For instance, at G = 0.2 and $\alpha > 0$, concave profiles appear even at Re = 1 for $n \ge 0.4$, indicating reverse flow near the cylinders. Overall, these results demonstrate that fluid rheology (n) and flow parameters (Re, G, α) strongly govern the velocity field characteristics: shear-thinning behavior promotes near-wall acceleration and double wake formation, while increasing α stabilizes the flow by forming circumferential fluid layers.

The complex interplay between the flow parameters (n, G, Re, α) is clearly illustrated in Fig. 4, where the shift in peak velocity $(U_{x,max})$ towards the cylinders for $G \ge 0.6$, $Re \ge 20$, and $\alpha \le 1$ highlights the transition from symmetric to wake-dominated flow in non-Newtonian regimes.

4.1.3. Pressure coefficient (C_p) profiles

The pressure coefficient (C_p) distributions over the surfaces of the cylinders $(\phi = 0^\circ \text{ to } 360^\circ)$, presented in Fig. 5 (Figs. 1(a)–5(b) in Appendix F), display a clear inverse symmetry, where the C_p profiles of upper cylinder (UC) and lower cylinder (LC) mirror each other. This symmetric behavior persists across all examined conditions (Re, G, n, α) . The polar plots effectively capture $C_p(\phi)$ variation over the surface of cylinders, highlighting the opposing C_p distributions on the upper and lower cylinders resulting from their counter-rotating motion and geometric symmetry.

At Re = 1, the pressure coefficient (C_p) profiles maintain a nearly circular shape for all gaps (G) when the power-law index (n > 0.6), indicating uniform pressure distribution around both cylinders. As Reincreases for stationary cylinders ($\alpha = 0$), the polar plots gradually transform into hypercardioid shapes, characterized by a large high-pressure lobe at the front and a smaller one at the rear. The minima in these hypercardioid profiles correspond to regions of flow separation and wake formation behind the cylinders, marking the onset of vortex structures. With increasing rotational rate (α) , the pressure contours evolve distinctly depending on the rheological behavior of the fluid. For shear-thinning and Newtonian $(n \le 1)$ fluids, the plots largely retain their circular symmetry, whereas shear-thickening (n > 1) fluids develop an inverse one-loop limaçon shape with a slight tilt, reflecting asymmetric pressure distribution caused by rotation-induced shear effects. Furthermore, at $\alpha = 0$, the maximum C_p occurs at the front stagnation point (FSP, $\phi = 0^{\circ}$), shifting inward for smaller G and outward as the gap (G) increases. As the cylinders rotate $(\alpha > 0)$, the maxima of negative C_p shifts towards the outer side at specific angles (ϕ) , and negative C_p values are prevalent across the entire surface of the cylinders. When $\alpha > 0$, negative C_p values emerge along the outer cylinder surfaces, indicating recirculation zones. The magnitude of these negative C_p values intensify with increasing rotations (α), increasing difference in C_p between the inner and outer sides of the cylinders. Similar flow and pressure patterns have also been reported in literature [37, 39].

This symmetry in the pressure coefficient (C_p) distribution results from the counter-rotating motion of the cylinders, producing mirror-like pressure patterns on the upper surface of UC $(0^{\circ} \le \phi \le 180^{\circ})$ and the lower

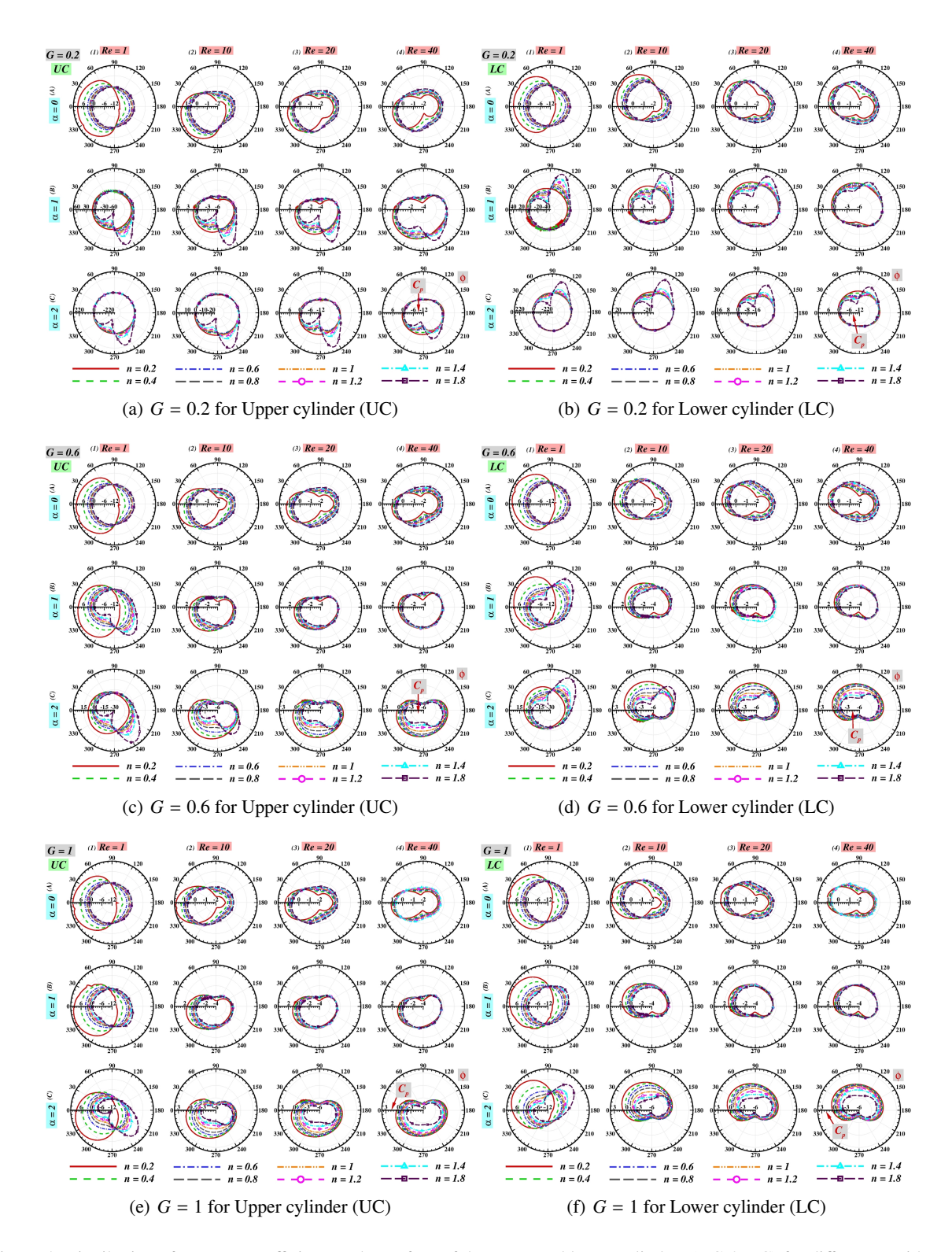


Figure 5: Distribution of pressure coefficient on the surface of the upper and lower cylinders (UC & LC) for different n with α (in rows) and Re (in columns) at gap ratio G = 0.2 - 1.

surface of LC (180° $\leq \phi \leq$ 360°). Therefore, subsequent discussions focus on the upper cylinder (UC) for clarity. The angular positions (ϕ) corresponding to maximum pressure coefficient ($C_{p,\text{max}}$) and minimum pressure coefficient ($C_{p,\text{min}}$) are denoted as ϕ_h and ϕ_l , respectively.

For stationary cylinders ($\alpha = 0$), as the Reynolds number (Re) increases from 1 to 40, the surface locations (ϕ) on the UC, corresponding to the maximum and minimum C_p values, shift noticeably. Specifically, at G = 0.2, G = 0.6, and G = 1, see panel A in Figs. 5(a), 5(c), and 5(e), the angular positions, ϕ_h and ϕ_l , vary by approximately 5% and 52% with the power-law index (n), respectively. This substantial shift in ϕ_l highlights the growing influence of inertial and rheological effects with increasing Re and n, which alter the surface pressure distribution and promote asymmetric flow separation around the cylinders. Furthermore, at low Re, the minimum pressure zones are shifted anticlockwise from the rear stagnation point (RSP, $\phi = 180^{\circ}$), indicating that they do not form directly behind the cylinder. This offset enhances the dominance of positive shear stress on one side of the cylinder, inducing a net clockwise torque. As Re increases, the single low-pressure region divides into two distinct minima, and one maxima on C_p curves; both minima shift azimuthally along the cylinder surface. This asymmetrical C_p distribution causes unequal surface areas to experience positive and negative shear stresses. With further increases in Re, these minimum C_p zones gradually become more symmetric and their magnitudes converge, reducing the imbalance between positive and negative shear stresses and leading to a more stable and uniform flow pattern around the cylinders. As the rotational rate (α) increases from 0 to 2, the pressure coefficient (C_p) exhibits a general rise with increasing power-law index (n) but decreases with Reynolds number (Re) and gap ratio (G). Broadly, $C_{p,\text{max}}$ typically occurs between $300^{\circ} \le \phi_h \le 360^{\circ}$ for shear-thinning (n < 1) fluids and $240^{\circ} \le \phi_h \le 270^{\circ}$ for shear-thickening (n > 1) fluids. For example, when Re increases from 1 to 40 at $\alpha = 2$, the angular location (ϕ_h) of maxima varies by approximately 7%, 31%, and 2% for n = 0.2, 1, and 1.8 at G = 0.2 (panel C in Fig. 5(a)); by 0%, 31%, and 8% at G = 0.6 (panel C in Fig. 5(c)); and by 1%, 26%, and 11% at G = 1(panel C in Fig. 5(e)). Similarly, the angular location (ϕ_l) of minima shifts by approximately 39%, 70%, and 1% at G = 0.2; 39%, 72%, and 73% at G = 0.6; and 40%, 31%, and 74% at G = 1 for n = 0.2, 1, and 1.8, respectively. These variations indicate that flow acceleration around the rotating cylinders, influenced by fluid rheology and gap spacing, governs the azimuthal position of C_p extrema, with stronger sensitivity

observed for Newtonian and shear-thickening regimes.

Table 3: The maximum and minimum values of the pressure coefficients ($C_{p,\max}$ and $C_{p,\min}$) with their angular positions (ϕ_h and ϕ_l) over the surface of the upper cylinder (UC) as a function of flow parameters (Re, α , n, G).

		Re = 1				Re = 10			Re = 20				Re = 40				
G	n	$C_{p,\max}$	$\phi_{ m h}$	$C_{p,\min}$	ϕ_{l}	$C_{p,\max}$	$\phi_{ m h}$	$C_{p,\min}$	ϕ_{l}	$C_{p,\max}$	$\phi_{ m h}$	$C_{p,\min}$	ϕ_{l}	$C_{p,\max}$	$\phi_{ m h}$	$C_{p,\min}$	ϕ_{l}
		•				•			$\alpha = 0$	-							
	0.2	9.680	320.7	-9.020	178.7	1.7989	318.7	-1.5410	95.3	1.3514	330.0	1.2373	78.0	1.1031	336.0	-1.3204	266.0
0.2	1	1.916	357.3	-1.605	138.7	0.8260	338.7	-0.8025	100.7	0.7517	332.0	-0.6889	89.3	0.7174	329.3	-0.5582	78.7
1	1.8	1.054	351.3	-0.839	120.7	0.6812	338.7	-0.5641	96.0	0.6502	334.0	-0.4588	89.3	0.6358	330.0	-0.3094	79.3
	0.2	10.347	327.3	-9.516	208.0	1.8556	335.3	-1.4660	95.3	1.3612	342.0	-1.3571	264.0	1.1066	343.3	-1.2817	268.0
0.4	1	1.912	357.3	-1.610	137.3	0.8528	337.3	-0.7952	99.3	0.7823	335.3	-0.6666	90.0	0.7411	337.3	-0.5498	82.0
	1.8	1.066	351.3	-0.854	121.3	0.7075	337.3	-0.5482	95.3	0.6754	335.3	-0.4317	90.0	0.6881	335.3	-0.4242	82.0
	0.2	10.663	332.0	-9.650	178.0	1.8672	341.3	-1.4207	98.7	1.3648	344.7	-1.3497	264.0	1.1093	351.3	-1.2375	270.7
0.6	1	1.928	352.7	-1.620	139.3	0.8865	336.0	-0.7786	98.7	0.8088	339.3	-0.6482	89.3	0.7550	343.3	-0.6056	82.7
	1.8	1.094	348.7	-0.866	118.7	0.7393	339.3	-0.5301	95.3	0.6991	336.0	-0.4155	89.3	0.6701	339.3	-0.3096	82.0
	0.2	10.738	338.7	-9.687	172.7	1.8739	346.0	-1.4667	254.0	1.3674	348.0	-1.3237	265.3	1.1117	348.0	-1.2208	270.7
0.8	1	1.957	351.3	-1.632	137.3	0.9171	340.7	-0.7583	100.7	0.8263	343.3	-0.6561	89.3	0.7615	346.0	-0.6614	253.3
	1.8	1.129	348.0	-0.876	118.7	0.7690	338.7	-0.5142	94.0	0.7181	340.7	-0.4245	89.3	0.6834	343.3	-0.4046	83.3
	0.2	10.735	342.0	-9.658	170.0	1.8752	348.7	-1.4935	256.0	1.3695	349.3	-1.3008	266.7	1.1126	354.7	-1.2108	274.7
1	1	1.989	351.3	-1.649	138.0	0.9405	342.0	-0.7432	100.0	0.8366	346.7	-0.6797	89.3	0.7657	348.7	-0.6814	255.3
	1.8	1.168	346.7	-0.885	118.7	0.7918	341.3	-0.5055	96.0	0.7338	344.0	-0.4578	89.3	0.7056	346.7	-0.5340	248.7
									$\alpha = 1$	1							
	0.2	8.9611	351.3	-8.9999	138.0	1.6283	329.3	-3.0267	104.7	1.2683	314.0	-2.8813	85.3	1.0834	322.0	-2.9155	80.7
0.2	1	13.5150	252.0	-13.6770	287.3	0.9590	250.0	-1.9795	90.7	0.5337	333.3	-2.0506	83.3	0.5221	326.7	-2.1204	79.3
	1.8	57.5850	250.0	-57.3600	290.0	5.4734	249.3	-5.5715	289.3	2.5557	248.0	-2.7350	288.0	1.1009	247.3	-1.9864	85.3
	0.2	9.0062	360.0	-8.4540	163.3	1.7852	323.3	-2.9535	94.0	1.3415	327.3	-2.8490	84.7	1.0570	327.3	-3.7585	84.7
0.4	1	4.2206	248.0	-4.6468	292.7	0.4603	338.7	-2.0780	91.3	0.4483	327.3	-2.1434	82.7	0.1673	324.7	-3.2651	82.7
	1.8	15.7560	243.3	-15.6860	298.0	1.1678	241.3	-1.9415	91.3	0.3544	240.7	-2.0519	80.7	0.0424	234.7	-3.2285	80.7
	0.2	10.1751	330.0	-8.9016	147.3	1.8436	331.3	-2.9399	94.0	1.3494	334.0	-2.8636	85.3	0.9447	357.3	-2.5709	106.0
0.6	1	1.7999	245.3	-2.7724	129.3	0.4149	334.0	-2.1571	90.7	0.4820	322.7	-2.1703	81.3	0.3773	341.3	-1.4369	101.3
	1.8	6.9144	237.3	-7.0066	303.3	0.2078	232.7	-2.0558	90.7	0.1172	334.0	-2.1432	79.3	0.1402	348.7	-1.3052	102.7
	0.2	10.6179	336.0	-9.2196	184.7	1.8620	335.3	-2.9373	94.7	0.5423	318.7	-2.1620	80.7	1.1067	337.3	-3.0113	82.7
0.8	1	1.5071	4.0	-2.7431	134.0	0.4479	326.7	-2.1853	90.7	0.5423	318.7	-2.1620	80.7	0.5832	322.7	-2.1663	78.0
	1.8	3.6135	230.0	-3.9070	307.3	-0.0248	337.3	-2.1366	90.7	0.1142	326.7	-2.2057	77.3	0.2813	315.3	-2.1617	79.3
	0.2	10.7997	340.0	-9.4567	178.7	1.8711	338.0	-2.9408	95.3	1.3609	338.7	-2.8908	86.7	1.1081	338.7	-3.0150	82.7
1	1	1.3846	0.0	-2.7156	127.3	0.5119	323.3	-2.1720	85.3	0.5765	322.7	-2.1521	80.7	1.1081	338.7	-3.0150	82.7
	1.8	1.9938	226.0	-2.4010	309.3	-0.0290	328.7	-2.1888	81.3	0.1674	318.7	-2.2350	77.3	0.3253	311.3	-2.1612	79.3
									$\alpha = 2$	2							
0.2	0.2	8.3354	344.0	-9.2446	145.3	1.3464	326.7	-5.1605	91.3	1.0562	322.7	-4.7635	90.7	0.9345	320.0	-4.5247	88.7
	1	26.9520	252.0	-29.6460	287.3	1.6472	242.7	-4.8244	280.7	0.4386	237.3	-3.9452	90.7	-0.0119	329.3	-4.0290	87.3
	1.8	200.8700	250.0	-201.3400	290.0	19.4750	248.7	-21.0370	289.3	9.3241	248.0	-11.2210	288.0	4.2200	246.0	-6.4592	286.7
	0.2	8.7925	336.7	-9.1592	147.3	1.4765	320.0	-5.0783	91.3	1.1547	312.7	-4.8249	90.7	0.9835	320.0	-4.5691	89.3
0.4	1	8.1040	247.3	-11.7890	290.7	-0.5063	339.3	-4.1972	91.3	-0.4948	334.7	-4.3217	86.0	-0.3880	332.0	-4.4529	86.0
	1.8	52.8709	242.0	-54.6624	298.7	4.3929	240.7	-7.1340	295.3	1.5121	237.3	-4.5043	86.0	0.0878	230.0	-4.4813	86.0
	0.2	9.7286	326.0	-9.2987	147.3	1.6119	316.0	-4.8948	91.3	1.1940	318.0	-4.9037	90.0	0.9894	325.3	-4.6088	89.3
0.6	1	3.2190	242.0	-7.2584	295.3	-0.8267	337.3	-4.4667	90.7	1.1940	318.0	-4.9037	90.0	-0.3525	318.0	-4.6121	84.0
	1.8	24.4520	237.3	-27.0910	303.3	1.0188	229.3	-4.9490	90.7	-0.3613	229.3	-4.8357	90.7	-0.9700	218.7	-4.8401	83.3
	0.2	10.1157	328.7	-9.4493	147.3	1.6472	320.7	-4.9328	92.0	1.2007	322.7	-4.9281	90.0	0.9930	327.3	-4.6478	90.7
0.8	1	1.0984	238.7	-5.2951	294.0	-0.9755	333.3	-4.6384	90.7	-0.6508	320.7	-4.7056	83.3	-0.1709	306.0	-4.5965	83.3
	1.8	13.0660	230.0	-16.4580	307.3	-0.4922	223.3	-5.0829	82.0	-1.2219	218.7	-5.1096	90.7	-1.4234	207.3	-5.1602	81.3
	0.2	10.2471	332.0	-9.5838	148.0	1.6630	324.0	-4.9429	93.3	1.2049	325.3	-4.9006	90.7	0.9956	328.7	-4.6737	89.3
1	1	-0.0343	237.3	-4.9303	120.7	-0.9612	323.3	-4.7148	83.3	-0.4773	311.3	-4.7258	81.3	-0.0892	300.0	-4.5813	83.3
	1.8	7.4525	226.0	-11.2970	310.0	-1.3064	218.7	-5.3396	81.3	-1.6917	210.0	-5.3666	82.0	-1.5865	202.0	-5.4126	81.3

Table 3 presents a detailed analysis of the maximum $(C_{p,\text{max}})$ and minimum $(C_{p,\text{min}})$ pressure coefficients, along with their corresponding angular positions (ϕ_h , and ϕ_l) for UC across different flow conditions (1 \leq $Re \le 40, 0 \le \alpha \le 2, 0.2 \le G \le 1, 0.2 \le n \le 1.8$). Overall, $C_{p,\text{max}}$ decreases with increasing Re and α , while $C_{p,\text{min}}$ shows an increasing trend. At $\alpha = 0$, $C_{p,\text{max}}$ decreases and $C_{p,\text{min}}$ increases with increasing power-law index (n) and gap ratio (G). For example, at G = 0.2 and $\alpha = 0$ (see panel A in Fig. 5(a)), when Re increases from 1 to 40, $C_{p,\text{max}}$ decreases by approximately 89%, 63%, and 40%, while $C_{p,\text{min}}$ increases by 85%, 65%, and 63% for n = 0.2, 1, and 1.8, respectively. For G = 0.2 and $\alpha = 2$ (Fig. 5(a).C), as Re increases from 1 to 40, the $C_{p,\text{max}}$ decreases by 89%, 100%, and 98%, while $C_{p,\text{min}}$ increases by 51%, 86%, and 97% for n=0.2, 1, and 1.8, respectively; similarly, for G=1 and $\alpha=2$ (Fig. 5(e).C), the $C_{p,\text{max}}$ decreases by 90%, 160%, and 121%, whereas $C_{p,\text{min}}$ increases by 51%, 7%, and 74% for n = 0.2, 1, and 1.8, respectively. These trends highlight the contrasting rheological behaviors of non-Newtonian fluids, i.e., shear-thinning fluids (n < 1) exhibit reduced viscosity and resistance with increasing shear rate, resulting in lower pressure coefficients, while shear-thickening fluids (n > 1) show the opposite behavior, with increased viscosity and higher pressure coefficients. Further, as the power-law index (n) increases, the angular positions (ϕ) progressively shifts in the direction of cylinder rotation. With increasing Re (from 1 to 40), ϕ_h shows a 5% increase for n = 0.2, while it decreases by approximately 8% and 6% for n = 1 and n = 1.8, respectively.

The analysis also indicates that increasing gap (G) from 0.2 to 1 results in a systematic increase in $C_{p,\max}$ for $\alpha=0$, irrespective of the power-law index (n). However, at a higher rotational rate ($\alpha=2$), $C_{p,\max}$ increases with G for shear-thinning fluids (n<1) but decreases for Newtonian and shear-thickening (n>1) fluids. For instance, when G increases from 0.2 to 1, $C_{p,\max}$ reduces by 11%, 4%, and 11% at Re=1 (see panel A1 in Fig. 5) and by 1%, 6%, and 10% at Re=40 (see panel A4 in Fig. 5) for n=0.2,1, and 1.8, respectively. In contrast, at $\alpha=2$, $C_{p,\max}$ increases by 23% for n=0.2 but decreases by 100% and 96% for n=1 and 1.8 at Re=1 (see panel C1 in Fig. 5), following similar trends at Re=40 (see panel C4 in Fig. 5) as increase by 7%, 600%, and 138% for n=0.2,1, and 1.8, respectively.. For stationary cylinders, the angular position (ϕ_h) shifts by 5% for n=0.2 and -7% for n=1 and n=1.8 as G increases from 0.2 to 1 with rising Re. At $\alpha=2$, ϕ_h decreases by 7% for n=0.2, increases by 31% for n=1, and decreases by 2% for n=1.8 over the same range of G and Re. The higher C_p values observed at lower gaps and higher rotations,

particularly for shear-thickening fluids (n = 1.8), stem from enhanced flow confinement and intensified fluid-cylinder interactions. The smaller spacing increases local shear and pressure buildup, while rotation amplifies shear-induced viscosity changes, collectively leading to elevated pressure coefficients.

In context of the fluid behavior, it is observed that $C_{p,\text{max}}$ increases with decreasing n (from Newtonian to shear-thinning, $n \le 1$) and decreases with increasing n (from Newtonian to shear-thickening, $n \ge 1$) for a given Re and G in the stationary cylinder case. For example, at G = 0.2 and $\alpha = 0$ (see panel A in Fig. 5(a)), $C_{p,\text{max}}$ increases by 405% and 54% for $n \le 1$, while it decreases by 45% and 11% for $n \ge 1$ at Re = 1 and 40, respectively. Similarly, at G=1 and $\alpha=0$ (panel A in Fig. 5(e)), $C_{p,\text{max}}$ increases by 440% and 45% for $n \le 1$, but decreases by 41% and 8% for $n \ge 1$. When the cylinders rotate, these trends reverse. At G = 0.2 and $\alpha = 2$ (panel A in Fig. 5(a)), $C_{p,\text{max}}$ decreases by 69% and increases by 79 folds for $n \le 1$, while it increases by 6 and 355 folds for $n \ge 1$ at Re = 1 and 40, respectively. For a higher gap (G = 1)and $\alpha = 2$ (panel A in Fig. 5(e)), $C_{p,\text{max}}$ increases with decreasing n but decreases (except at Re = 1) with increasing n, showing increases of 300 and 12 folds for $n \le 1$ and an increase of 218 folds followed by a 17-fold decrease for $n \ge 1$. The opposite behavior is observed for $C_{p,\min}$. The physical explanation lies in the shear-dependent viscosity relationship. For $n \leq 1$, viscosity decreases with shear rate, reducing flow resistance and increasing velocity, thereby increasing $C_{p,\text{max}}$. In contrast, for $n \ge 1$, viscosity increases with shear rate, enhancing resistance and lowering $C_{p,\text{max}}$. Cylinder rotation further modifies flow separation, vortex formation, and pressure distribution, leading to reversed $C_{p,\text{max}}$ trends compared to the stationary case. Additionally, higher gap (G) and rotation rate (α) influence boundary layer interaction and vortex strength, significantly affecting the overall pressure and shear distributions around the cylinders. Overall, the combination of flow parameters (Reynolds number, gap ratio, and rotational rate) influences the forces distributions of the cylinders, leading to various patterns and symmetries in the pressure coefficients across their surfaces.

4.2. Macroscopic Characteristics

This section examines the influences the flow behavior index (n), Reynolds number (Re), rotation rate (α) , and gap ratio (G) on the individual and global force (drag and lift) coefficients $(C_{DF}, C_{DP}, C_{LF}, C_{LF}, C_{D}, C_{L})$, which are key indicators of macroscopic flow behavior.

4.2.1. Components of Drag Coefficient

Figs. 6 - 7 (see also Appendix G) illustrate the effects of Reynolds number (Re), power-law index (n), rotational rate (α), and gap ratio (G) on the friction and pressure drag coefficients (C_{DF} and C_{DP}) for both cylinders, respectively. In these figures, the numerical data for the upper cylinder (UC) are represented by solid lines (—) with filled markers, while those for the lower cylinder (LC) are shown by dashed lines (----) with unfilled markers. To avoid redundancy, only the results for the upper cylinder (UC) are discussed, since the upper and lower cylinders exhibit mirror-symmetric behavior. The comprehensive datasets obtained in this work for the pressure and frictional components of the drag coefficient (C_{DP} and C_{DF}) as a function of flow governing parameters (n, Re, G, α) are included in Tables B.1 to B.5 in Appendix B.

(a) Friction drag coefficient (C_{DF})

The friction drag coefficient (C_{DF}) shows a strong dependence on the Reynolds number (Re), consistently decreasing with increasing Re across all values of n and G; however, distinct behaviors are observed in the low Re (\leq 1), intermediate Re (= 5), and high Re (\geq 10) regimes. The effect of power-law rheology (n) on C_{DF} is more pronounced at low and moderate Re, which becomes less significant at higher Re. For stationary cylinders ($\alpha = 0$) at low Re (\leq 1), C_{DF} decreases by about 68% as n increases for all G (see panel A1 in Figs. 6(a)). This reduction is attributed to the increase in apparent viscosity with increasing n, which enhances resistant to flow and thereby reduces drag, consistent with previous findings [40, 41]. However, for rotating cylinders ($\alpha > 0$) (see panels B and C in Fig. 6(a)) at $Re \leq 1$, C_{DF} initially decreases within $0.2 \leq n \leq 0.8$ for $0.2 \leq G \leq 0.6$ and within $0.2 \leq n \leq 1$ for $0.8 \leq G \leq 1$, then increases beyond these ranges. The maximum increase, observed at $\alpha = 2$, Re = 1, and G = 0.2, is about 34.5 folds as n increases from 0.2 to 1.8 (panel A1 in Fig. 6(a)). This occurs because rotation thickens the boundary layer, increasing frictional resistance, initially reducing C_{DF} but later enhancing it as rotational effects dominate.

For the intermediate Reynolds number (Re = 5) at $\alpha = 0$, C_{DF} shows a mild increase with $n \le 0.4$, followed by a decrease for n > 0.4 as G increases from 0.2 to 1. When $\alpha > 0$, however, C_{DF} consistently increases with n for all $G \ge 0.4$ (refer panels 2 to 4 in Fig. 6(a)). At smaller gaps (G = 0.2), C_{DF} initially decreases for $n \le 0.6$ and then increases for higher n values (refer panels B1 and C1 in Fig. 6(a)), as the flow behavior resembles that around a single cylinder rather than strong cylinder-cylinder interaction, leading to a different

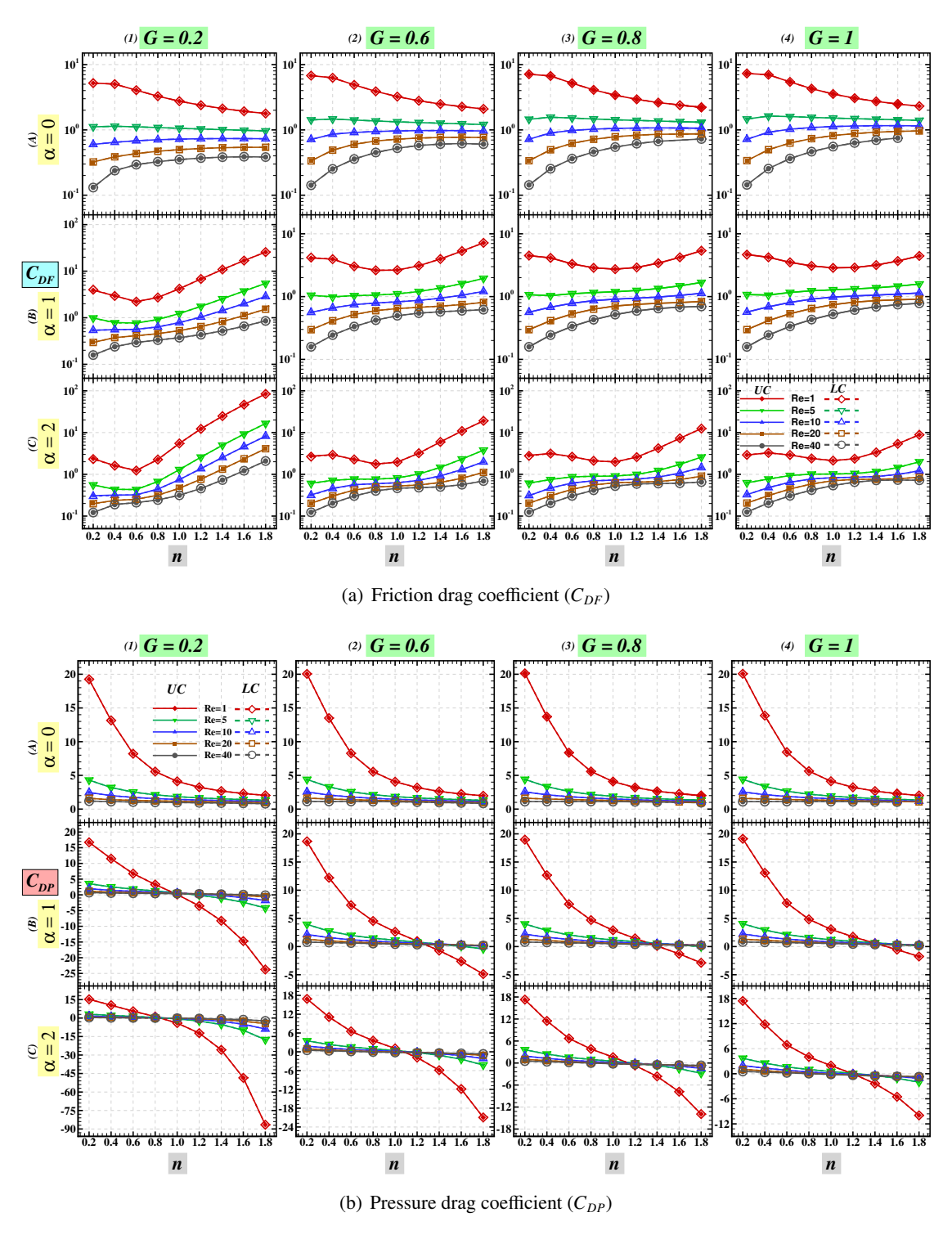


Figure 6: Variation of individual drag coefficients (C_{DP} and C_{DF}) of the both cylinders (— for UC and --- for LC) with Re and n at different α (in rows) and G (in columns).

trend in the C_{DF} compared to higher G where cylinders interaction is more significant. At higher Re (≥ 10) and $\alpha \geq 0$ for all gaps (G), C_{DF} increases with n, indicating greater frictional resistance with higher viscosity [11]. The highest C_{DF} , observed for G=1 and Re=40 (panel A4 in Fig. 6(a)), is about five times larger as n increases from 0.2 to 1.8. As n increases, viscosity and flow resistance increase, enhancing frictional drag. Similarly, increasing α thickens the fluid layer around the cylinders, enhancing viscous forces and C_{DF} , though this effect weakens with larger G.

Regarding the influence of the gap (G) between the cylinders on the friction drag coefficient (C_{DF}), consistent trends are observed for both stationary and rotating ($\alpha \ge 0$) cylinders. For stationary cylinders ($\alpha = 0$), C_{DF} consistently increases with increasing G, regardless of Re and n. However, the dependence on n shows more complexity, at low Reynolds number (Re = 1), C_{DF} decreases with increasing n, while for Re > 1, it increases with n (panel A1 in Fig. 7(a)). Overall, C_{DF} generally increases with increasing n. When the cylinders rotate ($\alpha > 0$), C_{DF} decreases with G for $Re \le 10$ and n > 1 (panels 1 and 2 in Fig. 7(a)); conversely, for shear-thinning fluids ($n \le 1$), it increases with G, showing a maximum increase of about 23% for Re = 1, n = 0.2, and $\alpha = 2$ (panel C1 in Fig. 7(a)). This effect, however, weakens as Re increases. For shear-thickening fluids (n = 1.8), C_{DF} increases with G for $\alpha = 0$ at Re = 40 (panel A4 in Fig. 7(a)) but decreases by nearly 89% for $\alpha = 2$ at Re = 1 (panel C4 in Fig. 7(a)). Additionally, at $\alpha = 1$ (for Re = 20 - 40) and $\alpha = 2$ (for Re = 40), C_{DF} first decreases and then increases with G for n > 1 (panels B3 to C4 in Fig. 7(a)). Overall, larger G tends to reduce friction drag, while the combined effects of Re, n, and α modulate C_{DF} in complex ways. These interactions significantly affect flow resistance and are crucial for optimizing rotating cylinder systems, particularly in shear-thickening fluids.

(b) Pressure drag coefficient (C_{DP})

The pressure drag coefficient (C_{DP}) decreases exponentially with increasing n and Re, as shown in Fig. 6(b), for all G and α . For stationary cylinders ($\alpha=0$) at low Reynolds number (Re=1), C_{DP} reduces by about 90% as n increases from 0.2 to 1.8 across all G (panel A1 in Fig. 6(b)); however, for rotating cylinders ($\alpha>0$), C_{DP} exhibits a sign reversal with increasing n: it changes from positive to negative at n=1 for G=0.2 (panels B1 to C1 in Fig. 6(b)), at n=1.2 for G=0.6 (panels B2 to C2 in Fig. 6(b)), and at n=1.4 for $G\geq0.8$ (panels B3 to C4 in Figs. 6(b)). Similar partial transitions occur for Re=5-10 with $G\leq0.6$, and for Re=5 with $G\geq0.8$ at $\alpha=2$. The maximum C_{DP} occurs at $\alpha=2$, G=0.2, and

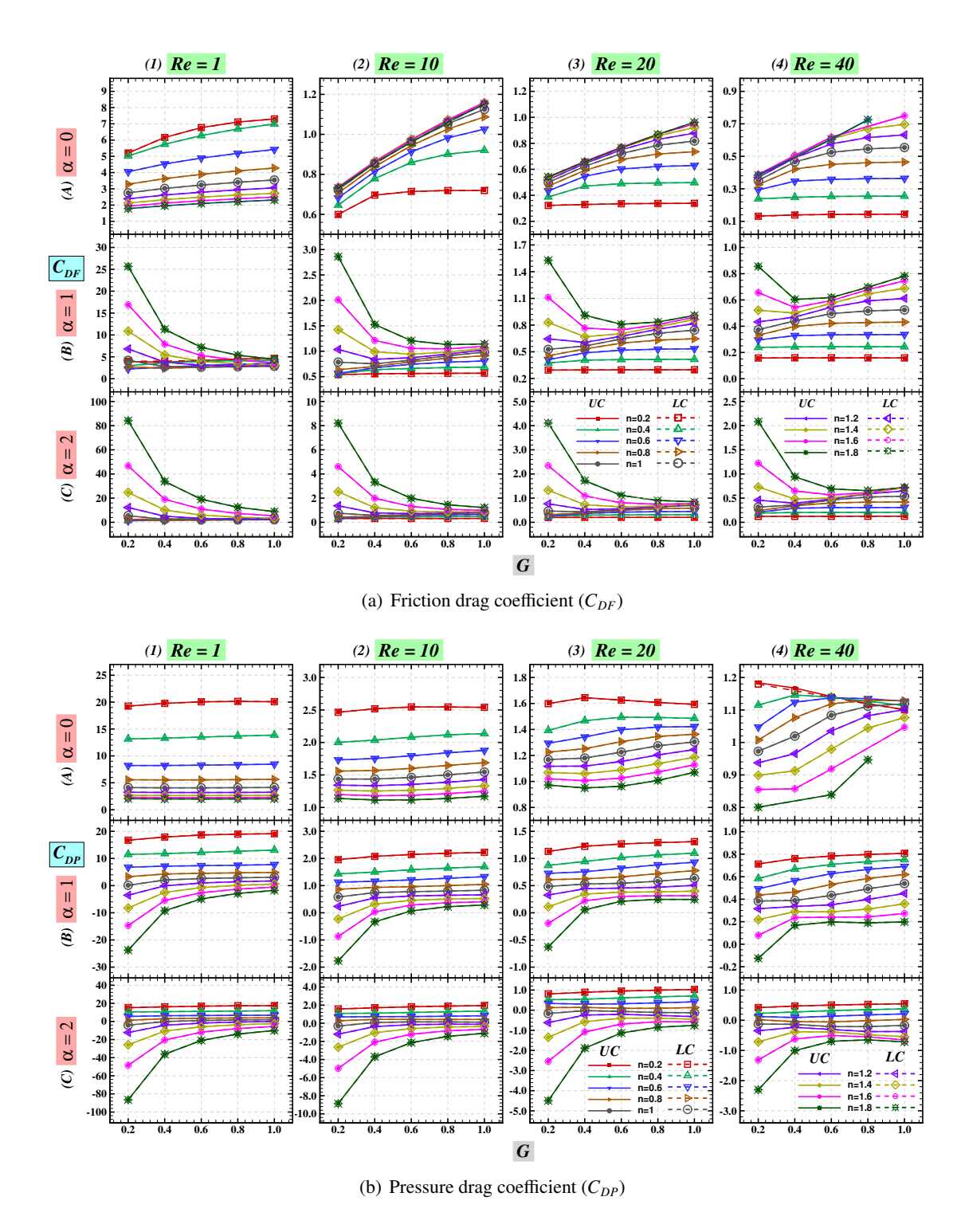


Figure 7: Variation of individual drag coefficients (C_{DP} and C_{DF}) for the both cylinders (— for UC and — for LC) with n and G at different α (in rows) and Re (in columns).

Re=1, increasing nearly seven-folds as n increases from 0.2 to 1.8 (panel C1 in Fig. 6(b)). This behavior arises from the increasing apparent viscosity (η) with n, which enhances flow resistance and alters pressure distribution around the cylinders. The observed 'positive-to-negative' transitions in C_{DP} is attributed to shear-thickening layer formation and modified vortex structures induced by cylinder rotation.

In contrast, the effect of the gap (G) on the pressure drag coefficient (C_{DP}) is shown in Fig. 7(b), where C_{DP} consistently decreases with increasing n and Re across all G and $\alpha > 0$ values. For stationary cylinders ($\alpha = 0$) at low Reynolds number (Re = 1), C_{DP} decreases slightly ($\approx 1\%$) in shear-thickening fluids (panel A1 in Fig. 7(b)), while at Re = 40, a similar trend occurs only for n = 0.2, with a larger reduction by about 7% (panel A4 in Fig. 7(b)). Interestingly, C_{DP} tends to increase with G (from 0.2 to 1) as α increases, especially in shear-thickening fluids. This effect intensifies at higher rotation rates, indicating stronger fluid-structure interactions. For instance, at $\alpha = 1$ and Re = 40, C_{DP} enhances by about 2.6 times as G increases from 0.2 to 1 for n = 1.8 (panel B4 in Fig. 7(b)). Conversely, at $\alpha = 2$ and Re = 40, C_{DP} decreases sharply with G, showing up to a 69% reduction (panel C4 in Fig. 7(b)).

These results underscore the complex interplay among α , G, Re, and n in determining the individual drag coefficients (C_{DF} and C_{DP}). Understanding these inter-dependencies is essential for optimizing the performance of rotating cylinder systems, particularly in shear-thickening fluids, where such effects strongly influence overall flow behavior.

4.2.2. Components of Lift Coefficient

Figs. 8 - 9 (see also Appendix H) illustrate the effects of Reynolds number (Re), power-law index (n), rotational rate (α), and gap ratio (G) on the friction and pressure lift coefficients (C_{LF} and C_{LP}) for both cylinders, respectively. In these figures, the numerical data for the upper cylinder (UC) are represented by solid lines (—) with filled markers, while those for the lower cylinder (LC) are shown by dashed lines (----) with unfilled markers. To avoid redundancy, only the results for the upper cylinder (UC) are discussed, since the upper and lower cylinders exhibit mirror-symmetric behavior. The comprehensive datasets obtained in this work for the pressure and frictional components of the lift coefficient (C_{LP} and C_{LF}) as a function of flow governing parameters (n, Re, G, α) are included in Tables C.1 to C.5 in Appendix C.

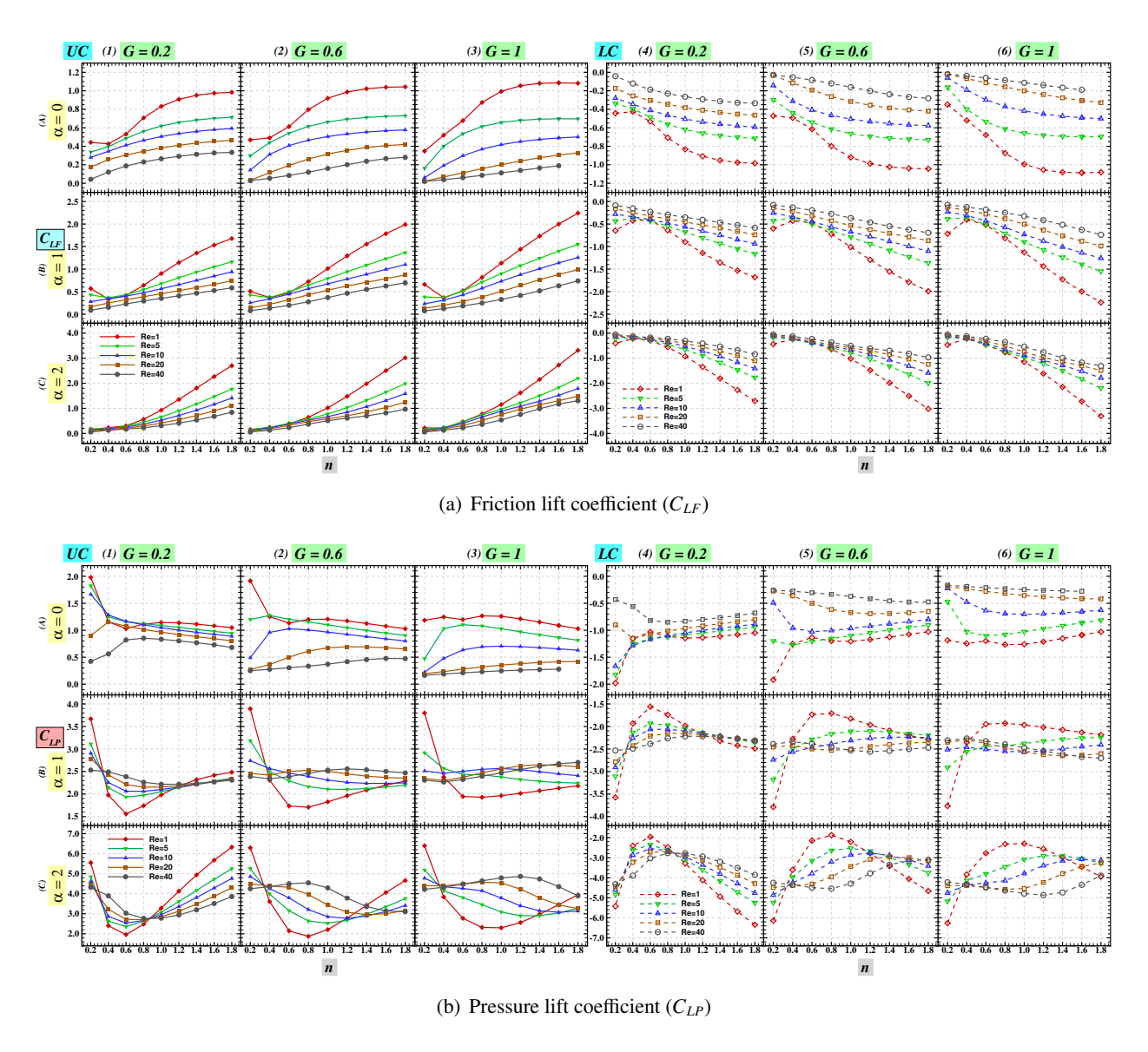


Figure 8: Variation of individual lift coefficients (C_{LP} and C_{LF}) for the both cylinders (— for UC and — for LC) with n and Re at different α (in rows) and G (in columns).

(a) Friction lift coefficient (C_{LF})

The friction lift coefficient (C_{LF}) generally increases with increasing rotational rate $(\alpha \ge 0)$ for $0.8 \le n \le 1.8$ across all G and Re values, as shown in Fig. 8(a). Higher α and n enhance fluid circulation and flow resistance in non-Newtonian fluids, producing stronger lift forces. For $\alpha = 0$ at Re = 1 and $G \le 0.4$ (panel A1 in Fig. 8(a)), and for $\alpha = 1$ at $Re \le 5$ (panel B1 in Fig. 8(a)), C_{LF} decreases for $n \le 0.4$ due to dominant shear-thinning effects, while for n > 0.4, C_{LF} increases as shear-thinning behavior weakens. The increase

in apparent viscosity with higher n enhances flow resistance, and thereby, increasing C_{LF} . For $\alpha=2$, C_{LF} varies slightly for shear-thinning fluids but significantly for shear-thickening fluids as Re increases from 1 to 40 (panel C1 in Fig. 8(a)). At G=0.4 and $\alpha=2$ with Re=1 (refer Fig. H.2), C_{LF} enhances nearly 23-fold as n increases from 0.2 to 1.8. Similarly, notable variations occur at $\alpha=2$, G=1, and Re=40 (panel C3 in Fig. 8(a)). Overall, shear-thinning fluids exhibit lower lift due to reduced viscosity, while shear-thickening fluids show higher C_{LF} from increased resistance at elevated Re and α .

In Fig. 9(a), the influence of the gap ratio (G) on C_{LF} is illustrated, showing its dependence on n, α , and Re. Only the upper cylinder (UC) results are presented due to mirror symmetry; corresponding lower cylinder (LC) results are shown in Fig. H.6. Broadly, C_{LF} decreases with increasing G and Re for all n and α , mainly due to enhanced flow stabilization, reduced separation, and thinner boundary layers at higher G and Re. For $\alpha = 0$, C_{LF} decreases with increasing G for $Re \ge 10$ and all n, reducing maximally by 88% at Re = 20, n = 0.2 (panel A3 in Fig. 9(a)). At Re = 1, the reduction is about 21% for n = 0.2, while a slight 10% increase is seen for n = 1.8 (panel A1 in Fig. 9(a)) due to enhanced flow separation at larger gaps. At $\alpha = 1$, C_{LF} increases with increasing G for Re = 1 across all n, with a 34% maximum increase at n = 1.8 (panels B1 to B3 in Fig. 9(a)). Similar upward trends occur for $5 \le Re \le 10$ and $n \ge 0.6$, and for $Re \ge 20$ with n > 1 (panels B2 to B4 in Fig. 9(a)). At $\alpha = 2$, C_{LF} increases with increases G for Re = 1, reaching a 54% increase at n = 0.6 (panel C1 in Fig. 9(a)). For $Re \ge 5$ and $n \ge 0.4$, the maximum increase is 85% at Re = 40, n = 1.2 (panels C2 to C4 in Fig. 9(a)). Thus, higher rotation enhances lift generation, especially at larger gap (G).

(b) Pressure lift coefficient (C_{LP})

The pressure lift coefficient (C_{LP}) exhibits a complex dependence on the flow parameters (G, Re, α , n) in Figs. 8(b). For stationary cylinders ($\alpha = 0$) and Re = 1, C_{LP} initially decreases with increasing $n \le 0.6$ (for $G \le 0.8$) (Panels A1 to A2 in Fig. 8(b) and in Fig. H.4), then increases up to n = 1.2 (for $G \le 0.4$) and n = 1 (for $0.6 \le G \le 0.8$), followed by another decline. Overall, C_{LP} varies by about 47% as n increases from 0.2 to 1.8 for $G \le 0.8$. For G = 1, C_{LP} increases with $n \le 0.4$, decreases at n = 0.6, increases again near n = 1, and finally reduces at higher n (panel A3 in Fig. 8(b)). At Re = 5 and $G \le 0.4$, as well as Re = 10 and G = 0.2, C_{LP} decreases with increasing n (panel A1 in Fig. 8(b)), primarily due to enhanced vortex shedding and stronger flow separation (Figs. 2 to 3), which lower pressure lift (C_{LP}). For higher Re,

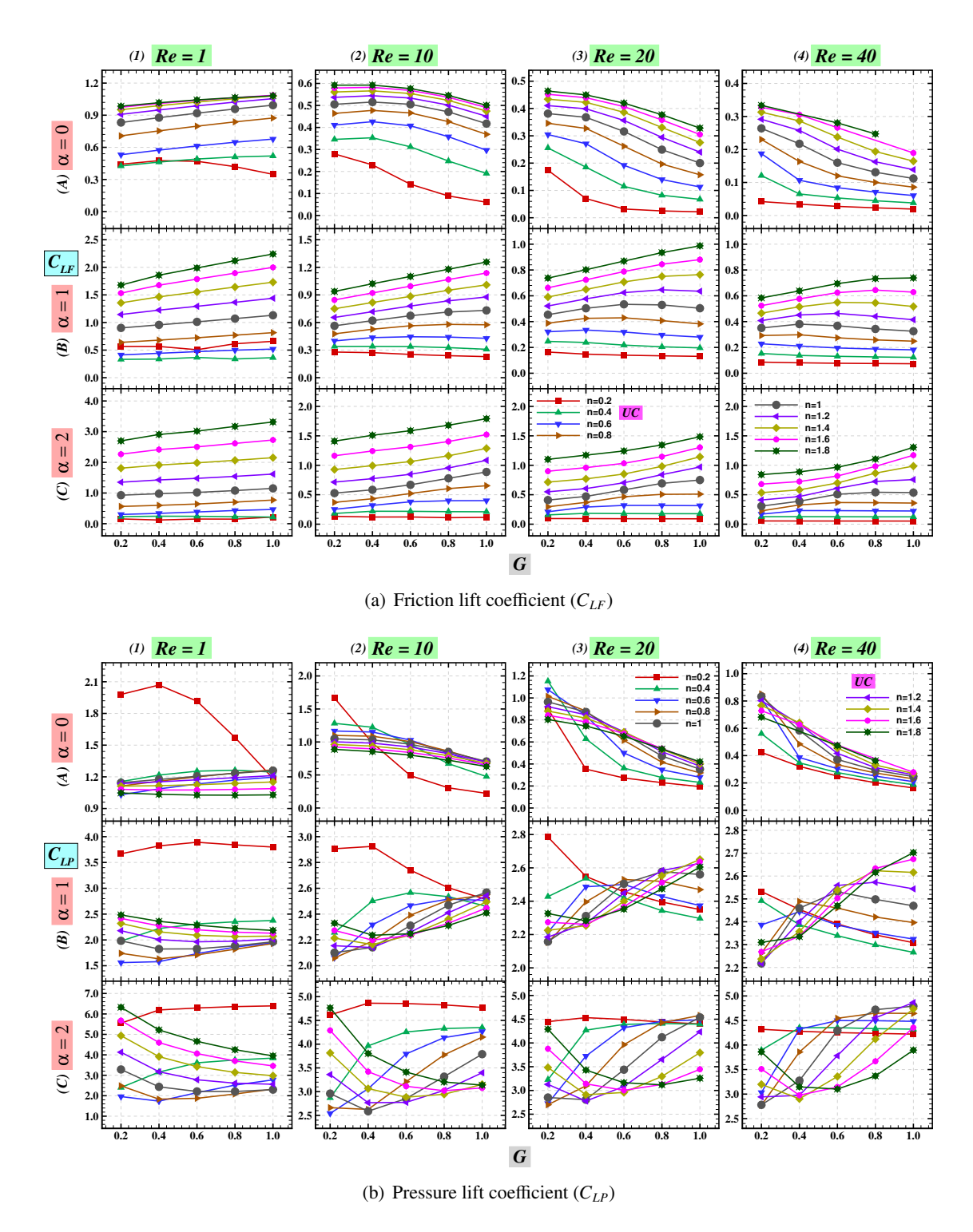


Figure 9: Variation of individual drag coefficients (C_{DP} and C_{DF}) for the both cylinders (— for UC and — for LC) with n and G at different α (in rows) and Re (in columns).

 C_{LP} shows an interesting non-monotonic trend, i.e., initially enhancing with increasing n (up to a threshold) before declining. This occurs, for instance, at $n \le 0.4$ for Re = 20 (at G = 0.2), Re = 10 (at G = 0.4), and Re = 5 (at G = 0.6); beyond these threshold points, C_{LP} slightly decreases (panel A in Fig. 8(b)). The increase in C_{LP} with n reflects shear-thickening behavior, where higher n enhances viscosity and lift due to increased flow resistance. The subsequent decline results from competing effects of viscosity, flow inertia, and geometric spacing. When n increases from 0.2 to 1.8, C_{LP} generally rises for Re = 20 (at $G \ge 0.8$) and for Re = 40 (at $G \ge 0.4$), where larger gap (G) weaken cylinder interactions and promote stronger individual vortex formation, leading to elevated pressure lift

Further, the pressure lift coefficient (C_{LP}) increases with rotations $(\alpha > 0)$ and remains relatively stable in highly shear-thinning (n = 0.2) to shear-thickening (n = 1.8) fluids for all G and Re (panels B to C in Fig. 8(b)). However, for intermediate n values, C_{LP} decreases with increasing G across all Re. The increasing α generates a thin high-velocity fluid layer around the cylinders, enhancing lift through the Magnus effect, which increases C_{LP} . Broadly, three distinct trends are observed in lift coefficient (C_{LP}) curves for $\alpha > 0$ in Fig. 8(b) as follows. (i) In the first trend, C_{LP} initially decreases with increasing n up to a critical value, beyond which it rises. For example, when $\alpha \ge 1$, C_{LP} decreases for n < 0.6 at G = 0.2and $Re \le 10$, and for n < 0.8 at $Re \le 40$ (panels B1 to C1 in Fig. 8(b)). Similar patterns occur at G = 0.6and G = 1 with critical n values shifting higher as Re increases (panels B2 to C3 in Fig. 8(b)). At $\alpha = 1$, G = 0.2, and Re = 1, C_{LP} decreases by about 32% as n increases from 0.2 to 1.8, whereas for $\alpha = 2$ it increases by approximately 14%. These variations arise from changes in fluid resistance and the stability of the thin layer around the cylinders. (ii) The second trend is non-monotonic: C_{LP} decreases initially and then increases, or vice versa. For instance, at $\alpha = 1$ and $G \ge 0.6$, C_{LP} decreases for $n \le 0.4$, then increases for $0.4 \le n \le 1.2$, and finally decreases again (panels B2 to B3 in Fig. 8(b)) at $Re \ge 20$. This behavior results from competing effects of shear-thickening viscosity and flow separation. (iii) In the third trend, for $\alpha = 2$ and $G \ge 0.6$, C_{LP} increases with n < 0.8 at Re = 40 (G = 0.6) and Re = 20 (G = 1), but decreases beyond these n values (panels C2 to C3 in Fig. 8(b)). These changes are governed by the interaction between rotation, gap width, and non-Newtonian rheology, which modulate the flow structure, shear rate, and pressure distribution around the cylinders.

Furthermore, for stationary ($\alpha = 0$) cylinders, C_{LP} generally decreases with increasing G (from 0.2 to 1) for

 $Re \ge 5$ and all values of n (refer Fig. 9(b) for UC and Fig. H.6 for LC). However, a distinct trend appears at Re = 1, i.e., for n = 0.2 and 1.8, C_{LP} decreases, whereas for $0.4 \le n \le 1.6$, it increases with G (panel A1) in Fig. 9(b)). This behavior can be attributed to the expanded flow passage and enhanced fluid recirculation in wider gaps, which collectively reduce the net lift on the cylinders. At $\alpha = 0$ and Re = 10, C_{LP} shows a significant reduction of about 87% as G increases, particularly for the strongly shear-thinning case (n = 0.2)(panel A2 in Fig. 9(b)). With increasing α , the variation of C_{LP} becomes increasingly complex across the range $0.2 \le G \le 1$. The rotational motion alters the vortex-shedding dynamics, and as G increases, the flow transitions from a single attached vortex to separated twin vortices between the cylinders. For shear-thinning fluids, C_{LP} first increases with G and then decreases for higher n values at Re = 1 ($\alpha = 1$) (panel B1 in Fig. 9(b)) and $Re \le 10$ ($\alpha = 2$) (panels B1 to B2 in Fig. 9(b)). Similarly, for Re = 5 - 10 ($\alpha = 1$) and $Re \ge 20$ $(\alpha = 2)$ (panels B3 to B4 in Fig. 9(b)), C_{LP} decreases with increasing G for n = 0.2 before subsequently increasing. At $\alpha = 1$, C_{LP} decreases with increasing G by approximately 16% for Re = 20 and $n \le 0.4$ (panel B3 in Fig. 9(b)), and by about 9% for Re = 40 and $n \le 0.6$ (panel B4 in Fig. 9(b)), followed again by an upward trend. At higher rotation rates ($\alpha = 2$), C_{LP} demonstrates contrasting behaviors depending on Re and n. For instance, at Re = 1, C_{LP} decreases markedly by about 40% as G increases, particularly at n = 1.4 (panel C1 in Fig. 9(b)). Conversely, for Re = 20, it increases by nearly 70% at n = 0.6 (panel C3 in Fig. 9(b)). Overall, these findings emphasize the intricate coupling between gap geometry, rotational effects, flow inertia, and non-Newtonian rheology in shaping the pressure lift behavior of the cylinders.

4.2.3. Total force coefficients over the cylinders

Figs. 10 - 11 (and Appendix I) illustrate the variations of total drag and lift coefficients ($C_D = C_{DP} + C_{DF}$, $C_L = C_{LP} + C_{LF}$) with Reynolds number (Re) and power-law index (n) for different gap ratios (G) and rotational rates (α). Solid lines (—) with filled markers represent the data for the upper cylinder (UC), while dashed lines (----) with unfilled markers denote for the lower cylinder (LC).

(a) Total drag coefficient (C_D)

The drag coefficient (C_D) for both cylinders broadly exhibit close similarity. The variation of C_D with n (Fig. 10(a)) closely resembles that of C_{DP} (panel 2 in Fig. 6), consistent with earlier studies [40–42]. The contribution of C_{DF} shifts the crossover point toward higher Re. Moreover, as n increases, lower C_D values

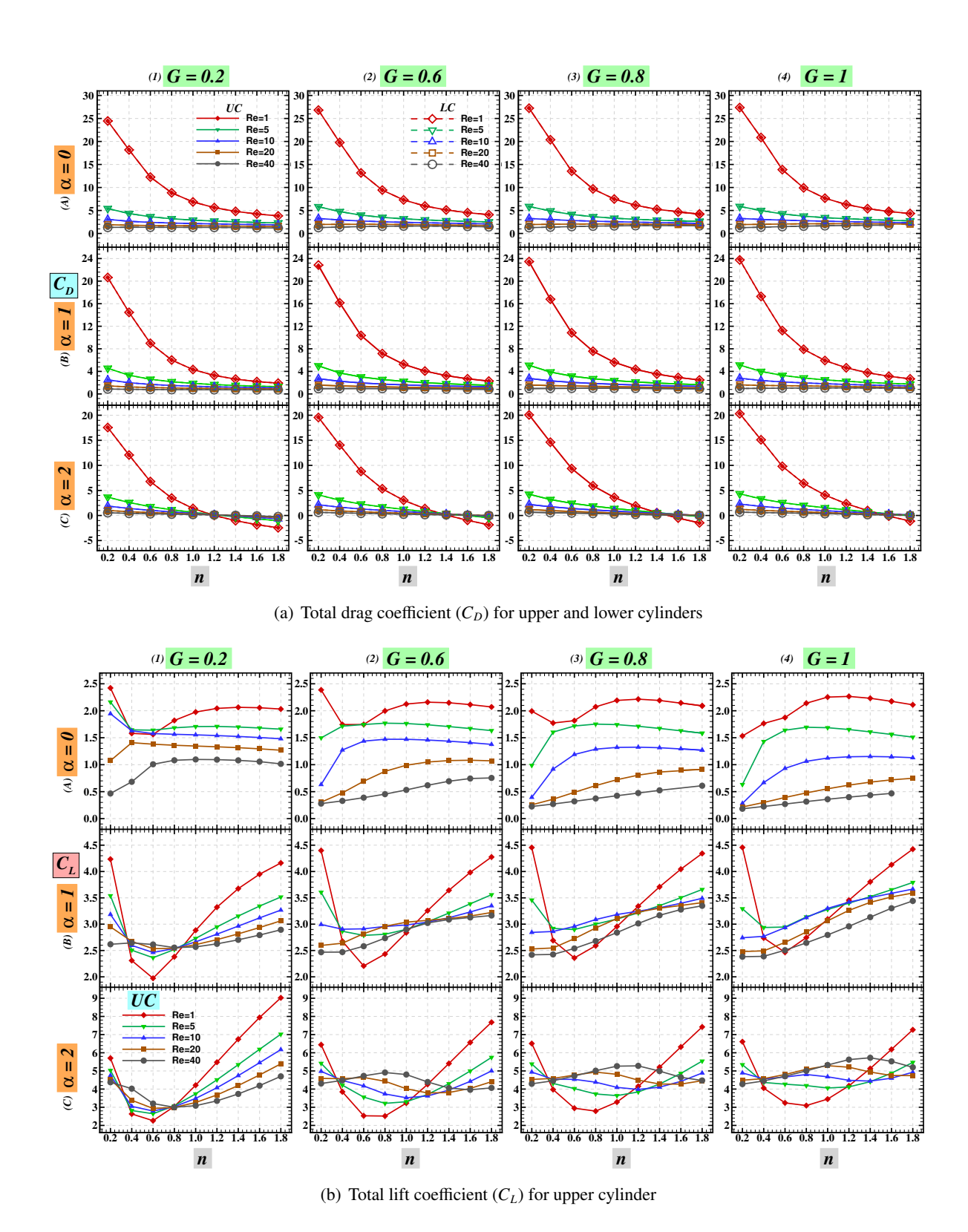
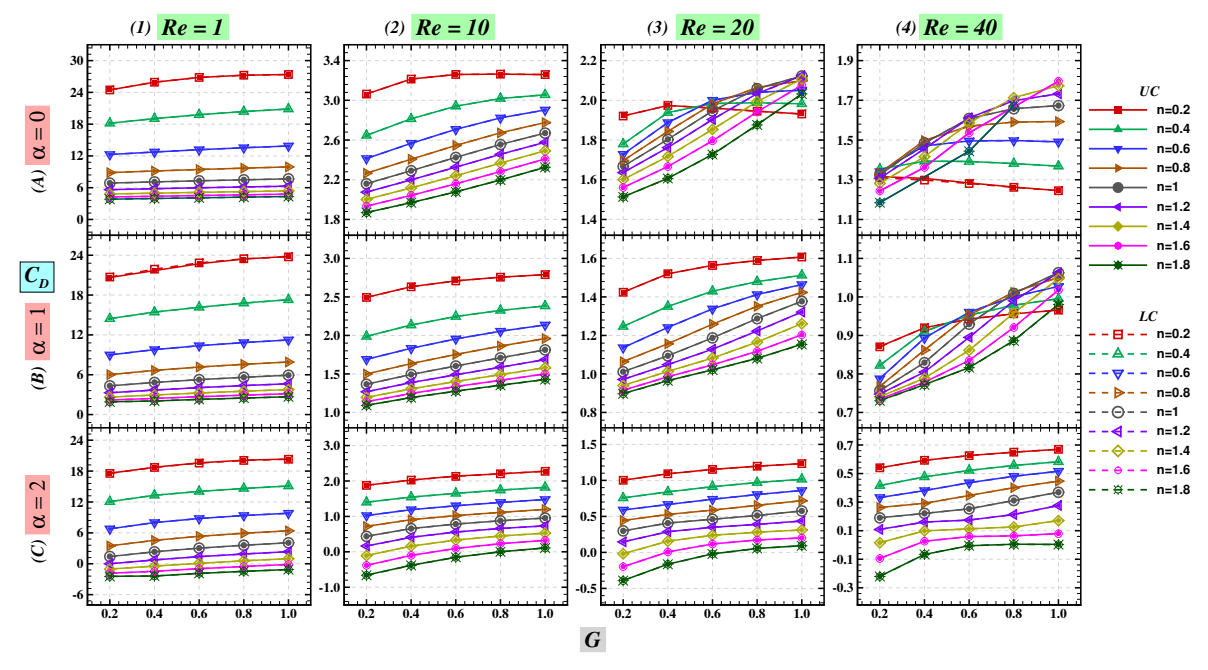


Figure 10: Variation of total drag and lift coefficient (C_D and C_L) for Re with n at different α (in row) and G (in column).

are observed at higher Re [42].

Generally, for $\alpha \leq 1$, C_D decreases with increasing Re and increases with G for all n (panels A and B in Fig. 10(a)). For $\alpha = 0$, C_D decreases exponentially with increasing n across all G for $Re \le 20$, leading to a substantial reduction of about 85% at Re = 1 (panel A in Fig. 10(a)). However, at Re = 40, a more complex dependence on G is observed. For example, as n increases from 0.2 to 1.8, C_D decreases by approximately 10% at G = 0.2 (panel A1 in Fig. 10(a)) but increases by 44% at G = 1 (panel A4 in Fig. 10(a)). For intermediate gaps (0.4 $\leq G \leq$ 0.8), C_D first rises up to a certain n and then declines beyond it (panels A2 to A3 in Fig. 10(a)). Remarkably, at higher rotations ($\alpha = 2$), C_D follows a similar trend to lower α , but becomes negative $(C_D < 0)$ for $n \ge 1.4$ when $G \le 0.6$ at all Re (panels C1 to C2 in Fig. 10), and for $n \ge 1.6$ at low $Re \leq 5$ when $G \geq 0.8$ (panels C3 to C4 in Fig. 10). At sufficiently high rotation speeds ($\alpha = 2$), the shear layers can reattach to the cylinder surface, causing wake deflection or even suppression, which results in the formation of bi-stable wakes. This wake asymmetry induces a streamwise thrust, analogous to the Magnus-type propulsion effect, and can consequently yield negative drag ($C_D < 0$). The occurrence of negative drag ($C_D < 0$) is primarily attributed to the pressure distribution around the cylinders rather than viscous shear effects; in such cases, the pressure-induced thrust surpasses the viscous resistance, leading to a net negative drag force. This observation is consistent with earlier studies [12, 46] conducted for Newtonian fluids (n = 1), where similar wake suppression and thrust generation phenomena were reported at high rotation rates.

Focusing on the influence of G (Fig. 11(a)), C_D generally increases with G but decreases with increasing other parameters $(n, \alpha, \text{ and } Re)$, except for $\alpha = 0$ (at $Re \geq 20$) and $\alpha = 1$ (at Re = 40). For Re = 20 and $\alpha = 0$, C_D initially increases with $G \leq 0.4$ for $n \leq 0.4$, then decreases for G > 0.4 (panel A3 in Fig. 11(a)). Similarly, at Re = 40, C_D decreases with G for strongly shear-thinning $(n \leq 0.6)$ fluids but increases for weakly shear-thinning to shear-thickening (n > 0.8) fluids (panel A4 in Fig. 11(a)). Notably, at $\alpha \leq 1$ and G = 1, C_D increases with n, particularly for shear-thinning (n < 1) fluids (panel B4 in Fig. 11(a)). These complex dependencies underscore the sensitivity of drag coefficinet (C_D) to flow governing parameters $(G, Re, \alpha, \text{ and } n)$, resulting in diverse hydrodynamic behaviors across flow regimes. Furthermore, as α increases, C_D consistently decreases with G for all G and G and G are and G and G are and G are and G are an anomalous to the larger surface area exposed to the flow at higher G, which modifies boundary-layer behavior and drag distribution.



(a) Total drag coefficient (C_D) for upper and lower cylinders

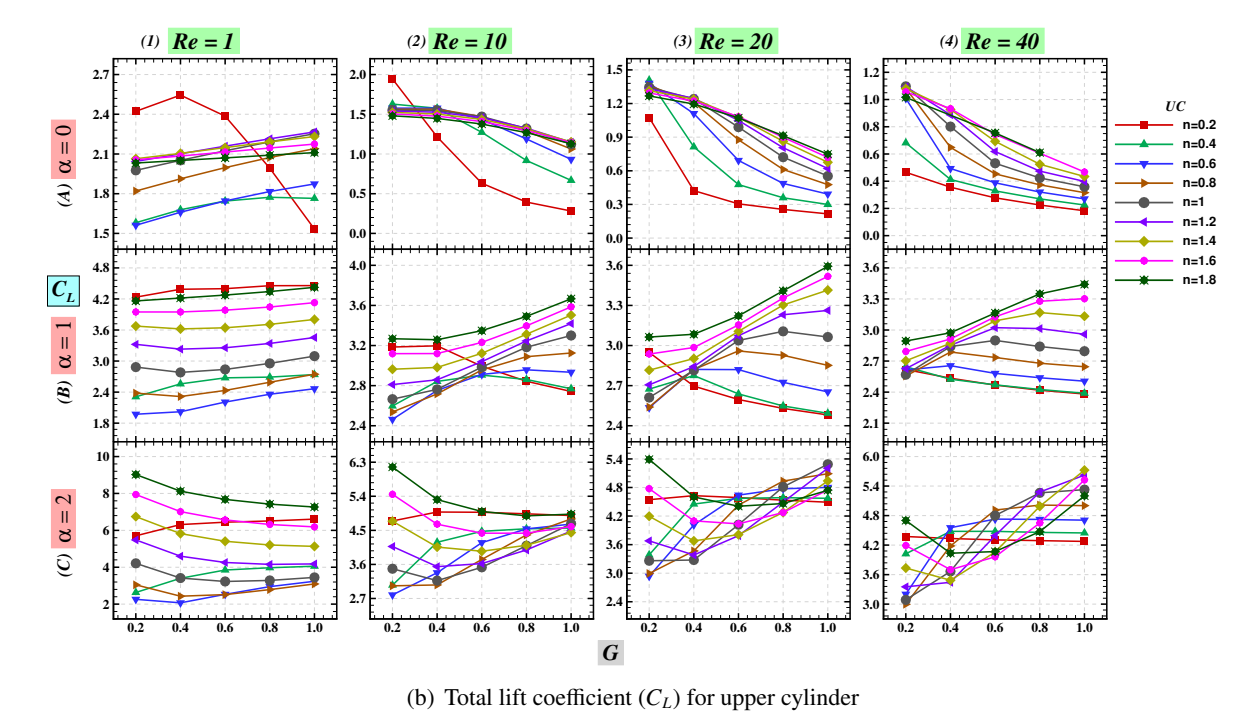


Figure 11: Variation of total drag and lift coefficient (C_D and C_L) for n with G at different α (in rows) and Re (in columns).

(b) Total lift coefficient (C_L)

The total lift coefficient (C_L) exhibits opposite signs for the upper and lower cylinders due to symmetry. The variation of C_L with n (Fig. 10(b) for UC and Fig. I.6(a) for LC) resembles that of C_{LP} (Fig. 8(b)).

In general, C_L decreases with increasing Re at both low (n=0.2) and high (n=1.8) power-law indices, whereas it increases with α for all G and Re. Complex transitions are observed at intermediate n due to shifts in rheological behavior from shear-thinning (n<1) to Newtonian (n=1) and then to shear-thickening (n>1). For stationary cylinders ($\alpha=0$), C_L initially decreases (up to 36%) with increasing $n\le0.6$ for $Re\le5$ and $G\le0.4$, then increases up to n=1.4 up to 32% (for G=0.2) and by 27% (for G=0.4) at Re=1, before decreasing again (panels A1 to A2 in Fig. 10(b)). At Re=10, C_L decreases by 24% with increasing n (from 0.2 to 1.8) for G=0.2 (panel A1 in Fig. 10(b)). Further, C_L increases with n for $0.4\le G\le0.6$ at Re=40 and for $G\ge0.8$ at $Re\ge20$ (panel A in Fig. 10(b)). A similar pattern appears at $\alpha=1$, where C_L rises with n for G=0.4 at G=0.6 at G=0.6 at G=0.8 at G=0

For rotating cylinders ($\alpha \ge 1$), C_L often decreases with n up to a threshold (e.g., $n \le 0.6$ for $Re \le 20$ at G = 0.2), then increases thereafter. The largest decreases ($\sim 60\%$) and subsequent increases (about 3-fold) occur at $\alpha = 2$, Re = 1 (panel C1 in Fig. 10(b)). Similar multi-phase complex trends are observed at $\alpha = 1$ (for G = 0.4, Re = 20) and $\alpha = 2$ (for G = 0.4, Re = 40) (panels B2 to B3 in Fig. I.2). For $\alpha = 2$, G = 1, and G = 10, G = 10, G = 10, decreases by 7% at G = 10, increases by 5% at G = 10, decreases again by 8% at G = 10, and G = 10, G =

Regarding the effect of G (Fig. 11(b) for UC and Fig. I.6(b) for LC), at $\alpha=0$, C_L decreases with increasing G for $Re \geq 5$ and all n, and also at Re=1, n=0.2 (panel A1 in Fig. 11(b)). The largest reduction (about 86%) occurs at Re=10, n=0.2 (panel A2 in Fig. 11(b)). Conversely, at Re=1 and $n \geq 0.4$, C_L increases with G. At G = 1, G increases with G for all G (at G = 1) and for G = 1. And for G = 2. And for G = 3. And for G = 3. And for G = 4. And G = 4

n, it decreases. The maximum increase (73%) is recorded at Re = 40, n = 1 (panel C4 in Fig. 11(b)), while the largest reduction (24%) occurs at Re = 1, n = 1.2 (panel C1 in Fig. 11(b)). Overall, the variation of C_L with G reflects the intricate coupling of Re, n, and α . Changes in G modify vortex-shedding structures and inter-cylinder flow, which in turn alter lift generation. These findings highlight the complex interactions governing the aerodynamic characteristics of rotating cylinder pairs in non-Newtonian fluids.

4.2.4. Drag and lift ratio (C_{DR} and C_{LR})

To emphasize the relative contributions of the individual drag and lift components, the drag ratio (C_{DR} = C_{DP}/C_{DF}) and lift ratio ($C_{LR} = C_{LP}/C_{LF}$) are shown over a range of Reynolds numbers (Re), power-law indices (n), rotational speeds (α) and gap ratios (G), as illustrated in Fig. 12 (see also Appendix J). In these figures, the solid and dashed lines represent the upper and lower cylinders, respectively. The near overlap of these lines reflects the mirror-symmetric flow behavior, making their responses effectively indistinguishable. Both the drag ratio (C_{DR}) and lift ratio (C_{LR}) show a decreasing trend with increasing power-law index (n)for all gap ratios (G) and rotation rates (α). For stationary cylinders ($\alpha = 0$), both ratios increase with Reynolds number (Re) across all G and n. Higher values of C_{DR} and C_{LR} occur at lower n (shear-thinning fluids), while lower values correspond to higher n (shear-thickening fluids). For $\alpha = 0$, as n increases from 0.2 to 1.8, C_{DR} decreases by 68% (for Re = 1) and 81% (for Re = 40) across all G, refer panel A in Fig. 12(a); similarly, C_{LR} decreases by 75% (for Re = 1) and 81% (for Re = 40), refer panel A in Fig. 12(b). At $\alpha = 1$, for shear-thickening fluids $(n \ge 1.4)$, a negative C_{DR} is observed at $Re \le 10$ and $G \le 0.4$ (panel B1 in Fig. 12(a)), particularly for Re = 1, G = 1 (panel B4 in Fig. 12(a)). This negative trend arises from increased flow resistance, leading to reversed pressure contributions. For example, for $\alpha = 1$, C_{DR} and C_{LR} decrease by 115% and 81% at Re = 1, and by 94% and 88% at Re = 40, respectively (panel B in Figs. 12(a) and 12(b)). These reductions demonstrate the strong influence of cylinder rotation on hydrodynamic forces and system sensitivity to flow conditions. Further, at $\alpha = 2$, a similar trend is noted for $n \ge 1$ across all Re and G (panel C1 in Fig. 12(a)), while for shear-thinning fluids $(n \le 1)$, C_{DR} increases with Re. For α = 2, C_{DR} and C_{LR} decrease by 118% and 96% at Re = 1, and by 128% and 96% at Re = 40 (panel C1 in Fig. 12(a), and panel C4 in 12(b)). Furthermore, C_{LR} increases with α for all G, Re, and n (panel 2 in Fig. 12), reflecting the Magnus effect, where rotation induces circulation and enhances lift. These findings underscore the interplay between fluid rheology (n), flow parameters (Re), and geometric configuration (G)

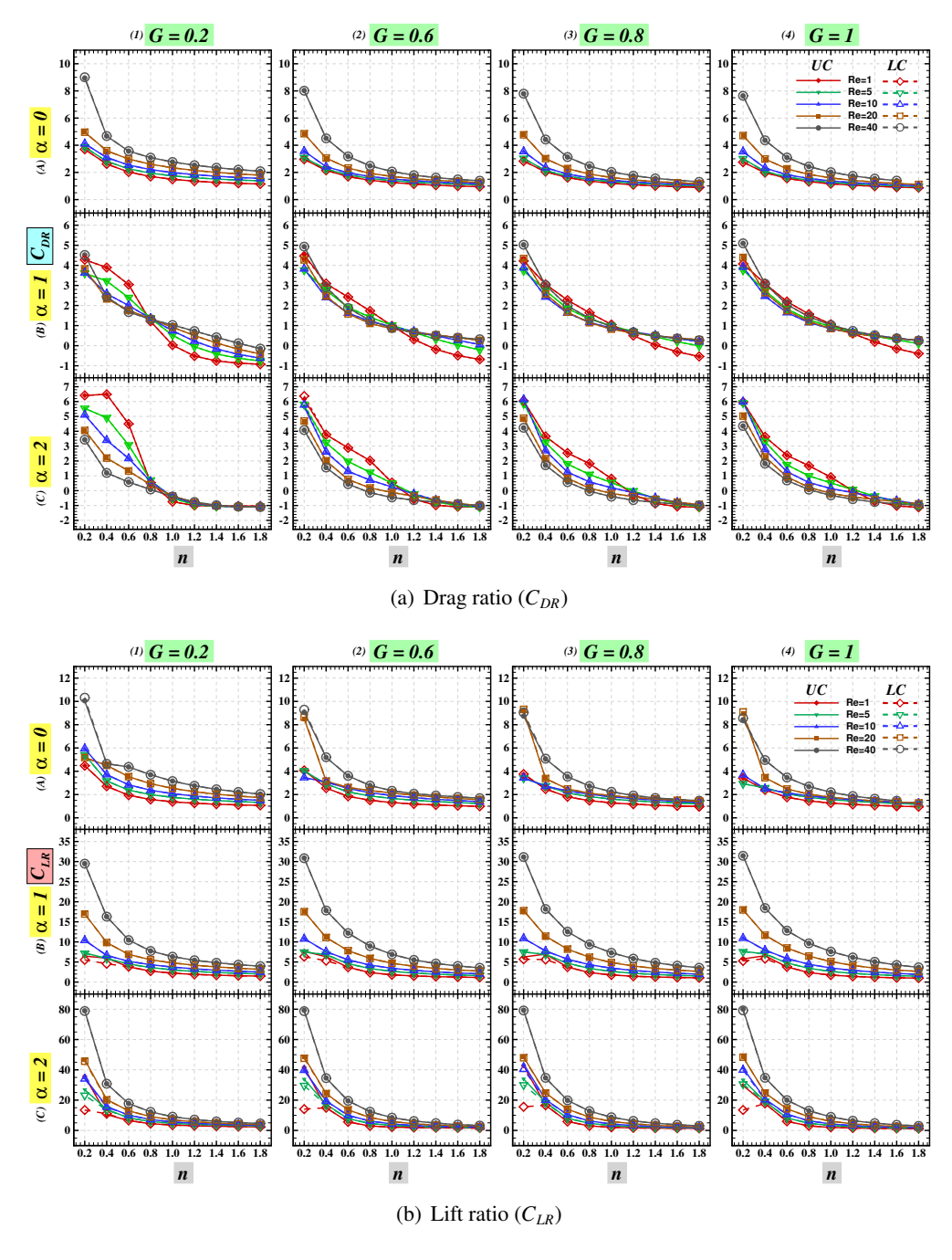


Figure 12: Variation of drag and lift ratio (C_{DR} and C_{LR}) for Re with n at different α (in rows) and G (in columns).

in shaping the hydrodynamic response of rotating cylinders.

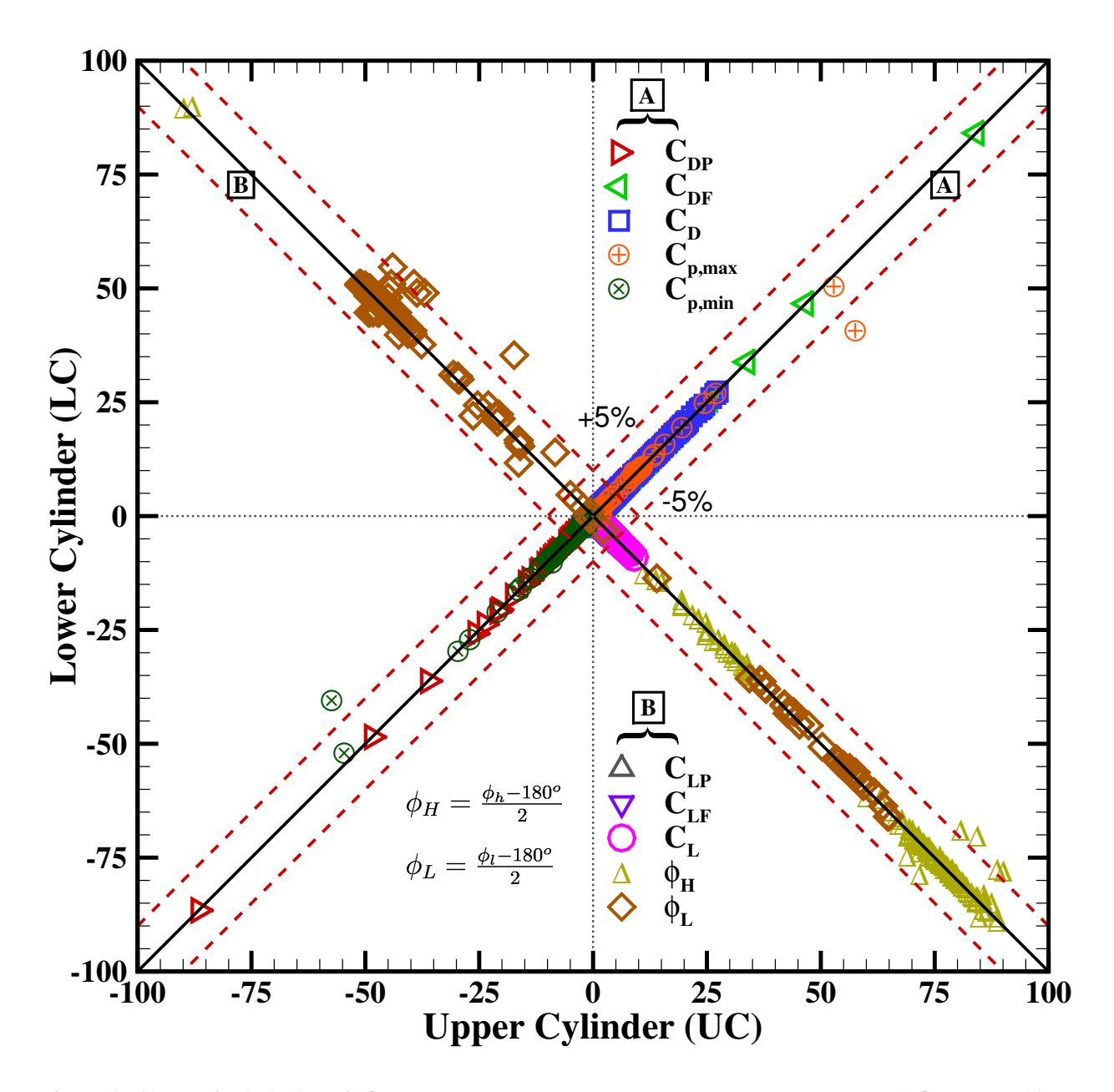


Figure 13: Comparative hydrodynamic features ($\Phi = C_{DP}, C_{DF}, C_D, C_{LP}, C_L, C_{p,max}, C_{p,min}, \phi_H, \phi_L$) for upper and lower cylinders (UC and LC) for the considered ranges of conditions (n, Re, α, G).

4.3. Comparative hydrodynamic features for upper and lower cylinders

Fig. 13 illustrates the comparative hydrodynamic characteristics (Φ) between the upper and lower cylinders (UC and LC), such as pressure drag (C_{DP}), friction drag (C_{DF}), total drag (C_D), pressure lift (C_{LP}), friction lift (C_{LF}), total lift (C_L), and minimum and maximum values of pressure coefficients ($C_{p,max}$, $C_{p,min}$) and their corresponding angular positions ($\phi_h = 2\phi_H + 180^\circ$, $\phi_l = 2\phi_L + 180^\circ$) for the ranges of conditions (n,

Re, α , G) covered in this work. The solid diagonal line (labeled A) in Fig. 13 represents the line of perfect symmetry ($\Phi_{LC} = \Phi_{UC}$), corresponding primarily to the drag coefficients (C_{DP} , C_{DF} , C_D) and pressure coefficients ($C_{p,max}$, $C_{p,min}$). In contrast, the line labeled B, which is inclined at -45° to line A, depict the anti-symmetric relationship ($\Phi_{LC} = -\Phi_{UC}$) between the lift-related quantities (C_{LP} , C_{LF} , C_L) and the angular positions (ϕ_H , ϕ_L). Further, the dashed sub- and super-diagonal lines denote $\pm 5\%$ deviation bands to main diagonal lines A and B. While line A reflects equal magnitude and direction of hydrodynamic quantities ($\Phi_{LC} = \Phi_{UC}$), line B corresponds to equal magnitude but opposite direction ($\Phi_{LC} = -\Phi_{UC}$). This anti-symmetric distribution is a direct manifestation of the counter-rotating flow configuration, where the induced circulations around each cylinder produce lift forces of equal strength but opposite sense. The data points aligned along line B confirm that the lift components and angles are mirror images between the upper and lower cylinders. Minor deviations from this line (within $\pm 5\%$) indicate the influence of small asymmetries in gap flow.

Most data points cluster closely around the diagonal line, confirming a high degree of symmetry between the UC and LC for both drag and lift components. The nearly linear correlation between drag coefficients (C_{DF}, C_{DP}, C_D) for both cylinders signifies balanced drag forces, implying that flow parameters (n, Re, α, G) do not significantly disturb the stream-wise force equilibrium. In contrast, the lift-related coefficients (C_{LP}, C_{LF}, C_L) exhibit a mirror-symmetric relationship (reflected across the origin, line B), indicating opposite lift directions acting on the cylinders. This anti-symmetric lift distribution arises from the counter-rotating flow patterns generated by the cylinders, which induce upward and downward pressure gradients, respectively. Further, the pressure coefficients $(C_{p,\text{max}}, C_{p,\text{min}})$ also follow symmetric distributions but with slight asymmetry in magnitude, where the UC tends to experience lower $C_{p,\text{min}}$ values than the LC. This difference results from flow acceleration near the UC due to rotation direction and gap-induced flow interactions. The angular positions (ϕ_H, ϕ_L) corresponding to pressure coefficients $(C_{p,\text{max}}, C_{p,\text{min}})$ for both cylinders further validate this symmetry, following nearly identical trends with a phase shift of 180° , consistent with the anti-symmetric pressure field between the cylinders.

Overall, the results in Fig. 13 confirm that (a) the drag forces are symmetric, indicating balanced stream-wise resistance, (b) the lift forces are anti-symmetric, confirming opposite transverse forces, (c) the pressure distribution and corresponding angular positions variation between the cylinders are responsible

for the observed lift reversal. Furthermore, the deviations ($\pm 5\%$) suggest minor influence of flow conditions, such as gap ratio (G), Reynolds number (Re), rotational rate (α), and power-law index (n) on overall force symmetry around both cylinders (UC and LC). These comparative features emphasize the inherent hydrodynamic mirror symmetry in the counter-rotating cylinder pair system and validate the numerical consistency of the computed results.

In summary, the Reynolds number (Re), gap ratio (G), rotation rate (α) , and fluid behavior index (n)collectively govern the local and overall hydrodynamic characteristics of the counter-rotating cylinders. As α increases from 0 to 2, the pressure coefficient (C_p) generally increases with increases n but decreases with increasing Re and G. At $\alpha = 2$, $C_{p,\text{max}}$ decreases with G for shear-thickening fluids (n > 1) but increases for shear-thinning fluids (n < 1), showing strong rheological dependence. The stagnation points $(\phi_h \text{ and } \phi_l)$ shift with both G and α , reflecting viscosity variations with shear rate and the influence of rotation-induced circulation. The friction coefficient (C_{DF}) decreases with Re for all conditions. For stationary cylinders ($\alpha = 0$) and low $Re \leq 1$, C_{DF} decreases with n, whereas at higher Re and $\alpha > 0$, it increases with n, indicating enhanced viscous resistance in shear-thickening fluids. Rotation initially reduces C_{DF} by stabilizing the boundary layer but later increases it as the shear intensifies. The pressure drag coefficient (C_{DP}) decreases exponentially with n and Re for all α and G. For $\alpha > 0$ at Re = 1, C_{DP} transitions from positive to negative in shear-thinning fluids, caused by viscosity reduction and reversed pressure gradients near the surface. Increasing G further decreases C_{DP} for all conditions. The friction lift coefficient (C_{LF}) increases with α and n but decreases with G and Re. The pressure lift coefficient (C_{LP}) , though enhanced by rotation, exhibits non-monotonic variation with n, decreasing with G and Re but increasing with α . Overall, the total drag (C_D) decreases with Re and increases with G, while the total lift (C_L) shows non-monotonic dependence on n, Re, α , and G. The drag and lift ratios (C_{DR}, C_{LR}) generally decrease with increasing n and vary non-linearly with Re and α . These complex inter-dependencies underscore the strong coupling between non-Newtonian fluid rheology, flow and geometrical parameters, and rotational effects in determining the hydrodynamic performance of the system.

5. Concluding remarks

The steady unconfined flow of power-law non-Newtonian fluids past a pair of side-by-side rotating circular cylinders was investigated numerically using the finite element method over a range of rotational rates ($0 \le$ $\alpha \le 2$), gap ratios (0.2 $\le G \le 1$), Reynolds numbers (0 $\le Re \le 40$), and power-law indices (0.2 $\le n \le 1.8$). The analysis focused on macroscopic hydrodynamic quantities, including drag and lift coefficients, and on detailed flow features such as streamline patterns, centerline velocity, and surface pressure distributions. The results reveal that increasing the rotational rate suppresses vortex shedding and promotes the formation of a thin fluid layer along the cylinder surfaces. In shear-thickening fluids, the wake structure is strongly altered by rotation, exhibiting enhanced asymmetry and reduced flow separation. The centerline velocity increases with both Re and α , while the pressure coefficient (C_p) attains its maximum and minimum at the front and rear stagnation points, respectively. For shear-thickening fluids, the location of maximum pressure shifts toward the direction of rotation, reflecting the influence of rheology on surface pressure distribution. The total drag coefficient (C_D) decreases with increasing Re, n, and α , indicating reduced form and frictional resistance, whereas the total lift coefficient (C_L) exhibits a complex dependence on these parameters due to competing effects of rotation and viscous dissipation. The interplay between gap ratio, rotational speed, and non-Newtonian rheology governs the balance between pressure- and shear-induced forces, determining the overall hydrodynamic response of the system. These findings provide a unified understanding of the coupled influence of rotation, rheology, and geometric confinement on non-Newtonian flow around bluff bodies. The results are expected to inform the design of fluid-structure systems in applications such as heat exchangers, particulate transport, and mixing processes involving complex fluids.

Additional Supplementary Information

Readers may refer Appendix B to Appendix J for the detailed data sets and enlarged figures.

References

- [1] V. L. Streeter (Ed.), Handbook of Fluid Dynamics, McGraw-Hill, New York, 1961.
- [2] M. M. Zdravkovich, Review of flow interference between two circular cylinders in various arrangements, Journal of Fluids Engineering 99 (4) (1977) 618–633.
- [3] M. M. Zdravkovich, Flow Around Circular Cylinders: Volume I: Fundamentals, Oxford University Press, New York, ISBN 9780198563969, 1997.

- [4] M. M. Zdravkovich, Flow Around Circular Cylinders: Volume 2: Applications, Oxford University Press, New York, ISBN 9780198565611, 2003.
- [5] Z. Zapryanov, S. Tabakova, Dynamics of Bubbles, Drops and Rigid Particles, Springer, Netherlands, ISBN 9789401592550, doi:10.1007/978-94-015-9255-0, 2013.
- [6] R. Clift, J. R. Grace, M. E. Weber, Bubbles, drops, and particles, Dover Publications, Mineola, New York, ISBN 9780486445809, 2005.
- [7] E. E. Michaelides, Particles, Bubbles and Drops: Their Motion, Heat and Mass Transfer, World Scientific Publishing Company, Singapore, ISBN 9789812774316, 2006.
- [8] R. W. Johnson (Ed.), Handbook of Fluid Dynamics, CRC Press, Boca Raton, FL, 2nd edn., 2016.
- [9] P. Hishikar, S. K. Dhiman, A. K. Tiwari, V. K. Gaba, Analysis of flow characteristics of two circular cylinders in cross-flow with varying Reynolds number: a review, Journal of Thermal Analysis and Calorimetry 147 (10) (2022) 5549–5574.
- [10] R. P. Chhabra, S. A. Patel, Bubbles, drop and particles in non-Newtonian fluids, CRC Press, Boca Raton, FL, 3rd edn., 2023.
- [11] R. P. Chhabra, J. F. Richardson, Non-Newtonian Flow and Applied Rheology, Butterworth-Heinemann, Oxford, 2 edn., 2008.
- [12] J. R. Meneghini, F. Saltara, C. d. L. R. Siqueira, J. Ferrari Jr, Numerical simulation of flow interference between two circular cylinders in tandem and side-by-side arrangements, Journal of Fluids and Structures 15 (2) (2001) 327–350.
- [13] S. Kang, Characteristics of flow over two circular cylinders in a side-by-side arrangement at low Reynolds numbers, Physics of Fluids 15 (9) (2003) 2486–2498.
- [14] S. Xu, Y. Zhou, R. So, Reynolds number effects on the flow structure behind two side-by-side cylinders, *Physics* of Fluids 15 (5) (2003) 1214–1219.
- [15] L. Kun, D.-j. SUN, X.-y. YIN, et al., Wake patterns of flow past a pair of circular cylinders in side-by-side arrangements at low Reynolds numbers, Journal of Hydrodynamics, Series B 19 (6) (2007) 690–697.
- [16] J. Mizushima, Y. Ino, Stability of flows past a pair of circular cylinders in a side-by-side arrangement, Journal of Fluid Mechanics 595 (2008) 491–507.
- [17] H. Sarvghad-Moghaddam, N. Nooredin, B. Ghadiri-Dehkordi, Numerical simulation of flow over two side-by-side circular cylinders, Journal of Hydrodynamics, Ser. B 23 (6) (2011) 792–805.
- [18] A. Vakil, S. I. Green, Two-dimensional side-by-side circular cylinders at moderate Reynolds numbers, Computers & Fluids 51 (1) (2011) 136–144.
- [19] Y. Bao, D. Zhou, J. Tu, Flow characteristics of two in-phase oscillating cylinders in side-by-side arrangement, Computers & Fluids 71 (2013) 124–145.
- [20] K. Supradeepan, A. Roy, Characterisation and analysis of flow over two side by side cylinders for different gaps at low Reynolds number: A numerical approach, Physics of Fluids 26 (6) (2014) 063602.
- [21] M. Carini, F. Auteri, F. Giannetti, Secondary instabilities of the in-phase synchronized wakes past two circular cylinders in side-by-side arrangement, Journal of Fluids and Structures 53 (2015) 70–83.
- [22] J. Thapa, M. Zhao, L. Cheng, T. Zhou, Three-dimensional simulations of flow past two circular cylinders in side-by-side arrangements at right and oblique attacks, Journal of Fluids and Structures 55 (2015) 64–83.
- [23] S. Singha, K. K. Nagarajan, K. Sinhamahapatra, Numerical study of two-dimensional flow around two side-by-side circular cylinders at low Reynolds numbers, *Physics of Fluids* 28 (5) (2016) 053603.
- [24] X. Qiu, Z.-x. Bi, J.-p. Luo, Y.-l. Liu, Vortex shedding in the flow around two side-by-side circular cylinders of different diameters, Journal of Hydrodynamics 29 (3) (2017) 470–478.
- [25] E. Adeeb, B. A. Haider, C. H. Sohn, Flow interference of two side-by-side square cylinders using IB-LBM–Effect of corner radius, Results in Physics 10 (2018) 256–263.
- [26] A. Sanyal, A. Dhiman, Impact of gap-ratios on buoyancy-assisted mixed convection flow and heat transfer in unconfined framework with two side-by-side cylinders, Proceedings of the Institution of Mechanical Engineers,

- Part C: Journal of Mechanical Engineering Science 236 (1) (2022) 165–178.
- [27] H. S. Yoon, J. H. Kim, H. H. Chun, H. J. Choi, Laminar flow past two rotating circular cylinders in a side-by-side arrangement, *Physics of Fluids* 19 (12).
- [28] H. S. Yoon, H. H. Chun, J. H. Kim, I. R. Park, Flow characteristics of two rotating side-by-side circular cylinder, Computers & Fluids 38 (2) (2009) 466–474.
- [29] H. Yoon, J. Seo, J. Kim, Laminar forced convection heat transfer around two rotating side-by-side circular cylinder, International Journal of Heat and Mass Transfer 53 (21-22) (2010) 4525–4535.
- [30] X.-h. Guo, J.-z. Lin, C.-x. Tu, H.-l. Wang, Flow past two rotating circular cylinders in a side-by-side arrangement, Journal of Hydrodynamics 21 (2) (2009) 143–151.
- [31] G. Xiao-Hui, L. Jian-Zhong, N. De-Ming, Vortex structures and behavior of a flow past two rotating circular cylinders arranged side-by-side, Chinese Physics Letters 26 (8) (2009) 084701.
- [32] H. Nemati, K. Sedighi, M. Farhadi, M. M. Pirouz, E. Fattahi, Numerical simulation of fluid flow of two rotating side-by-side circular cylinders by Lattice Boltzmann method, International Journal of Computational Fluid Dynamics 24 (3-4) (2010) 83–94.
- [33] A. S. Chan, P. A. Dewey, A. Jameson, C. Liang, A. J. Smits, Vortex suppression and drag reduction in the wake of counter-rotating cylinders, Journal of Fluid Mechanics 679 (2011) 343–382.
- [34] S. Kumar, B. Gonzalez, O. Probst, Flow past two rotating cylinders, Physics of Fluids 23 (1) (2011) 014102.
- [35] K. Supradeepan, A. Roy, Low Reynolds number flow characteristics for two side by side rotating cylinders, Journal of Fluids Engineering 137 (10).
- [36] H. Dou, S. Zhang, H. Yang, T. Setoguchi, Y. Kinoue, Effect of rotational speed on the stability of two rotating side-by-side circular cylinders at low reynolds number, Journal of Thermal Science 27 (2) (2018) 125–134.
- [37] M. Darvishyadegari, R. Hassanzadeh, Analysis of the convective heat transfer and flow behavior around two counter-rotating side-by-side cylinders, Heat Transfer—Asian Research 47 (6) (2018) 835–854.
- [38] R. Hassanzadeh, M. Darvishyadegari, Analysis of heat and fluid flow around two co-rotating side-by-side cylinders, Sadhana 44 (5) (2019) 1–18.
- [39] N. Krishna Chaitanya, D. Chatterjee, Mixed convective flow past counter-rotating side-by-side cylinders at low Reynolds number, Numerical Heat Transfer, Part A: Applications 83 (2) (2023) 141–159.
- [40] N. Chaitanya, A. Dhiman, Non-Newtonian power-law flow and heat transfer across a pair of side-by-side circular cylinders, International Journal of Heat and Mass Transfer 55 (21-22) (2012) 5941–5958.
- [41] A. Daniel, A. Dhiman, Aiding-buoyancy mixed convection from a pair of side-by-side heated circular cylinders in power-law fluids, Industrial & Engineering Chemistry Research 52 (48) (2013) 17294–17314.
- [42] S. K. Panda, Two-dimensional flow of power-law fluids over a pair of cylinders in a side-by-side arrangement in the laminar regime, Brazilian Journal of Chemical Engineering 34 (2) (2017) 507–530.
- [43] H. Zhu, Y. Li, Y. Xie, W. Zhang, T. Zhou, Numerical investigation of power-law flow past two side-by-side identical circular cylinders, *Physics of Fluids* 36 (7).
- [44] H. M. Badr, S. C. R. Dennis, P. J. S. Young, Steady and unsteady flow past a rotating circular cylinder at low Reynolds numbers, Computers & Fluids 17 (4) (1989) 579–609.
- [45] S. Kang, H. Choi, S. Lee, Laminar flow past a rotating circular cylinder, Physics of Fluids 11 (11) (1999) 3312–3321.
- [46] S. Mittal, B. Kumar, Flow past a rotating cylinder, Journal of Fluid Mechanics 476 (2003) 303–334.
- [47] R. P. Chhabra, A. A. Soares, J. M. Ferreira, Steady non-Newtonian flow past a circular cylinder: A numerical study, Acta Mechanica 172 (1-2) (2004) 1–16.
- [48] W. A. Khan, J. R. Culham, M. M. Yovanovich, Fluid flow and heat transfer in power-law fluids across circular cylinders: Analytical study, Journal of Heat Transfer 128 (9) (2006) 870.
- [49] S. Kang, Laminar flow over a steadily rotating circular cylinder under the influence of uniform shear, Physics of Fluids 18 (4).
- [50] R. P. Bharti, R. P. Chhabra, V. Eswaran, Steady flow of power Law fluids across a circular cylinder, Canadian

- Journal of Chemical Engineering 84 (4) (2006) 406–421.
- [51] R. P. Bharti, R. P. Chhabra, V. Eswaran, Steady forced convection heat transfer from a heated circular cylinder to power-law fluids, International Journal of Heat and Mass Transfer 50 (5-6) (2007) 977–990.
- [52] R. P. Bharti, R. P. Chhabra, V. Eswaran, Two-dimensional steady poiseuille flow of power-law fluids across a circular cylinder in a plane confined channel: Wall effects and drag coefficients, Industrial & Engineering Chemistry Research 46 (11) (2007) 3820–3840.
- [53] S. N. Kumar, G. Biswas, A finite element study of the onset of vortex shedding in a flow past two-dimensional circular cylinder, Progress in Computational Fluid Dynamics 8 (5) (2008) 288–298.
- [54] S. B. Paramane, A. Sharma, Numerical investigation of heat and fluid flow across a rotating circular cylinder maintained at constant temperature in 2-D laminar flow regime, International Journal of Heat and Mass Transfer 52 (13-14) (2009) 3205–3216.
- [55] V. K. Patnana, R. P. Bharti, R. P. Chhabra, Two-dimensional unsteady flow of power-law fluids over a cylinder, Chemical Engineering Science 64 (12) (2009) 2978–2999.
- [56] S. Sen, S. Mittal, G. Biswas, Steady separated flow past a circular cylinder at low Reynolds numbers, Journal of Fluid Mechanics 620 (2009) 89–119.
- [57] M. K. Rao, A. K. Sahu, R. P. Chhabra, Effect of confinement on power-law fluid flow past a circular cylinder, Polymer Engineering and Science 51 (10) (2011) 2044–2065.
- [58] S. Sarkar, A. Dalal, G. Biswas, Unsteady wake dynamics and heat transfer in forced and mixed convection past a circular cylinder in cross flow for high Prandtl number, International Journal of Heat and Mass Transfer 54 (2011) 3536–3551.
- [59] P. Thakur, S. Mittal, N. Tiwari, R. P. Chhabra, The motion of a rotating circular cylinder in a stream of Bingham plastic fluid, Journal of Non-Newtonian Fluid Mechanics 235 (2016) 29–46.
- [60] B. Suru, V. Goutham, P. Gurugubelli, K. Supradeepan, Non-Newtonian flow past a rotating circular cylinder with forced convection heat transfer, <u>Materials Today</u>: <u>Proceedings</u> 47 (2021) 5737–5747.
- [61] D. Kumar, A. K. Sahu, Non-Newtonian fluid flow over a rotating elliptic cylinder in laminar flow regime, European Journal of Mechanics B: Fluids 93 (2022) 117–136.
- [62] L. Malviya, R. P. Bharti, Steady flow of power-law fluids over two rotating cylinders in side-by-side arrangement (paper no. OS12-39), in: Proceedings of Nineteenth International Conference on Flow Dynamics, November 9 11, 2022, Sendai, Miyagi, Japan, 2022.
- [63] P. K. Mohanty, R. P. Bharti, A. K. Sahu, Influence of solvent viscosity ratio on the creeping flow of viscoelastic fluid over a channel confined circular cylinder, *Physics of Fluids* 36 (7) (2024) 073103.
- [64] R. P. Chhabra, K. Rami, P. H. Uhlherr, Drag on cylinders in shear thinning viscoelastic liquids, Chemical Engineering Science 56 (6) (2001) 2221–2227.
- [65] P. Sivakumar, R. P. Bharti, R. P. Chhabra, Effect of power-law index on critical parameters for power-law flow across an unconfined circular cylinder, Chemical Engineering Science 61 (18) (2006) 6035–6046.
- [66] P. Sivakumar, R. P. Bharti, R. P. Chhabra, Steady flow of power-law fluids across an unconfined elliptical cylinder, Chemical Engineering Science 62 (6) (2007) 1682–1702.
- [67] R. C. Patil, R. P. Bharti, R. P. Chhabra, Forced convection heat transfer in power law liquids from a pair of cylinders in tandem arrangement, Industrial & Engineering Chemistry Research 47 (23) (2008) 9141–9164.
- [68] R. C. Patil, R. P. Bharti, R. P. Chhabra, Steady flow of power law fluids over a pair of cylinders in tandem arrangement, Industrial & engineering chemistry research 47 (5) (2008) 1660–1683.
- [69] V. K. Patnana, R. P. Bharti, R. P. Chhabra, Two-dimensional unsteady forced convection heat transfer in power-law fluids from a cylinder, International Journal of Heat and Mass Transfer 53 (19-20) (2010) 4152–4167.
- [70] N. Nirmalkar, R. P. Chhabra, Momentum and heat transfer from a heated circular cylinder in Bingham plastic fluids, International Journal of Heat and Mass Transfer 70 (2014) 564–577.
- [71] G. Vishal, J. Tomar, R. P. Bharti, Critical parameters for non-Newtonian shear-thickening power-law fluids flow across a channel confined circular cylinder, Journal of the Taiwan Institute of Chemical Engineers 123 (2021)

- 34-46.
- [72] M. S. Sabarinath, A. S. Kumar, Non-Newtonian effects in flow over circular cylinder at low Reynolds number, International Journal of Pure and Applied Mathematics 119 (12) (2018) 65–70.
- [73] S. Bailoor, J.-H. Seo, R. Mittal, Vortex shedding from a circular cylinder in shear-thinning Carreau fluids, *Physics* of Fluids 31, ISSN 1089-7666.
- [74] S. K. Panda, R. P. Chhabra, Laminar flow of power-law fluids past a rotating cylinder, Journal of Non-Newtonian Fluid Mechanics 165 (21-22) (2010) 1442–1461.
- [75] S. K. Panda, R. P. Chhabra, Laminar forced convection heat transfer from a rotating cylinder to power-law fluids, Numerical Heat Transfer; Part A: Applications 59 (4) (2011) 297–319.
- [76] R. Kumar, V. Pancholi, R. P. Bharti, Material flow visualization and determination of strain rate during friction stir welding, Journal of Materials Processing Technology 255 (2018) 470–476.
- [77] R. Kumar, A. K. Lal, R. P. Bharti, V. Pancholi, Experimental and computational analyses of material flow characteristics in friction stir welding, International Journal of Advanced Manufacturing Technology 115 (9–10) (2021) 3011–3020.
- [78] A. R. Dwivedi, A. K. Dhiman, Flow and heat transfer analysis around tandem cylinders: critical gap ratio and thermal cross-buoyancy, Journal of the Brazilian Society of Mechanical Sciences and Engineering 41 (11) (2019) 1–25
- [79] M. Darvishyadegari, R. Hassanzadeh, Convective heat transfer and fluid flow of two counter-rotating cylinders in tandem arrangement, Acta Mechanica 229 (4) (2018) 1783–1802.
- [80] M. Darvishyadegari, R. Hassanzadeh, Heat and fluid flow around two co-rotating cylinders in tandem arrangement, International Journal of Thermal Sciences 135 (2019) 206–220.
- [81] M. Rastan, A. Sohankar, M. M. Alam, Flow and heat transfer across two inline rotating cylinders: Effects of blockage, gap spacing, Reynolds number, and rotation direction, <u>International Journal of Heat and Mass Transfer</u> 174 (2021) 121324.
- [82] A. V. Durga Prasad, A. K. Dhiman, CFD analysis of momentum and heat transfer around a pair of square cylinders in side-by-side arrangement, Heat Transfer Engineering 35 (4) (2014) 398–411.
- [83] A. Sanyal, A. Dhiman, Wake interactions in a fluid flow past a pair of side-by-side square cylinders in presence of mixed convection, Physics of Fluids 29 (10) (2017) 103602, doi:10.1063/1.5005118.
- [84] C. G. Patel, S. Sarkar, S. K. Saha, Mixed convective vertically upward flow past side-by-side square cylinders at incidence, International Journal of Heat and Mass Transfer 127 (2018) 927–947.
- [85] R. Bird, W. Stewart, E. Lightfoot, Transport Phenomena, John Wiley, 2002.
- [86] R. P. Bharti, R. P. Ram, A. K. Dhiman, Computational analysis of cross-flow of power-law fluids through a periodic square array of circular cylinders, Asia-Pacific Journal of Chemical Engineering 17 (2) (2022) e2748, doi: 10.1002/apj.2748.
- [87] A. Daniel, A. Dhiman, Aiding-buoyancy mixed convection from a pair of side-by-side heated circular cylinders in power-law fluids, Industrial & Engineering Chemistry Research 52 (48) (2013) 17294–17314.

Appendix A. Selection of domain and grid size

The accuracy of the computational results inherently depends on the size of the computational domain and mesh. In the case of an unconfined flow problem, as considered in the present study, the physical domain is characterized by the upstream length (L_u) , downstream length (L_d) , and height (H) of the computational domain (refer Fig. 1).

A.1. Domain independence test

To represent the unconfined flow condition, the computational domain must be sufficiently large to minimize boundary effects on the flow characteristics. Although a larger domain provides a more accurate physical representation of unconfined flow, it also increases computational cost. Therefore, a domain independence test is performed to evaluate the trade-off between accuracy and computational efficiency by comparing the flow characteristics across different combinations of domain dimensions (L_u , L_d , H). In this study, various domain dimensions are considered to perform the domain independence test, with upstream length

Table A.1: The upstream length (L_u) independence test for extreme gap ratio (G), Reynolds numbers (Re) and power-law index (n) for the maximum rotational rate $(\alpha = 2)$ of the cylinders.

L	d = 20	00,				Re	= 1							Re	= 40			
I	H = 10	00	Ţ	Jpper cylin	der (UC)			Lower cyli	nder (LC)		τ	Jpper cylin	nder (UC)			Lower cyl	inder (LC)	
G	n	L_u	C_{DP}	C_D	C_{LP}	C_L	C_{DP}	C_D	C_{LP}	C_L	C_{DP}	C_D	C_{LP}	C_L	C_{DP}	C_D	C_{LP}	C_L
0.2	0.2	40	15.208	17.577	5.511	5.7432	15.254	17.534	-5.4128	-5.8419	0.4193	0.5409	4.3213	4.3760	0.4190	0.5406	-4.3219	-4.3768
		80	15.208	17.577	5.5105	5.7427	15.253	17.534	-5.4123	-5.8414	0.4188	0.5408	4.3208	4.3755	0.4190	0.5406	-4.3212	-4.3760
		120	15.208	17.576	5.5117	5.7405	15.253	17.534	-5.4123	-5.8413	0.4192	0.5408	4.3206	4.3753	0.4192	0.5407	-4.3211	-4.3760
		160	15.208	17.576	5.5117	5.7405	15.253	17.534	-5.4123	-5.8413	0.4192	0.5408	4.3206	4.3753	0.4193	0.5406	-4.3211	-4.3759
0.2	1	40	-4.0539	1.4674	3.3093	4.2509	-4.0556	1.4652	-3.3115	-4.251	-0.1236	0.1932	2.7932	3.1015	-0.1238	0.1927	-2.7932	-3.1015
		80	-4.0670	1.4453	3.2999	4.2368	-4.0687	1.443	-3.3021	-4.2369	-0.1242	0.1917	2.7862	3.0936	-0.1244	0.1913	-2.7861	-3.0936
		120	-4.0679	1.4438	3.2993	4.2358	-4.0696	1.4416	-3.3015	-4.2359	-0.1243	0.1916	2.7857	3.0930	-0.1245	0.1912	-2.7856	-3.0930
		160	-4.0680	1.4437	3.2992	4.2358	-4.0697	1.4415	-3.3014	-4.2359	-0.1243	0.1916	2.7856	3.0930	-0.1245	0.1912	-2.7856	-3.0930
0.2	1.8	40	-86.587	-2.5274	6.3149	9.004	-86.595	-2.5074	-6.3379	-9.0148	-2.3026	-0.2193	3.8602	4.7026	-2.3031	-0.2197	-3.8609	-4.7032
		80	-86.579	-2.5045	6.3238	9.0236	-86.587	-2.4845	-6.3469	-9.0343	-2.3032	-0.2203	3.8582	4.7000	-2.3036	-0.2207	-3.8589	-4.7005
		120	-86.578	-2.5026	6.3245	9.0251	-86.587	-2.4827	-6.3476	-9.0359	-2.3032	-0.2204	3.8580	4.6998	-2.3037	-0.2207	-3.8588	-4.7004
		160	-86.578	-2.5026	6.3245	9.0251	-86.587	-2.4827	-6.3476	-9.0359	-2.3032	-0.2204	3.8580	4.6998	-2.3034	-0.2198	-3.8592	-4.7016
1	0.2	40	17.4280	20.3510	6.4142	6.5914	17.4760	20.3100	-6.2918	-6.7128	0.5449	0.6700	4.2303	4.2835	0.5443	0.6692	-4.2225	-4.2758
		80	17.4270	20.3500	6.4139	6.5910	17.4760	20.3090	-6.2914	-6.7122	0.5447	0.6698	4.2293	4.2825	0.5441	0.6690	-4.2216	-4.2748
		120	17.4270	20.3500	6.4138	6.5910	17.4760	20.3090	-6.2913	-6.7122	0.5447	0.6698	4.2293	4.2825	0.5441	0.6689	-4.2216	-4.2748
		160	17.4290	20.3490	6.4104	6.5933	17.4760	20.3090	-6.2913	-6.7122	0.5446	0.6695	4.2311	4.2845	0.5443	0.6689	-4.2211	-4.2745
1	1	40	2.0571	4.2942	2.4009	3.6005	2.0568	4.2927	-2.4036	-3.6061	-0.1665	0.3765	4.8098	5.3472	-0.1665	0.3763	-4.8094	-5.3469
		80	2.0176	4.2178	2.3635	3.5443	2.0173	4.2163	-2.3662	-3.5499	-0.1688	0.3727	4.8002	5.3370	-0.1688	0.3724	-4.7998	-5.3366
		120	2.0150	4.2127	2.3610	3.5405	2.0147	4.2112	-2.3637	-3.5461	-0.1690	0.3724	4.7995	5.3363	-0.1690	0.3721	-4.7991	-5.3359
		160	2.0148	4.2124	2.3608	3.5403	2.0145	4.2108	-2.3635	-3.5458	-0.1690	0.3724	4.7995	5.3362	-0.1690	0.3721	-4.7991	-5.3358
1	1.8	40	-9.9801	-1.1282	3.9427	7.2487	-9.9781	-1.1252	-3.9465	-7.2514	-0.7161	0.0089	3.9224	5.2347	-0.7161	0.0083	-3.9222	-5.2359
		80	-9.9813	-1.1322	3.9409	7.2447	-9.9792	-1.1291	-3.9447	-7.2474	-0.7161	0.0048	3.9032	5.2101	-0.7161	0.0041	-3.9031	-5.2114
		120	-9.9814	-1.1324	3.9408	7.2445	-9.9793	-1.1293	-3.9446	-7.2472	-0.7161	0.0044	3.9019	5.2085	-0.7161	0.0038	-3.9017	-5.2096
		160	-9.9814	-1.1324	3.9408	7.2445	-9.9793	-1.1294	-3.9446	-7.2472	-0.7161	0.0043	3.9018	5.2083	-0.7161	0.0038	-3.9016	-5.2095

Table A.2: The downstream length (L_d) independence test for extreme gap ratio (G), Reynolds numbers (Re) and power-law index (n) for the maximum rotational rate $(\alpha = 2)$ of the cylinders.

L	u = 12	20,				Re	= 1							Re	= 40			
1	H = 10	00	Ţ	Jpper cylin	der (UC)			Lower cylii	nder (LC)		Ţ	Upper cylii	nder (UC)			Lower cyl	inder (LC)	
G	n	L_d	C_{DP}	C_D	C_{LP}	C_L	C_{DP}	C_D	C_{LP}	C_L	C_{DP}	C_D	C_{LP}	C_L	C_{DP}	C_D	C_{LP}	C_L
0.2	0.2	100	15.2050	17.5830	5.5282	5.7177	15.2350	17.5570	-5.4442	-5.8069	0.4185	0.5406	4.3196	4.3741	0.4190	0.5404	-4.3236	-4.3786
		200	15.2080	17.5760	5.5117	5.7405	15.2530	17.5340	-5.4123	-5.8413	0.4192	0.5408	4.3206	4.3753	0.4192	0.5407	-4.3211	-4.3760
		300	15.2050	17.5820	5.5534	5.7009	15.2420	17.5540	-5.4306	-5.8279	0.4190	0.5408	4.3197	4.3743	0.4191	0.5404	-4.3232	-4.3783
		400	15.2070	17.5790	5.5272	5.7239	15.2470	17.5500	-5.4224	-5.8318	0.4186	0.5406	4.3224	4.3771	0.4190	0.5406	-4.3214	-4.3763
0.2	1	100	-4.0539	1.4674	3.3093	4.2509	-4.0556	1.4652	-3.3115	-4.2510	-0.1243	0.1913	2.7856	3.0925	-0.1244	0.1914	-2.7858	-3.0932
		200	-4.0670	1.4453	3.2999	4.2368	-4.0687	1.4430	-3.3021	-4.2369	-0.1243	0.1916	2.7857	3.0930	-0.1245	0.1912	-2.7856	-3.0930
		300	-4.0679	1.4438	3.2993	4.2358	-4.0696	1.4416	-3.3015	-4.2359	-0.1243	0.1915	2.7857	3.0930	-0.1244	0.1910	-2.7859	-3.0933
		400	-4.0677	1.4452	3.2956	4.2265	-4.0686	1.4423	-3.2991	-4.2306	-0.1243	0.1913	2.7857	3.0930	-0.1244	0.1912	-2.7859	-3.0932
0.2	1.8	100	-86.5680	-2.4648	6.2902	8.9183	-86.5790	-2.4891	-6.3434	-9.0403	-2.3030	-0.2199	3.8573	4.6969	-2.3036	-0.2209	-3.8585	-4.7000
		200	-86.5780	-2.5026	6.3245	9.0251	-86.5870	-2.4827	-6.3476	-9.0359	-2.3032	-0.2204	3.8580	4.6998	-2.3037	-0.2207	-3.8588	-4.7004
		300	-86.5760	-2.4780	6.3077	8.9869	-86.5780	-2.5071	-6.3265	-9.0105	-2.3031	-0.2202	3.8579	4.6992	-2.3034	-0.2215	-3.8584	-4.6998
		400	-86.5700	-2.4812	6.2809	8.9307	-86.5790	-2.4951	-6.3304	-9.0152	-2.3030	-0.2205	3.8573	4.6979	-2.3035	-0.2211	-3.8584	-4.6998
1	0.2	100	17.4640	20.3300	6.3696	6.6119	17.4700	20.3140	-6.2826	-6.7150	0.5443	0.6694	4.2307	4.2837	0.5448	0.6695	-4.2226	-4.2759
		200	17.4270	20.3500	6.4138	6.5910	17.4760	20.3090	-6.2913	-6.7122	0.5447	0.6698	4.2293	4.2825	0.5441	0.6689	-4.2216	-4.2748
		300	17.4310	20.3490	6.4061	6.5968	17.4900	20.2930	-6.2618	-6.7380	0.5447	0.6698	4.2312	4.2843	0.5445	0.6690	-4.2224	-4.2757
		400	17.4230	20.3490	6.4236	6.5713	17.4710	20.3120	-6.2801	-6.7244	0.5446	0.6692	4.2327	4.2859	0.5444	0.6690	-4.2225	-4.2760
1	1	100	2.0155	4.2130	2.3601	3.5389	2.0141	4.2084	-2.3629	-3.5440	-0.1689	0.3725	4.7996	5.3362	-0.1690	0.3722	-4.7990	-5.3358
		200	2.0150	4.2127	2.3610	3.5405	2.0147	4.2112	-2.3637	-3.5461	-0.1690	0.3724	4.7995	5.3363	-0.1690	0.3721	-4.7991	-5.3359
		300	2.0151	4.2131	2.3606	3.5384	2.0157	4.2135	-2.3608	-3.5383	-0.1690	0.3725	4.7995	5.3362	-0.1690	0.3721	-4.7990	-5.3357
		400	2.0150	4.2128	2.3619	3.5434	2.0156	4.2125	-2.3627	-3.5443	-0.1690	0.3725	4.7996	5.3364	-0.1690	0.3722	-4.7991	-5.3359
1	1.8	100	-9.9802	-1.1305	3.9443	7.2521	-9.9813	-1.1357	-3.9466	-7.2530	-0.7157	0.0052	3.9014	5.2086	-0.7161	0.0041	-3.9017	-5.2094
		200	-9.9814	-1.1324	3.9408	7.2445	-9.9793	-1.1293	-3.9446	-7.2472	-0.7161	0.0044	3.9019	5.2085	-0.7161	0.0038	-3.9017	-5.2096
		300	-9.9792	-1.1334	3.9406	7.2265	-9.9845	-1.1397	-3.9464	-7.2548	-0.7161	0.0049	3.9017	5.2082	-0.7159	0.0038	-3.9014	-5.2093
		400	-9.9820	-1.1345	3.9442	7.2561	-9.9806	-1.1343	-3.9477	-7.2604	-0.7161	0.0048	3.9020	5.2088	-0.7160	0.0046	-3.9017	-5.2098

 $(40 \le L_u \le 160)$, downstream length $(100 \le L_d \le 400)$, and height $(100 \le H \le 400)$. Tables A.1 - A.3 summarize the influence of domain size parameters (L_u, L_d, H) on the force coefficients $(C_{DP}, C_D, C_{LP}, C_L)$ for both cylinders (UC and LC) at the extreme values of gap ratio (G = 0.2, 1), Reynolds number (Re = 1, 40), and power-law index (n = 0.2, 1, 1.8) for the maximum rotational rate $(\alpha = 2)$ using grid G1 (see Table A.4 for grid specifications).

The effect of upstream length (L_u) on the force coefficients $(C_{DP}, C_D, C_{LP}, C_L)$ is examined in Table A.1 by fixing the downstream length at $L_d = 200$ and the unconfined domain height at H = 100. At G = 0.2 and Re = 1, the absolute percentage variations in the individual and total drag (C_{DP}, C_D) and lift (C_{LP}, C_L) coefficients for $L_u = 40 - 80$ are below 0.01%, 1.5%, and 0.9%, respectively, for n = 0.2, 1, and 1.8 for both cylinders. The corresponding variations between $L_u = 80$ and 120 are below 0.02%, 0.10%, and 0.07%, while further increasing L_u from 120 to 160 results in negligible differences (0.00%, 0.006%, and 0.00% for n = 0.2, 1, and 1.8, respectively). At G = 0.2 and Re = 40, the relative variations for n = 0.2, 1, and 1.8 are below 0.11%, 0.75%, and 0.46% when comparing values for $L_u = 40$ and 80;

Table A.3: The domain height (H) independence test for extreme gap ratio (G), Reynolds numbers (Re) and power-law index (n) for the maximum rotational rate $(\alpha = 2)$ of the cylinders.

L	u = 12	20,				Re	= 1							Re	= 40			
I	_d = 30	00	ι	pper cylin	der (UC)		1	Lower cylii	nder (LC)		1	Upper cylii	nder (UC)			Lower cyl	inder (LC)	
G	n	Н	C_{DP}	C_D	C_{LP}	C_L	C_{DP}	C_D	C_{LP}	C_L	C_{DP}	C_D	C_{LP}	C_L	C_{DP}	C_D	C_{LP}	C_L
0.2	0.2	100	15.2050	17.5820	5.5534	5.7009	15.2420	17.5540	-5.4306	-5.8279	0.4190	0.5408	4.3197	4.3743	0.4191	0.5404	-4.3232	-4.3783
		200	15.2060	17.5830	5.5459	5.7072	15.2410	17.5530	-5.4295	-5.8267	0.4190	0.5407	4.3190	4.3735	0.4190	0.5403	-4.3226	-4.3775
		300	15.2040	17.5750	5.5547	5.6964	15.2410	17.5560	-5.4257	-5.8282	0.4188	0.5405	4.3187	4.3733	0.4188	0.5402	-4.3223	-4.3773
		400	15.2050	17.5760	5.5495	5.7029	15.2430	17.5530	-5.4259	-5.8290	0.4186	0.5405	4.3187	4.3732	0.4186	0.5402	-4.3223	-4.3772
0.2	1	100	-4.0679	1.4438	3.2993	4.2358	-4.0696	1.4416	-3.3015	-4.2359	-0.1243	0.1915	2.7857	3.0930	-0.1244	0.1910	-2.7859	-3.0933
		200	-4.0856	1.4173	3.2865	4.2159	-4.0863	1.4124	-3.2861	-4.2126	-0.1247	0.1906	2.7813	3.0881	-0.1249	0.1901	-2.7815	-3.0884
		300	-4.0893	1.4112	3.2841	4.2123	-4.0900	1.4062	-3.2837	-4.2089	-0.1248	0.1904	2.7806	3.0873	-0.1249	0.1899	-2.7808	-3.0876
		400	-4.0903	1.4094	3.2834	4.2113	-4.0910	1.4045	-3.2830	-4.2079	-0.1248	0.1904	2.7805	3.0871	-0.1250	0.1899	-2.7806	-3.0874
0.2	1.8	100	-86.5760	-2.4780	6.3077	8.9869	-86.5780	-2.5071	-6.3265	-9.0105	-2.3031	-0.2202	3.8579	4.6992	-2.3034	-0.2215	-3.8584	-4.6998
		200	-86.5630	-2.4386	6.3221	9.0180	-86.5650	-2.4677	-6.3409	-9.0415	-2.3028	-0.2195	3.8590	4.7006	-2.3031	-0.2208	-3.8595	-4.7012
		300	-86.5600	-2.4299	6.3254	9.0250	-86.5620	-2.4590	-6.3442	-9.0486	-2.3027	-0.2193	3.8594	4.7011	-2.3030	-0.2206	-3.8599	-4.7018
		400	-86.5590	-2.4273	6.3263	9.0271	-86.5610	-2.4564	-6.3451	-9.0507	-2.3026	-0.2192	3.8596	4.7013	-2.3029	-0.2205	-3.8600	-4.7020
1	0.2	100	17.4320	20.3470	6.4002	6.6037	17.4870	20.2960	-6.2653	-6.7254	0.5443	0.6694	4.2307	4.2837	0.5448	0.6695	-4.2226	-4.2759
		200	17.4300	20.3460	6.4002	6.5999	17.4850	20.2940	-6.2641	-6.7241	0.5447	0.6699	4.2316	4.2848	0.5445	0.6690	-4.2227	-4.2760
		300	17.4290	20.3450	6.3998	6.5993	17.4850	20.2930	-6.2637	-6.7236	0.5444	0.6693	4.2241	4.2771	0.5445	0.6692	-4.2232	-4.2765
		400	17.4290	20.3450	6.3996	6.5991	17.4850	20.2930	-6.2635	-6.7234	0.5445	0.6693	4.2331	4.2863	0.5444	0.6689	-4.2219	-4.2751
1	1	100	2.0151	4.2131	2.3606	3.5384	2.0157	4.2135	-2.3608	-3.5383	-0.1689	0.3725	4.7996	5.3362	-0.1690	0.3722	-4.7990	-5.3358
		200	1.9550	4.0981	2.3092	3.4627	1.9556	4.0985	-2.3094	-3.4626	-0.1707	0.3698	4.7930	5.3292	-0.1707	0.3693	-4.7926	-5.3288
		300	1.9428	4.0748	2.2986	3.4472	1.9434	4.0752	-2.2988	-3.4470	-0.1708	0.3693	4.7915	5.3276	-0.1710	0.3688	-4.7917	-5.3279
		400	1.9394	4.0682	2.2957	3.4428	1.9400	4.0687	-2.2959	-3.4427	-0.1710	0.3692	4.7917	5.3278	-0.1710	0.3688	-4.7913	-5.3274
1	1.8	100	-9.9819	-1.1338	3.9408	7.2401	-9.9805	-1.1312	-3.9422	-7.2413	-0.7157	0.0052	3.9014	5.2086	-0.7161	0.0041	-3.9017	-5.2094
		200	-9.9768	-1.1177	3.9473	7.2543	-9.9754	-1.1151	-3.9487	-7.2555	-0.7161	0.0036	3.8956	5.2003	-0.7159	0.0025	-3.8953	-5.2014
		300	-9.9754	-1.1134	3.9491	7.2583	-9.9741	-1.1108	-3.9506	-7.2595	-0.7160	0.0044	3.8953	5.2004	-0.7162	0.0019	-3.8951	-5.2008
		400	-9.9750	-1.1120	3.9497	7.2596	-9.9737	-1.1095	-3.9511	-7.2607	-0.7161	0.0035	3.8953	5.2000	-0.7159	0.0023	-3.8950	-5.2010

below 0.09%, 0.05%, and 0.02% for $L_u = 80 - 120$; and below 0.01% for $L_u = 120 - 160$, respectively, for both cylinders. Furthermore, for both cylinders at a gap ratio of G = 1 and Reynolds number Re = 1, the absolute percentage variations in the drag and lift coefficients are below 0.01%, 1.92%, and 0.36% for $L_u = 40$ compared to 80; below 0.002%, 0.13%, and 0.02% for $L_u = 80$ compared to 120; and below 0.05%, 0.01%, and 0.00% for $L_u = 120$ compared to 160, for n = 0.2, 1, and 1.8, respectively. Similarly, at G = 1 and Re = 40, the corresponding variations are below 0.03%, 1.40%, and 46.23% for $L_u = 40$ compared to 80; below 0.002%, 0.10%, and 7.66% for $L_u = 80$ compared to 120; and below 0.05%, 0.006%, and 1.22% for $L_u = 120$ compared to 160, respectively, for both cylinders. Overall, the relative percentage variations exhibit notable changes when the upstream length increases from $L_u/D = 40$ to 80, indicating a significant influence on the results. However, the variations become minimal between $L_u/D = 80$ and 120 and further diminish between $L_u/D = 120$ and 160. Therefore, $L_u/D = 120$ is chosen as the optimal upstream distance, providing a balance between computational accuracy and efficiency.

The effect of downstream length (L_d) on the force coefficients $(C_{DP}, C_D, C_{LP}, C_L)$ is examined in Table A.2

by fixing the upstream length at $L_u = 120$ and the unconfined domain height at H = 100. For the smallest gap ratio (G = 0.2) and Re = 1, the absolute percentage variations in force coefficients for n = 0.2, 1, and 1.8 are below 0.40%, 1.52%, and 1.53% for $L_d = 100 - 200$; below 0.76%, 0.10%, and 0.98% for $L_d = 200 - 300$; and below 0.45%, 0.22%, and 0.48% for $L_d = 300 - 400$, respectively, for both cylinders. At G = 1 and Re = 1, the corresponding variations are below 0.69%, 0.07%, and 0.56% for $L_d = 100 - 200$; below 0.47%, 0.22%, and 0.99% for $L_d = 200 - 300$; and below 0.39%, 0.17%, and 0.47% for $L_d = 300 - 400$, respectively. For G = 1 and Re = 40, the relative variations are below 0.12%, 0.05%, and 15.49% for $L_d = 100 - 200$; below 0.06%, 0.03%, and 11.14% for $L_d = 200 - 300$; and below 0.10%, 0.02%, and 4.85% for $L_d = 300 - 400$ at n = 0.2, 1, and 1.8, respectively. Since the force coefficients exhibit negligible changes beyond $L_d = 300$, a downstream length of $L_d = 300$ is adopted to ensure accurate flow representation while maintaining computational efficiency.

In unconfined flow analysis, the computational domain is bounded vertically (L_u, L_d) , and minimizing wall effects is essential for accurate flow characterization. The influence of the domain height (H) is examined for H = 100, 200, 300, and 400, while maintaining fixed upstream and downstream lengths of $L_u = 120$ and $L_d = 300$, respectively, with $\alpha = 2$. For G = 0.2, Re = 1, and n = 0.2, 1, and 1.8, the absolute percentage variations in force coefficients are below 0.14%, 1.84%, and 1.59% when comparing H = 100 - 200; below 0.19%, 0.43%, and 0.36% for H = 200-300; and below 0.11%, 0.13%, and 0.11% for H = 300 - 400, respectively. At Re = 40 and the same gap ratio, these variations further reduce to below 0.04%, 0.50%, and 0.30%; 0.04%, 0.08%, and 0.09%; and 0.05%, 0.02%, and 0.03%, respectively, for the same height intervals. For a wider gap ratio (G = 1) at Re = 1, the corresponding variations are below 0.06%, 2.98%, and 1.42% for H = 100 - 200; below 0.01%, 0.62%, and 0.39% for H = 200 - 300; and below 0.00%, 0.17%, and 0.12% for H = 300 - 400. At higher Reynolds number (Re = 40), the respective variations are below 0.08%, 1.05%, and 39.90%; 0.18%, 0.21%, and 24.19%; and 0.21%, 0.13%, and 21.48%. It is evident that domain heights of H = 100 and 200 are insufficient due to noticeable deviations from the results obtained at H = 300. However, only marginal differences are observed between H = 300 and 400. Therefore, H = 300 is selected as the optimal domain height, ensuring accurate results while maintaining computational efficiency.

In summary, a computational domain of size $L_u = 120$, $L_d = 300$, and H = 300 is found to be sufficiently

Table A.4: Grid characteristics. Here, N_c is the mesh points over the surface of a single cylinder, δ_r is the minimum mesh spacing, N_{te} is the triangular mesh elements near the cylinders, and N_e is the total number of mesh elements in the selected computational domain ($L_u = 120$, $L_d = 300$, H = 300).

Grid	N_c	$\delta_r - \delta - \Delta$	G =	= 0.2	G	= 3
Gila	1 V C	$O_r - O - \Delta$	N_{te}	N_e	N_e	N_e
G_1	90	0.005 - 0.1 - 0.5	244018	1320376	247506	1323796
G_2	135	0.005 - 0.1 - 0.5	249400	1388060	252236	1390896
G_3	180	0.005 - 0.1 - 0.5	254652	1455682	256784	1457814

large to accurately capture the hydrodynamic characteristics of unconfined non-Newtonian flow past a pair of rotating circular cylinders.

A.2. Grid independence test

The grid sensitivity analysis is performed using three levels of non-uniform unstructured meshes, denoted as G_1 , G_2 , and G_3 (refer to Table A.4 for detailed specifications), with the optimized computational domain ($L_u = 120$, $L_d = 300$, H = 300). Fig. A.1 shows the computational mesh structure used in this study. The influence of grid resolution on the computed flow characteristics is assessed by varying the number of mesh elements on each cylinder surface ($90 \le N_c \le 180$). Table A.5 presents the influence of mesh refinement

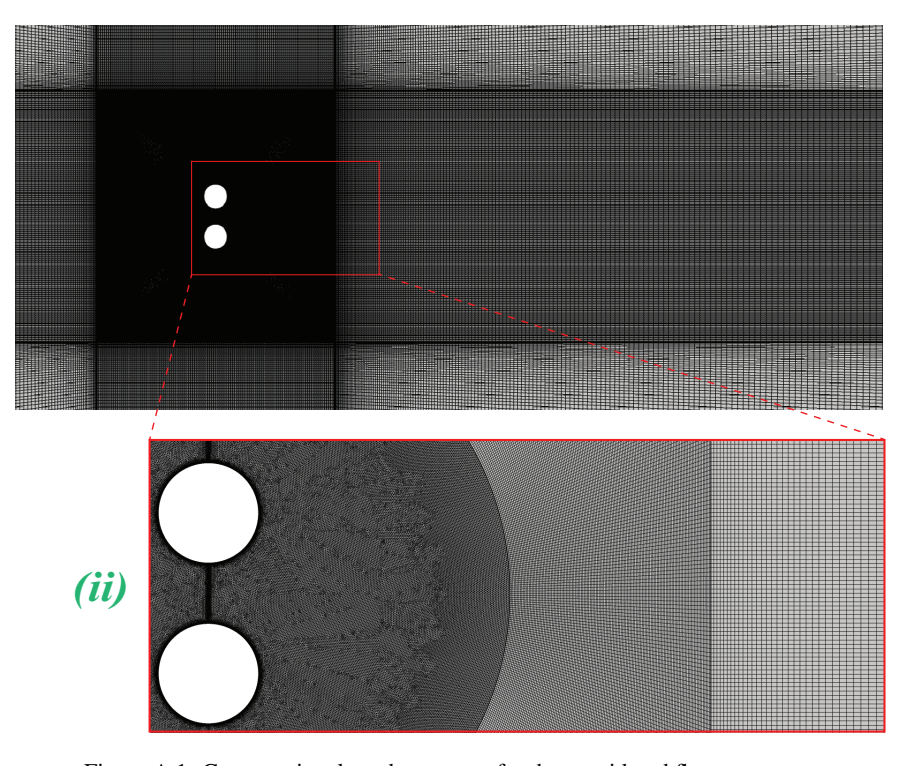


Figure A.1: Computational mesh structure for the considered flow geometry.

Table A.5: The grid independence test for extreme gap ratio (G), Reynolds numbers (Re) and power-law index (n) for the maximum rotational rate $(\alpha = 2)$ of the cylinders.

$L_u =$	120,	$L_d = 300$				Re	= 1							Re	= 40			
	H = 1	300	Į	Jpper cylin	der (UC)		1	Lower cyli	nder (LC)		Ţ	Jpper cylii	nder (UC)			Lower cyl	inder (LC)	
G	n	Grid	C_{DP}	C_D	C_{LP}	C_L	C_{DP}	C_D	C_{LP}	C_L	C_{DP}	C_D	C_{LP}	C_L	C_{DP}	C_D	C_{LP}	C_L
0.2	0.2	G_1	15.1950	17.5900	5.5378	5.7083	15.2250	17.5610	-5.4305	-5.8144	0.4179	0.5370	4.3275	4.3772	0.4181	0.5369	-4.3209	-4.3706
		G_2	15.2060	17.5770	5.5491	5.7045	15.2430	17.5530	-5.4261	-5.8293	0.4188	0.5405	4.3187	4.3733	0.4188	0.5402	-4.3223	-4.3773
		G_3	15.2070	17.5820	5.5382	5.7280	15.2360	17.5480	-5.4421	-5.8057	0.4192	0.5418	4.3244	4.3825	0.4188	0.5414	-4.3210	-4.3792
0.2	1	G_1	-4.0890	1.4250	3.2841	4.2011	-4.0912	1.4166	-3.2864	-4.2053	-0.1250	0.1902	2.7816	3.0816	-0.1252	0.1897	-2.7813	-3.0816
		G_2	-4.0893	1.4112	3.2841	4.2123	-4.0900	1.4062	-3.2837	-4.2089	-0.1248	0.1904	2.7806	3.0873	-0.1249	0.1899	-2.7808	-3.0876
		G_3	-4.0907	1.4026	3.2802	4.2085	-4.0885	1.4077	-3.2872	-4.2168	-0.1248	0.1903	2.7804	3.0904	-0.1248	0.1899	-2.7800	-3.0898
0.2	1.8	G_1	-86.5050	-2.2142	6.3250	9.0061	-86.5110	-2.2662	-6.3463	-9.0240	-2.3013	-0.2144	3.8594	4.6912	-2.3020	-0.2163	-3.8604	-4.6927
		G_2	-86.5600	-2.4299	6.3254	9.0250	-86.5620	-2.4590	-6.3442	-9.0486	-2.3027	-0.2193	3.8594	4.7010	-2.3030	-0.2207	-3.8599	-4.7018
		G_3	-86.5860	-2.5520	6.3076	9.0163	-86.5770	-2.5273	-6.3517	-9.0443	-2.3031	-0.2223	3.8591	4.7063	-2.3033	-0.2239	-3.8595	-4.7046
1	0.2	G_1	17.4340	20.3350	6.3912	6.5756	17.4550	20.3150	-6.2978	-6.7003	0.5437	0.6661	4.2304	4.2786	0.5434	0.6657	-4.2220	-4.2700
		G_2	17.4260	20.3450	6.3935	6.6095	17.4800	20.2990	-6.2645	-6.7295	0.5446	0.6697	4.2221	4.2748	0.5446	0.6692	-4.2236	-4.2769
		G_3	17.4250	20.3470	6.4295	6.5842	17.4710	20.3090	-6.2955	-6.7048	0.5445	0.6704	4.2323	4.2887	0.5448	0.6704	-4.2262	-4.2826
1	1	G_1	1.9442	4.0749	2.2977	3.4389	1.9399	4.0625	-2.3007	-3.4459	-0.1713	0.3698	4.7922	5.3169	-0.1714	0.3693	-4.7919	-5.3169
		G_2	1.9438	4.0746	2.2987	3.4495	1.9420	4.0713	-2.2988	-3.4469	-0.1708	0.3693	4.7915	5.3276	-0.1710	0.3688	-4.7917	-5.3279
		G_3	1.9426	4.0734	2.2990	3.4517	1.9430	4.0744	-2.3009	-3.4561	-0.1708	0.3687	4.7920	5.3340	-0.1709	0.3686	-4.7914	-5.3334
1	1.8	G_1	-9.9659	-1.0668	3.9483	7.2445	-9.9805	-1.1105	-3.9562	-7.2643	-0.7164	0.0049	3.8958	5.1905	-0.7169	0.0033	-3.8960	-5.1919
		G_2	-9.9732	-1.1135	3.9493	7.2648	-9.9783	-1.1241	-3.9510	-7.2594	-0.7160	0.0043	3.8953	5.2004	-0.7162	0.0025	-3.8950	-5.2014
		G_3	-9.9781	-1.1370	3.9496	7.2681	-9.9773	-1.1349	-3.9551	-7.2812	-0.7159	0.0019	3.8952	5.2044	-0.7157	0.0014	-3.8949	-5.2055

on the absolute percentage variations in the force coefficients (C_{DP} , C_{DP} , C_{LP} , and C_{L}) for both cylinders under different combinations of governing parameters: n=0.2, 1, and 1.8; Re=1 and 40; G=0.2 and 1; and $\alpha=2$ (maximum rotational rate). For Re=1, the variations between grids G_2 and G_1 are found to be under 0.256%, 0.968%, and 9.742%, whereas the corresponding differences between G_3 and G_2 are below 0.412%, 0.609%, and 5.025%. Similarly, for Re=40 and the same set of parameters, the variations between G_2 and G_1 were below 0.659%, 0.208%, and 2.280%, while those between G_3 and G_2 are below 0.231%, 0.1%, and 1.487%. Furthermore, at G=1 and Re=1, the variations in the drag and lift components are below 0.529%, 0.308%, and 4.378% between G_2 and G_1 , and below 0.563%, 0.267%, and 2.11% between G_3 and G_2 . Similarly, at G=1 and $G_2=40$, the corresponding variations are below 0.543%, 0.263%, and 0.191% between $G_2=40$ and $G_1=40$, and 0.079% between $G_3=40$ and $G_2=40$ and $G_3=40$ and $G_3=40$

Appendix B. Pressure and friction drag coefficients (C_{DP} and C_{DF})

Table B.1: Dependence of the pressure (C_{DP}) and friction (C_{DF}) drag coefficients on the Reynolds number (Re = 1), rotational velocity (α) and power-law index (n) for upper (UC) and lower (LC) cylinders.

Re	= 1				(C _{DP} (for U	C)								C _{DP} (for I	LC)			
α	G	$n \rightarrow 0.2$	0.4	0.6	0.8	1	1.2	1.4	1.6	1.8	0.2	0.4	0.6	0.8	1	1.2	1.4	1.6	1.8
0	0.2	19.255	13.149	8.2116	5.5667	4.1126	3.2396	2.6811	2.3058	2.0409	19.255	13.149	8.2113	5.5663	4.1123	3.2393	2.6808	2.3054	2.0406
	0.4	19.763	13.302	8.2119	5.5284	4.0639	3.1896	2.6327	2.2597	1.9965	19.762	13.301	8.2112	5.5278	4.0633	3.1891	2.6322	2.2592	1.996
	0.6	20.056	13.504	8.2746	5.5444	4.063	3.183	2.6243	2.2504	1.9864	20.056	13.503	8.2741	5.5439	4.0626	3.1826	2.6239	2.25	1.986
	0.8	20.132	13.699	8.3615	5.5862	4.0872	3.2006	2.6394	2.2639	1.9983	20.131	13.699	8.3611	5.5857	4.0867	3.2001	2.6389	2.2634	1.9979
	1	20.078	13.8680	8.4556	5.6403	4.1246	3.2317	2.6679	2.2908	2.0235	20.078	13.868	8.4552	5.6398	4.1241	3.2311	2.6674	2.2903	2.023
1	0.2	16.739	11.505	6.7605	3.2949	0.1225	-3.5203	-8.2432	-14.706	-23.744	16.719	11.511	6.7602	3.2945	0.1220	-3.5209	-8.2439	-14.706	-23.745
	0.4	17.885	11.783	7.1710	4.2744	2.0614	-0.079	-2.4979	-5.4682	-9.2591	17.881	11.793	7.1705	4.2738	2.0608	-0.0799	-2.4991	-5.4697	-9.2613
	0.6	18.607	12.203	7.3399	4.5387	2.6161	0.9635	-0.7199	-2.6209	-4.8874	18.668	12.209	7.3401	4.5389	2.6163	0.9636	-0.7198	-2.6209	-4.8874
	0.8	18.941	12.6540	7.5269	4.7001	2.8857	1.4544	0.1147	-1.2944	-2.8805	18.970	12.661	7.5269	4.7000	2.8856	1.4542	0.1144	-1.2947	-2.8808
	1	19.124	13.072	7.7258	4.8383	3.0601	1.7418	0.5902	-0.5472	-1.7626	19.100	13.075	7.725	4.8374	3.059	1.7404	0.5887	-0.549	-1.7647
2	0.2	15.206	10.457	5.5489	1.2151	-4.0893	-12.252	-25.782	-48.514	-86.560	15.243	10.457	5.5487	1.2147	-4.090	-12.253	-25.783	-48.516	-86.562
	0.4	16.087	10.78	6.3074	3.0788	-0.0835	-4.2704	-10.603	-20.548	-36.204	16.132	10.78	6.3072	3.0784	-0.0842	-4.2716	-10.605	-20.552	-36.209
	0.6	16.860	11.105	6.5269	3.5675	1.0715	-1.8288	-5.8689	-11.879	-20.954	16.905	11.106	6.5274	3.5682	1.0723	-1.8278	-5.8678	-11.878	-20.952
	0.8	17.256	11.482	6.7176	3.8232	1.6142	-0.6811	-3.6351	-7.8182	-13.919	17.301	11.482	6.7177	3.8234	1.6145	-0.6807	-3.6347	-7.8177	-13.918
	1	17.426	11.843	6.9104	4.0138	1.9438	-0.0188	-2.3595	-5.5157	-9.9732	17.480	11.842	6.9094	4.0124	1.942	-0.0211	-2.3626	-5.5196	-9.9783
Re	= 1				-	C _{DF} (for U	C)								C_{DF} (for I	LC)			
α	G	$n \rightarrow 0.2$	0.4	0.6	0.8	1	1.2	1.4	1.6	1.8	0.2	0.4	0.6	0.8	1	1.2	1.4	1.6	1.8
0	0.2	5.2057	5.0228	4.0525	3.2814	2.7519	2.3854	2.1237	1.9297	1.7807	5.2049	5.022	4.0521	3.2811	2.7516	2.3852	2.1236	1.9296	1.7806
	0.4	6.1607	5.7449	4.5309	3.6273	3.0254	2.6170	2.3297	2.1191	1.9584	6.1592	5.7443	4.5305	3.6269	3.025	2.6165	2.3293	2.1186	1.9579
	0.6	6.7665	6.2778	4.8925	3.8897	3.2328	2.7930	2.4875	2.2655	2.0971	6.7661	6.2775	4.8922	3.8894	3.2325	2.7928	2.4872	2.2653	2.0969
	0.8	7.1134	6.6834	5.1820	4.1025	3.4018	2.9370	2.6170	2.3863	2.2118	7.1133	6.6831	5.1816	4.1020	3.4012	2.9365	2.6164	2.3857	2.2112
	1	7.2992	6.9928	5.4182	4.2799	3.544	3.0593	2.7278	2.4901	2.3107	7.2987	6.9927	5.4179	4.2795	3.5435	3.0587	2.7272	2.4895	2.3101
1	0.2	3.9106	2.955	2.2211	2.7216	4.2015	6.8094	10.8700	16.9000	25.661	3.9973	2.9335	2.2200	2.7198	4.1993	6.8064	10.866	16.894	25.654
	0.4	3.8012	3.6613	2.6140	2.3826	2.7760	3.7792	5.4493	7.9007	11.309	4.0198	3.637	2.6137	2.3822	2.7754	3.7783	5.4481	7.8997	11.3100
	0.6	4.1098	3.9513	3.0322	2.6194	2.6436	3.0914	3.9685	5.3074	7.1701	4.1796	3.9434	3.0324	2.6197	2.6441	3.0919	3.969	5.3078	7.1704
	0.8	4.4878	4.1404	3.3149	2.869	2.7323	2.9115	3.4042	4.2159	5.3672	4.4989	4.1269	3.3149	2.8692	2.7326	2.912	3.405	4.2171	5.3689
	1	4.6951	4.2332	3.5111	3.0795	2.8687	2.8994	3.1725	3.6853	4.442	4.6548	4.2146	3.5107	3.0788	2.8677	2.8982	3.1709	3.6834	4.4398
2	0.2	2.3706	1.6122	1.2337	2.2634	5.5005	12.256	24.752	46.678	84.13	2.3099	1.6115	1.2322	2.2606	5.4962	12.249	24.741	46.661	84.103
	0.4	2.6616	2.5305	1.6958	1.4759	2.4068	5.0195	10.152	19.084	33.831	2.5787	2.5302	1.6956	1.4755	2.406	5.0181	10.150	19.084	33.834
	0.6	2.7406	2.9436	2.2666	1.7638	1.9591	3.2022	5.9596	10.918	19.091	2.6538	2.9434	2.2669	1.7646	1.9603	3.2037	5.9613	10.919	19.092
	0.8	2.8544	3.1401	2.6489	2.1046	1.9859	2.5807	4.2056	7.2897	12.442	2.7680	3.1400	2.649	2.1051	1.9871	2.5828	4.2090	7.2950	12.450
	1	2.9191	3.2598	2.905	2.3946	2.1308	2.3685	3.3517	5.3801	8.8597	2.8192	3.2596	2.9044	2.3937	2.1293	2.3664	3.3488	5.3761	8.8542

Table B.2: Dependence of the pressure (C_{DP}) and friction (C_{DF}) drag coefficients on the Reynolds number (Re = 5), rotational velocity (α) and power-law index (n) for upper (UC) and lower (LC) cylinders.

Re	= 5					C _{DP} (for U	C)								C_{DP} (for 1	LC)			
α	G	$n \rightarrow 0.2$	0.4	0.6	0.8	1	1.2	1.4	1.6	1.8	0.2	0.4	0.6	0.8	1	1.2	1.4	1.6	1.8
0	0.2	4.302	3.1987	2.5232	2.113	1.8451	1.6599	1.5232	1.4162	1.3284	4.3019	3.1985	2.523	2.1128	1.8449	1.6597	1.523	1.4159	1.3282
	0.4	4.3636	3.2396	2.5376	2.1134	1.8373	1.6468	1.506	1.3953	1.3039	4.3632	3.2392	2.5372	2.1131	1.837	1.6465	1.5057	1.395	1.3036
	0.6	4.3932	3.2881	2.572	2.1374	1.8546	1.6584	1.5129	1.3982	1.3032	4.3931	3.2879	2.5718	2.1372	1.8543	1.6581	1.5126	1.398	1.303
	0.8	4.4051	3.3302	2.613	2.1731	1.8857	1.6851	1.5354	1.4169	1.3184	4.405	3.33	2.6127	2.1728	1.8854	1.6848	1.535	1.4165	1.3181
	1	4.4072	3.363	2.6539	2.2135	1.924	1.7205	1.5674	1.4457	1.3444	4.4071	3.3627	2.6536	2.2132	1.9237	1.7201	1.5671	1.4454	1.344
1	0.2	3.5608	2.536	1.8363	1.2508	0.641	-0.091	-1.0466	-2.3513	-4.1705	3.5596	2.5364	1.8368	1.2507	0.6407	-0.0913	-1.047	-2.3517	-4.1709
	0.4	3.8081	2.6127	1.921	1.4409	1.0219	0.5921	0.1001	-0.5017	-1.2656	3.8089	2.6166	1.9213	1.4408	1.0215	0.5916	0.0996	-0.5023	-1.2664
	0.6	3.9357	2.7383	1.9802	1.4989	1.1262	0.7882	0.4412	0.053	-0.405	3.937	2.7385	1.981	1.4989	1.126	0.788	0.441	0.0528	-0.4053
	0.8	4.0029	2.8496	2.0535	1.5458	1.1779	0.8734	0.5889	0.2961	-0.0267	4.0044	2.8534	2.0537	1.5457	1.1776	0.873	0.5885	0.2956	-0.0272
	1	4.0444	2.9338	2.1297	1.5951	1.2161	0.9199	0.6633	0.4187	0.1667	4.0463	2.9359	2.1296	1.5949	1.2155	0.9192	0.6626	0.4179	0.1658
2	0.2	3.0965	2.1506	1.3284	0.4711	-0.6718	-2.4133	-5.227	-9.8676	-17.552	3.0987	2.1523	1.3282	0.4709	-0.672	-2.4137	-5.2275	-9.8682	-17.553
	0.4	3.3178	2.2174	1.4722	0.8595	0.1782	-0.7365	-2.0847	-4.1499	-7.3477	3.3211	2.22	1.4721	0.8593	0.1778	-0.737	-2.0855	-4.151	-7.3494
	0.6	3.4984	2.3217	1.5147	0.945	0.4064	-0.2337	-1.104	-2.3633	-4.2272	3.5023	2.3239	1.5148	0.9451	0.4064	-0.2337	-1.104	-2.3633	-4.2273
	0.8	3.6198	2.4359	1.5648	0.9796	0.4929	-0.0202	-0.6617	-1.5413	-2.7956	3.6241	2.4373	1.5647	0.9794	0.4926	-0.0205	-0.662	-1.5416	-2.796
	1	3.7045	2.5368	1.6272	1.0049	0.5283	0.079	-0.4347	-1.0996	-2.0138	3.7099	2.5371	1.6268	1.0044	0.5276	0.0781	-0.4358	-1.1009	-2.0155
Re	= 5					C _{DF} (for U	C)								C_{DF} (for	LC)			
α	G	$n \rightarrow 0.2$	0.4	0.6	0.8	1	1.2	1.4	1.6	1.8	0.2	0.4	0.6	0.8	1	1.2	1.4	1.6	1.8
0	0.2	1.1142	1.1361	1.1138	1.0861	1.0582	1.0324	1.0086	0.9859	0.9635	1.1138	1.1358	1.1136	1.0859	1.0581	1.0323	1.0085	0.9858	0.9634
	0.4	1.3296	1.3308	1.2855	1.244	1.2082	1.1773	1.1494	1.1232	1.0971	1.3294	1.3306	1.2854	1.2438	1.208	1.1771	1.1492	1.1229	1.0968
	0.6	1.4204	1.4677	1.4158	1.3675	1.328	1.2951	1.2655	1.2372	1.2087	1.4207	1.4676	1.4157	1.3674	1.3279	1.2949	1.2654	1.2371	1.2085
	0.8	1.4548	1.5626	1.5182	1.4696	1.4295	1.3964	1.3666	1.3375	1.3074	1.4547	1.5624	1.5179	1.4692	1.4291	1.396	1.3662	1.3371	1.307
	1	1.4669	1.6259	1.5983	1.5547	1.5171	1.4856	1.4568	1.4281	1.3976	1.4669	1.6257	1.5981	1.5544	1.5167	1.4853	1.4565	1.4277	1.3973
1	0.2	0.987	0.788	0.7673	0.9162	1.2308	1.7524	2.5522	3.7384	5.4666	0.9869	0.7765	0.7654	0.9155	1.2302	1.7517	2.5512	3.7372	5.4647
	0.4	1.0184	0.923	0.9162	0.9422	1.0479	1.2497	1.5682	2.0346	2.69	1.0158	0.9293	0.9143	0.9417	1.0477	1.2493	1.5678	2.0341	2.6893
	0.6	1.0482	0.9953	1.0354	1.0564	1.1052	1.2038	1.3664	1.6086	1.9487	1.0471	0.9798	1.0347	1.0562	1.1052	1.2038	1.3664	1.6087	1.9487
	0.8	1.0731	1.0401	1.113	1.1573	1.1944	1.251	1.3425	1.4816	1.6791	1.0688	1.0324	1.111	1.1569	1.1942	1.2507	1.3423	1.4813	1.6789
	1	1.0755	1.0683	1.1636	1.2388	1.2838	1.3251	1.3811	1.4644	1.5844	1.0751	1.0486	1.1615	1.238	1.2833	1.3245	1.3803	1.4636	1.5834
2	0.2	0.5589	0.4379	0.4326	0.6716	1.2947	2.5751	4.9635	9.2015	16.507	0.5558	0.4347	0.4324	0.6708	1.2936	2.5734	4.961	9.1976	16.502
	0.4	0.5996	0.6461	0.6091	0.6268	0.8017	1.2602	2.1803	3.8251	6.5989	0.5942	0.6412	0.609	0.6266	0.8015	1.2597	2.1797	3.8238	6.5975
	0.6	0.6122	0.7208	0.7691	0.7661	0.8156	1.0137	1.4677	2.323	3.7875	0.6045	0.7178	0.7691	0.7662	0.8158	1.014	1.4681	2.3234	3.7879
	0.8	0.618	0.7505	0.8721	0.8993	0.9093	0.9932	1.2321	1.7213	2.5884	0.6121	0.747	0.872	0.8992	0.9093	0.9933	1.2323	1.7218	2.5893
	1	0.6272	0.7698	0.9363	1.0101	1.0171	1.0453	1.1673	1.4548	1.9956	0.6163	0.7675	0.936	1.0096	1.0165	1.0444	1.1662	1.4534	1.9938

Table B.3: Dependence of the pressure (C_{DP}) and friction (C_{DF}) drag coefficients on the Reynolds number (Re = 10), rotational velocity (α) and power-law index (n) for upper (UC) and lower (LC) cylinders.

Re	= 10				(C _{DP} (for U	C)								C _{DP} (for I	LC)			
α	G	$n \rightarrow 0.2$	0.4	0.6	0.8	1	1.2	1.4	1.6	1.8	0.2	0.4	0.6	0.8	1	1.2	1.4	1.6	1.8
0	0.2	2.4644	2.0012	1.7318	1.559	1.4371	1.3429	1.2654	1.1984	1.1385	2.4642	2.001	1.7316	1.5588	1.4369	1.3428	1.2652	1.1982	1.1383
	0.4	2.5182	2.0354	1.7529	1.5678	1.4363	1.3352	1.252	1.18	1.1149	2.518	2.0351	1.7527	1.5675	1.436	1.3349	1.2517	1.1797	1.1147
	0.6	2.5459	2.0812	1.7948	1.6019	1.462	1.3535	1.264	1.1866	1.1165	2.5458	2.0811	1.7947	1.6017	1.4618	1.3533	1.2638	1.1864	1.1163
	0.8	2.5452	2.1175	1.8405	1.6463	1.5018	1.388	1.2935	1.2116	1.1374	2.5452	2.1174	1.8403	1.6461	1.5016	1.3877	1.2933	1.2113	1.1371
	1	2.5402	2.136	1.8768	1.6887	1.5449	1.4295	1.3328	1.2489	1.173	2.5401	2.1359	1.8766	1.6885	1.5447	1.4292	1.3326	1.2486	1.1728
1	0.2	1.9555	1.4332	1.1262	0.8638	0.5813	0.2333	-0.23	-0.8703	-1.7701	1.9552	1.4334	1.1262	0.8636	0.5811	0.2331	-0.23	-0.8703	-1.7701
	0.4	2.0774	1.4997	1.1596	0.9341	0.7431	0.5469	0.3188	0.034	-0.3325	2.0766	1.5	1.1596	0.9339	0.7428	0.5466	0.3185	0.0343	-0.3325
	0.6	2.147	1.5845	1.2109	0.9607	0.7772	0.619	0.4601	0.2819	0.0695	2.147	1.5848	1.2109	0.9606	0.777	0.6188	0.4601	0.2824	0.0698
	0.8	2.1919	1.6463	1.2717	0.9998	0.7998	0.644	0.5074	0.3719	0.2249	2.192	1.6468	1.2718	0.9995	0.7995	0.6436	0.5071	0.372	0.225
	1	2.2226	1.6953	1.3287	1.0481	0.8303	0.6617	0.5253	0.404	0.2865	2.223	1.6952	1.3286	1.0478	0.8299	0.6613	0.5249	0.4046	0.2869
2	0.2	1.5713	1.0823	0.7007	0.2749	-0.3102	-1.2041	-2.6396	-4.9907	-8.8632	1.5761	1.0836	0.7012	0.2747	-0.3104	-1.2044	-2.64	-4.9911	-8.8636
	0.4	1.7095	1.1119	0.7285	0.4264	0.0896	-0.3682	-1.0478	-2.0902	-3.7018	1.7112	1.1132	0.7293	0.4262	0.0893	-0.3686	-1.0483	-2.0909	-3.7029
	0.6	1.8187	1.1913	0.7358	0.4247	0.1554	-0.1568	-0.5838	-1.2076	-2.1366	1.8156	1.1932	0.7366	0.4246	0.1554	-0.1569	-0.5839	-1.2077	-2.1368
	0.8	1.8926	1.2719	0.7751	0.4131	0.1469	-0.1047	-0.4111	-0.8348	-1.4468	1.8914	1.2724	0.7757	0.4128	0.1466	-0.105	-0.4115	-0.8352	-1.4472
	1	1.9494	1.3383	0.8305	0.4218	0.1217	-0.1149	-0.3588	-0.6694	-1.1024	1.9532	1.3397	0.8313	0.4214	0.1212	-0.1155	-0.3596	-0.6704	-1.1036
Re	= 10					C _{DF} (for U	C)								C_{DF} (for I	LC)			
α	G	$n \rightarrow 0.2$	0.4	0.6	0.8	1	1.2	1.4	1.6	1.8	0.2	0.4	0.6	0.8	1	1.2	1.4	1.6	1.8
0	0.2	0.5994	0.6461	0.6818	0.7065	0.7225	0.732	0.7363	0.7359	0.7311	0.5992	0.6459	0.6817	0.7063	0.7223	0.7319	0.7362	0.7358	0.731
	0.4	0.696	0.7784	0.814	0.8389	0.8548	0.8634	0.8658	0.8627	0.8544	0.696	0.7783	0.8139	0.8388	0.8547	0.8632	0.8656	0.8625	0.8541
	0.6	0.7143	0.8595	0.9126	0.9436	0.9629	0.9734	0.9762	0.9722	0.9617	0.7143	0.8595	0.9126	0.9435	0.9628	0.9733	0.9761	0.9721	0.9616
	0.8	0.7189	0.9009	0.9823	1.0265	1.0533	1.0683	1.0739	1.0711	1.0604	0.7188	0.9008	0.9821	1.0263	1.053	1.068	1.0735	1.0708	1.0601
	1	0.7193	0.92	1.026	1.0873	1.1251	1.1478	1.1588	1.16	1.1523	0.7192	0.9199	1.0258	1.0871	1.1249	1.1475	1.1585	1.1597	1.152
1	0.2	0.5387	0.5544	0.5637	0.6353	0.7848	1.035	1.4255	2.0104	2.8626	0.5381	0.5536	0.5632	0.635	0.7845	1.0345	1.4247	2.0091	2.8613
	0.4	0.5551	0.6358	0.6735	0.7002	0.7502	0.8407	0.9879	1.2129	1.5255	0.5548	0.6344	0.6731	0.7001	0.75	0.8404	0.9874	1.2107	1.5235
	0.6	0.5613	0.6612	0.7439	0.7918	0.8259	0.8703	0.941	1.0541	1.2075	0.5608	0.6608	0.7441	0.7917	0.8259	0.8703	0.9408	1.0523	1.2061
	0.8	0.565	0.6787	0.783	0.8626	0.9095	0.9433	0.9833	1.0456	1.1285	0.5639	0.6781	0.7825	0.8623	0.9092	0.943	0.9833	1.0449	1.1275
_	1	0.5671	0.6878	0.8075	0.9117	0.9829	1.0251	1.0564	1.0969	1.1426	0.5664	0.6874	0.807	0.9114	0.9825	1.0247	1.0555	1.0951	1.1404
2	0.2	0.3078	0.3184	0.3229	0.4424	0.7479	1.37	2.534	4.61	8.2053	0.2986	0.3155	0.3216	0.442	0.7472	1.369	2.5326	4.6079	8.2021
	0.4	0.316	0.4326	0.4613	0.4807	0.5666	0.7789	1.209	1.989	3.3217	0.3135	0.4299	0.4597	0.4806	0.5664	0.7787	1.2086	1.9881	3.3196
	0.6	0.3215	0.4595	0.5641	0.5972	0.6291	0.7157	0.9155	1.3028	1.9822	0.3142	0.4572	0.5634	0.5973	0.6292	0.7158	0.9157	1.3031	1.9825
	0.8	0.3081	0.4719	0.6193	0.7006	0.7294	0.7634	0.8579	1.0643	1.4473	0.3107	0.4699	0.618	0.7005	0.7292	0.7633	0.8578	1.0643	1.4475
	1	0.3259	0.4818	0.6474	0.7756	0.8325	0.8489	0.8864	0.9925	1.2137	0.319	0.4786	0.645	0.7752	0.832	0.8482	0.8855	0.9914	1.2124

Table B.4: Dependence of the pressure (C_{DP}) and friction (C_{DF}) drag coefficients on the Reynolds number (Re=20), rotational velocity (α) and power-law index (n) for upper (UC) and lower (LC) cylinders.

Re	= 20				(C _{DP} (for U	(C)								C _{DP} (for I	LC)			
α	G	$n \rightarrow 0.2$	0.4	0.6	0.8	1	1.2	1.4	1.6	1.8	0.2	0.4	0.6	0.8	1	1.2	1.4	1.6	1.8
0	0.2	1.5988	1.3928	1.2941	1.2254	1.1681	1.1165	1.0677	1.0202	0.9722	1.5987	1.3927	1.294	1.2252	1.168	1.1163	1.0676	1.02	0.972
	0.4	1.6445	1.4675	1.3421	1.2519	1.18	1.1178	1.0606	1.0056	0.9499	1.6445	1.4673	1.3419	1.2517	1.1798	1.1176	1.0604	1.0054	0.9497
	0.6	1.6258	1.4943	1.398	1.3065	1.2254	1.1536	1.088	1.0256	0.9628	1.6257	1.4943	1.3979	1.3064	1.2253	1.1535	1.0879	1.0254	0.9627
	0.8	1.6081	1.4923	1.4184	1.3463	1.2741	1.204	1.137	1.0723	1.0076	1.6081	1.4923	1.4183	1.3463	1.274	1.2038	1.1368	1.0721	1.0074
	1	1.5929	1.4851	1.4219	1.3635	1.3046	1.2452	1.1861	1.1278	1.0699	1.5929	1.485	1.4218	1.3633	1.3044	1.245	1.1859	1.1276	1.0697
1	0.2	1.1296	0.8725	0.7256	0.6093	0.4842	0.326	0.1099	-0.1951	-0.6299	1.1295	0.8724	0.7254	0.6091	0.484	0.3259	0.1096	-0.1953	-0.6298
	0.4	1.2243	0.9443	0.7539	0.6247	0.5297	0.4424	0.3439	0.2196	0.055	1.2243	0.9442	0.7538	0.6245	0.5295	0.4421	0.3437	0.2194	0.0549
	0.6	1.2668	1.0175	0.8199	0.6615	0.5431	0.4544	0.3787	0.3017	0.2121	1.2668	1.0176	0.8199	0.6614	0.543	0.4543	0.3786	0.3016	0.2121
	0.8	1.2918	1.0654	0.8834	0.7206	0.5807	0.4696	0.3839	0.3132	0.2468	1.292	1.0656	0.8834	0.7205	0.5805	0.4694	0.3836	0.3131	0.2468
	1	1.3095	1.0974	0.9304	0.7771	0.6332	0.5047	0.3986	0.3145	0.2459	1.3095	1.0973	0.9303	0.7769	0.6329	0.5044	0.3982	0.3141	0.2457
2	0.2	0.8044	0.5197	0.3358	0.1274	-0.1654	-0.6187	-1.3485	-2.5404	-4.4959	0.8042	0.52	0.3359	0.1273	-0.1656	-0.6189	-1.3487	-2.5407	-4.4963
	0.4	0.8901	0.5459	0.3003	0.1365	-0.0255	-0.2425	-0.5709	-1.084	-1.8861	0.8905	0.5462	0.3003	0.1363	-0.0257	-0.2428	-0.5713	-1.0845	-1.8868
	0.6	0.9501	0.6092	0.3171	0.0911	-0.0629	-0.2076	-0.4	-0.689	-1.1328	0.9499	0.6095	0.3173	0.0911	-0.0629	-0.2076	-0.4	-0.6891	-1.1329
	0.8	0.9939	0.6627	0.366	0.0936	-0.1153	-0.2584	-0.3932	-0.5747	-0.8482	0.994	0.6629	0.3659	0.0934	-0.1155	-0.2587	-0.3935	-0.5751	-0.8486
	1	1.0282	0.7065	0.414	0.1301	-0.1279	-0.3196	-0.4514	-0.5797	-0.7568	1.0292	0.7068	0.4141	0.1298	-0.1283	-0.3201	-0.452	-0.5804	-0.7576
Re	= 20					C _{DF} (for U	C)								C_{DF} (for I	LC)			
α	G	$n \rightarrow 0.2$	0.4	0.6	0.8	1	1.2	1.4	1.6	1.8	0.2	0.4	0.6	0.8	1	1.2	1.4	1.6	1.8
0	0.2	0.3225	0.3874	0.4341	0.471	0.4992	0.5198	0.5334	0.5407	0.5416	0.3224	0.3873	0.434	0.471	0.4992	0.5197	0.5334	0.5406	0.5415
	0.4	0.3293	0.4709	0.5459	0.5916	0.6233	0.6445	0.6568	0.6611	0.6569	0.3293	0.4709	0.5459	0.5916	0.6232	0.6444	0.6567	0.6609	0.6567
	0.6	0.3353	0.4895	0.6024	0.6755	0.7213	0.7498	0.7655	0.7704	0.7644	0.3352	0.4895	0.6023	0.6754	0.7212	0.7497	0.7654	0.7703	0.7644
	0.8	0.3373	0.4954	0.622	0.7179	0.7853	0.8299	0.8569	0.8696	0.8691	0.3372	0.4954	0.6219	0.7177	0.7851	0.8297	0.8566	0.8693	0.8688
	1	0.3383	0.4974	0.6293	0.7356	0.8178	0.8787	0.9214	0.9487	0.9626	0.3383	0.4973	0.6291	0.7354	0.8177	0.8785	0.9212	0.9485	0.9624
1	0.2	0.2952	0.3745	0.4112	0.4547	0.5275	0.6458	0.8304	1.1104	1.528	0.2949	0.3742	0.411	0.4545	0.5272	0.6455	0.8301	1.1101	1.527
	0.4	0.2959	0.4063	0.4876	0.5322	0.5647	0.6059	0.669	0.7659	0.9103	0.2959	0.4061	0.4874	0.5321	0.5646	0.6058	0.6688	0.7654	0.9097
	0.6	0.2969	0.4123	0.5179	0.597	0.6441	0.6741	0.7039	0.7455	0.8092	0.2968	0.4121	0.5178	0.5969	0.6441	0.6741	0.7039	0.7458	0.8089
	0.8	0.2975	0.4142	0.5292	0.6309	0.7071	0.7538	0.7817	0.8047	0.8345	0.2972	0.4138	0.5289	0.6307	0.7069	0.7536	0.7814	0.8042	0.8337
	1	0.298	0.4153	0.5339	0.6466	0.7442	0.8173	0.863	0.8891	0.9084	0.2978	0.4151	0.5337	0.6463	0.744	0.817	0.8626	0.8886	0.9076
2	0.2	0.1983	0.2375	0.2536	0.3161	0.4644	0.7652	1.3301	2.3429	4.1062	0.1975	0.2368	0.2529	0.3156	0.4639	0.7646	1.3292	2.3417	4.1043
	0.4	0.2014	0.2947	0.3653	0.3911	0.4329	0.5297	0.7268	1.0909	1.7231	0.2013	0.2941	0.3652	0.391	0.4328	0.5296	0.7265	1.0903	1.7219
	0.6	0.203	0.3035	0.4207	0.4959	0.5232	0.5567	0.6381	0.8057	1.1116	0.2025	0.3031	0.4204	0.4959	0.5232	0.5568	0.6382	0.8058	1.1118
	0.8	0.2037	0.3075	0.4381	0.5602	0.6278	0.6479	0.6737	0.7472	0.9031	0.2034	0.3071	0.4379	0.56	0.6276	0.6477	0.6735	0.747	0.903
	1	0.2047	0.3098	0.4457	0.5885	0.7041	0.7559	0.7633	0.7814	0.8504	0.2037	0.3088	0.4451	0.5881	0.7037	0.7553	0.7626	0.7806	0.8495

Table B.5: Dependence of the pressure (C_{DP}) and friction (C_{DF}) drag coefficients on the Reynolds number (Re = 40), rotational velocity (α) and power-law index (n) for upper (UC) and lower (LC) cylinders.

Re	= 40					C _{DP} (for U	C)								C _{DP} (for L	.C)			
α	G	$n \rightarrow 0.2$	0.4	0.6	0.8	1	1.2	1.4	1.6	1.8	0.2	0.4	0.6	0.8	1	1.2	1.4	1.6	1.8
0	0.2	1.1836	1.115	1.0474	1.0075	0.9729	0.9374	0.8989	0.85541	0.80074	1.1797	1.1148	1.0473	1.0074	0.9728	0.9373	0.8988	0.8553	0.8006
	0.4	1.1674	1.1462	1.1238	1.0763	1.0196	0.9656	0.9129	0.8573		1.1593	1.1457	1.1236	1.0762	1.0195	0.9655	0.9127	0.8572	
	0.6	1.1417	1.1394	1.1374	1.119	1.0836	1.0352	0.9793	0.9182	0.8391	1.1388	1.139	1.1373	1.1189	1.0835	1.0351	0.9792	0.9181	0.839
	0.8	1.1194	1.1267	1.1348	1.1297	1.1115	1.0824	1.0443		0.9465	1.1182	1.1265	1.1347	1.1296	1.1114	1.0823	1.0442		0.9464
	1	1.101	1.1136	1.1268	1.1285	1.1192	1.1011	1.0765	1.047		1.1007	1.1133	1.1267	1.1284	1.1191	1.101	1.0764	1.0469	
1	0.2	0.7132	0.5837	0.493	0.4364	0.3835	0.3155	0.219	0.0789	-0.1251	0.7127	0.5835	0.4928	0.4362	0.3834	0.3153	0.2188	0.0788	-0.1252
	0.4	0.7609	0.6681	0.5647	0.4639	0.3888	0.3354	0.2888	0.2363	0.168	0.7606	0.668	0.5646	0.4637	0.3886	0.3352	0.2886	0.2361	0.1678
	0.6	0.7836	0.709	0.6268	0.5314	0.4335	0.3502	0.2877	0.2401	0.198	0.7836	0.709	0.6268	0.5314	0.4335	0.3501	0.2876	0.24	0.1979
	0.8	0.7975	0.7344	0.665	0.5838	0.4926	0.398	0.312	0.2426	0.1896	0.7978	0.7345	0.665	0.5838	0.4925	0.3979	0.3118	0.2424	0.1896
	1	0.8074	0.7521	0.6911	0.6197	0.5393	0.4512	0.3595	0.2728	0.1986	0.8073	0.7519	0.6909	0.6196	0.5391	0.4509	0.3593	0.2725	0.1984
2	0.2	0.4186	0.2264	0.1217	0.0198	-0.1248	-0.3491	-0.7149	-1.3157	-2.3027	0.4188	0.2266	0.1218	0.0197	-0.1249	-0.3493	-0.715	-1.316	-2.303
	0.4	0.4703	0.2733	0.0901	-0.0482	-0.1356	-0.2345	-0.3836	-0.6223	-1.007	0.4705	0.2734	0.0901	-0.0482	-0.1357	-0.2347	-0.3838	-0.6227	-1.0076
	0.6	0.5026	0.3175	0.1328	-0.0558	-0.2111	-0.3061	-0.3874	-0.5055	-0.6964	0.5021	0.3177	0.133	-0.0557	-0.211	-0.306	-0.3873	-0.5053	-0.6964
	0.8	0.5256	0.3514	0.1758	-0.0149	-0.2112	-0.376	-0.4772	-0.5506	-0.6492	0.5257	0.3514	0.1758	-0.0149	-0.2113	-0.3761	-0.4774	-0.5505	-0.6493
	1	0.5446	0.3763	0.2102	0.0281	-0.1708	-0.374	-0.545	-0.6506	-0.716	0.5446	0.3764	0.2101	0.028	-0.171	-0.3743	-0.5453	-0.6503	-0.7162
Re	= 40					C_{DF} (for U									C_{DF} (for I				
α	G	$n \rightarrow 0.2$	0.4	0.6	0.8	1	1.2	1.4	1.6	1.8	0.2	0.4	0.6	0.8	1	1.2	1.4	1.6	1.8
0	0.2	0.1323	0.2384	0.2935	0.3261	0.3514	0.3704	0.3829	0.3884	0.3838	0.131	0.2383	0.2934	0.3261	0.3514	0.3703	0.3829	0.3884	0.3838
	0.4	0.1395	0.2475	0.3468	0.4217	0.4658	0.4905	0.5031	0.505		0.1389	0.2475	0.3468	0.4217	0.4658	0.4905	0.5031	0.5049	
	0.6	0.1422	0.2528	0.3581	0.4509	0.5249	0.5765	0.6066	0.6182	0.6046	0.1421	0.2528	0.358	0.4508	0.5249	0.5764	0.6066	0.6182	0.6046
	0.8	0.1436	0.2547	0.3625	0.4609	0.5461	0.616	0.6695		0.725	0.1434	0.2547	0.3625	0.4608	0.5459	0.6158	0.6693		0.7248
	1	0.1442	0.2552	0.364	0.4648	0.5545	0.6319	0.6968	0.7495		0.144	0.2551	0.3639	0.4647	0.5543	0.6317	0.6966	0.7494	
1	0.2	0.1579	0.2387	0.2949	0.3314	0.373	0.4326	0.522	0.6562	0.856	0.1578	0.2385	0.2947	0.3312	0.3728	0.4324	0.5218	0.6559	0.8555
	0.4	0.1591	0.2424	0.3286	0.3983	0.4406	0.4695	0.5	0.5423	0.6042	0.1592	0.2424	0.3285	0.3982	0.4405	0.4694	0.4999	0.542	0.6038
	0.6	0.1589	0.2438	0.3337	0.4219	0.4958	0.5449	0.5739	0.595	0.6185	0.1588	0.2438	0.3337	0.4219	0.4958	0.5449	0.5738	0.595	0.6185
	0.8	0.1587	0.2438	0.3357	0.4283	0.5167	0.5923	0.6463	0.6784	0.6971	0.1585	0.2438	0.3356	0.4282	0.5166	0.5921	0.646	0.678	0.6965
	1	0.1583	0.2435	0.3363	0.4311	0.5241	0.6118	0.688	0.7457	0.7822	0.1583	0.2434	0.3363	0.431	0.5239	0.6115	0.6878	0.7453	0.7817
2	0.2	0.122	0.1895	0.2105	0.2431	0.3152	0.4584	0.7312	1.2218	2.0834	0.1215	0.1894	0.2102	0.2428	0.3149	0.458	0.7305	1.221	2.0823
	0.4	0.1224	0.2031	0.2907	0.3396	0.3568	0.395	0.4825	0.6485	0.9407	0.1224	0.2029	0.2905	0.3396	0.3567	0.395	0.4823	0.6488	0.9417
	0.6	0.1233	0.2044	0.3029	0.4019	0.4641	0.4802	0.5003	0.5647	0.691	0.1231	0.2043	0.3029	0.4018	0.4641	0.4802	0.5002	0.5642	0.691
	0.8	0.1242	0.2053	0.3051	0.4163	0.523	0.5894	0.6031	0.6144	0.6543	0.1238	0.2051	0.3049	0.4161	0.5228	0.5891	0.6028	0.6135	0.6537
	1	0.1251	0.2066	0.306	0.4193	0.5402	0.6506	0.7164	0.7306	0.7204	0.1247	0.2063	0.3059	0.419	0.5399	0.6502	0.7156	0.7286	0.7186

Appendix C. Pressure and friction lift coefficients (C_{LP} and C_{LF})

Table C.1: Dependence of the pressure (C_{LP}) and friction (C_{LF}) lift coefficients on the Reynolds number (Re = 1), rotational velocity (α) and power-law index (n) for upper (UC) and lower (LC) cylinders.

Re	2 = 1				C_I	P (for UC	<u>.</u>							(C _{LP} (for LC	<u>.</u>)			
α	G	$n \rightarrow 0.2$	0.4	0.6	0.8	1	1.2	1.4	1.6	1.8	0.2	0.4	0.6	0.8	1	1.2	1.4	1.6	1.8
0	0.2	1.9803	1.1548	1.0302	1.1129	1.1445	1.1362	1.112	1.0815	1.0474	-1.9818	-1.1565	-1.0316	-1.1141	-1.1455	-1.137	-1.1128	-1.0822	-1.048
	0.4	2.069	1.2165	1.0858	1.1586	1.1751	1.1524	1.1157	1.0751	1.0342	-2.0716	-1.2185	-1.0874	-1.1598	-1.1761	-1.1533	-1.1165	-1.0758	-1.0349
	0.6	1.9164	1.2535	1.1322	1.1996	1.2052	1.1718	1.1252	1.0756	1.0273	-1.9189	-1.2557	-1.1339	-1.201	-1.2064	-1.1728	-1.1261	-1.0764	-1.0281
	0.8	1.5728	1.2623	1.1689	1.2354	1.2335	1.192	1.1377	1.0809	1.0264	-1.5756	-1.2646	-1.1707	-1.2368	-1.2346	-1.193	-1.1386	-1.0816	-1.0272
	1	1.1846	1.2453	1.1967	1.2662	1.2593	1.2117	1.1511	1.0884	1.029	-1.1869	-1.2477	-1.1985	-1.2676	-1.2605	-1.2127	-1.1521	-1.0893	-1.0298
1	0.2	3.6681	1.9769	1.5602	1.7404	1.9824	2.1783	2.3196	2.4168	2.4843	-3.5751	-1.935	-1.5607	-1.7404	-1.9827	-2.1793	-2.3216	-2.4209	-2.4892
	0.4	3.8216	2.221	1.5784	1.6339	1.8241	2.0065	2.1565	2.2723	2.3599	-3.7453	-2.1856	-1.5795	-1.635	-1.8254	-2.0083	-2.1591	-2.2775	-2.3688
	0.6	3.8916	2.3088	1.7347	1.7092	1.827	1.9634	2.0891	2.1968	2.2864	-3.787	-2.2778	-1.7353	-1.7095	-1.8273	-1.9638	-2.0897	-2.1978	-2.2879
	0.8	3.8411	2.3516	1.8605	1.8197	1.885	1.9748	2.0659	2.15	2.2244	-3.8575	-2.3235	-1.8622	-1.8213	-1.8866	-1.9764	-2.0677	-2.1521	-2.2269
	1	3.7988	2.3759	1.9469	1.9292	1.9643	2.0155	2.0728	2.1301	2.1839	-3.7639	-2.3547	-1.9478	-1.93	-1.965	-2.0162	-2.0736	-2.131	-2.1851
2	0.2	5.5491	2.4029	1.9593	2.4833	3.2841	4.128	4.9387	5.6753	6.3254	-5.4261	-2.4069	-1.9596	-2.4824	-3.2837	-4.129	-4.9426	-5.6864	-6.3442
	0.4	6.1933	3.1559	1.7355	1.8319	2.4351	3.1724	3.9113	4.598	5.2158	-6.0867	-3.157	-1.7363	-1.8329	-2.4368	-3.1755	-3.9195	-4.6134	-5.2423
	0.6	6.2907	3.6077	2.1484	1.8747	2.2104	2.7812	3.4242	4.062	4.6597	-6.1401	-3.6085	-2.1484	-1.8743	-2.2098	-2.7807	-3.4243	-4.0632	-4.663
	0.8	6.3598	3.7484	2.5187	2.0849	2.2076	2.6128	3.1403	3.7015	4.2503	-6.2343	-3.7504	-2.5205	-2.0867	-2.2096	-2.6152	-3.1435	-3.706	-4.2568
	1	6.3935	3.8394	2.7764	2.3222	2.2987	2.5617	2.9779	3.4579	3.9493	-6.2645	-3.8402	-2.777	-2.3226	-2.2988	-2.5617	-2.9781	-3.4586	-3.951
Re	= 1				C_{I}	F (for UC	<u>:</u>)							C	CLF (for LC	C)			
α	G	$n \rightarrow 0.2$	0.4	0.6	0.8	1	1.2	1.4	1.6	1.8	0.2	0.4	0.6	0.8	1	1.2	1.4	1.6	1.8
0	0.2	0.442	0.4258	0.5311	0.7071	0.8319	0.9077	0.9516	0.9748	0.9842	-0.4427	-0.4268	-0.5321	-0.7081	-0.8329	-0.9085	-0.9525	-0.9756	-0.9849
	0.4	0.4757	0.4622	0.5738	0.7537	0.8769	0.949	0.989	1.0093	1.0169	-0.477	-0.4634	-0.5748	-0.7546	-0.8777	-0.9497	-0.9897	-1.0099	-1.0175
	0.6	0.4696	0.4908	0.6128	0.7974	0.9191	0.9873	1.0229	1.0388	1.043	-0.4707	-0.4925	-0.6143	-0.7987	-0.9201	-0.9883	-1.0237	-1.0395	-1.0436
	0.8	0.4197	0.5105	0.6476	0.8377	0.9582	1.0227	1.0534	1.0644	1.0643	-0.4194	-0.5113	-0.6483	-0.8382	-0.9586	-1.023	-1.0537	-1.0646	-1.0645
	1	0.3477	0.5193	0.677	0.8738	0.9937	1.0546	1.0805	1.0863	1.0814	-0.3482	-0.5204	-0.678	-0.8747	-0.9945	-1.0554	-1.0812	-1.087	-1.0821
1	0.2	0.5664	0.3324	0.4123	0.6399	0.9013	1.1449	1.3559	1.5321	1.6777	-0.646	-0.4254	-0.4096	-0.6386	-0.9003	-1.1444	-1.3561	-1.5335	-1.6797
	0.4	0.5655	0.3373	0.442	0.6803	0.9571	1.2239	1.4645	1.6763	1.8575	-0.607	-0.4172	-0.4421	-0.6804	-0.9573	-1.2243	-1.4653	-1.672	-1.8471
	0.6	0.5068	0.3664	0.4719	0.7234	1.0113	1.2934	1.5538	1.7861	1.9887	-0.599	-0.429	-0.4722	-0.7234	-1.0114	-1.2936	-1.5545	-1.7874	-1.9908
	0.8	0.6149	0.3388	0.4984	0.7702	1.0704	1.3658	1.6427	1.8945	2.1187	-0.6803	-0.4141	-0.4996	-0.7713	-1.0715	-1.3669	-1.6438	-1.8956	-2.1199
	1	0.6592	0.3624	0.518	0.8158	1.131	1.4393	1.7306	1.9986	2.2408	-0.716	-0.4051	-0.5175	-0.8151	-1.13	-1.4382	-1.7293	-1.9973	-2.2393
2	0.2	0.1554	0.2294	0.3014	0.5617	0.9282	1.3518	1.8082	2.266	2.6996	-0.4033	-0.2188	-0.297	-0.5588	-0.9252	-1.3492	-1.807	-2.2682	-2.7044
	0.4	0.1197	0.2442	0.3354	0.5976	0.9777	1.4265	1.9118	2.4157	2.9077	-0.3371	-0.2441	-0.335	-0.5971	-0.9773	-1.4267	-1.9099	-2.3897	-2.8564
	0.6	0.1511	0.2407	0.3827	0.6415	1.0193	1.4778	1.9833	2.5043	3.0175	-0.4363	-0.241	-0.3822	-0.6405	-1.0182	-1.4771	-1.9834	-2.5061	-3.0221
	0.8	0.1486	0.2252	0.4295	0.7031	1.0788	1.5421	2.0653	2.6171	3.1708	-0.3997	-0.2264	-0.4309	-0.7047	-1.0806	-1.5443	-2.0678	-2.6201	-3.1742
	1	0.2161	0.2166	0.4643	0.7708	1.1508	1.6169	2.1522	2.728	3.3155	-0.465	-0.2158	-0.4631	-0.7689	-1.1481	-1.6133	-2.1475	-2.7221	-3.3084

Table C.2: Dependence of the pressure (C_{LP}) and friction (C_{LF}) lift coefficients on the Reynolds number (Re = 5), rotational velocity (α) and power-law index (n) for upper (UC) and lower (LC) cylinders.

Re	= 5				Cı	P (for UC	<u> </u>								C _{I,P} (for LC	2)			
α	G	$n \rightarrow 0.2$	0.4	0.6	0.8	1	1.2	1.4	1.6	1.8	0.2	0.4	0.6	0.8	1	1.2	1.4	1.6	1.8
0	0.2	1.8243	1.2511	1.1551	1.1212	1.0877	1.0515	1.0144	0.9786	0.9445	-1.8248	-1.2515	-1.1555	-1.1216	-1.0881	-1.0519	-1.0148	-0.979	-0.9449
1	0.4	1.7022	1.3002	1.1974	1.1502	1.1035	1.0562	1.0108	0.9683	0.9285	-1.7027	-1.3006	-1.1978	-1.1506	-1.1039	-1.0565	-1.0112	-0.9687	-0.9288
	0.6	1.1998	1.2745	1.204	1.1543	1.1008	1.0465	0.995	0.947	0.9022	-1.2004	-1.275	-1.2045	-1.1548	-1.1013	-1.047	-0.9954	-0.9475	-0.9026
	0.8	0.7624	1.1741	1.1711	1.1304	1.0758	1.0186	0.9639	0.9127	0.8648	-0.7629	-1.1746	-1.1716	-1.1309	-1.0763	-1.0191	-0.9643	-0.9132	-0.8652
	1	0.4706	1.0297	1.1034	1.0794	1.0282	0.9711	0.9155	0.8633	0.8144	-0.4714	-1.0303	-1.1039	-1.0799	-1.0287	-0.9716	-0.916	-0.8638	-0.8149
1	0.2	3.1114	2.1408	1.9338	1.9731	2.0537	2.1401	2.2205	2.292	2.3542	-3.1081	-2.137	-1.9314	-1.973	-2.0539	-2.1404	-2.221	-2.2928	-2.3561
	0.4	3.2192	2.423	2.0957	1.998	2.0057	2.0531	2.1126	2.1728	2.2287	-3.2169	-2.4181	-2.0949	-1.9981	-2.0062	-2.0536	-2.1133	-2.1736	-2.23
	0.6	3.1824	2.4974	2.2884	2.1638	2.1092	2.1029	2.1231	2.1563	2.1952	-3.1797	-2.4986	-2.2874	-2.1639	-2.1095	-2.1033	-2.1234	-2.1567	-2.1958
	0.8	3.0512	2.5478	2.3893	2.3174	2.2473	2.2048	2.1881	2.1896	2.2028	-3.0502	-2.5444	-2.39	-2.3178	-2.2479	-2.2054	-2.1888	-2.1903	-2.2035
	1	2.9138	2.5683	2.4357	2.4271	2.3793	2.3242	2.2823	2.2564	2.244	-2.9142	-2.5622	-2.436	-2.4272	-2.3797	-2.3247	-2.2828	-2.2569	-2.2445
2	0.2	4.8487	2.6302	2.3581	2.629	3.0785	3.6093	4.1673	4.7207	5.2529	-4.8376	-2.6273	-2.3576	-2.629	-3.0785	-3.6096	-4.1681	-4.7228	-5.2561
	0.4	5.2381	3.5843	2.527	2.3068	2.4906	2.855	3.2969	3.7625	4.2263	-5.2332	-3.5798	-2.5272	-2.3071	-2.491	-2.8557	-3.2981	-3.7655	-4.2315
	0.6	5.2606	3.9831	3.1537	2.6404	2.5274	2.6775	2.9751	3.349	3.7562	-5.2474	-3.9797	-3.1539	-2.6406	-2.5275	-2.6777	-2.9753	-3.3494	-3.757
	0.8	5.2277	4.0927	3.5807	3.0742	2.7735	2.731	2.8735	3.1304	3.4522	-5.2174	-4.0904	-3.5813	-3.0748	-2.7742	-2.7318	-2.8744	-3.1315	-3.4536
	1	5.1869	4.1483	3.8091	3.459	3.091	2.9033	2.9042	3.0434	3.2725	-5.1784	-4.1474	-3.8093	-3.4593	-3.0913	-2.9036	-2.9045	-3.0438	-3.273
Re	= 5				C_{I}	F (for UC	()							C	C _{LF} (for LC	C)			
α	G	$n \rightarrow 0.2$	0.4	0.6	0.8	1	1.2	1.4	1.6	1.8	0.2	0.4	0.6	0.8	1	1.2	1.4	1.6	1.8
0	0.2	0.3371	0.3951	0.4852	0.5626	0.619	0.6579	0.6843	0.7023	0.7142	-0.3373	-0.3954	-0.4855	-0.563	-0.6194	-0.6583	-0.6847	-0.7027	-0.7147
	0.4	0.3476	0.4271	0.5194	0.5943	0.6457	0.6801	0.7033	0.7188	0.7285	-0.348	-0.4274	-0.5198	-0.5947	-0.6461	-0.6805	-0.7037	-0.7192	-0.7289
	0.6	0.2977	0.4398	0.541	0.6151	0.6628	0.6928	0.7119	0.7239	0.7302	-0.2979	-0.4403	-0.5415	-0.6156	-0.6632	-0.6932	-0.7123	-0.7243	-0.7305
	0.8	0.224	0.4294	0.5465	0.6222	0.6672	0.6935	0.7088	0.7169	0.7194	-0.2239	-0.4295	-0.5466	-0.6223	-0.6674	-0.6937	-0.7089	-0.717	-0.7195
	1	0.161	0.4003	0.5355	0.6142	0.6577	0.6809	0.6927	0.6972	0.6962	-0.1611	-0.4005	-0.5358	-0.6145	-0.658	-0.6813	-0.6931	-0.6976	-0.6966
1	0.2	0.4282	0.3646	0.4293	0.5458	0.6761	0.8075	0.9333	1.0515	1.1619	-0.4356	-0.3647	-0.4336	-0.5464	-0.6761	-0.8076	-0.9335	-1.0519	-1.1625
	0.4	0.4284	0.3634	0.4698	0.5957	0.7339	0.8754	1.0138	1.1459	1.2706	-0.4344	-0.3743	-0.4737	-0.5966	-0.7342	-0.8758	-1.0143	-1.1465	-1.2709
	0.6	0.4235	0.3679	0.4987	0.644	0.792	0.9413	1.0879	1.2294	1.3642	-0.4272	-0.3631	-0.5011	-0.6447	-0.7922	-0.9415	-1.0882	-1.2298	-1.3648
	0.8	0.4066	0.3714	0.5085	0.6839	0.8493	1.009	1.1638	1.3133	1.4566	-0.409	-0.3688	-0.5095	-0.6844	-0.8495	-1.0093	-1.1641	-1.3135	-1.4568
_	1	0.3795	0.3684	0.5101	0.7103	0.8997	1.0749	1.2401	1.3978	1.5488	-0.3872	-0.3613	-0.5134	-0.7108	-0.8997	-1.075	-1.2402	-1.3979	-1.5488
2	0.2	0.1804	0.1892	0.2858	0.4475	0.6562	0.9018	1.1759	1.4685	1.7693	-0.2089	-0.1948	-0.2856	-0.4471	-0.6558	-0.9015	-1.1757	-1.469	-1.7703
	0.4	0.1665	0.2271	0.3428	0.5009	0.7111	0.9658	1.2544	1.5702	1.8977	-0.1822	-0.2356	-0.343	-0.5011	-0.7114	-0.9662	-1.255	-1.565	-1.8866
	0.6	0.1557	0.2316	0.4051	0.5738	0.7774	1.0283	1.321	1.6451	1.9887	-0.1771	-0.2383	-0.4052	-0.5738	-0.7773	-1.0282	-1.3212	-1.6455	-1.9897
	0.8	0.154	0.2202	0.4455	0.6575	0.8668	1.1126	1.403	1.732	2.0889	-0.1738	-0.2251	-0.4457	-0.6578	-0.8671	-1.113	-1.4035	-1.7325	-2.0894
	1	0.1559	0.2166	0.4616	0.7327	0.969	1.217	1.5037	1.8324	2.196	-0.1696	-0.2182	-0.4614	-0.7325	-0.9686	-1.2165	-1.503	-1.8315	-2.1948

Table C.3: Dependence of the pressure (C_{LP}) and friction (C_{LF}) lift coefficients on the Reynolds number (Re = 10), rotational velocity (α) and power-law index (n) for upper (UC) and lower (LC) cylinders.

Re	= 10	$=10$ C_{LP} (for UC)								C_{LP} (for LC)										
α	G	$n \rightarrow 0.2$	0.4	0.6	0.8	1	1.2	1.4	1.6	1.8	0.2	0.4	0.6	0.8	1	1.2	1.4	1.6	1.8	
0	0.2	1.665	1.2825	1.1663	1.0995	1.0477	1.0025	0.9618	0.924	0.8882	-1.6653	-1.2828	-1.1665	-1.0998	-1.0479	-1.0028	-0.962	-0.9243	-0.8885	
	0.4	0.9853	1.2226	1.1507	1.087	1.0316	0.9823	0.9374	0.8954	0.8554	-0.9856	-1.2229	-1.151	-1.0873	-1.0319	-0.9826	-0.9376	-0.8957	-0.8556	
	0.6	0.4897	0.9601	1.0286	1.0053	0.9656	0.9233	0.8813	0.8404	0.8002	-0.49	-0.9604	-1.0289	-1.0056	-0.9659	-0.9236	-0.8817	-0.8407	-0.8005	
	0.8	0.3053	0.671	0.8308	0.8613	0.8495	0.8233	0.7918	0.7581	0.7233	-0.3052	-0.6712	-0.8311	-0.8617	-0.8499	-0.8237	-0.7921	-0.7584	-0.7237	
	1	0.2215	0.4766	0.6352	0.6938	0.7052	0.6959	0.6773	0.6543	0.6288	-0.2222	-0.4769	-0.6356	-0.6942	-0.7056	-0.6963	-0.6777	-0.6547	-0.6292	
1	0.2	2.9064	2.257	2.0635	2.0603	2.1015	2.1551	2.2141	2.2735	2.3295	-2.9061	-2.257	-2.0632	-2.0605	-2.1017	-2.1554	-2.2141	-2.2735	-2.33	
	0.4	2.9248	2.5017	2.3172	2.1906	2.1422	2.141	2.164	2.1984	2.2363	-2.9245	-2.5021	-2.3174	-2.1909	-2.1424	-2.1414	-2.1642	-2.198	-2.2362	
	0.6	2.7402	2.5662	2.4666	2.3915	2.3112	2.2601	2.2379	2.2365	2.2478	-2.7397	-2.5656	-2.4666	-2.3917	-2.3114	-2.2603	-2.2381	-2.236	-2.2475	
	0.8	2.6044	2.5348	2.5166	2.5092	2.4689	2.4106	2.3615	2.3294	2.3119	-2.6037	-2.5348	-2.5165	-2.5096	-2.4694	-2.411	-2.3618	-2.3292	-2.3118	
	1	2.5128	2.4602	2.5056	2.5502	2.5681	2.542	2.4946	2.4477	2.4091	-2.5128	-2.4599	-2.5058	-2.5504	-2.5685	-2.5424	-2.4948	-2.447	-2.4084	
2	0.2	4.6154	2.8698	2.5419	2.6629	2.9594	3.3604	3.8147	4.289	4.7623	-4.6034	-2.868	-2.5409	-2.663	-2.9594	-3.3605	-3.8151	-4.2899	-4.7652	
	0.4	4.8629	3.9654	3.0609	2.6262	2.5875	2.7676	3.0642	3.4198	3.8033	-4.866	-3.9636	-3.0596	-2.6264	-2.5877	-2.7679	-3.0649	-3.4214	-3.8062	
	0.6	4.8546	4.2566	3.7947	3.2091	2.8549	2.7743	2.8839	3.1124	3.4112	-4.8607	-4.2535	-3.7935	-3.2092	-2.8551	-2.7745	-2.8842	-3.1128	-3.4117	
	0.8	4.8268	4.3292	4.1383	3.7747	3.3161	3.0267	2.9444	3.0203	3.2032	-4.8264	-4.3283	-4.1375	-3.7751	-3.3166	-3.0273	-2.945	-3.021	-3.204	
	1	4.7745	4.3504	4.2656	4.1483	3.7893	3.3978	3.1539	3.0788	3.1375	-4.7658	-4.3481	-4.2643	-4.1486	-3.7896	-3.3981	-3.1542	-3.0792	-3.1379	
Re	= 10	C_{LF} (for UC)								C_{LF} (for LC)										
α	G	$n \rightarrow 0.2$	0.4	0.6	0.8	1	1.2	1.4	1.6	1.8	0.2	0.4	0.6	0.8	1	1.2	1.4	1.6	1.8	
0	0.2	0.2797	0.3458	0.4109	0.4639	0.5052	0.537	0.5613	0.5795	0.5923	-0.2798	-0.346	-0.4111	-0.4642	-0.5055	-0.5373	-0.5616	-0.5798	-0.5926	
	0.4	0.23	0.3531	0.4263	0.4776	0.5155	0.5444	0.5663	0.5821	0.5925	-0.2301	-0.3533	-0.4265	-0.4779	-0.5158	-0.5447	-0.5665	-0.5824	-0.5928	
	0.6	0.1419	0.3121	0.4077	0.4659	0.5054	0.5337	0.5542	0.5683	0.5766	-0.142	-0.3124	-0.408	-0.4662	-0.5057	-0.534	-0.5545	-0.5686	-0.5769	
	0.8	0.0887	0.2473	0.358	0.4264	0.471	0.5016	0.523	0.5372	0.5454	-0.0887	-0.2473	-0.3581	-0.4265	-0.4711	-0.5017	-0.523	-0.5373	-0.5454	
	1	0.0602	0.1911	0.2968	0.3688	0.4174	0.4509	0.4745	0.4907	0.5009	-0.0601	-0.1912	-0.297	-0.3691	-0.4176	-0.4512	-0.4748	-0.491	-0.5012	
1	0.2	0.2787	0.3398	0.3997	0.4767	0.5637	0.6551	0.7494	0.8452	0.9381	-0.2798	-0.3407	-0.4004	-0.4768	-0.5638	-0.6553	-0.75	-0.8467	-0.9395	
	0.4	0.2721	0.3405	0.4356	0.527	0.6202	0.7173	0.8174	0.9213	1.0215	-0.2746	-0.3414	-0.4371	-0.5274	-0.6205	-0.7177	-0.8179	-0.9228	-1.0229	
	0.6	0.2532	0.3385	0.4452	0.5646	0.6738	0.7788	0.8843	0.9948	1.1004	-0.2545	-0.3397	-0.4463	-0.5649	-0.674	-0.7791	-0.8848	-0.996	-1.1017	
	0.8	0.2393	0.3267	0.4414	0.5795	0.7141	0.8357	0.9509	1.0671	1.1787	-0.2393	-0.3276	-0.4425	-0.5796	-0.7142	-0.8358	-0.9517	-1.069	-1.1804	
	1	0.229	0.3089	0.428	0.5753	0.7318	0.877	1.0091	1.1379	1.2574	-0.2298	-0.3106	-0.4292	-0.5755	-0.7319	-0.8772	-1.0095	-1.1409	-1.2601	
2	0.2	0.1328	0.1817	0.2521	0.3707	0.5268	0.7139	0.9275	1.162	1.4102	-0.1353	-0.186	-0.254	-0.3706	-0.5267	-0.7139	-0.9275	-1.1622	-1.4108	
	0.4	0.1213	0.2198	0.3191	0.4316	0.5837	0.7728	0.9938	1.2423	1.5092	-0.1246	-0.224	-0.3218	-0.4319	-0.584	-0.7732	-0.9942	-1.2396	-1.5031	
	0.6	0.1224	0.2182	0.3797	0.5212	0.6683	0.8475	1.0636	1.3124	1.5871	-0.1223	-0.2203	-0.3826	-0.5212	-0.6684	-0.8475	-1.0637	-1.3126	-1.5876	
	0.8	0.1101	0.2127	0.3987	0.6039	0.7783	0.9544	1.1609	1.4039	1.6797	-0.1195	-0.2165	-0.4012	-0.604	-0.7784	-0.9545	-1.1611	-1.404	-1.6799	
	1	0.116	0.2103	0.3994	0.6532	0.8867	1.0839	1.2869	1.5207	1.7907	-0.1194	-0.2149	-0.4019	-0.6532	-0.8866	-1.0838	-1.2866	-1.5204	-1.7903	

Table C.4: Dependence of the pressure (C_{LP}) and friction (C_{LF}) lift coefficients on the Reynolds number (Re = 20), rotational velocity (α) and power-law index (n) for upper (UC) and lower (LC) cylinders.

Re	= 20	= 20								C_{LP} (for LC)										
α	G	$n \rightarrow 0.2$	0.4	0.6	0.8	1	1.2	1.4	1.6	1.8	0.2	0.4	0.6	0.8	1	1.2	1.4	1.6	1.8	
0	0.2	0.9002	1.1523	1.0757	1.0141	0.9643	0.9208	0.8808	0.8425	0.8042	-0.9004	-1.1525	-1.0759	-1.0143	-0.9645	-0.921	-0.881	-0.8426	-0.8044	
	0.4	0.3528	0.6282	0.8394	0.8817	0.8726	0.8475	0.8163	0.7821	0.7451	-0.3526	-0.6285	-0.8396	-0.8819	-0.8728	-0.8477	-0.8165	-0.7823	-0.7453	
	0.6	0.2729	0.3622	0.5002	0.6148	0.6735	0.693	0.6905	0.6756	0.6519	-0.2732	-0.3623	-0.5004	-0.6151	-0.6738	-0.6932	-0.6908	-0.6758	-0.6521	
	0.8	0.2303	0.277	0.3473	0.4152	0.4723	0.5115	0.5329	0.5401	0.5358	-0.2304	-0.2771	-0.3475	-0.4154	-0.4726	-0.5118	-0.5332	-0.5404	-0.5361	
	1	0.1942	0.2323	0.2792	0.3193	0.3529	0.3802	0.4006	0.4139	0.4202	-0.1941	-0.2325	-0.2794	-0.3196	-0.3532	-0.3805	-0.4009	-0.4142	-0.4205	
1	0.2	2.7848	2.4275	2.2136	2.1521	2.1576	2.185	2.2254	2.2739	2.3261	-2.7854	-2.4277	-2.2138	-2.1523	-2.1578	-2.1851	-2.2256	-2.2741	-2.3261	
	0.4	2.5484	2.5369	2.4867	2.3956	2.3114	2.2661	2.2531	2.2613	2.2823	-2.5486	-2.537	-2.4869	-2.3958	-2.3116	-2.2663	-2.2533	-2.2614	-2.2822	
	0.6	2.4563	2.4201	2.5002	2.5303	2.5044	2.4485	2.3987	2.3669	2.3527	-2.456	-2.42	-2.5002	-2.5304	-2.5046	-2.4487	-2.3989	-2.3669	-2.3525	
	0.8	2.395	2.3433	2.4284	2.519	2.5768	2.5839	2.5528	2.511	2.4745	-2.3946	-2.3432	-2.4286	-2.5192	-2.5771	-2.5842	-2.5531	-2.5112	-2.4746	
	1	2.3501	2.2966	2.3736	2.4695	2.5605	2.6271	2.6507	2.6368	2.6048	-2.3503	-2.2967	-2.3738	-2.4697	-2.5607	-2.6274	-2.6511	-2.637	-2.6047	
2	0.2	4.4488	3.2269	2.7247	2.6986	2.8514	3.1287	3.4825	3.8775	4.2897	-4.4495	-3.2271	-2.725	-2.6986	-2.8514	-3.1288	-3.4827	-3.878	-4.2911	
	0.4	4.5331	4.2687	3.7232	3.0964	2.8055	2.7773	2.9097	3.1394	3.4292	-4.5344	-4.2691	-3.7232	-3.0965	-2.8056	-2.7775	-2.91	-3.1402	-3.4306	
	0.6	4.4957	4.3916	4.3212	3.963	3.4368	3.0837	2.9582	3.0031	3.1629	-4.4936	-4.3899	-4.3202	-3.9625	-3.4367	-3.0838	-2.9584	-3.0034	-3.1632	
	0.8	4.4421	4.4089	4.4553	4.4278	4.1196	3.6526	3.2954	3.1271	3.1184	-4.4388	-4.4072	-4.4549	-4.4277	-4.1198	-3.6529	-3.2957	-3.1275	-3.1188	
	1	4.4004	4.3957	4.4881	4.5794	4.5388	4.2333	3.7953	3.4447	3.2572	-4.3997	-4.3945	-4.4878	-4.5796	-4.539	-4.2336	-3.7956	-3.4449	-3.2575	
Re	= 20		C _{LF} (for UC)								C_{LF} (for LC)									
α	G	$n \rightarrow 0.2$	0.4	0.6	0.8	1	1.2	1.4	1.6	1.8	0.2	0.4	0.6	0.8	1	1.2	1.4	1.6	1.8	
0	0.2	0.174	0.2556	0.3046	0.3459	0.3813	0.4106	0.4341	0.4519	0.4637	-0.1741	-0.2557	-0.3047	-0.3461	-0.3815	-0.4108	-0.4344	-0.4521	-0.464	
	0.4	0.0702	0.1852	0.271	0.3271	0.3678	0.3989	0.4225	0.4396	0.4498	-0.0697	-0.1853	-0.2712	-0.3273	-0.368	-0.3991	-0.4228	-0.4398	-0.4501	
	0.6	0.0321	0.1149	0.1922	0.2619	0.3161	0.3564	0.386	0.407	0.4197	-0.0316	-0.115	-0.1923	-0.2621	-0.3163	-0.3566	-0.3862	-0.4072	-0.4199	
	0.8	0.0251	0.0823	0.1399	0.1966	0.2493	0.2944	0.3306	0.3581	0.3771	-0.0247	-0.0822	-0.1399	-0.1966	-0.2493	-0.2944	-0.3306	-0.3582	-0.3772	
	1	0.0216	0.0674	0.1128	0.1573	0.2003	0.2402	0.2754	0.3049	0.3283	-0.0213	-0.0674	-0.1129	-0.1574	-0.2005	-0.2404	-0.2756	-0.3052	-0.3287	
1	0.2	0.1642	0.2466	0.3214	0.3877	0.4535	0.5209	0.5903	0.6621	0.7372	-0.1645	-0.2468	-0.3215	-0.3878	-0.4536	-0.5211	-0.5905	-0.6626	-0.7382	
	0.4	0.1479	0.2383	0.3347	0.4254	0.5033	0.5763	0.6493	0.724	0.8019	-0.1482	-0.2387	-0.3349	-0.4257	-0.5035	-0.5766	-0.6496	-0.7245	-0.8031	
	0.6	0.1399	0.218	0.3194	0.4293	0.5339	0.6247	0.7074	0.7875	0.8691	-0.1402	-0.2183	-0.3197	-0.4294	-0.534	-0.6248	-0.7075	-0.7881	-0.8698	
	0.8	0.1347	0.2049	0.2964	0.4076	0.5294	0.6465	0.7505	0.8445	0.9347	-0.1346	-0.2051	-0.2964	-0.4077	-0.5294	-0.6466	-0.7506	-0.8449	-0.9354	
	1	0.1307	0.1965	0.2798	0.3823	0.5034	0.6354	0.7637	0.8802	0.9873	-0.1309	-0.1968	-0.2799	-0.3824	-0.5036	-0.6355	-0.7638	-0.8808	-0.9885	
2	0.2	0.0953	0.1577	0.2105	0.2955	0.4095	0.5499	0.7141	0.8991	1.1004	-0.0974	-0.16	-0.2108	-0.2956	-0.4096	-0.55	-0.7142	-0.8993	-1.1008	
	0.4	0.0949	0.1841	0.29	0.3707	0.471	0.6049	0.769	0.9597	1.172	-0.0953	-0.1846	-0.2905	-0.3711	-0.4713	-0.6052	-0.7693	-0.9595	-1.171	
	0.6	0.0929	0.1801	0.3188	0.4662	0.5829	0.703	0.852	1.0331	1.2433	-0.0944	-0.1807	-0.319	-0.4664	-0.5829	-0.703	-0.852	-1.0333	-1.2436	
	0.8	0.0918	0.1779	0.3177	0.5064	0.6928	0.8407	0.9817	1.1469	1.3448	-0.0925	-0.1788	-0.3179	-0.5065	-0.6928	-0.8407	-0.9818	-1.1469	-1.3448	
	1	0.0909	0.1772	0.3143	0.5103	0.7499	0.9705	1.1432	1.3032	1.4846	-0.091	-0.1777	-0.3143	-0.5103	-0.7499	-0.9706	-1.1432	-1.3031	-1.4845	

Table C.5: Dependence of the pressure (C_{LP}) and friction (C_{LF}) lift coefficients on the Reynolds number (Re = 40), rotational velocity (α) and power-law index (n) for upper (UC) and lower (LC) cylinders.

Re	= 40		C_{LP} (for UC)										C_{LP} (for LC)									
α	G	$n \rightarrow 0.2$	0.4	0.6	0.8	1	1.2	1.4	1.6	1.8	0.2	0.4	0.6	0.8	1	1.2	1.4	1.6	1.8			
0	0.2	0.4234	0.561	0.8201	0.8518	0.8327	0.8021	0.7674	0.7288	0.6817	-0.4301	-0.5613	-0.8203	-0.8519	-0.8328	-0.8023	-0.7675	-0.729	-0.6819			
	0.4	0.3214	0.3474	0.3863	0.485	0.5839	0.6307	0.6402	0.6275		-0.3287	-0.3484	-0.3866	-0.4851	-0.584	-0.6308	-0.6404	-0.6276				
	0.6	0.2505	0.2759	0.3041	0.3337	0.3717	0.4169	0.4555	0.4773	0.4741	-0.2576	-0.2769	-0.3043	-0.3339	-0.3719	-0.417	-0.4557	-0.4775	-0.4743			
	0.8	0.2019	0.2257	0.25	0.2731	0.293	0.3116	0.3307		0.3628	-0.2076	-0.2262	-0.2503	-0.2734	-0.2932	-0.3118	-0.3309		-0.3631			
	1	0.1635	0.1873	0.2097	0.23	0.2468	0.2598	0.2699	0.2782		-0.1657	-0.1885	-0.21	-0.2303	-0.2471	-0.26	-0.2702	-0.2785				
1	0.2	2.5323	2.492	2.3862	2.2631	2.2176	2.2184	2.237	2.2686	2.3098	-2.5339	-2.4926	-2.3865	-2.2633	-2.2178	-2.2185	-2.2372	-2.2688	-2.3099			
	0.4	2.4537	2.3868	2.4442	2.4892	2.4595	2.4006	2.3571	2.3367	2.335	-2.4564	-2.3872	-2.4445	-2.4895	-2.4597	-2.4008	-2.3573	-2.337	-2.3353			
	0.6	2.3906	2.3391	2.3853	2.4602	2.5316	2.5589	2.5393	2.5026	2.4699	-2.3918	-2.3392	-2.3854	-2.4603	-2.5317	-2.5591	-2.5395	-2.5028	-2.4699			
	0.8	2.3428	2.299	2.3515	2.4208	2.498	2.5729	2.6231	2.6335	2.6159	-2.3418	-2.2989	-2.3515	-2.4209	-2.4982	-2.5732	-2.6234	-2.6338	-2.6161			
	1	2.3084	2.2663	2.3244	2.3966	2.4699	2.5439	2.616	2.674	2.7026	-2.3079	-2.2668	-2.3247	-2.3968	-2.4702	-2.5442	-2.6163	-2.6743	-2.7029			
2	0.2	4.3197	3.8966	3.0317	2.7718	2.7806	2.9423	3.1987	3.5118	3.8594	-4.3208	-3.8968	-3.0322	-2.772	-2.7808	-2.9424	-3.1988	-3.5121	-3.8599			
	0.4	4.2803	4.3516	4.3228	3.8569	3.2744	2.9738	2.9034	2.9769	3.1471	-4.2829	-4.3528	-4.3233	-3.8571	-3.2745	-2.9739	-2.9034	-2.9773	-3.1481			
	0.6	4.2526	4.3538	4.4978	4.5453	4.293	3.7829	3.3584	3.1438	3.102	-4.2493	-4.3516	-4.4954	-4.5439	-4.2922	-3.7824	-3.3581	-3.1434	-3.102			
	0.8	4.2373	4.3334	4.4956	4.649	4.72	4.5534	4.1213	3.668	3.369	-4.2301	-4.3295	-4.4938	-4.648	-4.7194	-4.5533	-4.1213	-3.6675	-3.3689			
	1	4.2221	4.3231	4.4829	4.644	4.7915	4.8656	4.7371	4.3547	3.8953	-4.2236	-4.3231	-4.4828	-4.6442	-4.7917	-4.8659	-4.7373	-4.354	-3.895			
Re	= 40	C_{LF} (for UC)									C _{LF} (for LC)											
α	G	$n \rightarrow 0.2$	0.4	0.6	0.8	1	1.2	1.4	1.6	1.8	0.2	0.4	0.6	0.8	1	1.2	1.4	1.6	1.8			
0	0.2	0.0421	0.1209	0.1874	0.2303	0.264	0.2915	0.313	0.3279	0.3336	-0.0417	-0.121	-0.1875	-0.2304	-0.2642	-0.2916	-0.3131	-0.3281	-0.3338			
	0.4	0.0344	0.0653	0.1067	0.1635	0.2173	0.2576	0.2865	0.3054		-0.0344	-0.0653	-0.1068	-0.1636	-0.2174	-0.2578	-0.2866	-0.3055				
	0.6	0.0276	0.0532	0.0843	0.1202	0.16	0.201	0.2377	0.266	0.2805	-0.0277	-0.0532	-0.0844	-0.1203	-0.1602	-0.2012	-0.2379	-0.2662	-0.2807			
	0.8	0.0231	0.0446	0.0708	0.1001	0.1311	0.1627	0.1938		0.2471	-0.0229	-0.0445	-0.0707	-0.1001	-0.1311	-0.1627	-0.1939		-0.2472			
	1	0.0194	0.038	0.0605	0.0858	0.1122	0.1388	0.1647	0.1894		-0.0194	-0.038	-0.0606	-0.0859	-0.1124	-0.139	-0.1649	-0.1897				
1	0.2	0.0859	0.1529	0.2281	0.2924	0.3507	0.4078	0.4654	0.5239	0.5837	-0.0859	-0.153	-0.2282	-0.2925	-0.3508	-0.408	-0.4657	-0.5244	-0.5841			
	0.4	0.0807	0.1377	0.211	0.298	0.3807	0.4511	0.5148	0.5763	0.638	-0.0809	-0.138	-0.2112	-0.2982	-0.381	-0.4514	-0.515	-0.5765	-0.6383			
	0.6	0.0774	0.1311	0.1957	0.2746	0.3679	0.4635	0.5491	0.6245	0.6943	-0.0775	-0.1313	-0.1957	-0.2747	-0.368	-0.4636	-0.5492	-0.6246	-0.6945			
	0.8	0.0753	0.1264	0.1873	0.2584	0.3427	0.4408	0.5454	0.6442	0.7331	-0.0752	-0.1264	-0.1873	-0.2584	-0.3427	-0.4408	-0.5455	-0.6442	-0.7331			
	1	0.0734	0.1229	0.1813	0.2485	0.3255	0.4147	0.5172	0.6285	0.7386	-0.0734	-0.123	-0.1814	-0.2486	-0.3257	-0.4148	-0.5174	-0.6287	-0.7388			
2	0.2	0.0547	0.1264	0.1705	0.226	0.3067	0.4098	0.5352	0.6799	0.8417	-0.0548	-0.1264	-0.1706	-0.2262	-0.3068	-0.41	-0.5355	-0.6801	-0.8419			
	0.4	0.0539	0.1272	0.2307	0.3262	0.3904	0.47	0.5821	0.7237	0.8884	-0.0543	-0.1277	-0.2311	-0.3266	-0.3907	-0.4703	-0.5825	-0.7234	-0.8868			
	0.6	0.0536	0.1259	0.23	0.3675	0.5077	0.6088	0.6998	0.8181	0.966	-0.054	-0.1261	-0.2299	-0.3675	-0.5077	-0.6087	-0.7	-0.8187	-0.9664			
	0.8	0.0534	0.1249	0.2263	0.3646	0.5417	0.7253	0.8666	0.9816	1.1053	-0.0534	-0.1248	-0.2262	-0.3645	-0.5416	-0.7252	-0.8666	-0.9825	-1.1058			
	1	0.0527	0.1244	0.2241	0.3583	0.5362	0.7571	0.9861	1.1709	1.3051	-0.0533	-0.1245	-0.224	-0.3583	-0.5362	-0.7572	-0.9862	-1.1727	-1.3064			

Appendix D. Streamline profiles

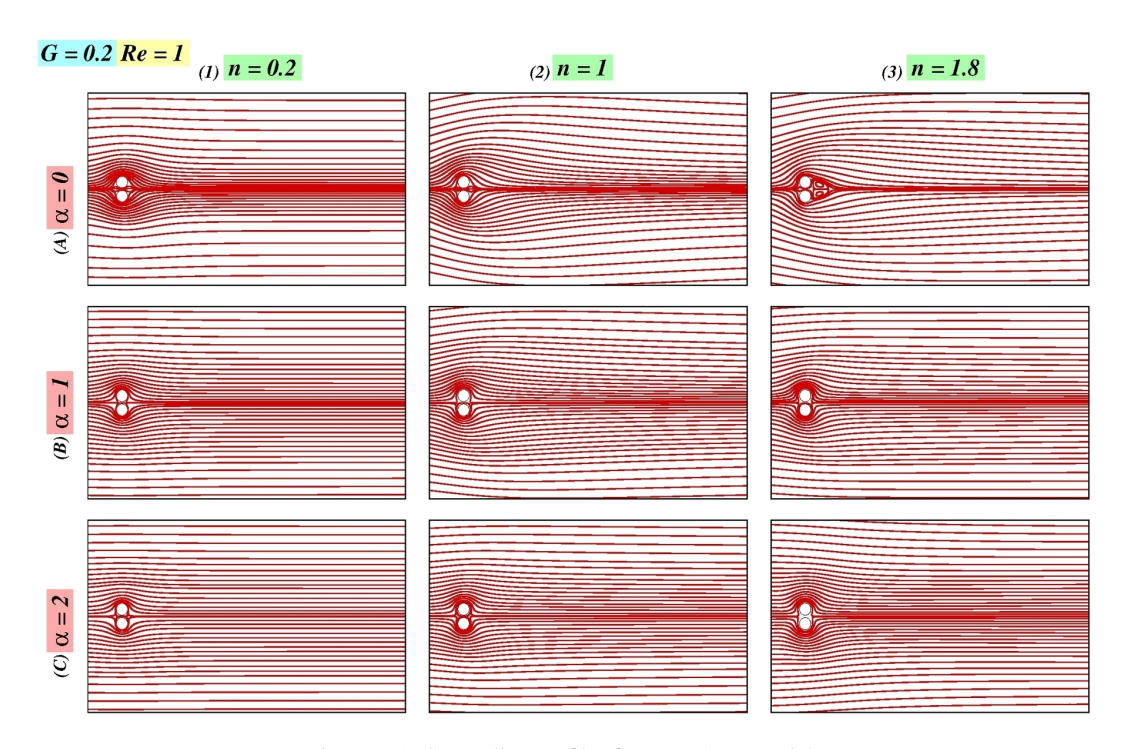


Figure D.1: Streamline profiles for Re = 1 at G = 0.2.

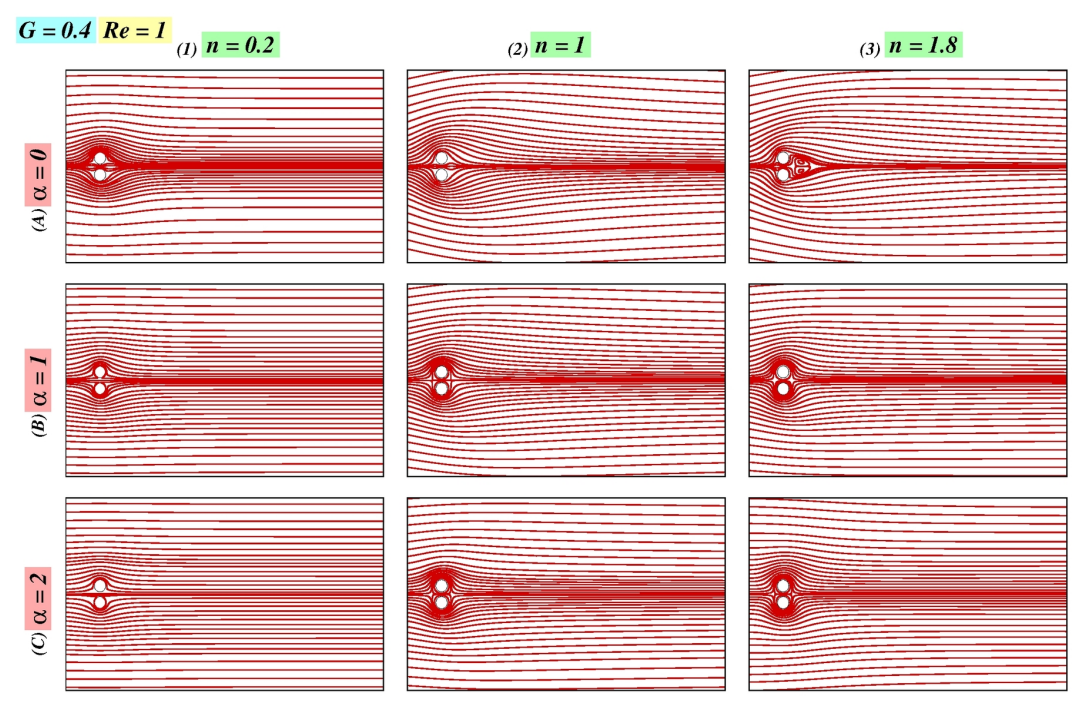


Figure D.2: Streamline profiles for Re = 1 at G = 0.4.

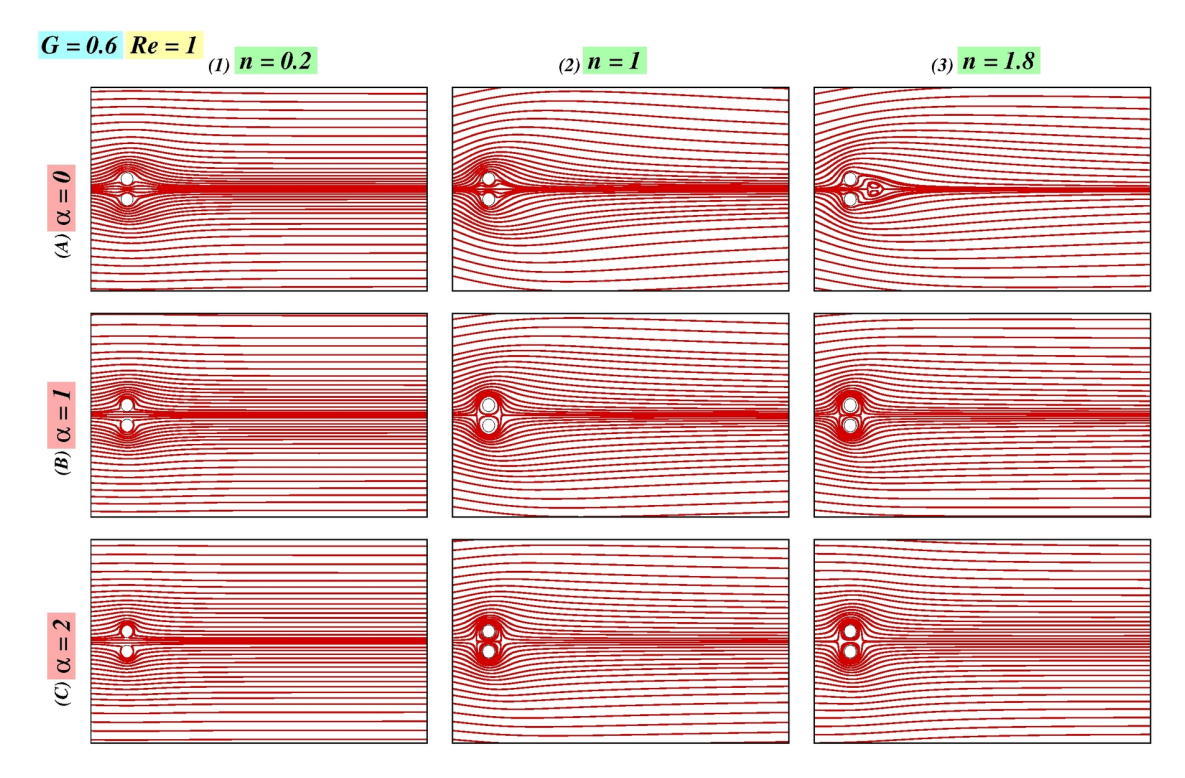


Figure D.3: Streamline profiles for Re = 1 at G = 0.6.

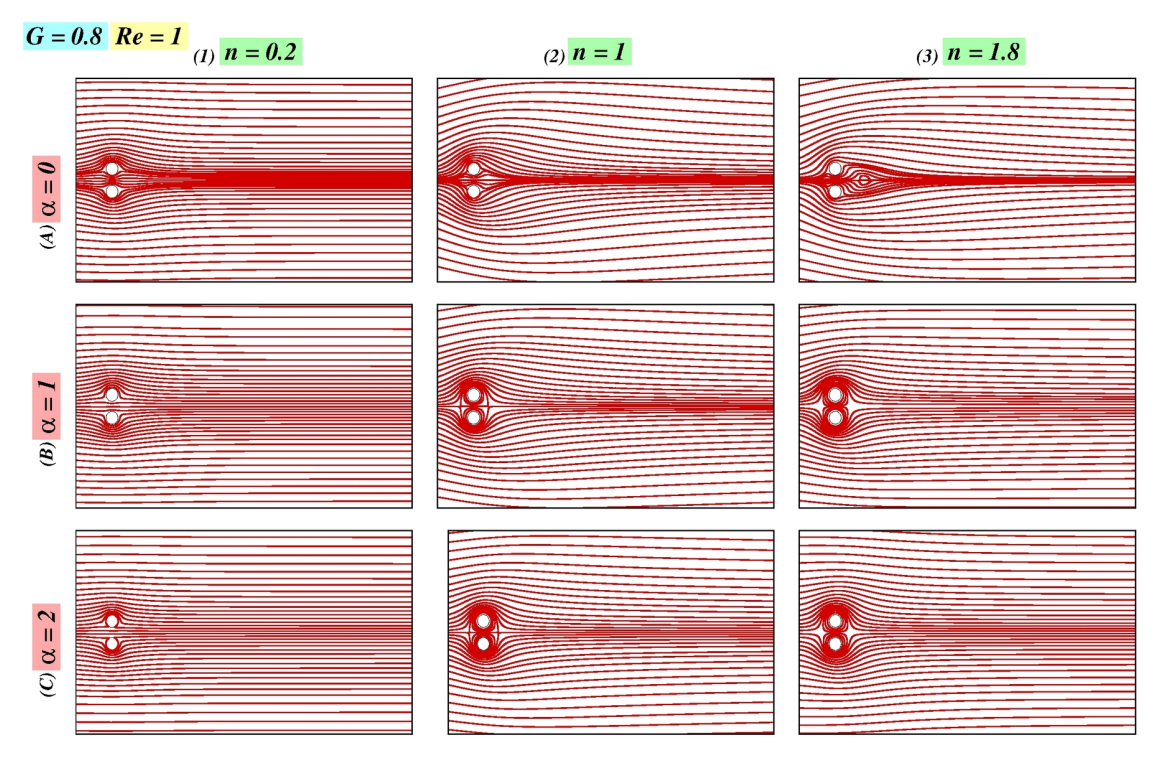


Figure D.4: Streamline profiles for Re = 1 at G = 0.8.

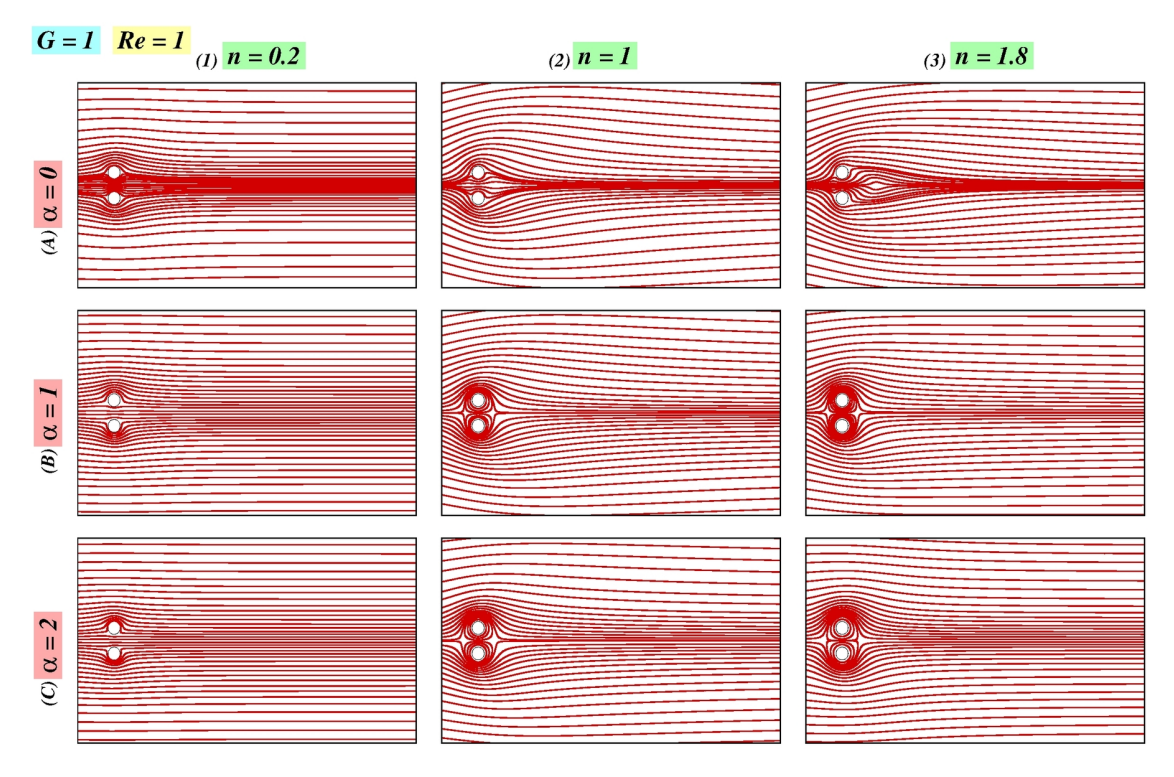


Figure D.5: Streamline profiles for Re = 1 at G = 1.

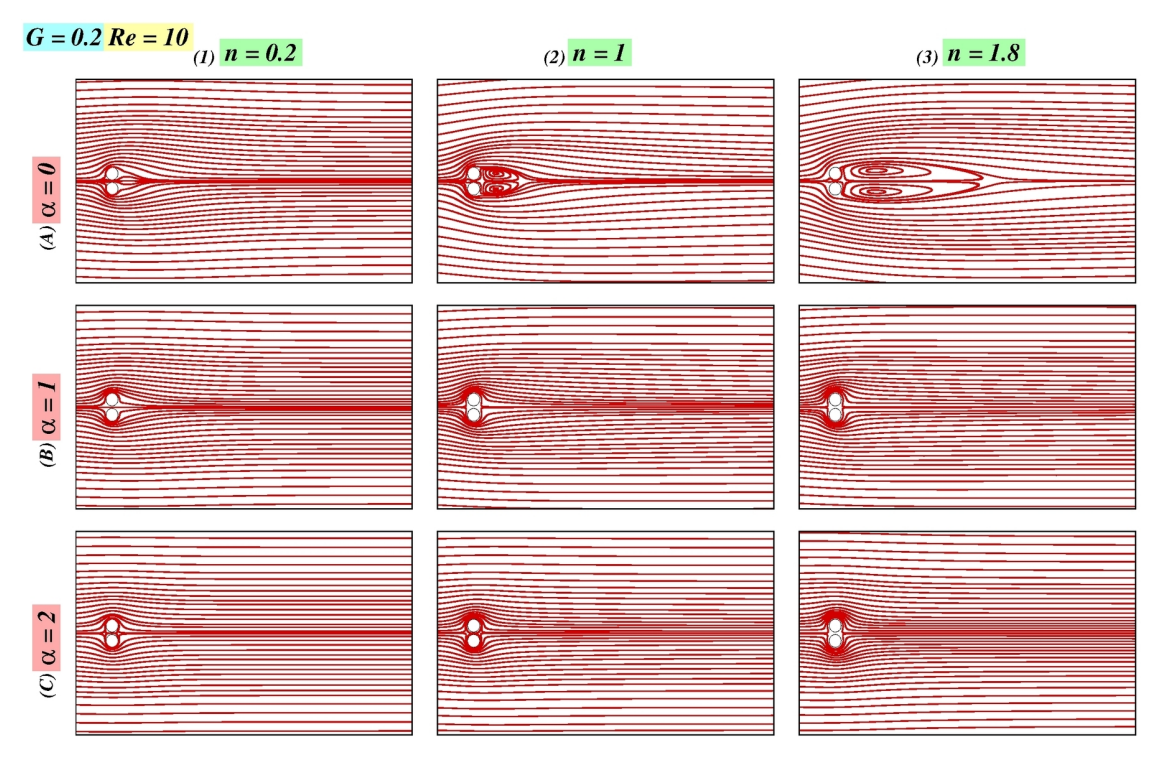


Figure D.6: Streamline profiles for Re = 10 at G = 0.2.

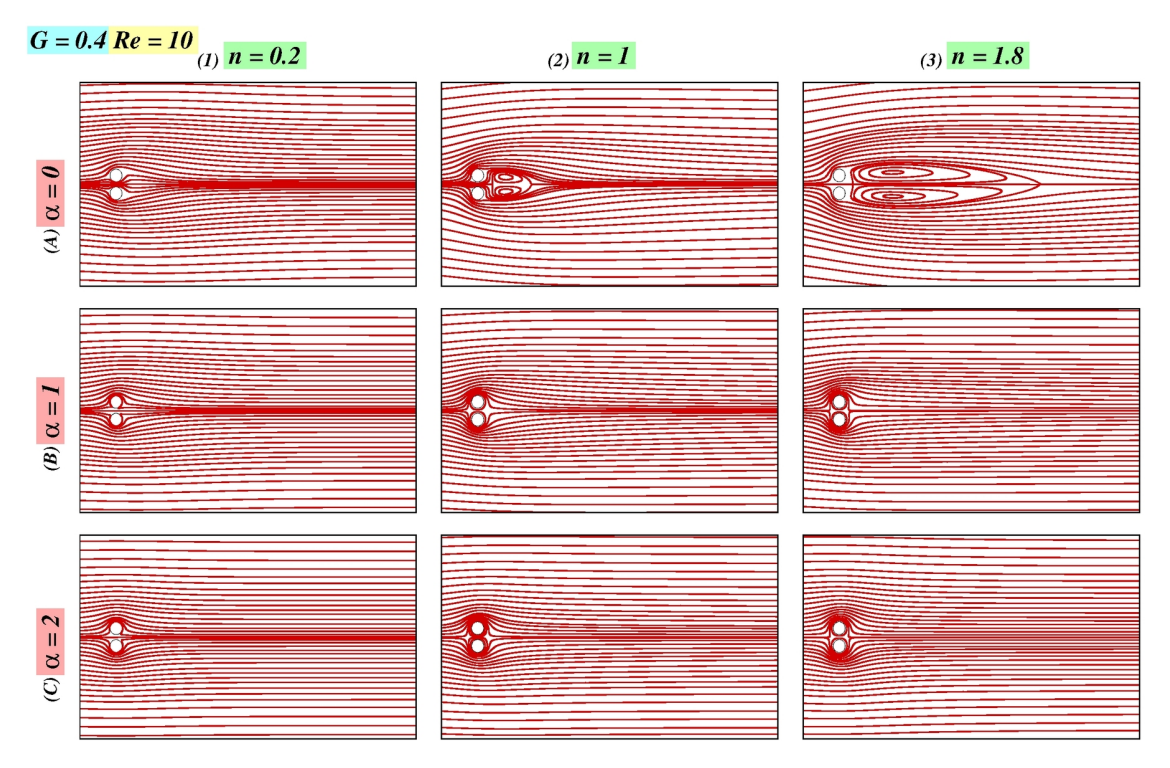


Figure D.7: Streamline profiles for Re = 10 at G = 0.4.

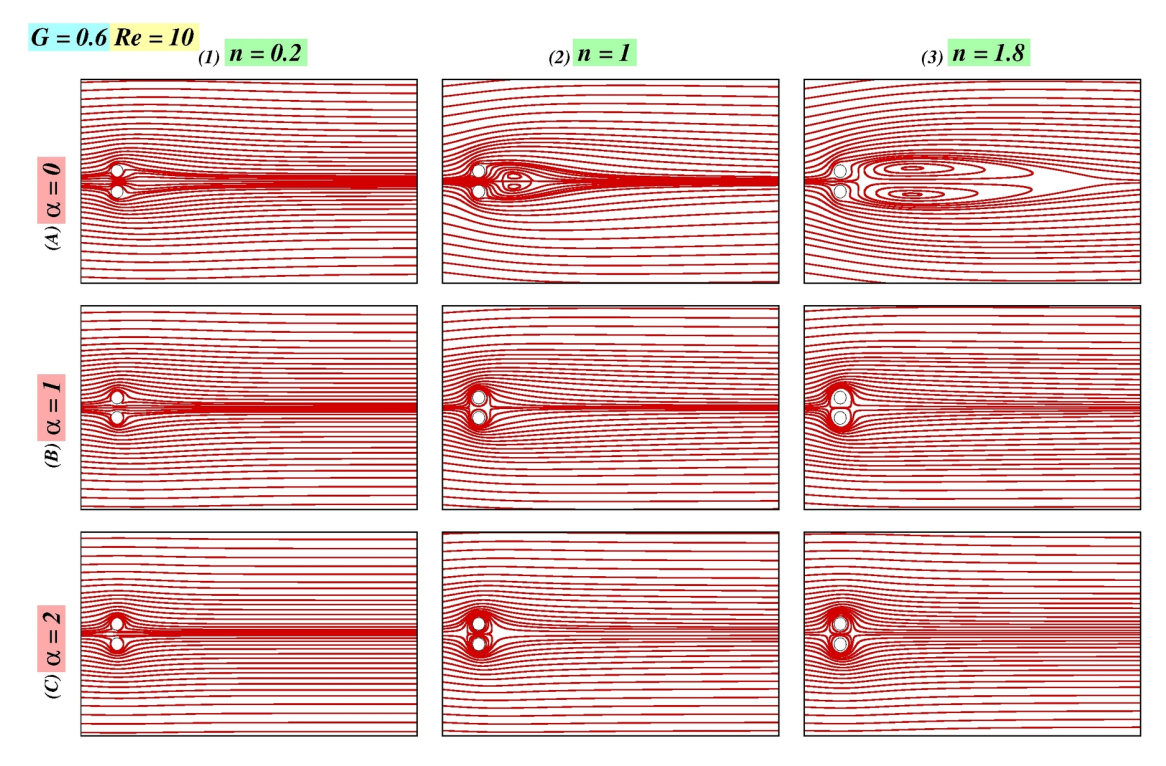


Figure D.8: Streamline profiles for Re = 10 at G = 0.6.

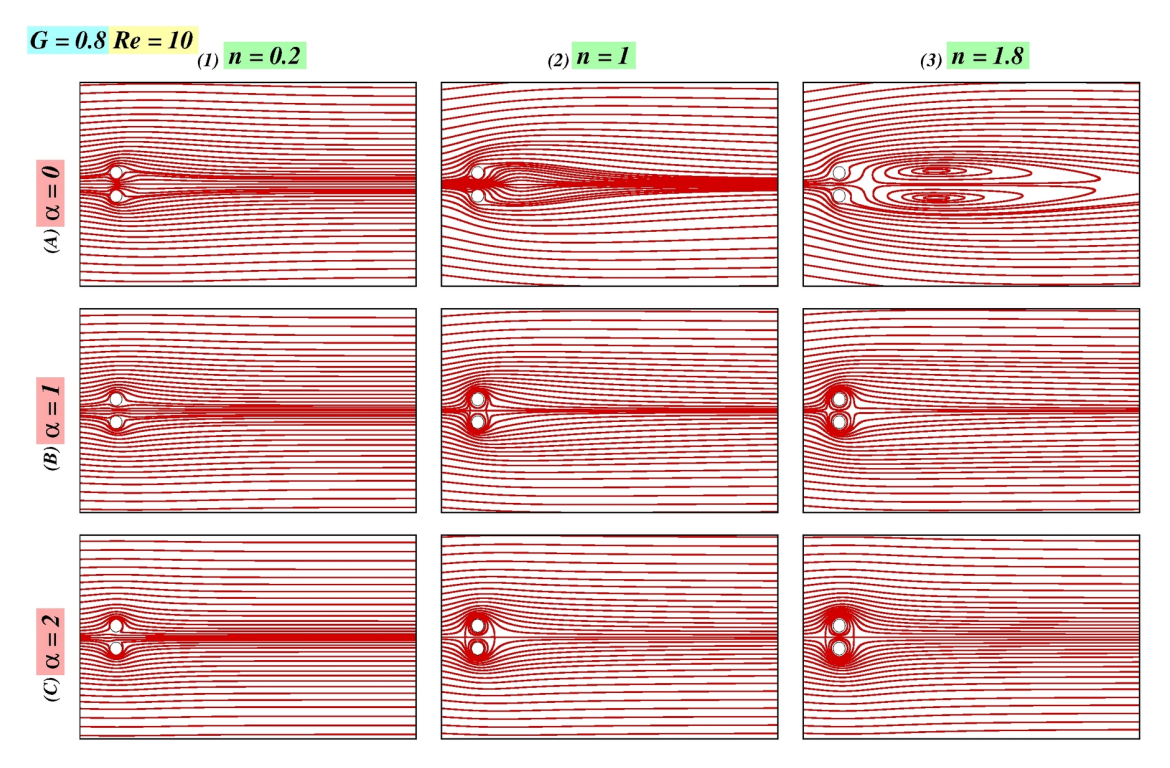


Figure D.9: Streamline profiles for Re = 10 at G = 0.8.

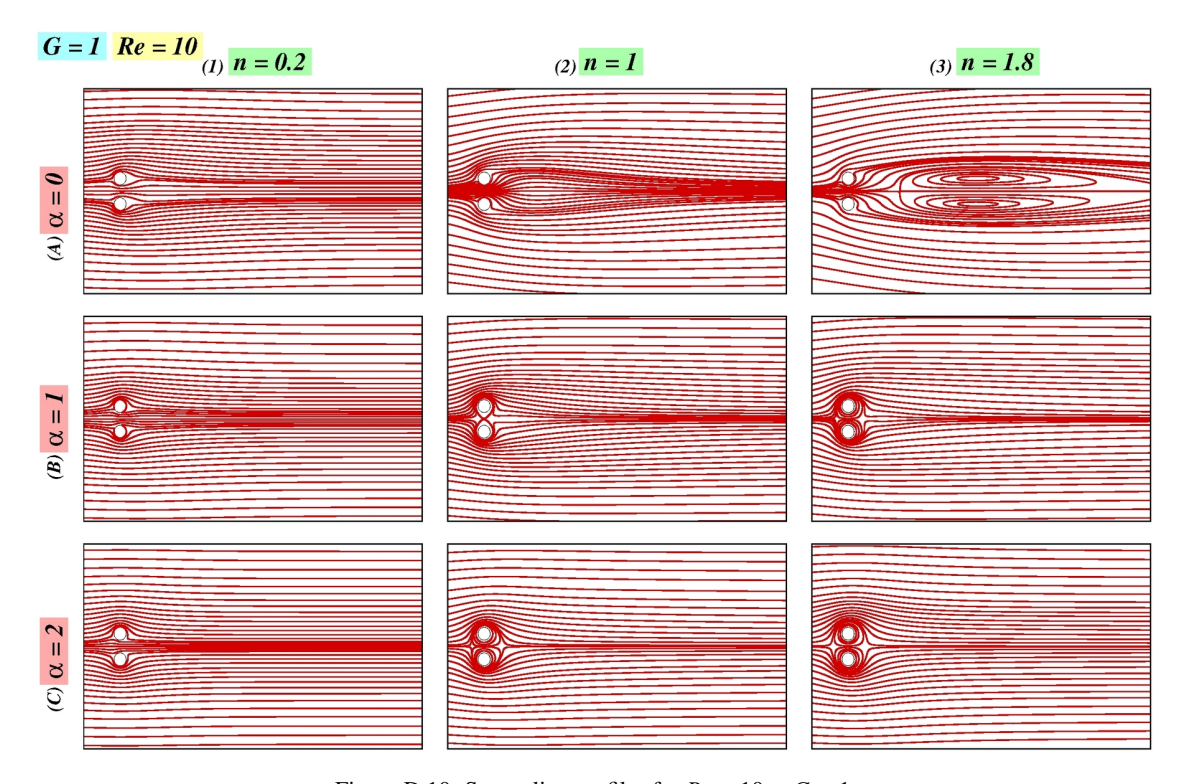


Figure D.10: Streamline profiles for Re = 10 at G = 1.

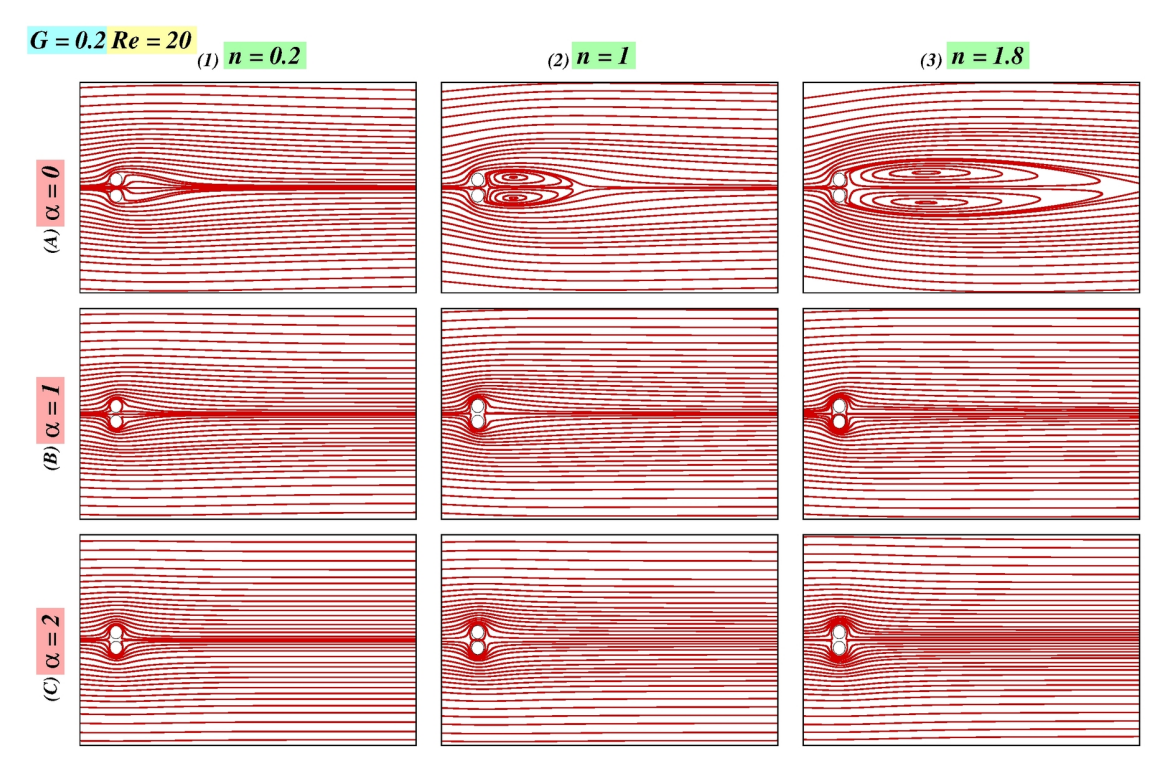


Figure D.11: Streamline profiles for Re = 20 at G = 0.2.

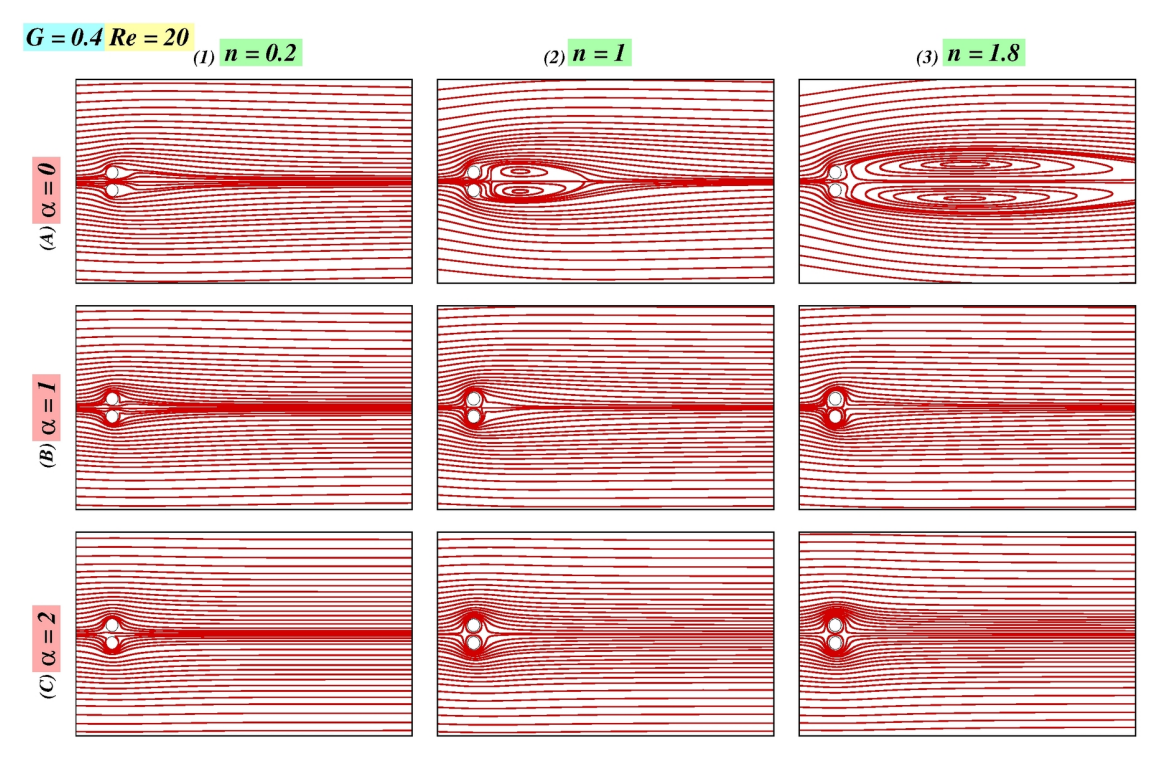


Figure D.12: Streamline profiles for Re = 20 at G = 0.4.

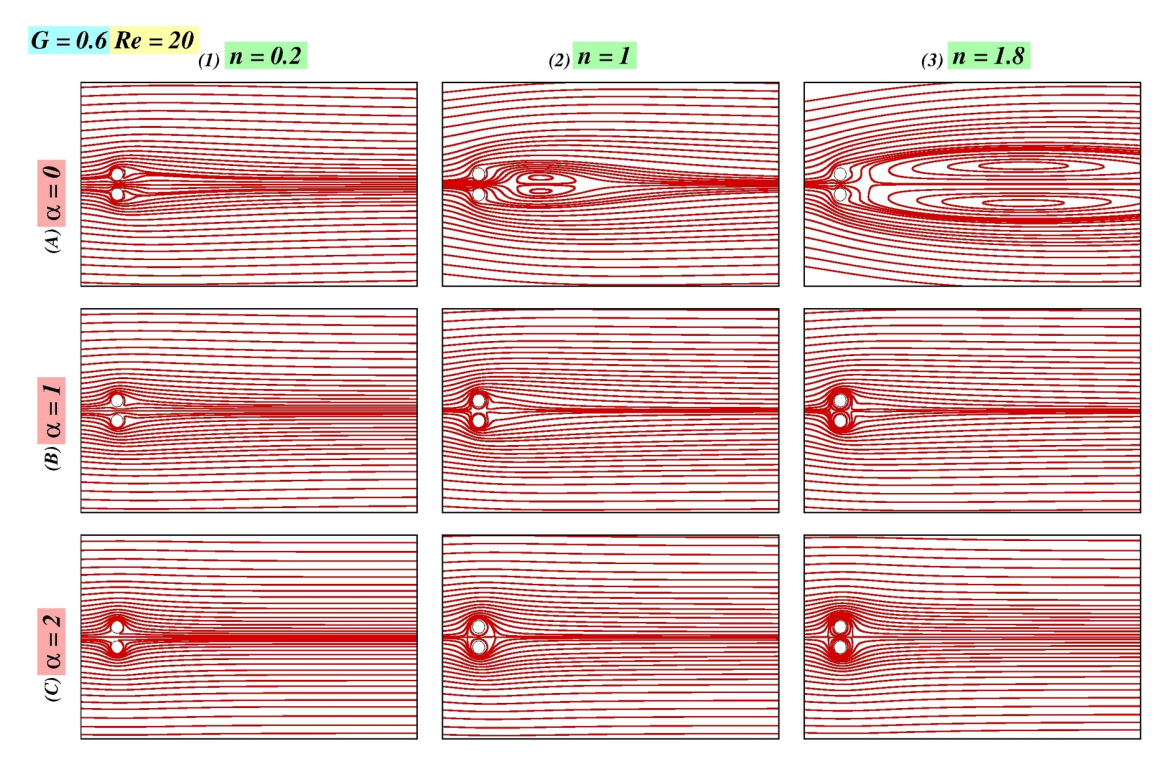


Figure D.13: Streamline profiles for Re = 20 at G = 0.6.

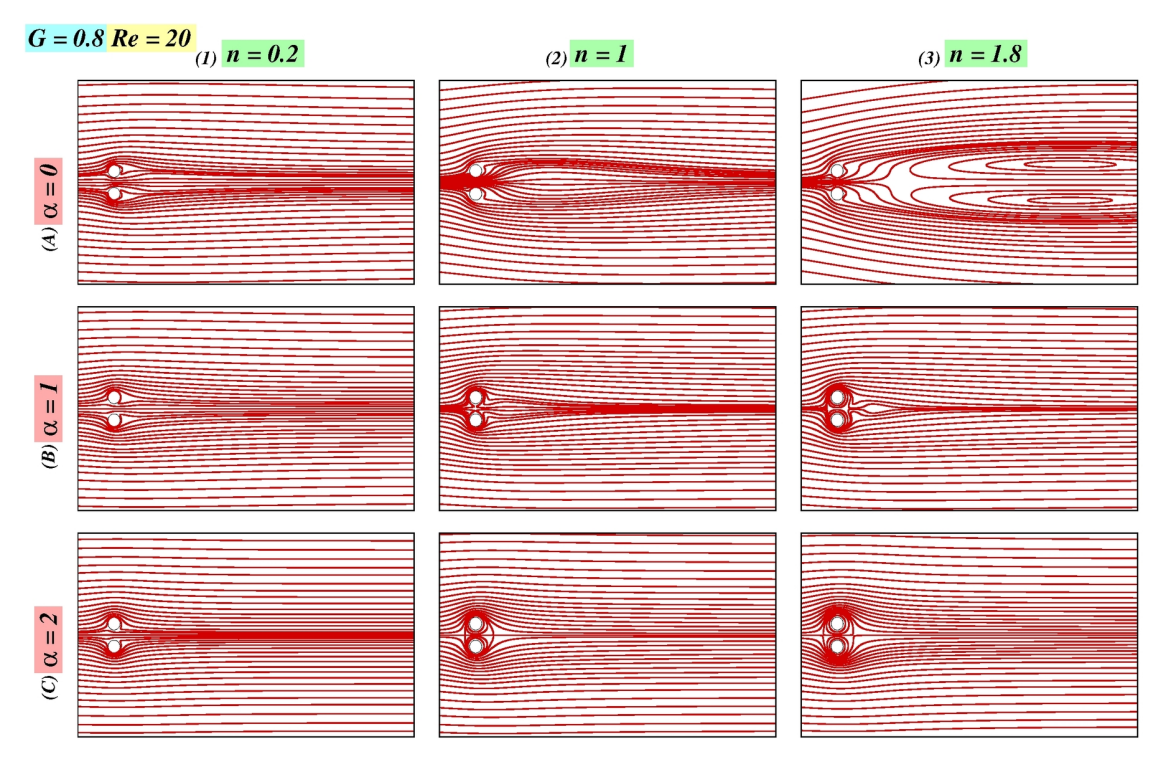


Figure D.14: Streamline profiles for Re = 20 at G = 0.8.

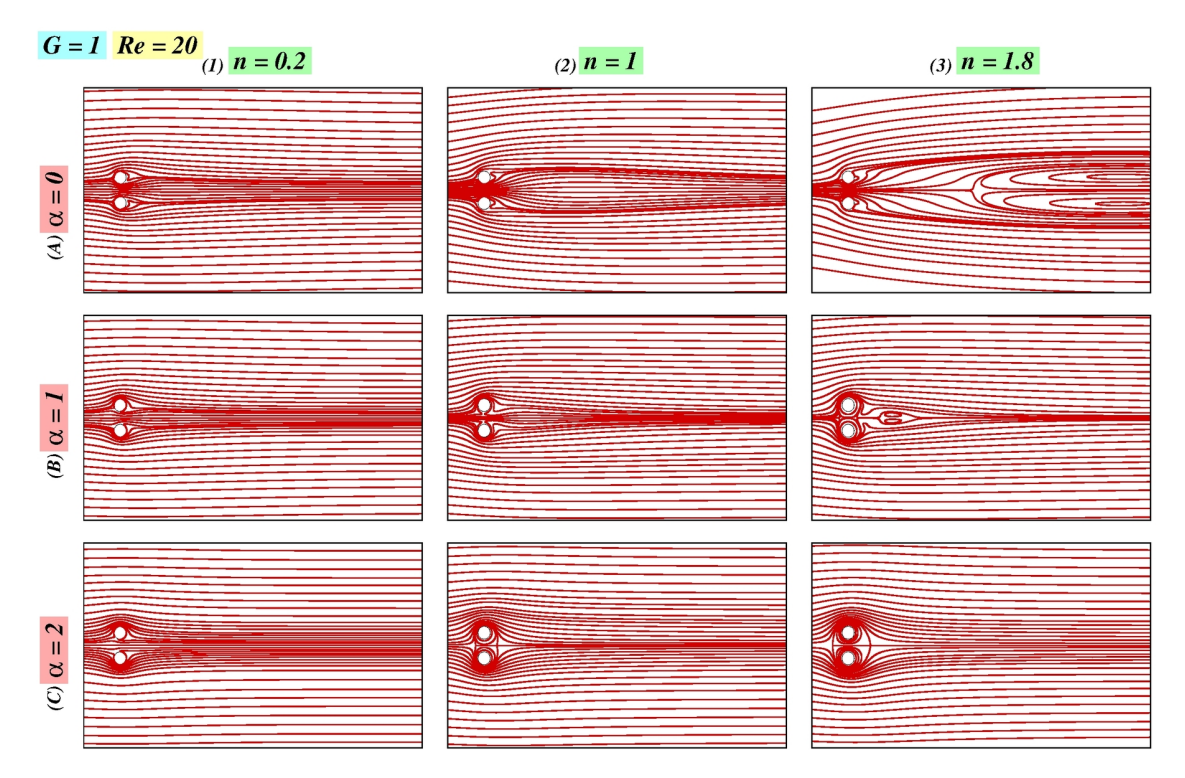


Figure D.15: Streamline profiles for Re = 20 at G = 1.

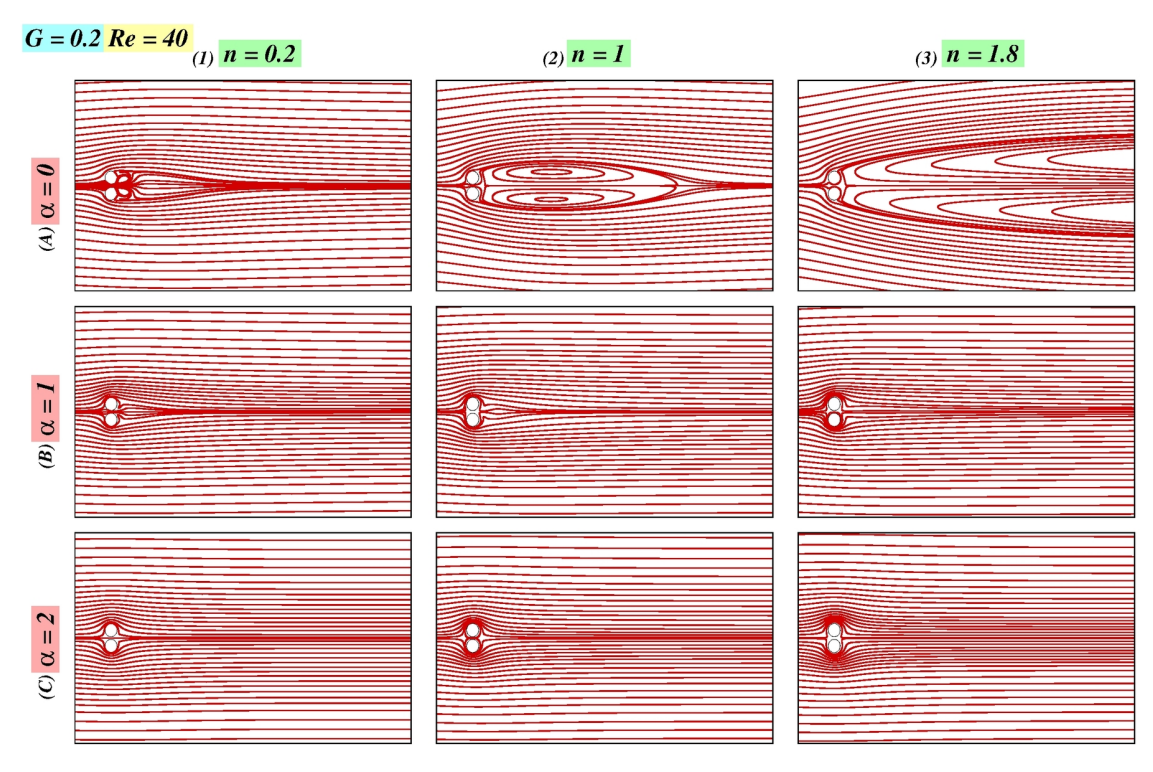


Figure D.16: Streamline profiles for Re = 40 at G = 0.2.

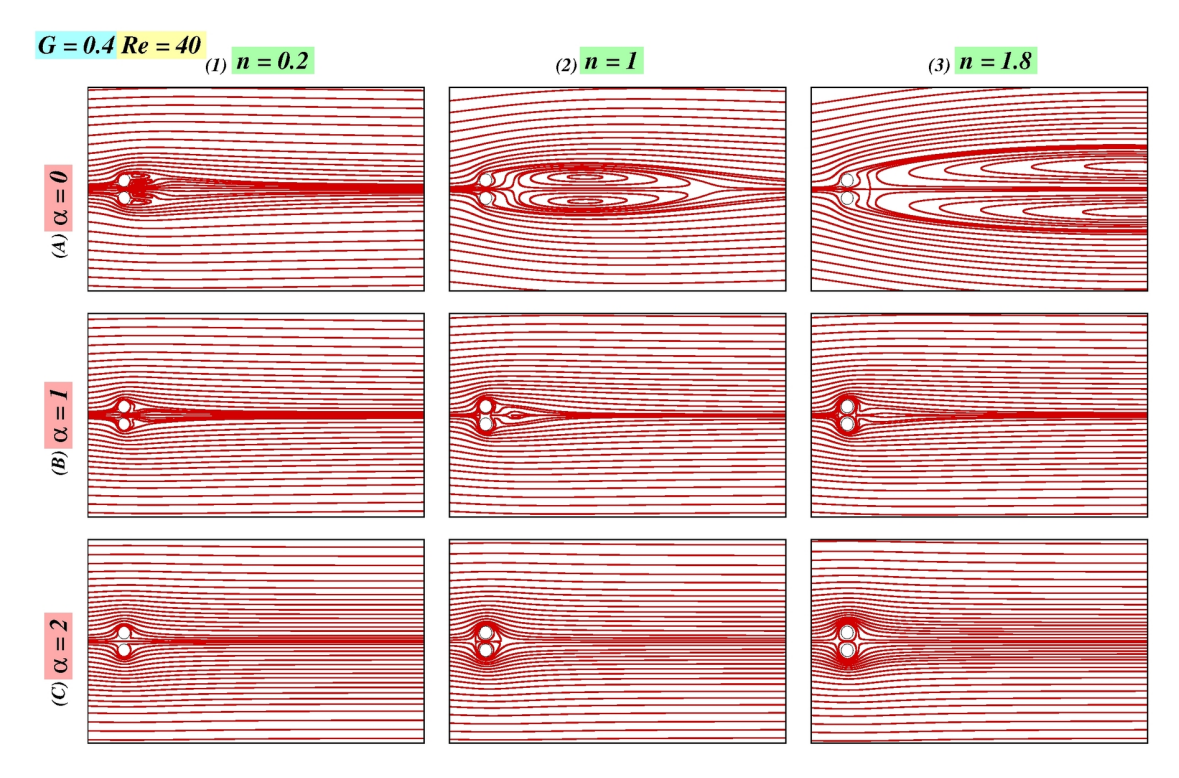


Figure D.17: Streamline profiles for Re = 40 at G = 0.4.

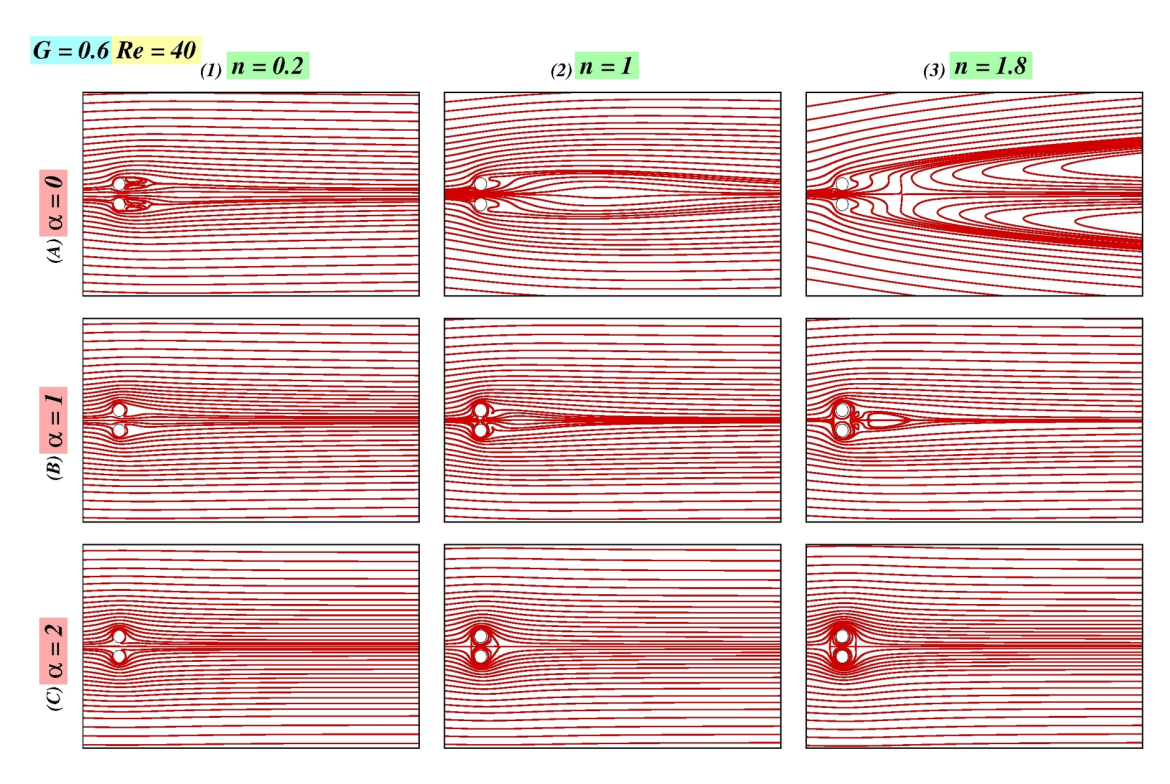


Figure D.18: Streamline profiles for Re = 40 at G = 0.6.

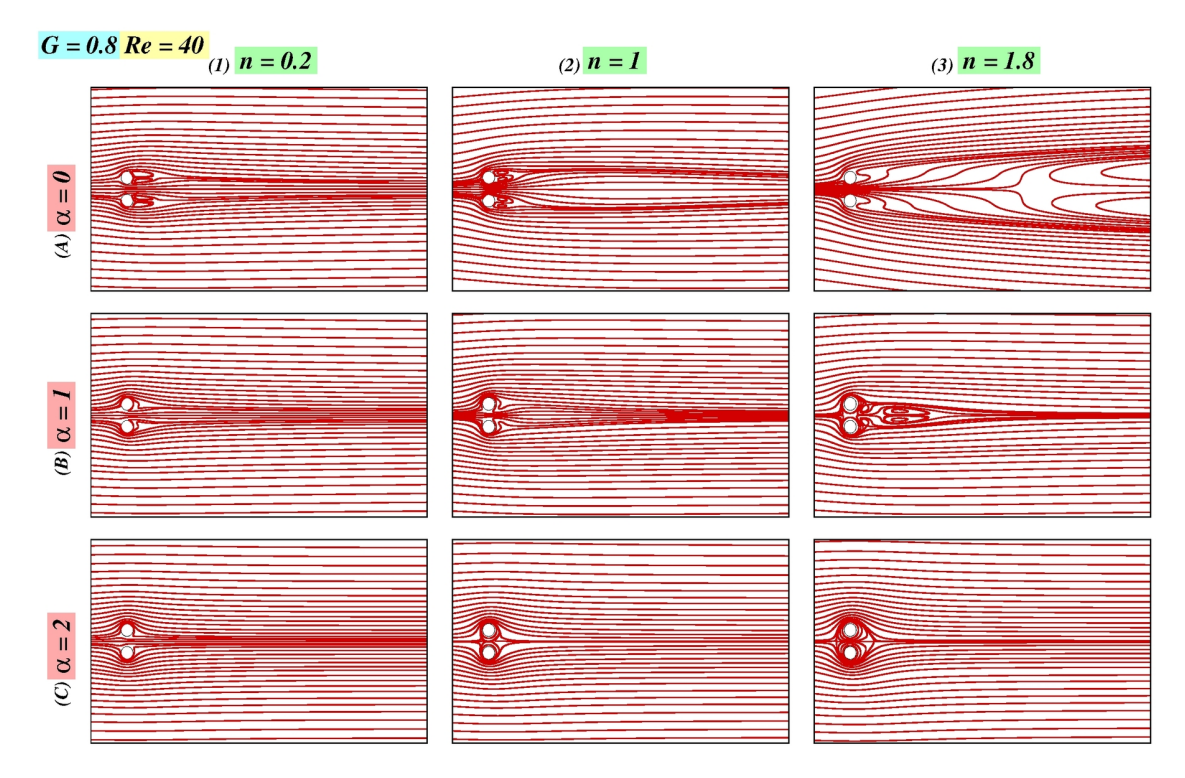


Figure D.19: Streamline profiles for Re = 40 at G = 0.8.

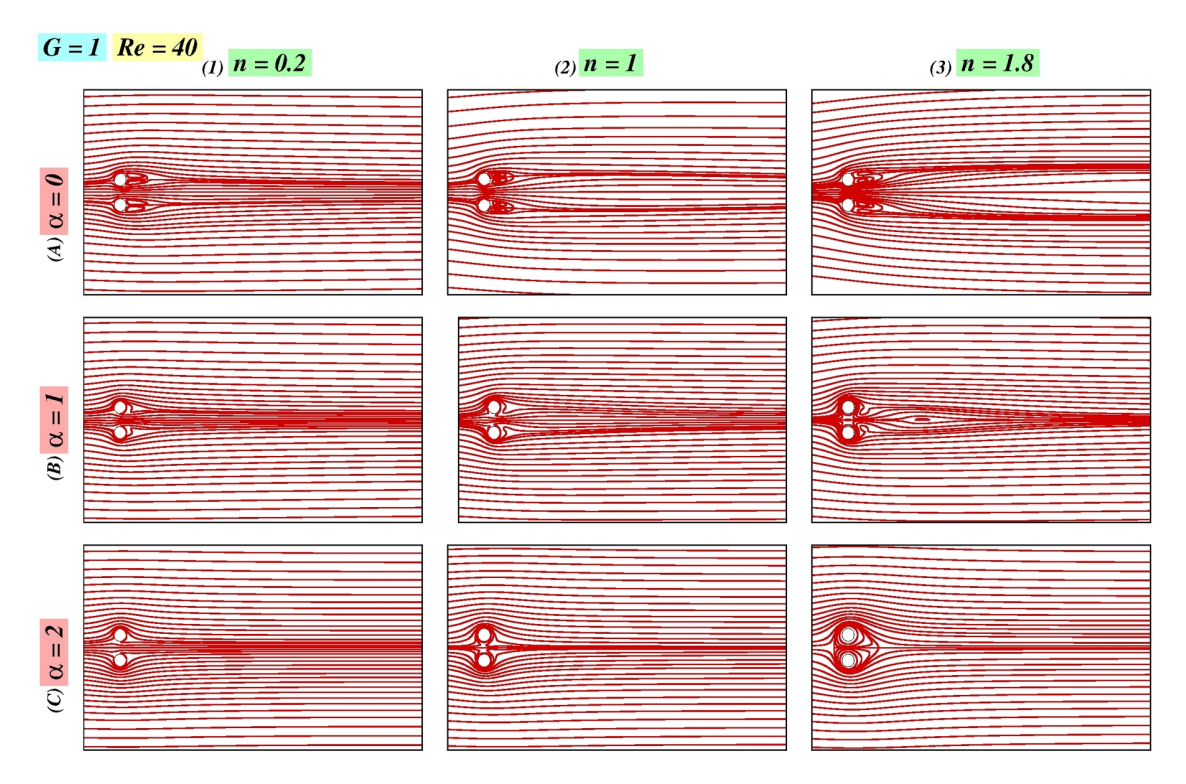


Figure D.20: Streamline profiles for Re = 40 at G = 1.

Appendix E. Centerline velocity profiles:

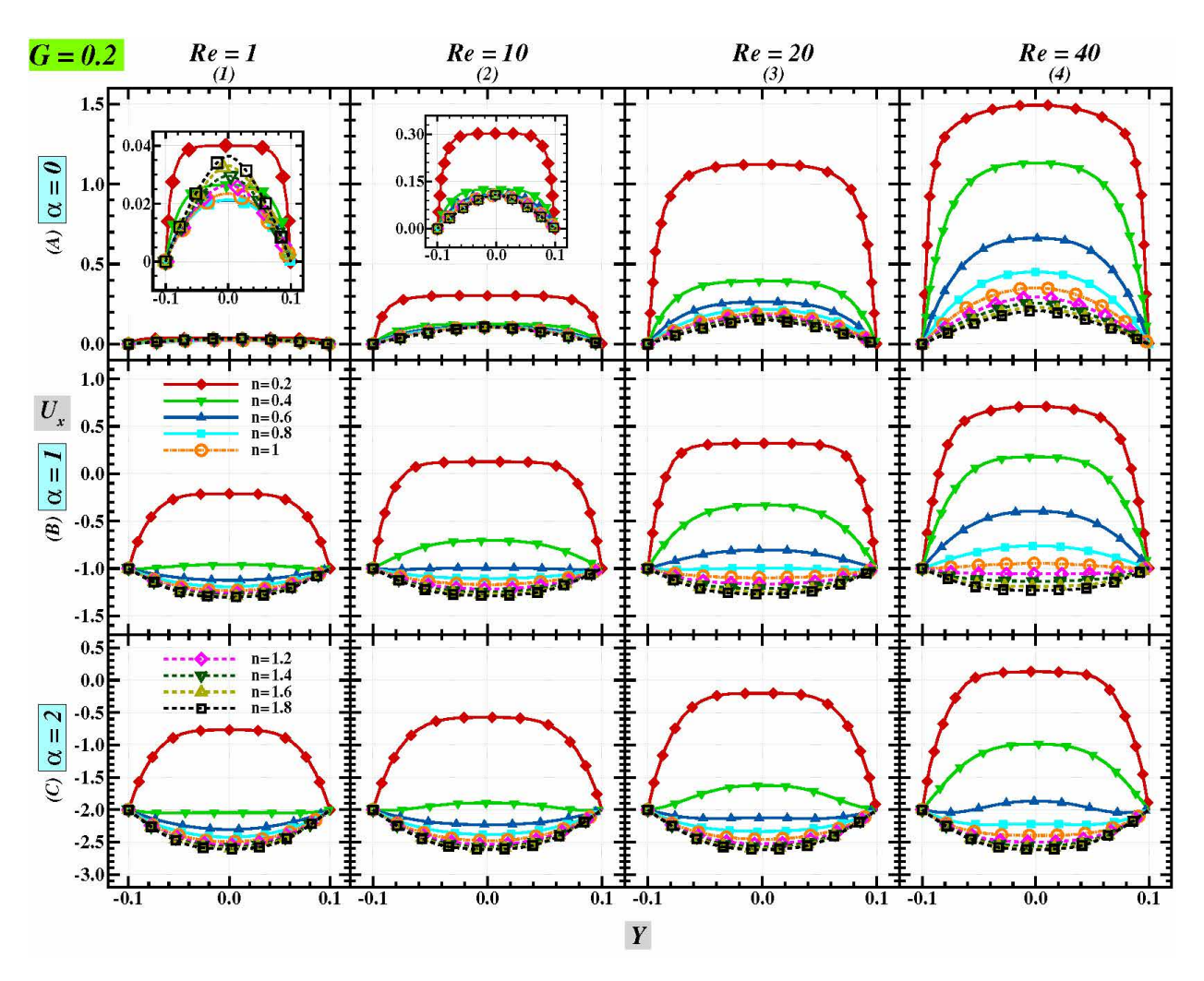


Figure E.1: Centerline velocity profiles (U_x at line 6, Fig. 1) for different power-law indices (n) at various rotational rates (α , rows) and Reynolds numbers (Re, columns) for G = 0.2.

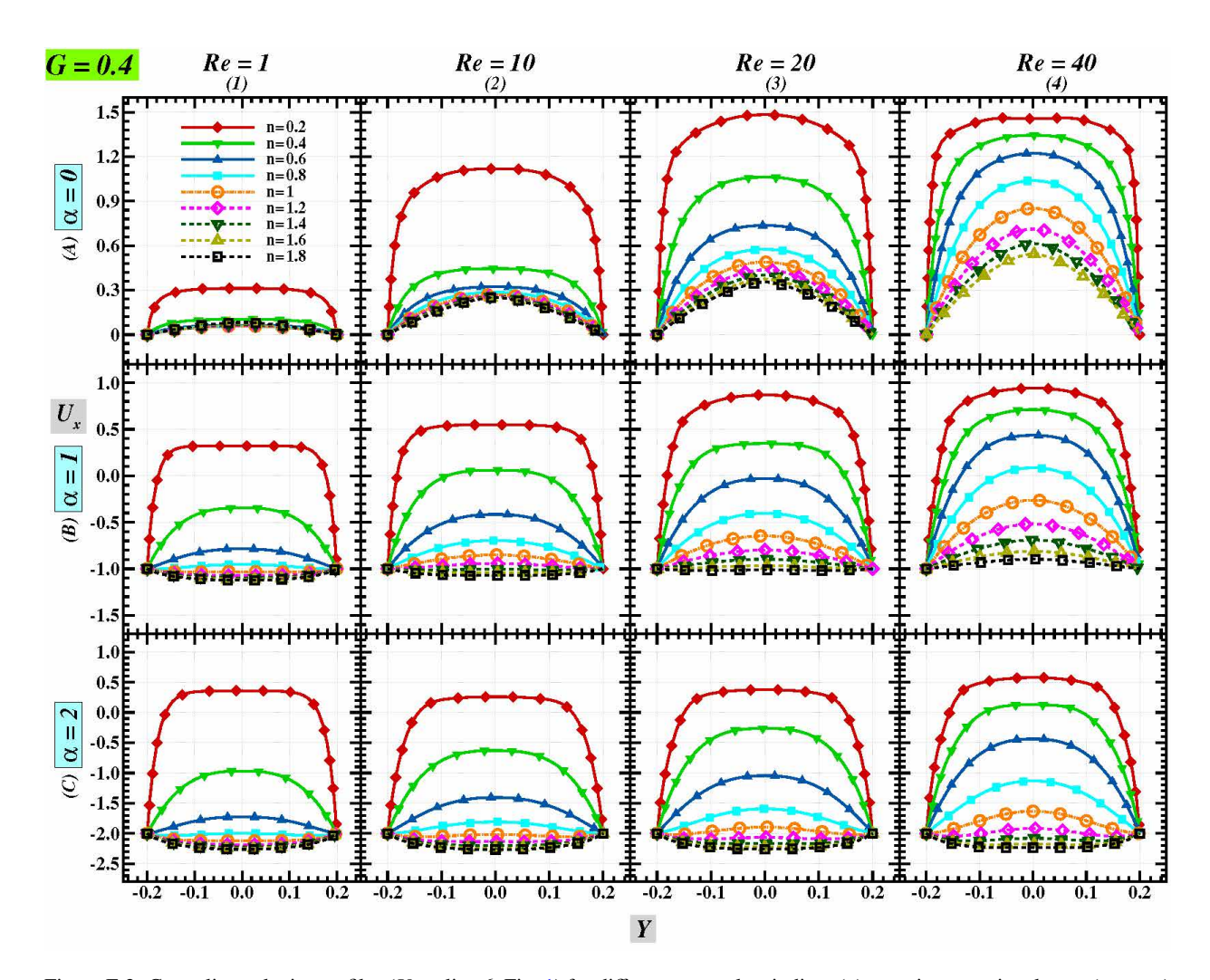


Figure E.2: Centerline velocity profiles (U_x at line 6, Fig. 1) for different power-law indices (n) at various rotational rates (α , rows) and Reynolds numbers (Re, columns) for G = 0.4.

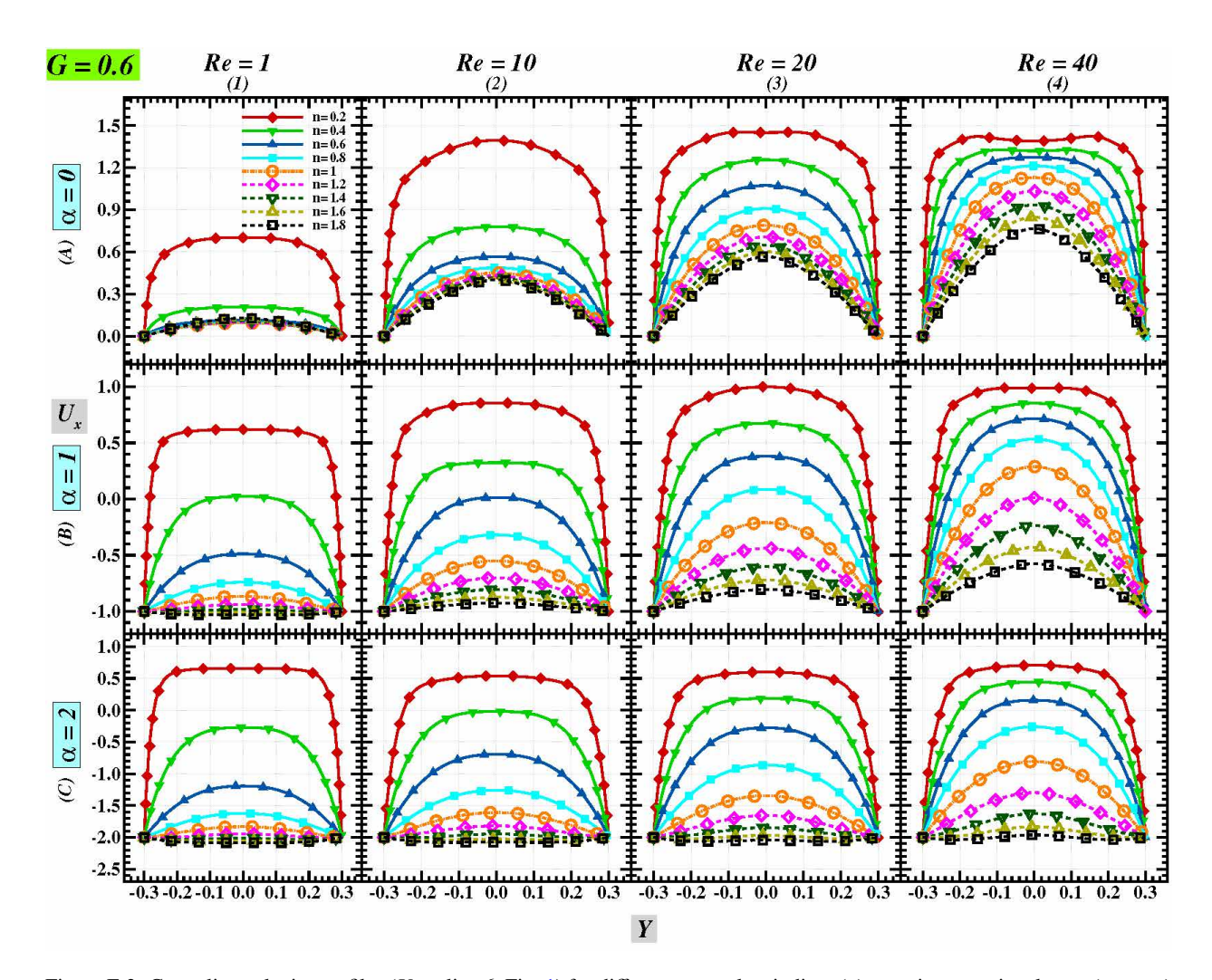


Figure E.3: Centerline velocity profiles (U_x at line 6, Fig. 1) for different power-law indices (n) at various rotational rates (α , rows) and Reynolds numbers (Re, columns) for G = 0.6.

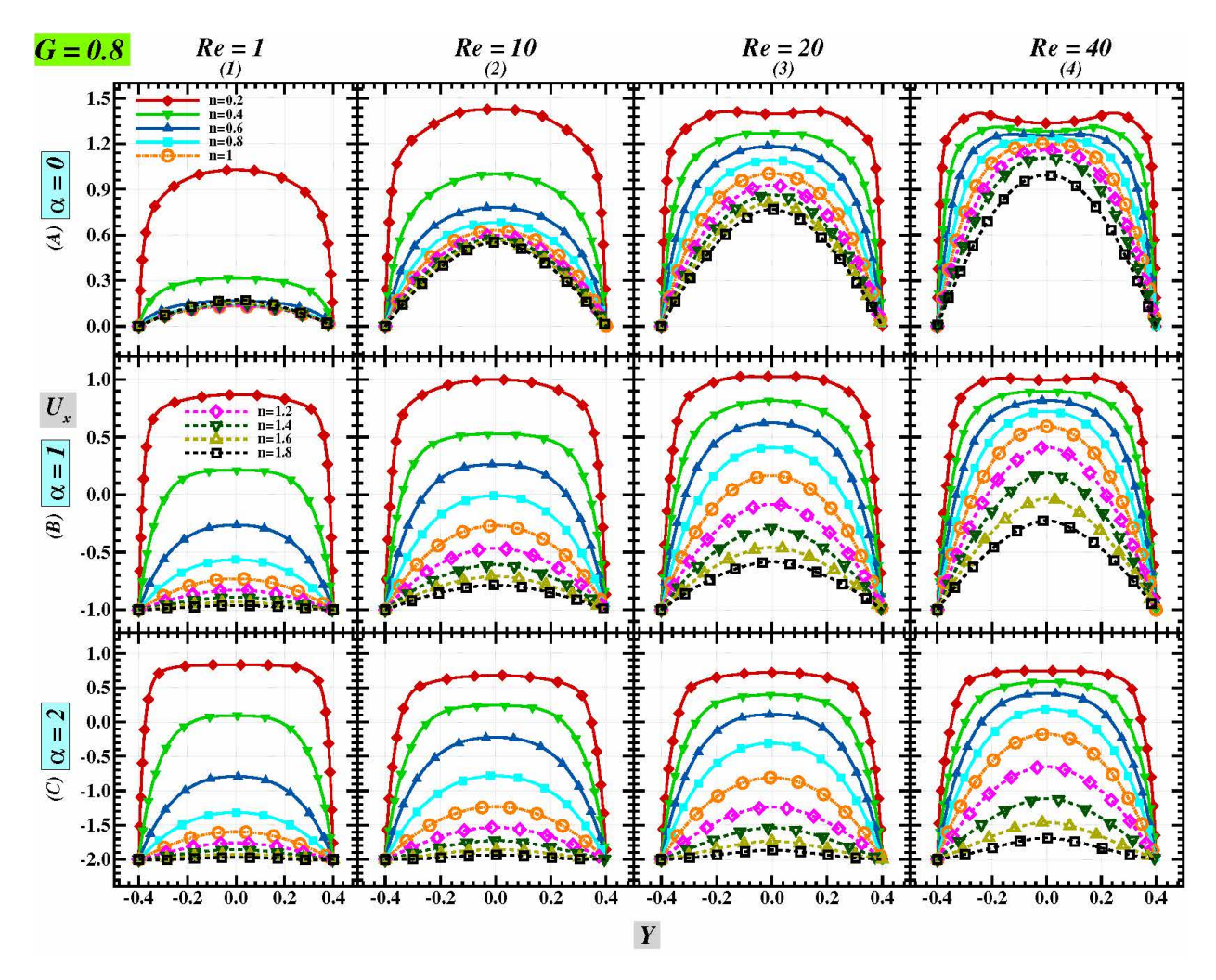


Figure E.4: Centerline velocity profiles (U_x at line 6, Fig. 1) for different power-law indices (n) at various rotational rates (α , rows) and Reynolds numbers (Re, columns) for G = 0.8.

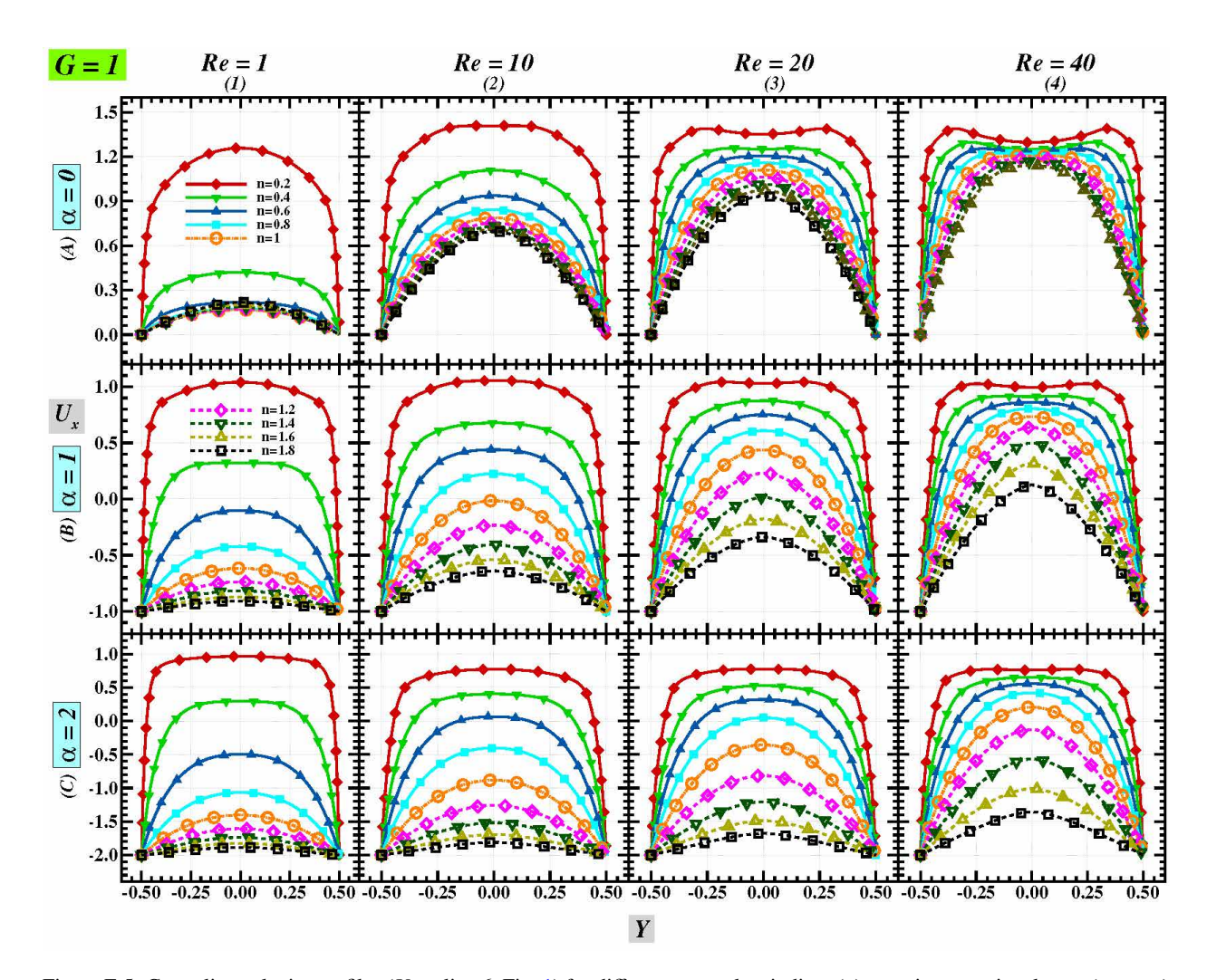


Figure E.5: Centerline velocity profiles (U_x at line 6, Fig. 1) for different power-law indices (n) at various rotational rates (α , rows) and Reynolds numbers (Re, columns) for G = 1.

Appendix F. Pressure coefficient (C_p) profiles

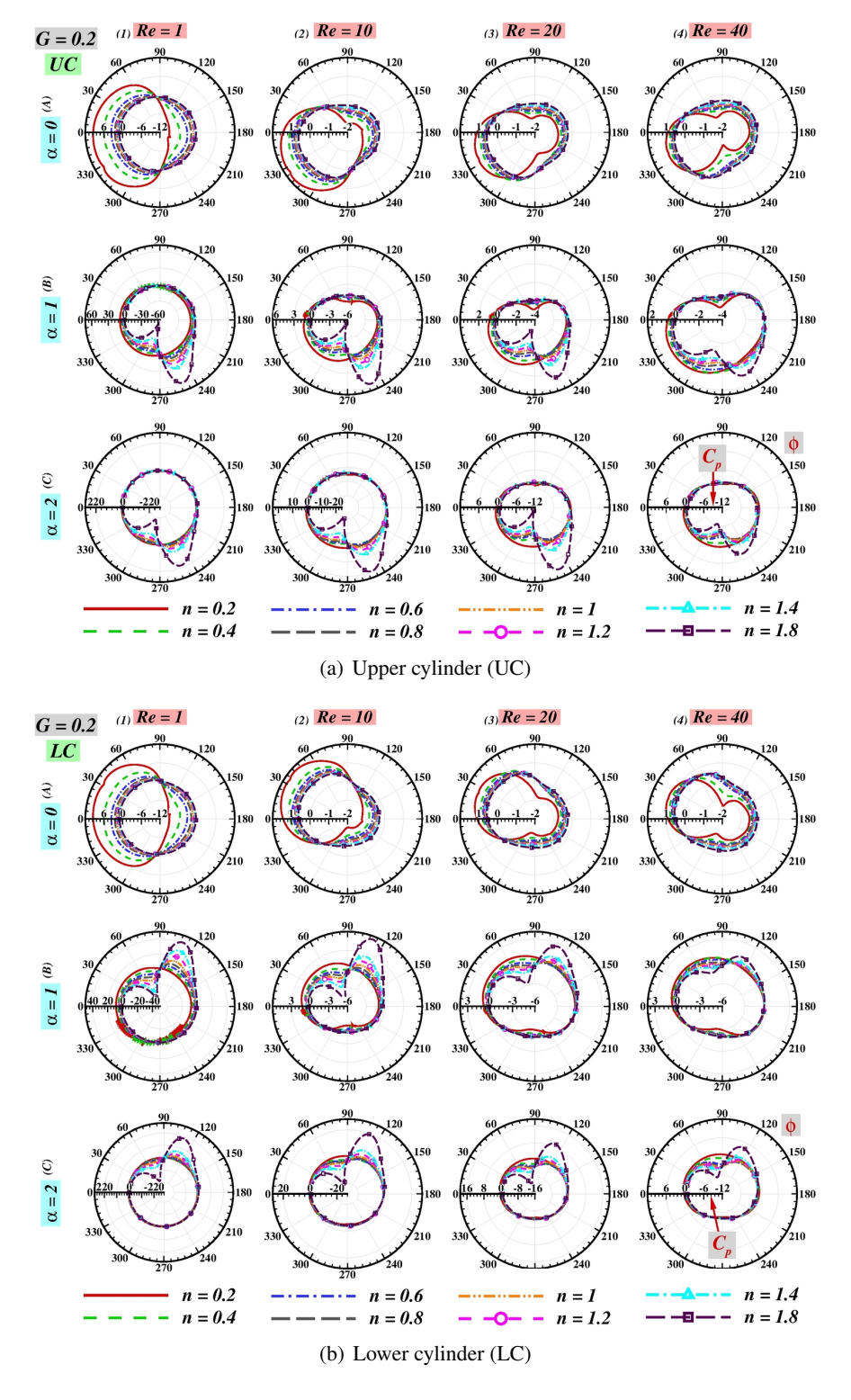


Figure F.1: Distribution of pressure coefficient on the surface of cylinders at G = 0.2.

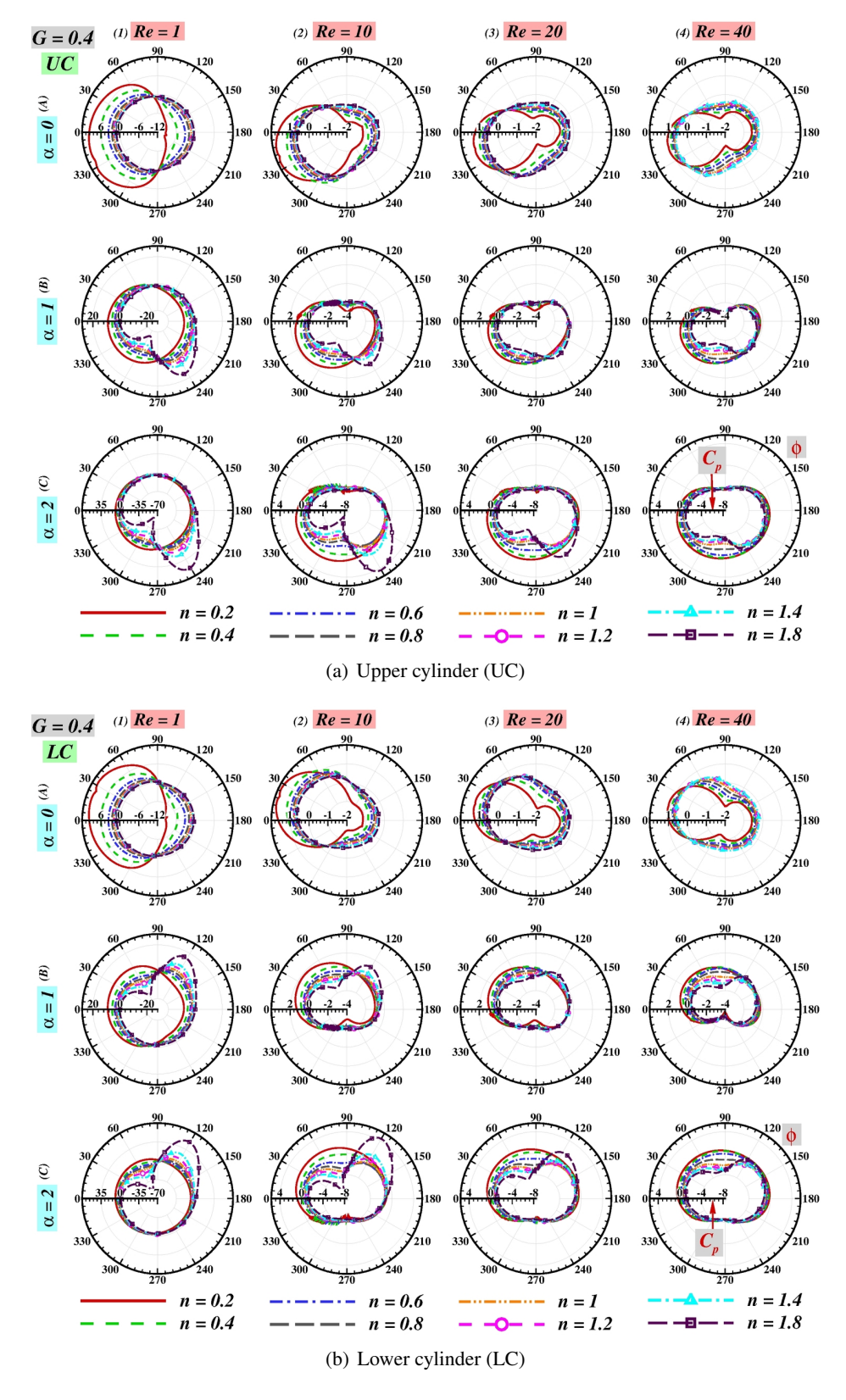


Figure F.2: Distribution of pressure coefficient on the surface of cylinders at G = 0.4.

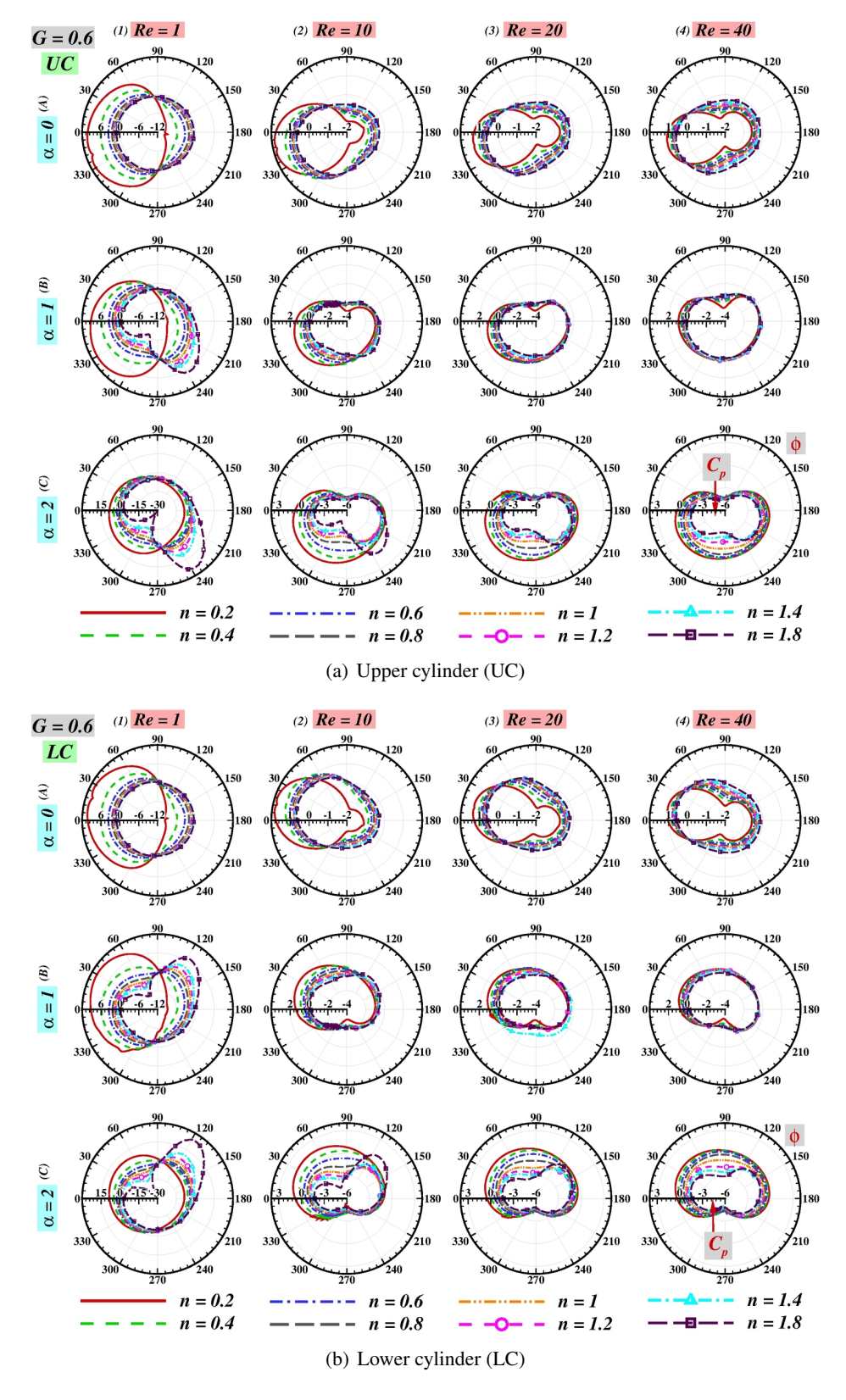


Figure F.3: Distribution of pressure coefficient on the surface of cylinders at G = 0.6.

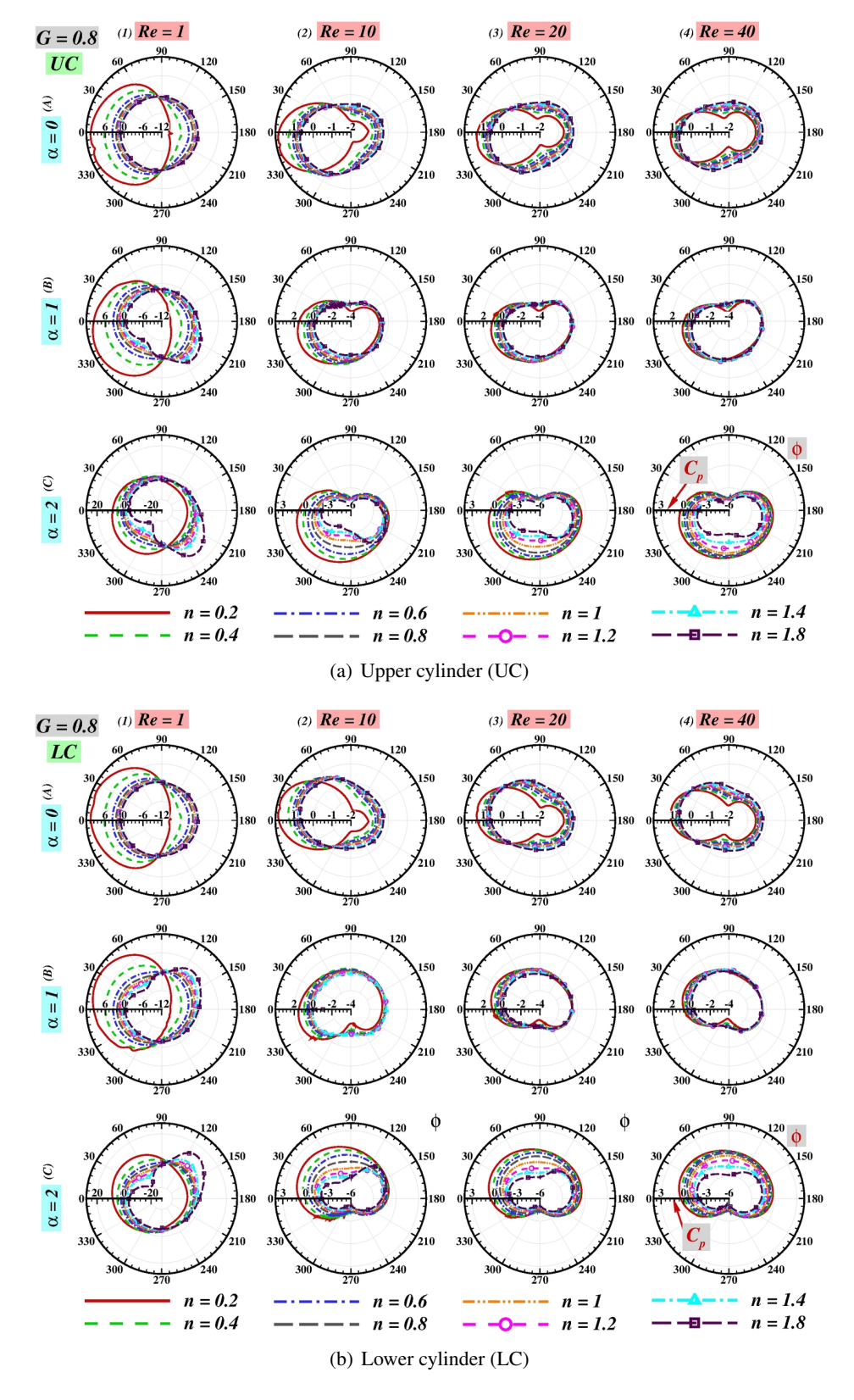


Figure F.4: Distribution of pressure coefficient on the surface of cylinders at G = 0.8.

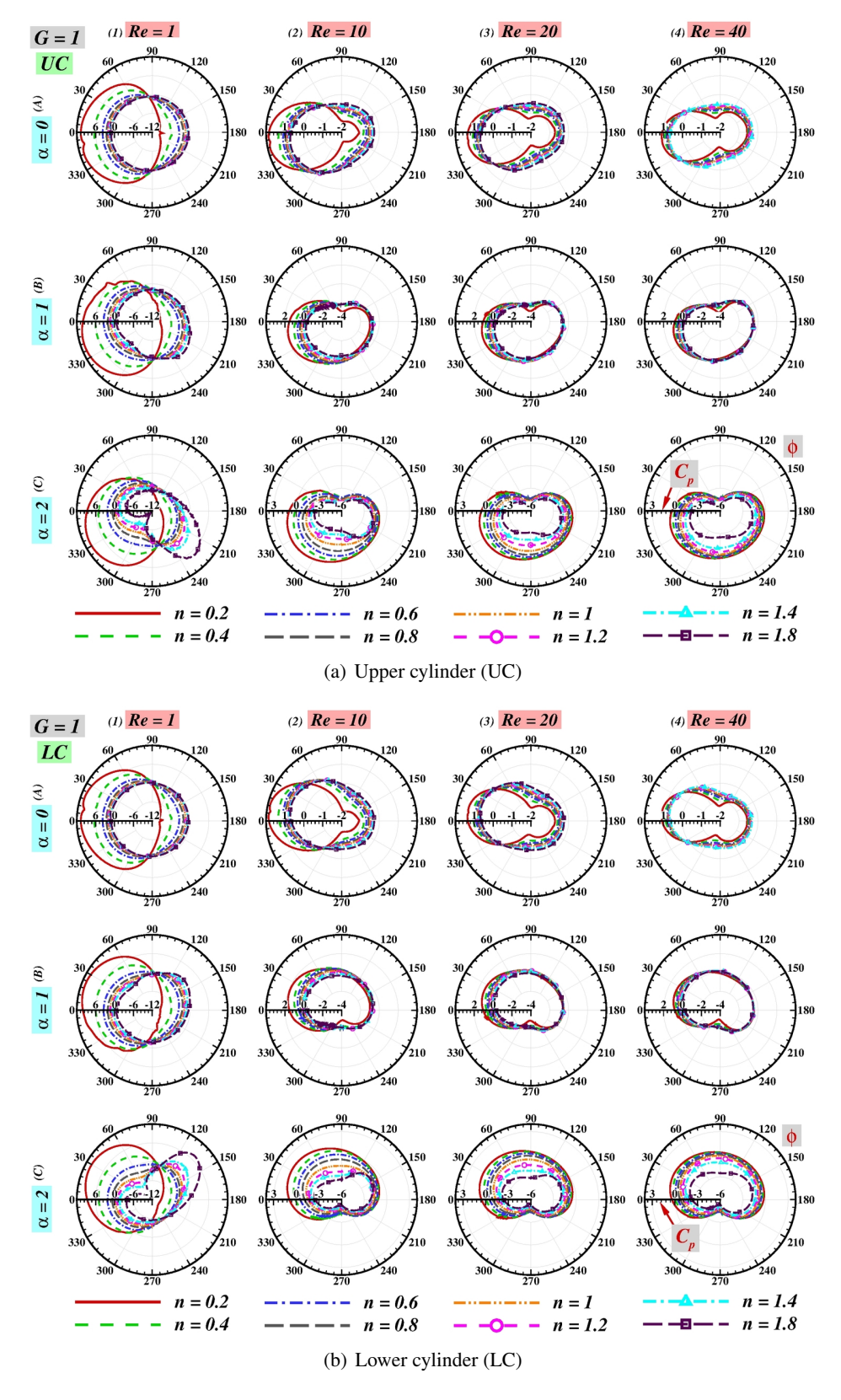


Figure F.5: Distribution of pressure coefficient on the surface of cylinders at G = 1.

Appendix G. Friction and pressure drag coefficient (C_{DF} and C_{DP})

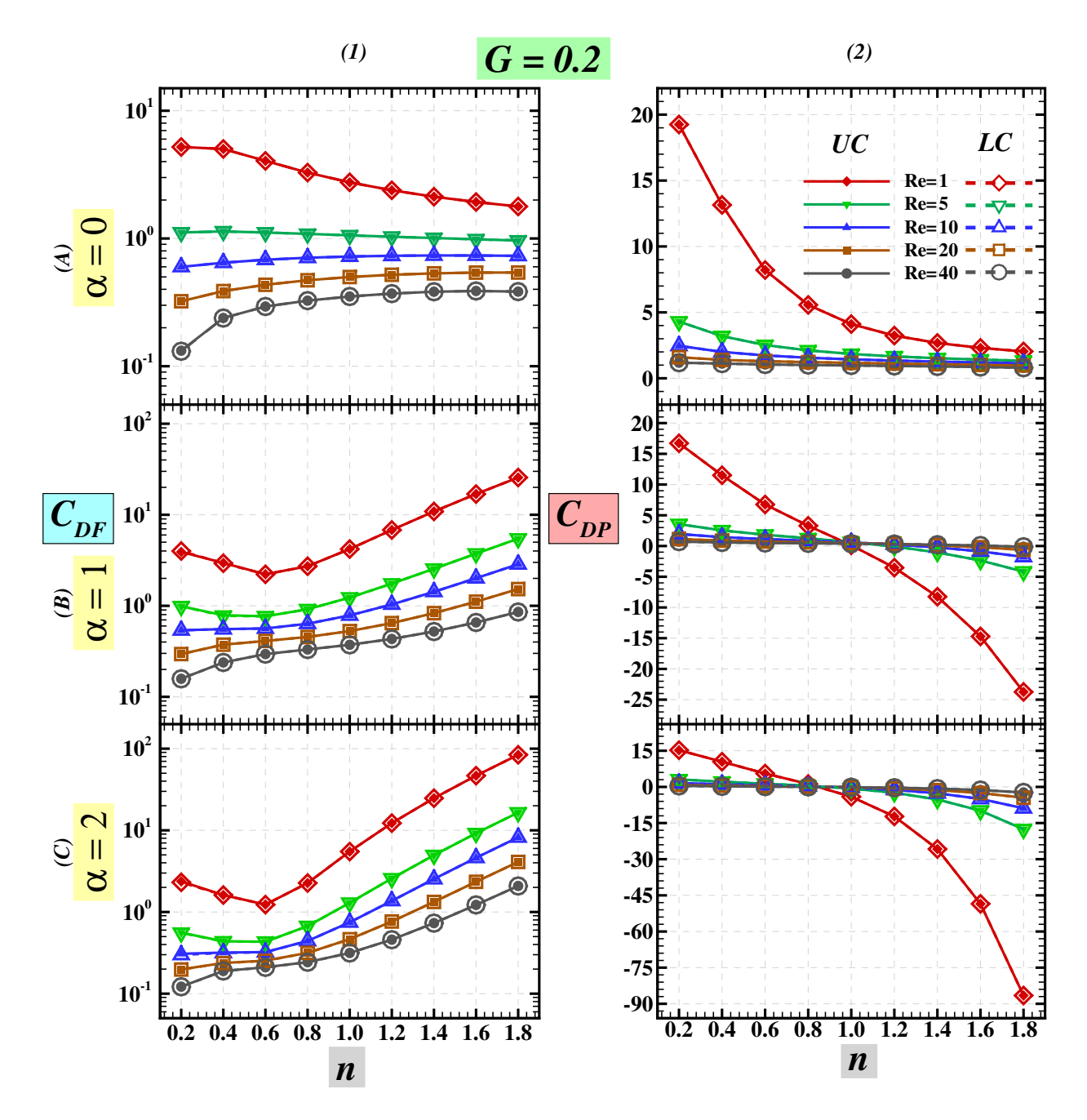


Figure G.1: The variation of friction and pressure drag coefficient (C_{DF} and C_{DP}) with n and Re for G=0.2.

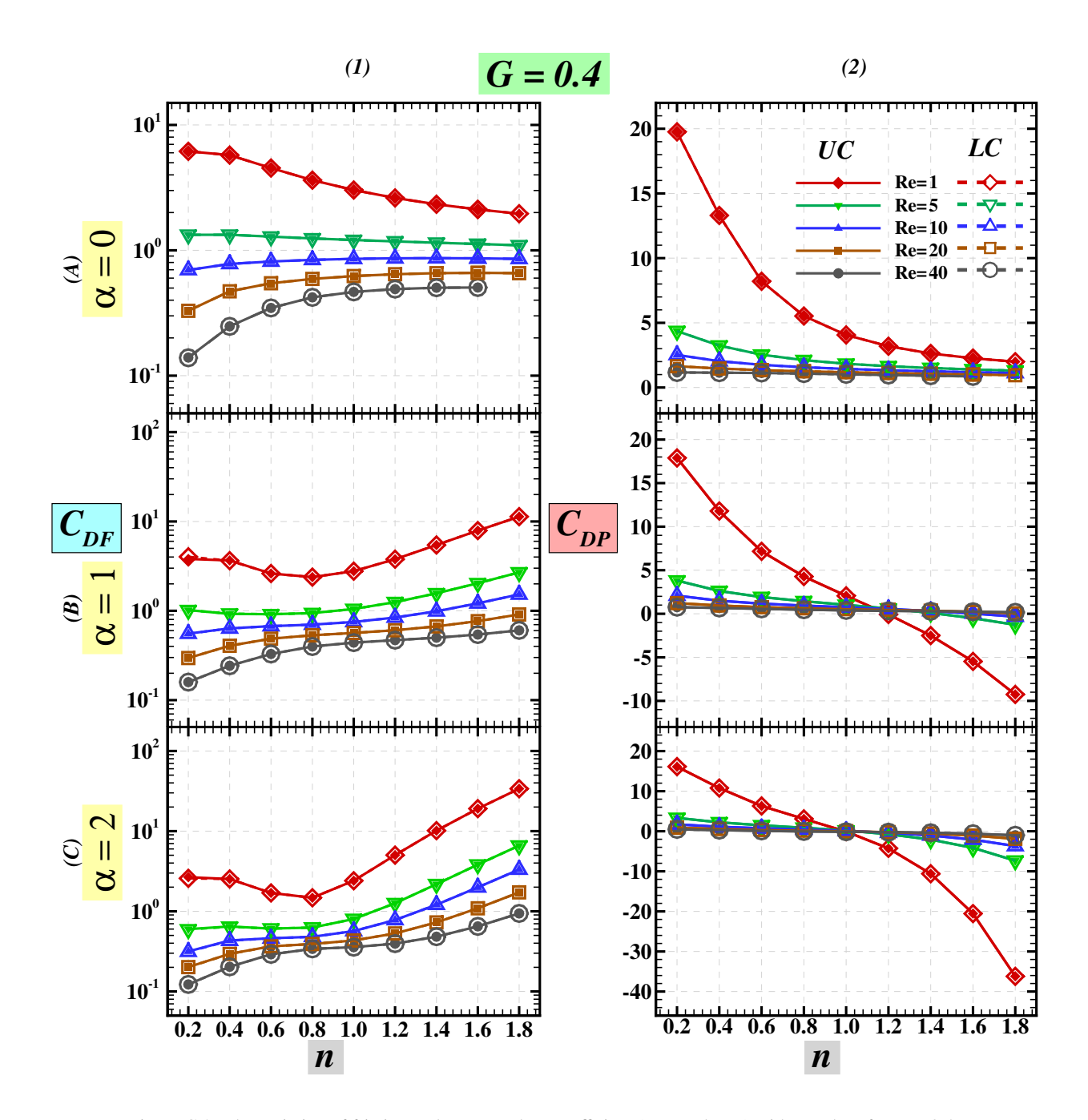


Figure G.2: The variation of friction and pressure drag coefficient (C_{DF} and C_{DP}) with n and Re for G=0.4.

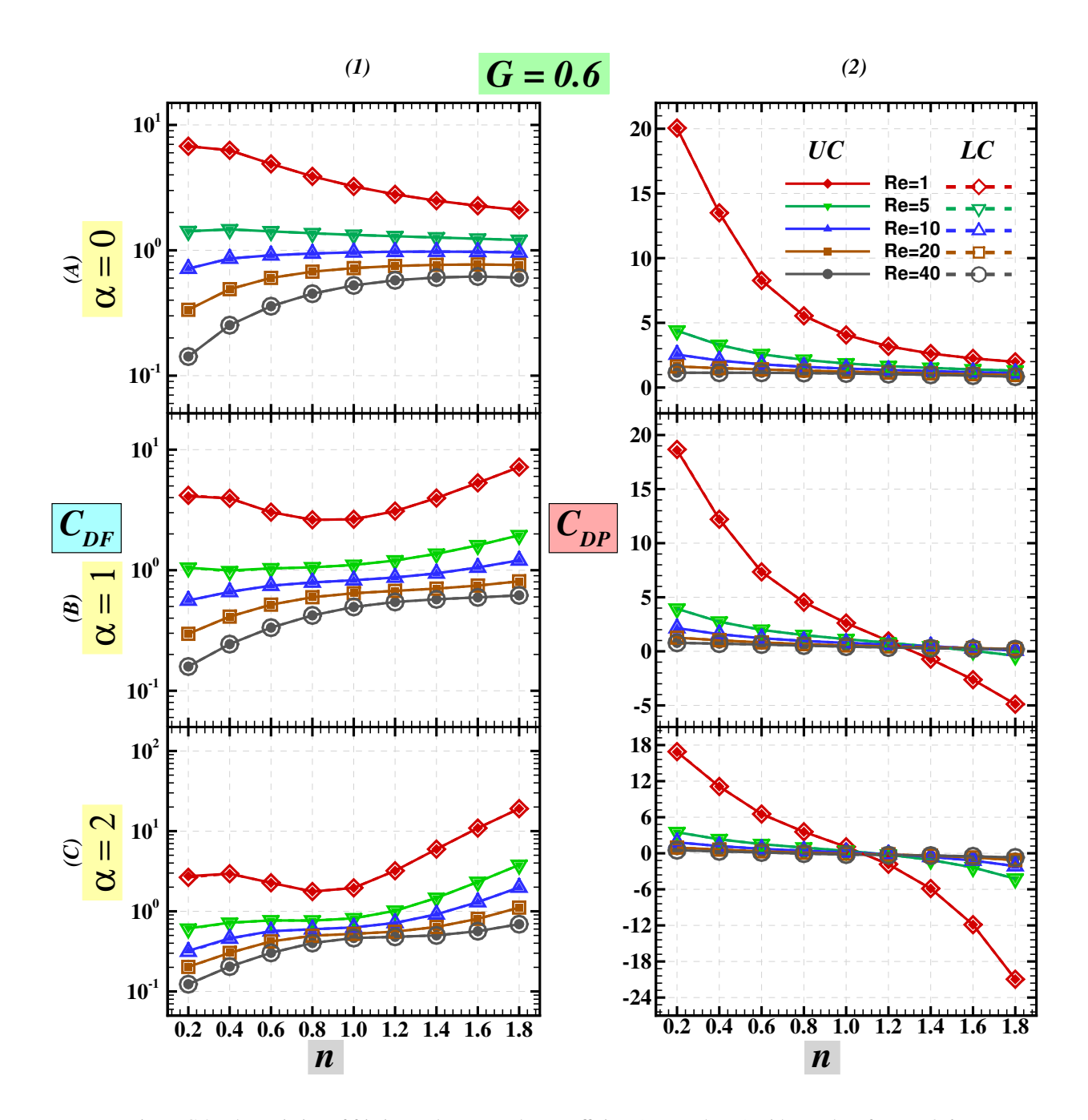


Figure G.3: The variation of friction and pressure drag coefficient (C_{DF} and C_{DP}) with n and Re for G=0.6.

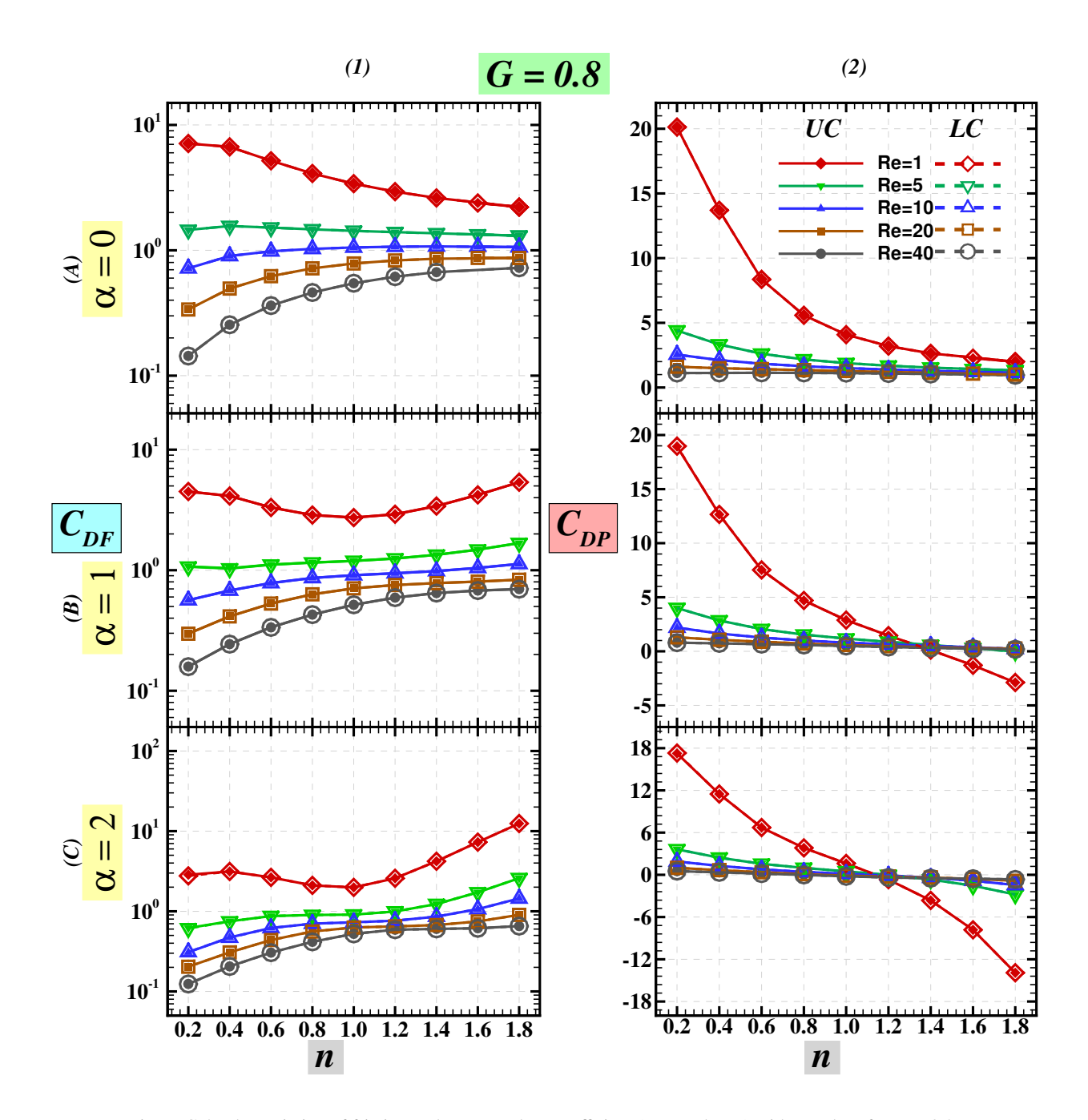


Figure G.4: The variation of friction and pressure drag coefficient (C_{DF} and C_{DP}) with n and Re for G=0.8.

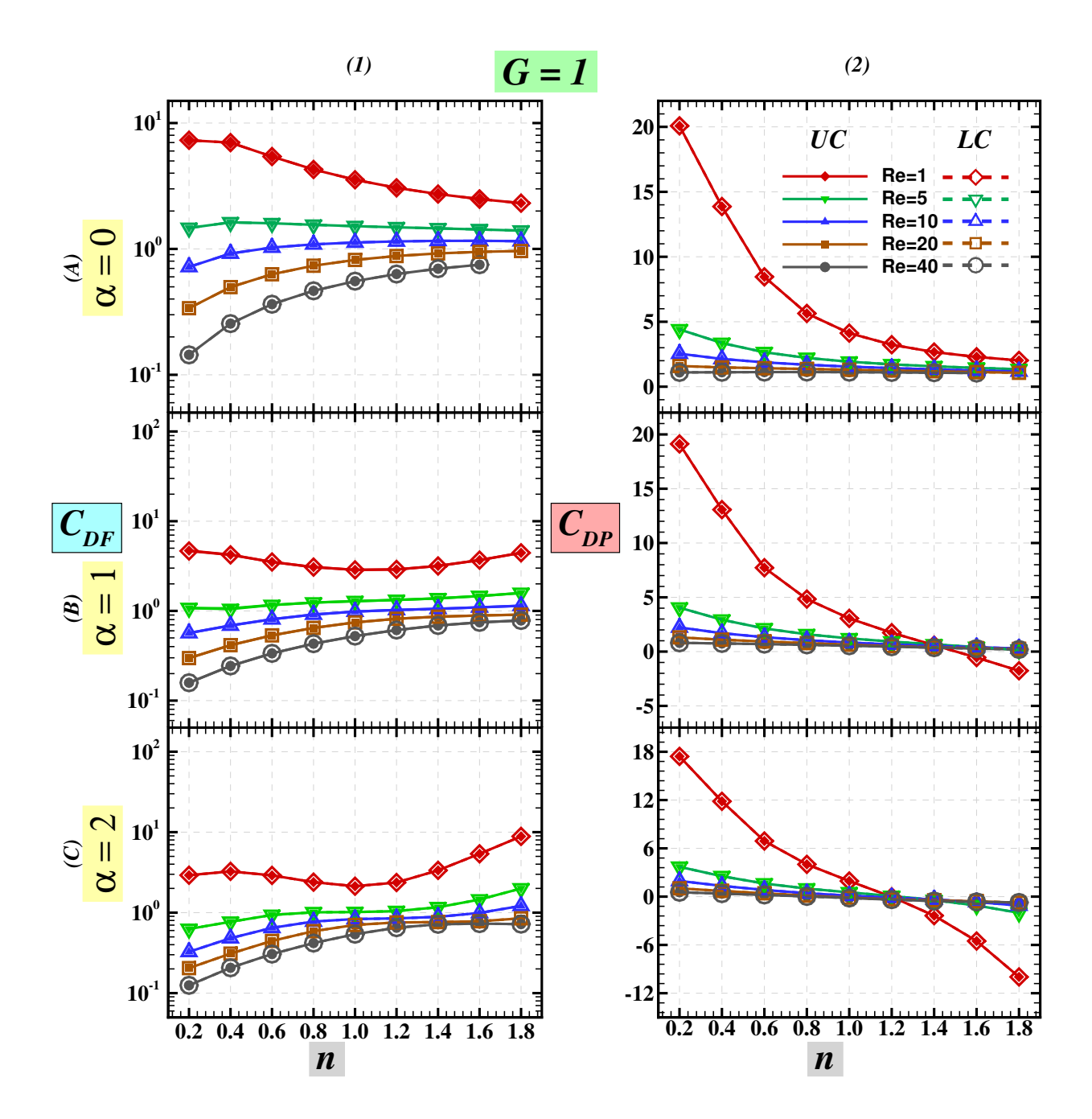


Figure G.5: The variation of friction and pressure drag coefficient (C_{DF} and C_{DP}) with n and Re for G=1.

Appendix H. Friction and pressure lift coefficient (C_{LF} and C_{LP})

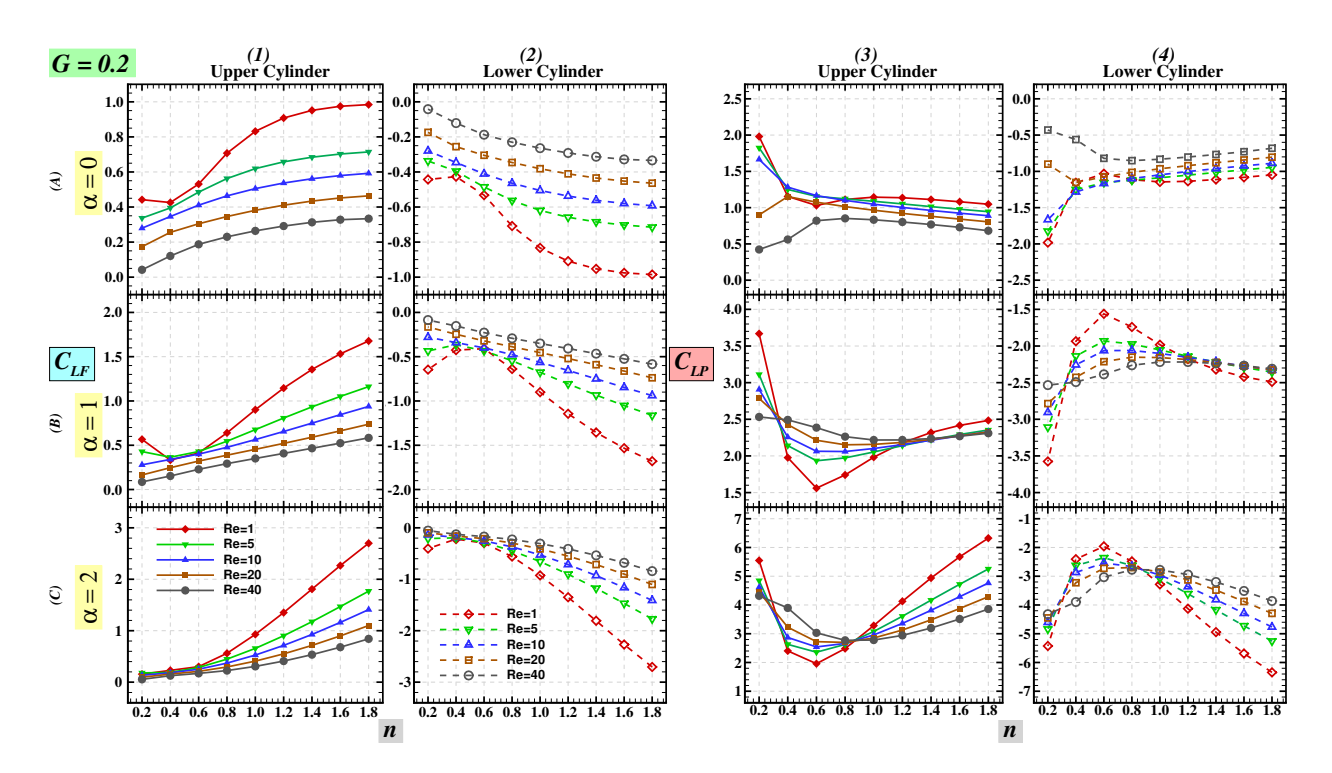


Figure H.1: Variation of friction and pressure lift coefficient (C_{LF} and C_{LP}) with n and Re for G=0.2.

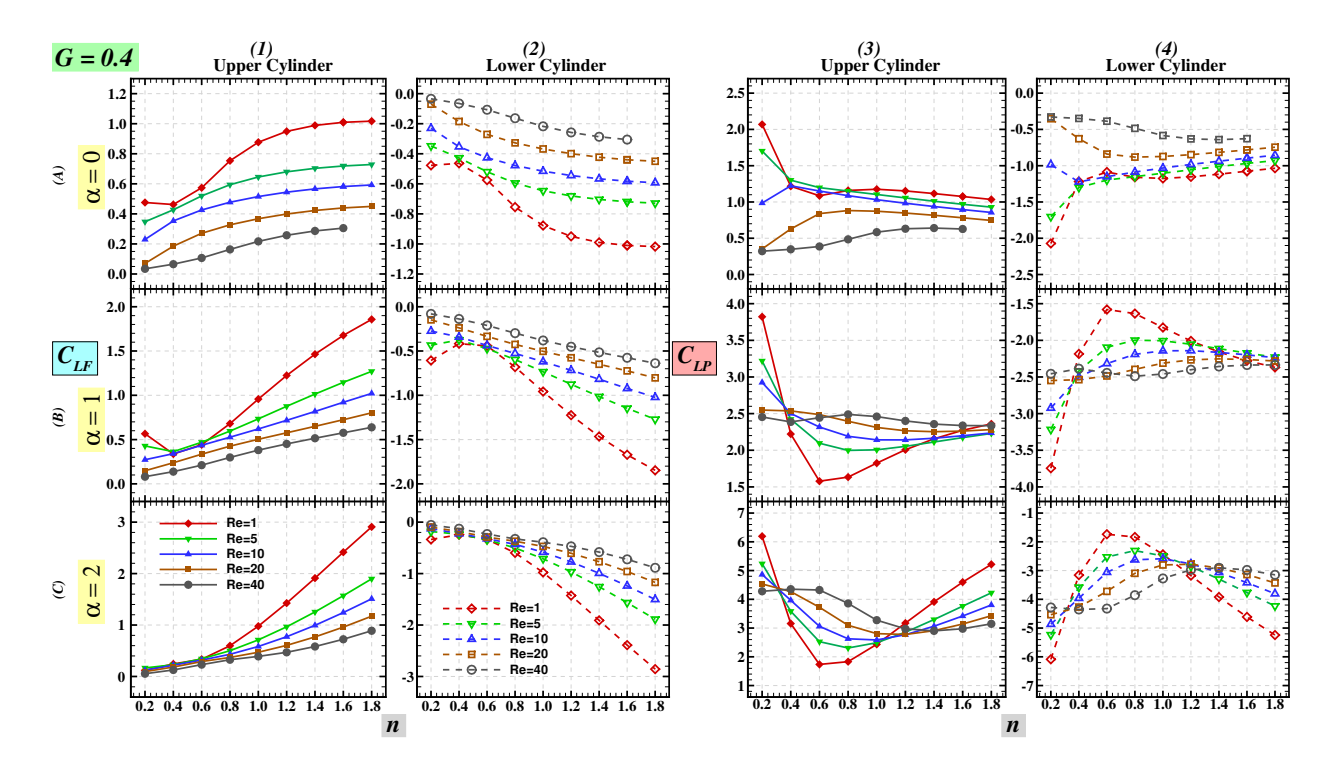


Figure H.2: Variation of friction and pressure lift coefficient (C_{LF} and C_{LP}) with n and Re for G=0.4.

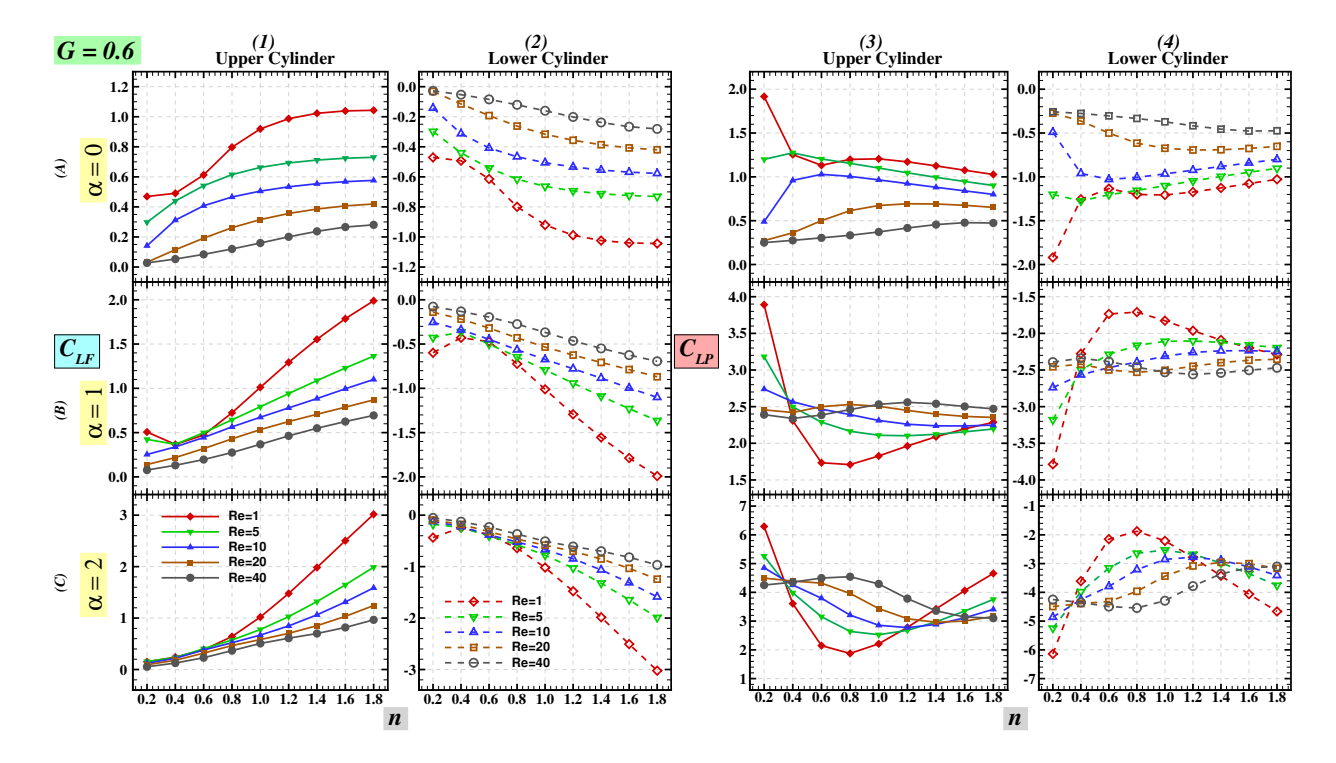


Figure H.3: Variation of friction and pressure lift coefficient (C_{LF} and C_{LP}) with power-law index (n) and Reynolds number (Re) for gap ratio G = 0.6

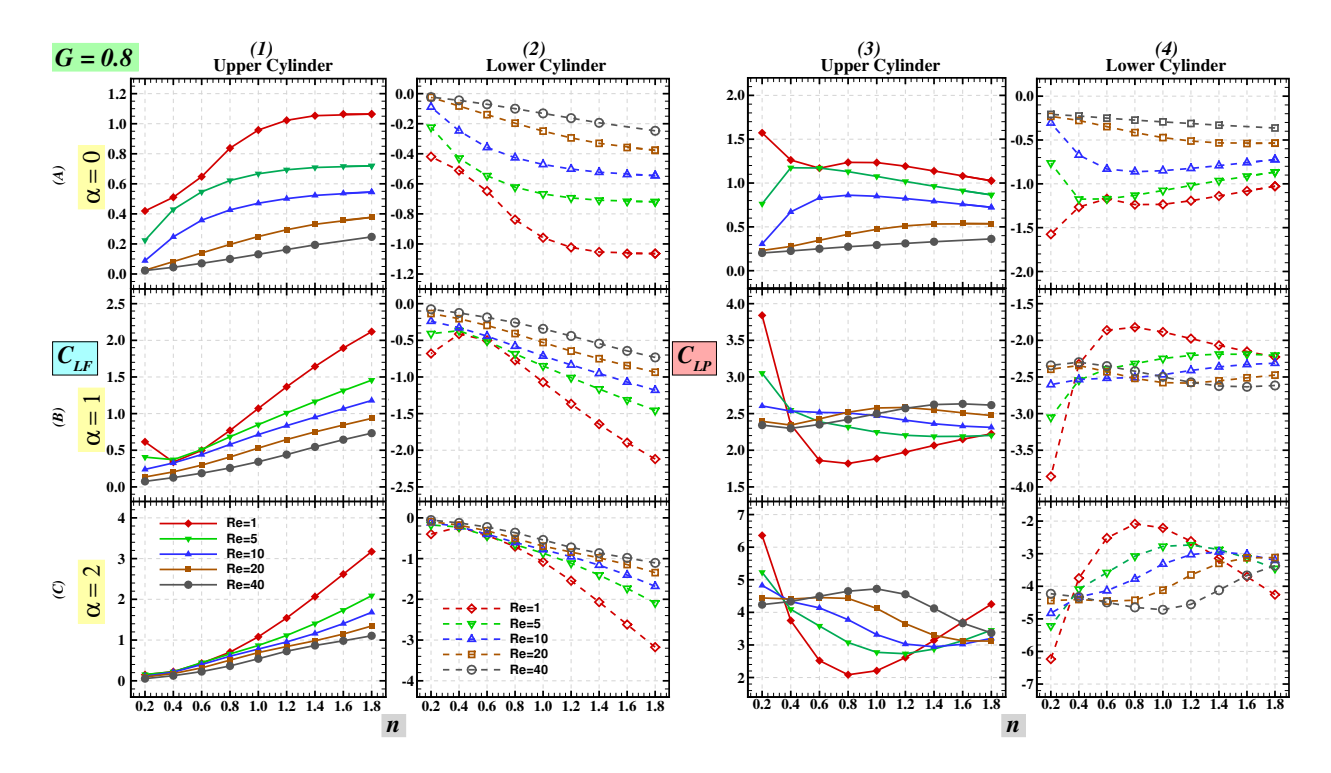


Figure H.4: Variation of friction and pressure lift coefficient (C_{LF} and C_{LP}) with n and Re for G=0.8.

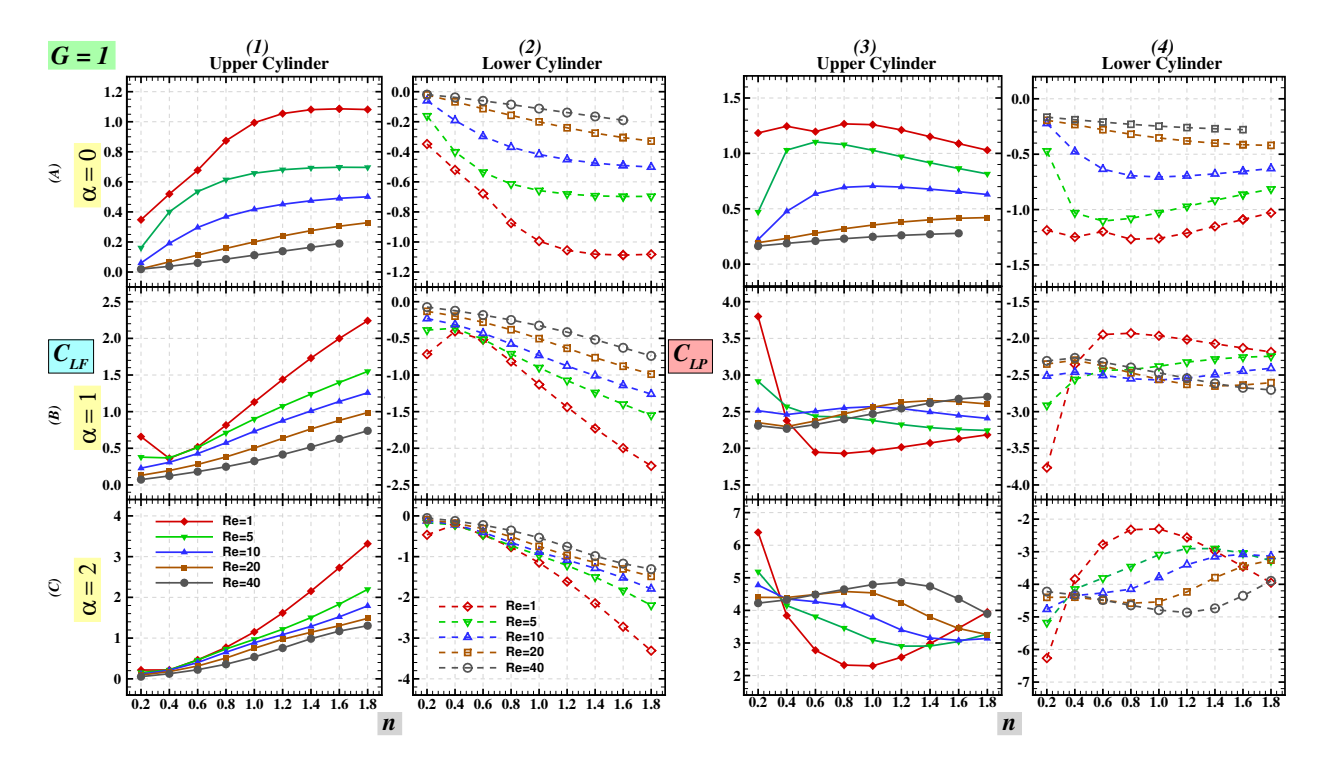
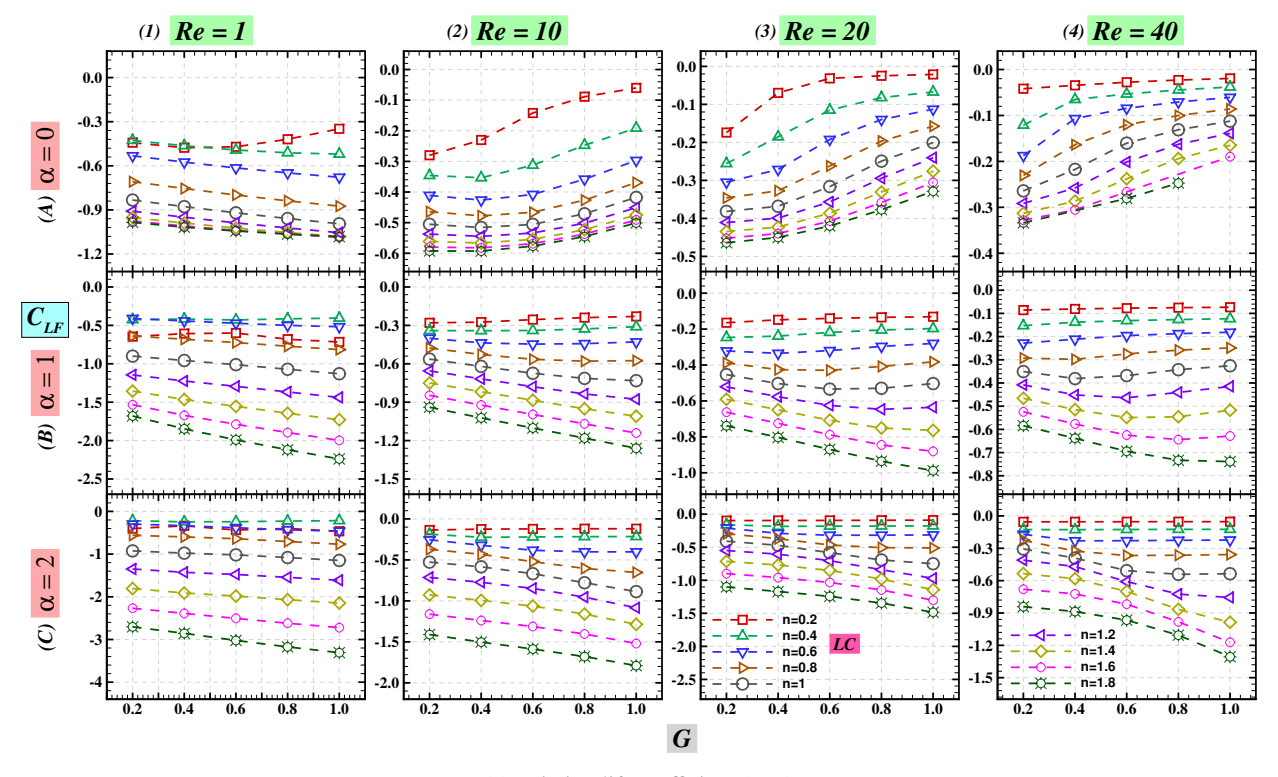
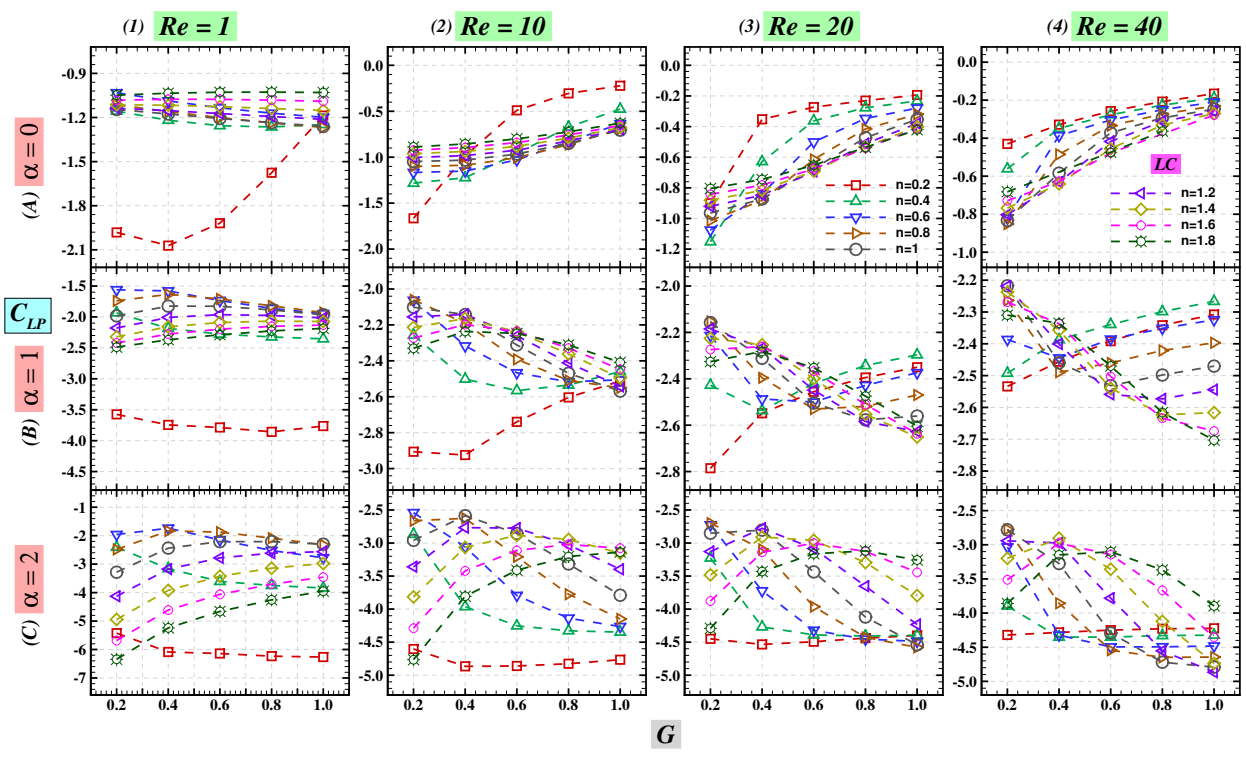


Figure H.5: Variation of friction and pressure lift coefficient (C_{LF} and C_{LP}) with n and Re for G=1.



(a) Friction lift coefficient (C_{LF})



(b) Pressure lift coefficient (C_{LP})

Figure H.6: Variation of individual lift coefficients (C_{LF} and C_{LP}) for LC with G and n for different Re.

Appendix I. Total drag and lift coefficients (C_D and C_L)

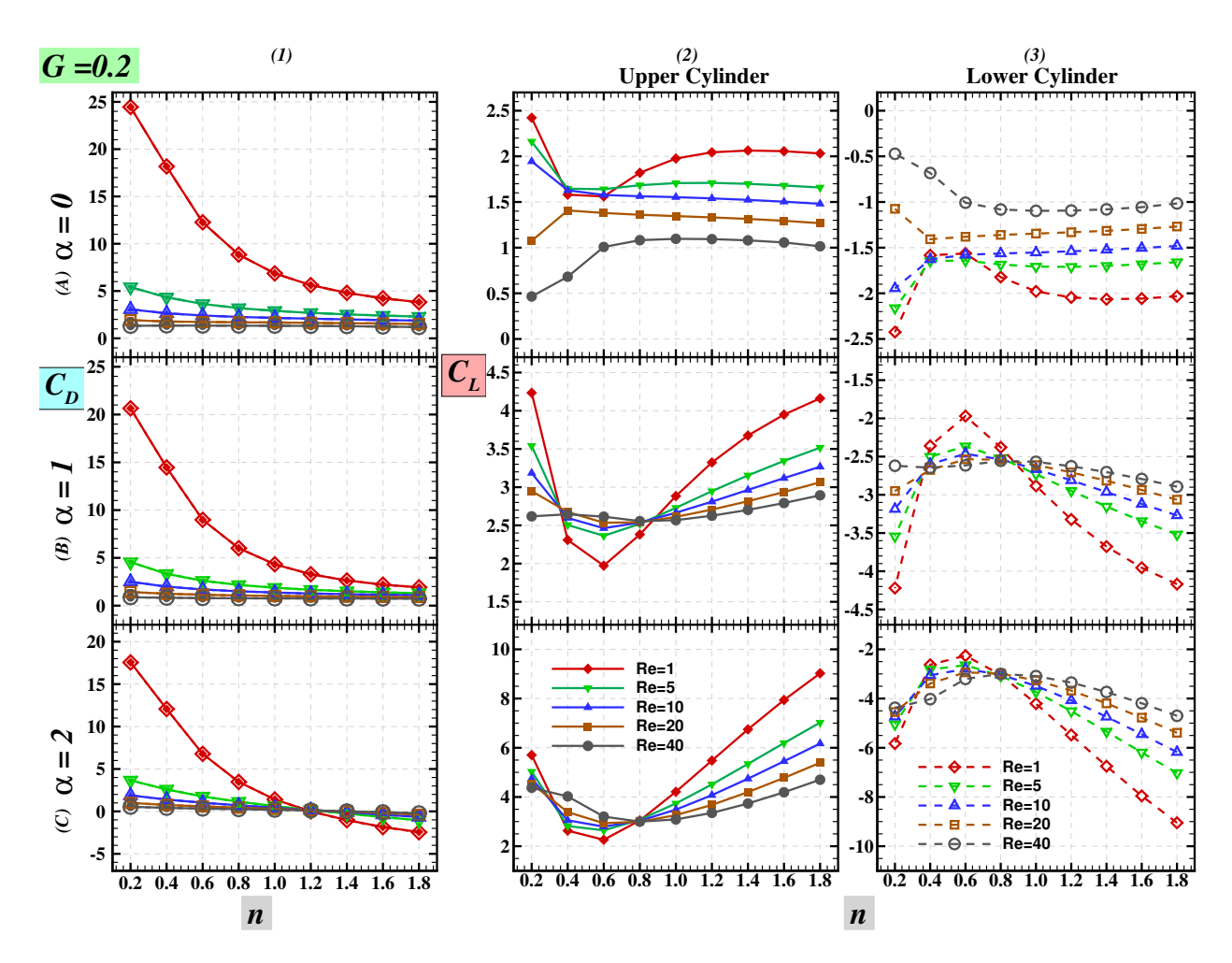


Figure I.1: Variation of drag and lift coefficients (C_D and C_L) with n and Re for G = 0.2.

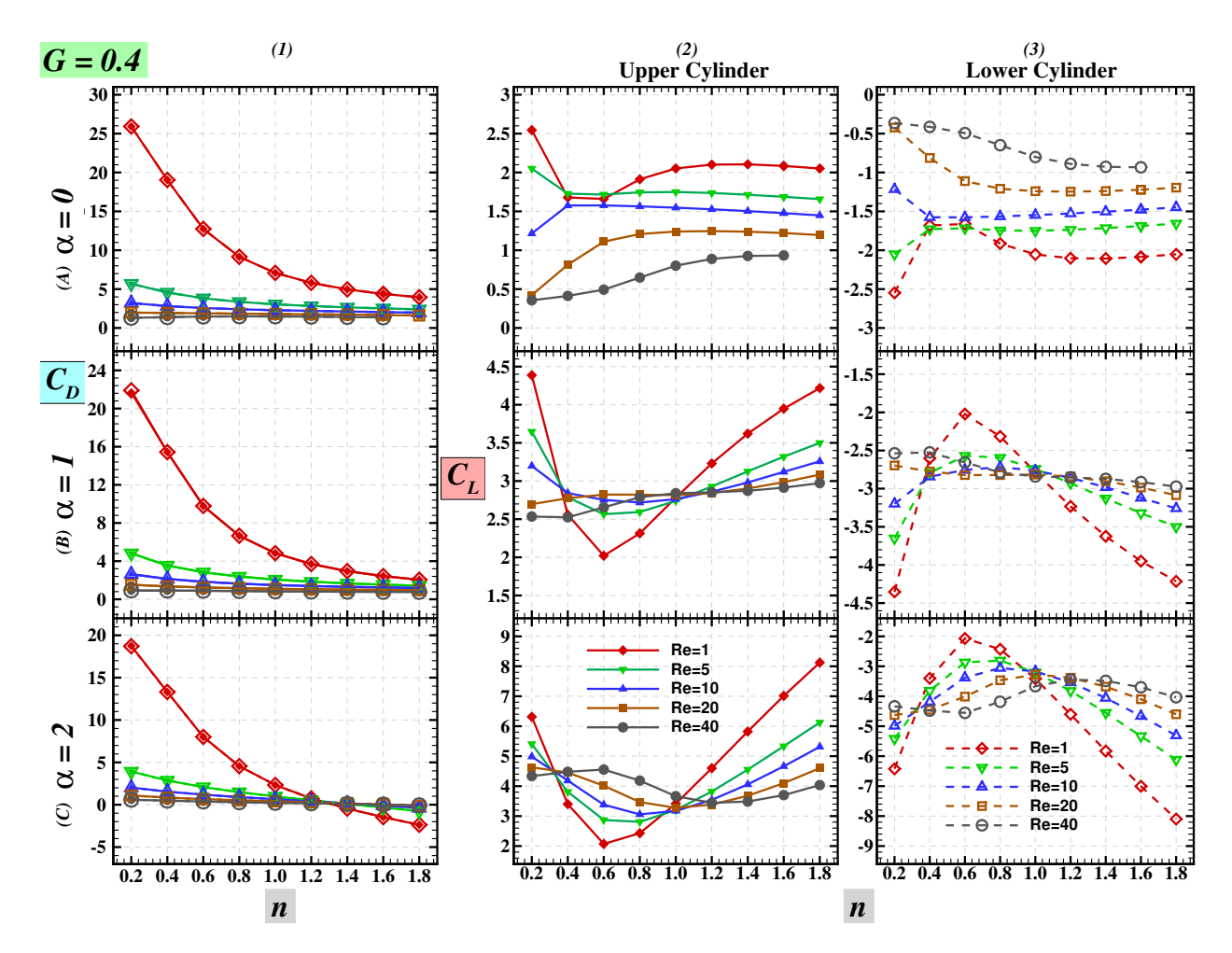


Figure I.2: Variation of drag and lift coefficients (C_D and C_L) with n and Re for G = 0.4.

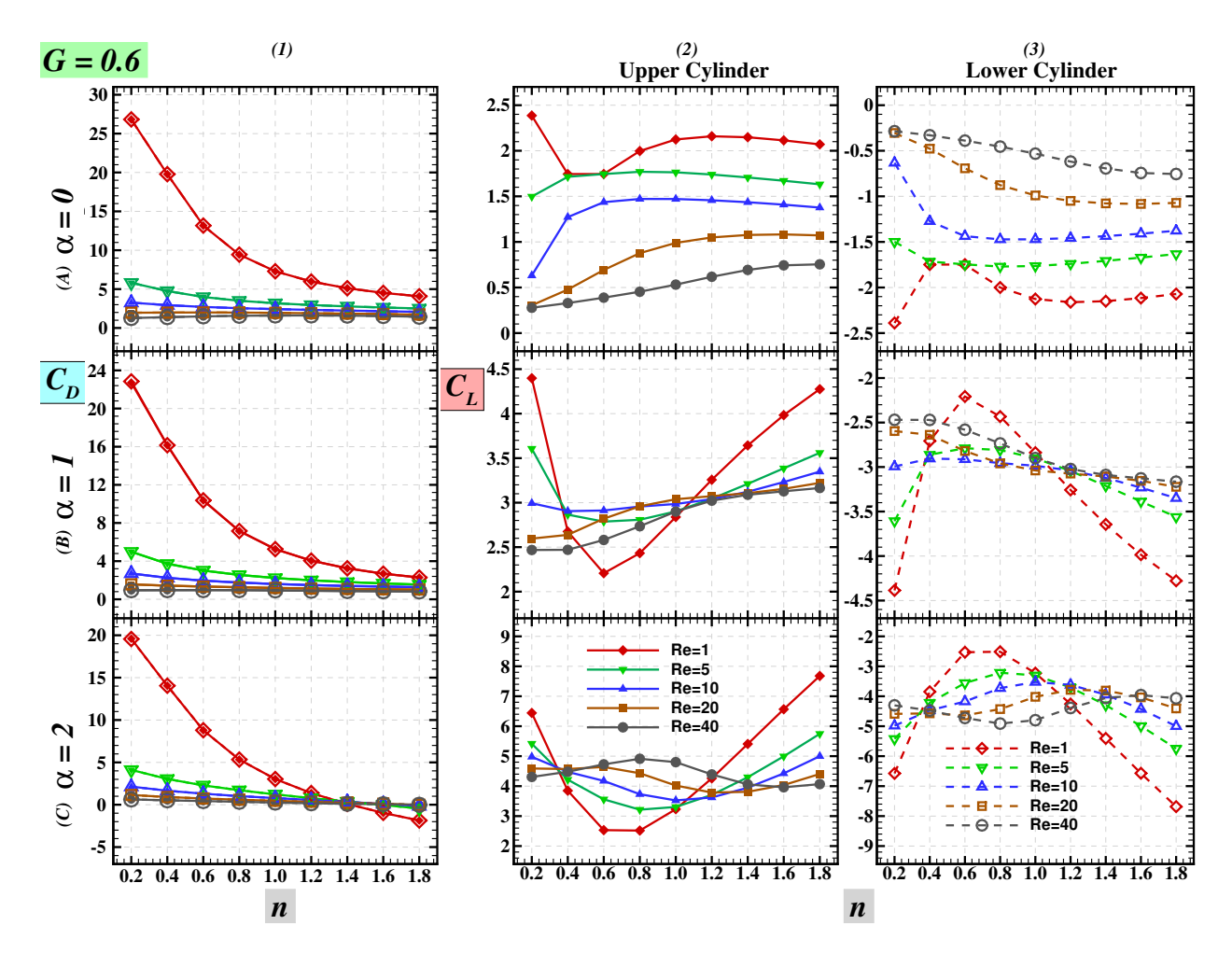


Figure I.3: Variation of drag and lift coefficients (C_D and C_L) with n and Re for G = 0.6.

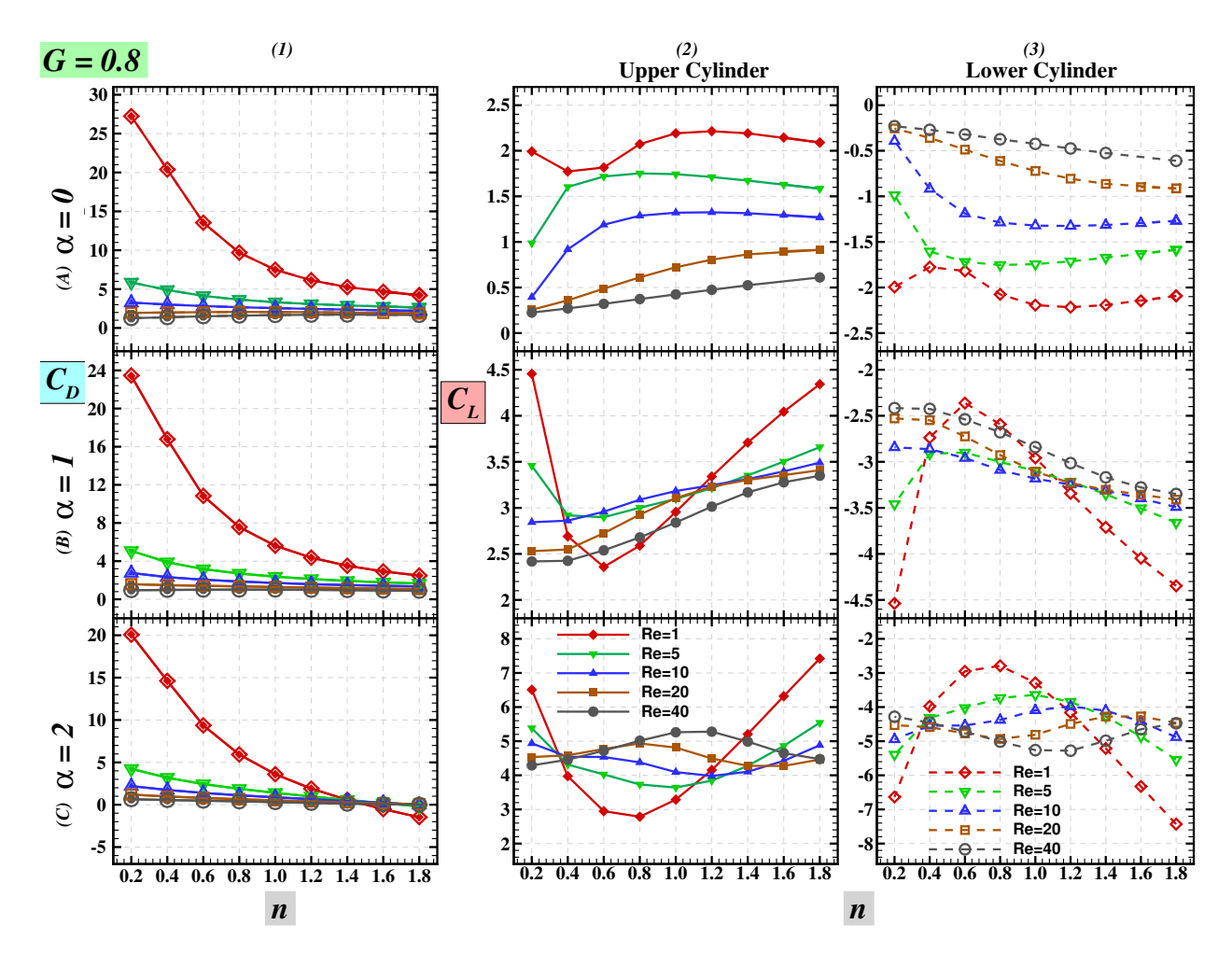


Figure I.4: Variation of drag and lift coefficients (C_D and C_L) with n and Re for G=0.8.

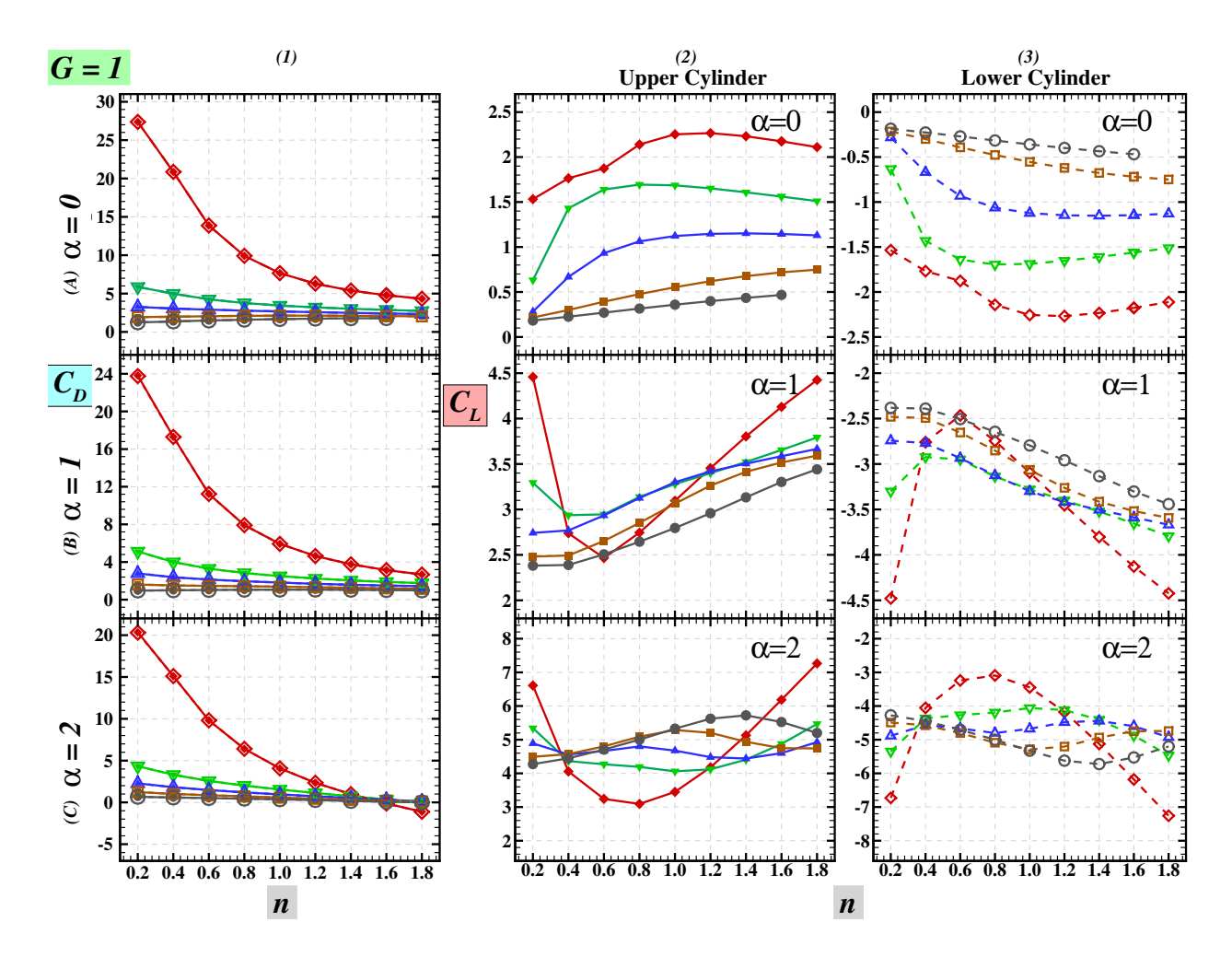


Figure I.5: Variation of drag and lift coefficients (C_D and C_L) with n and Re for G=1.

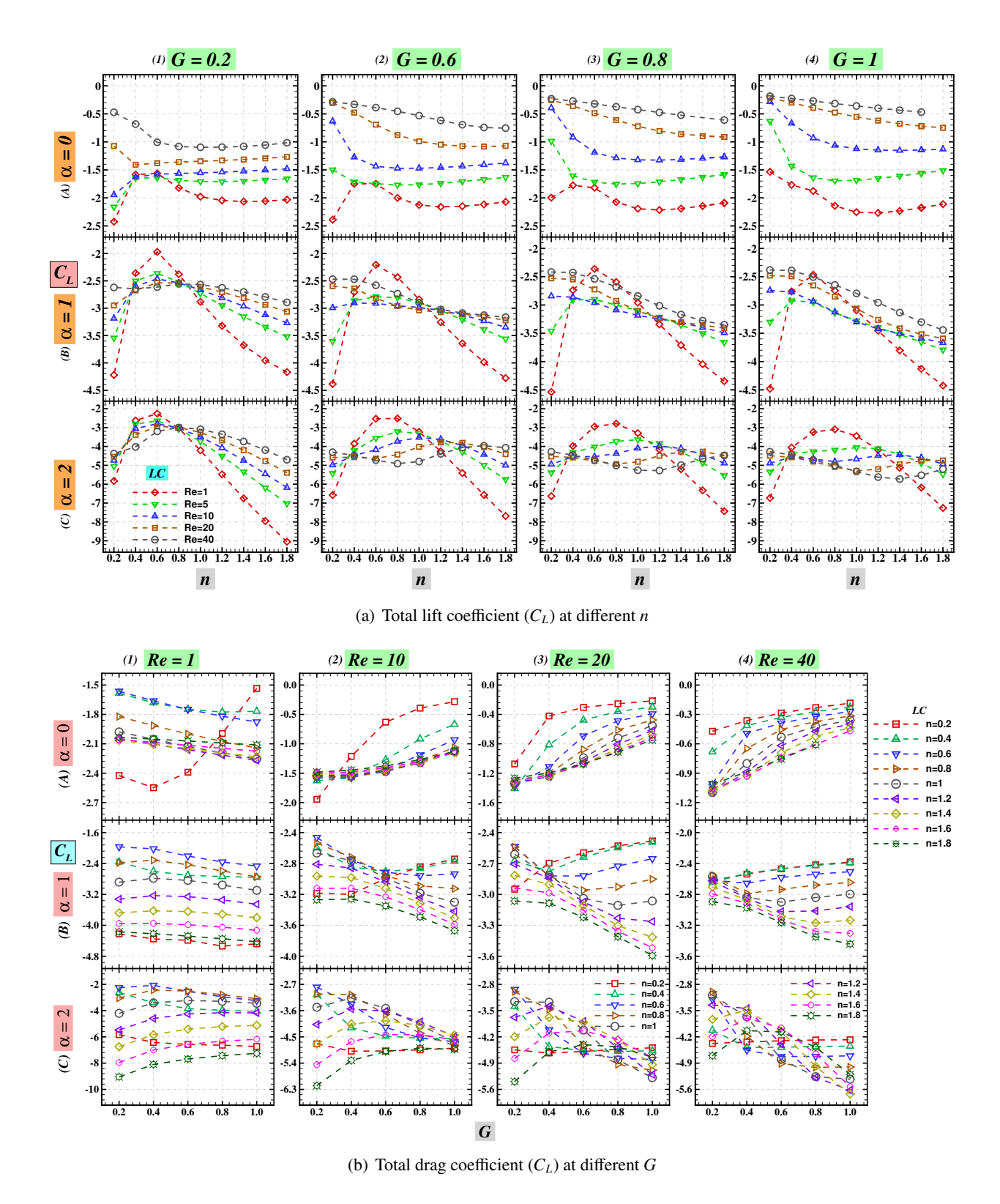


Figure I.6: Variation of total lift coefficient (C_L) for LC with Re.

Appendix J. Drag and lift ratio (C_{DR} and C_{LR})

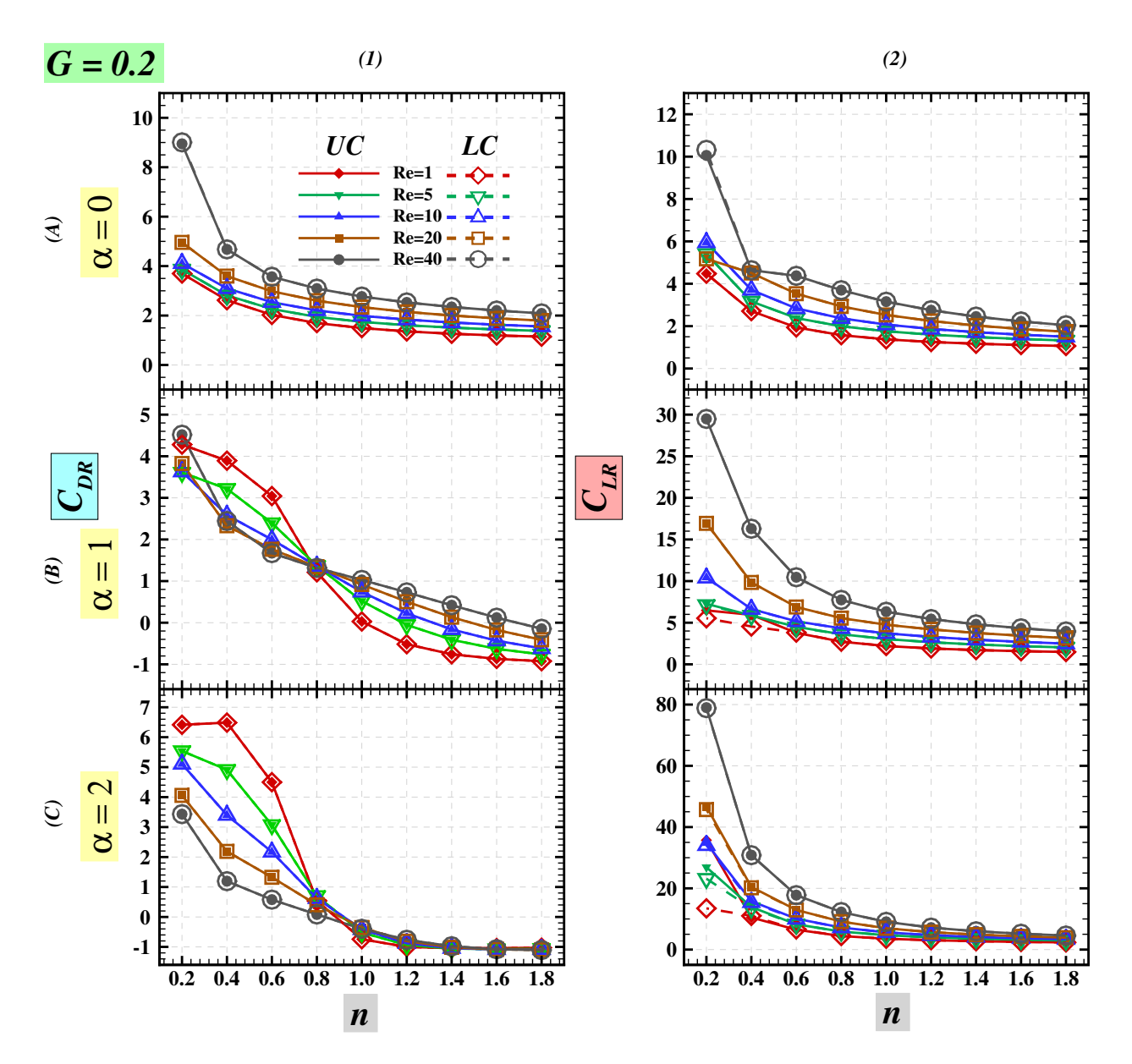


Figure J.1: Variation of drag and lift ratio (C_{DR} and C_{LR}) with n and Re for G=0.2.

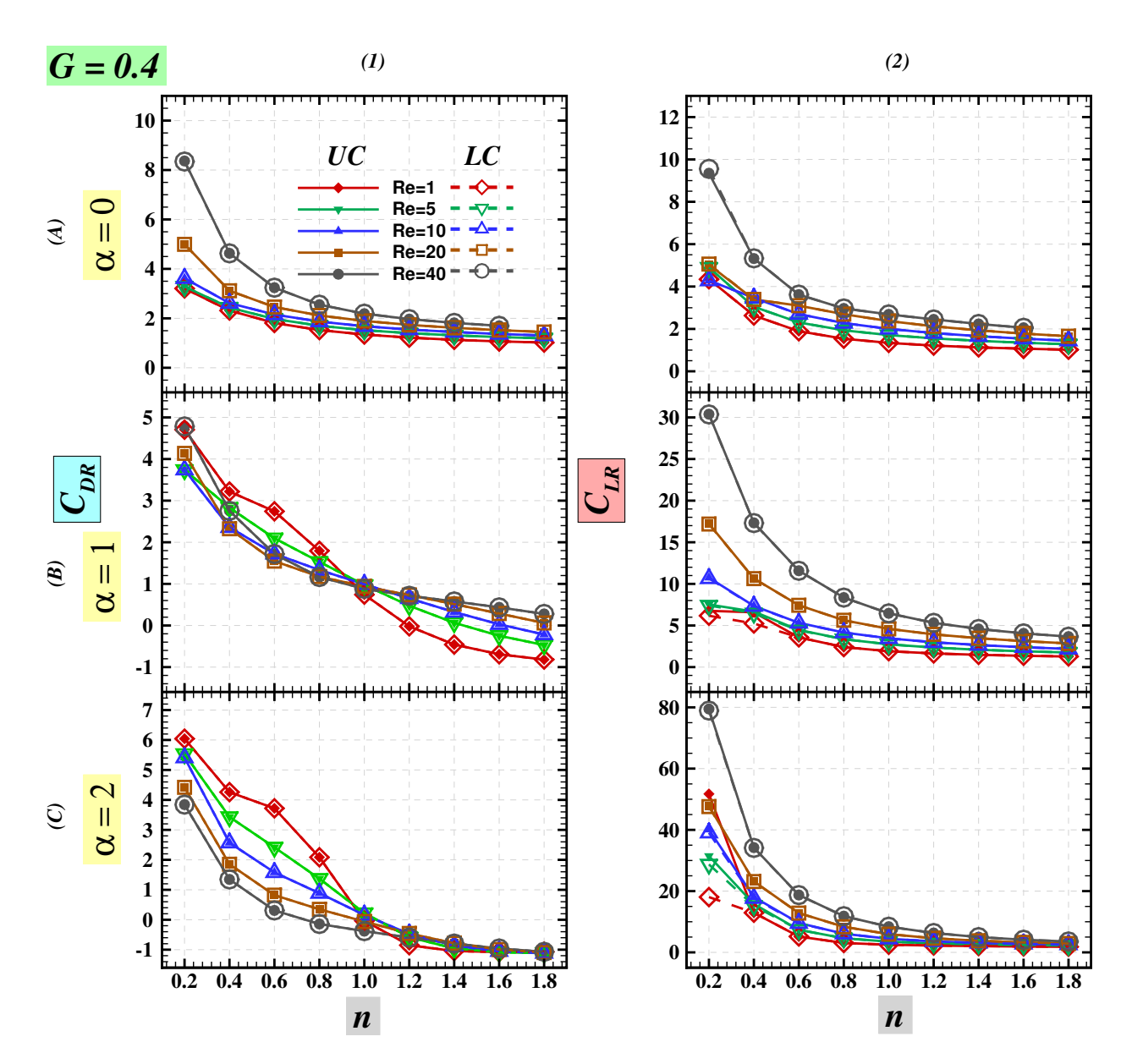


Figure J.2: Variation of drag and lift ratio (C_{DR}) and C_{LR} with n and Re for G=0.4.

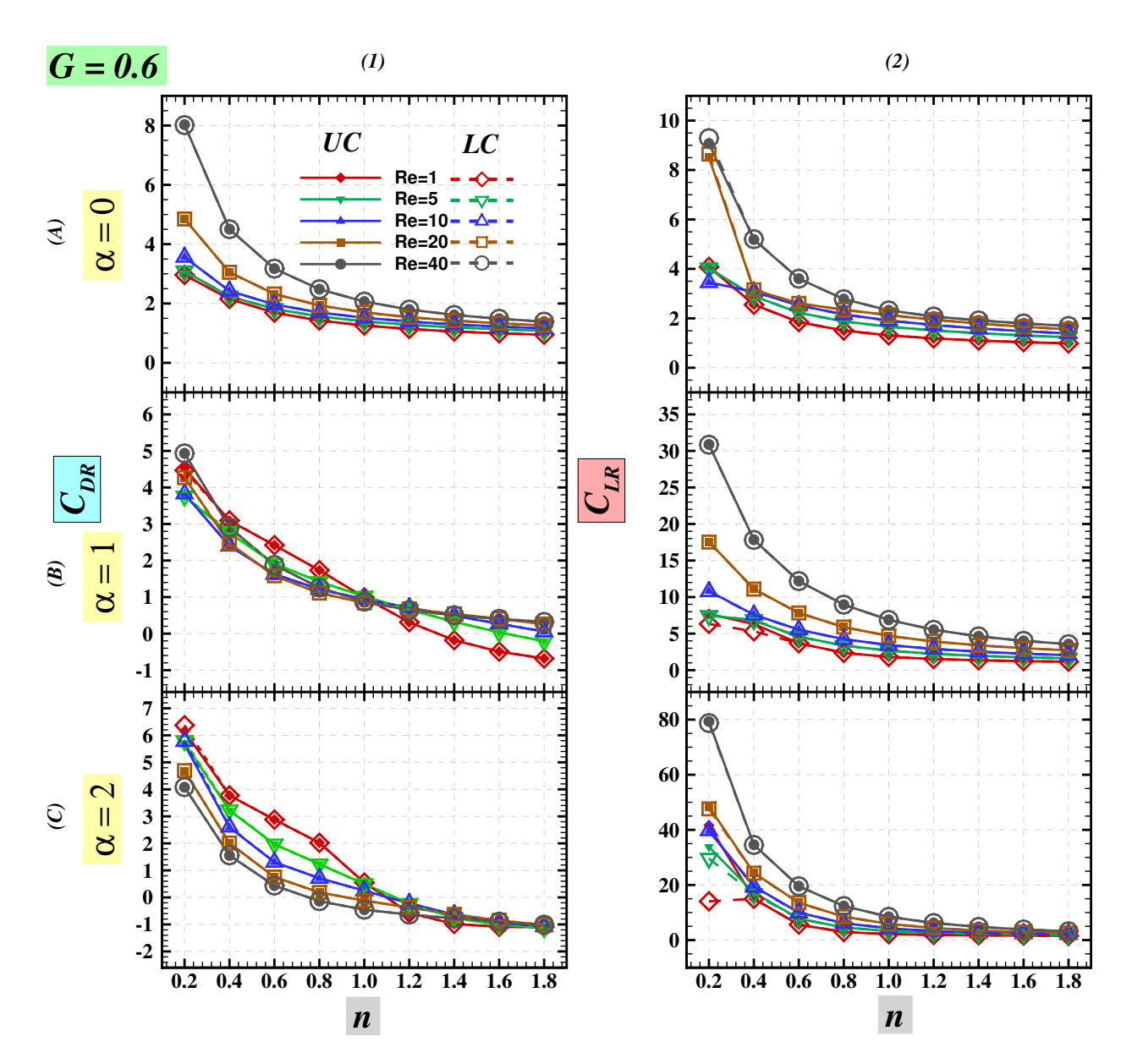


Figure J.3: Variation of drag and lift ratio (C_{DR} and C_{LR}) with n and Re for G=0.6.

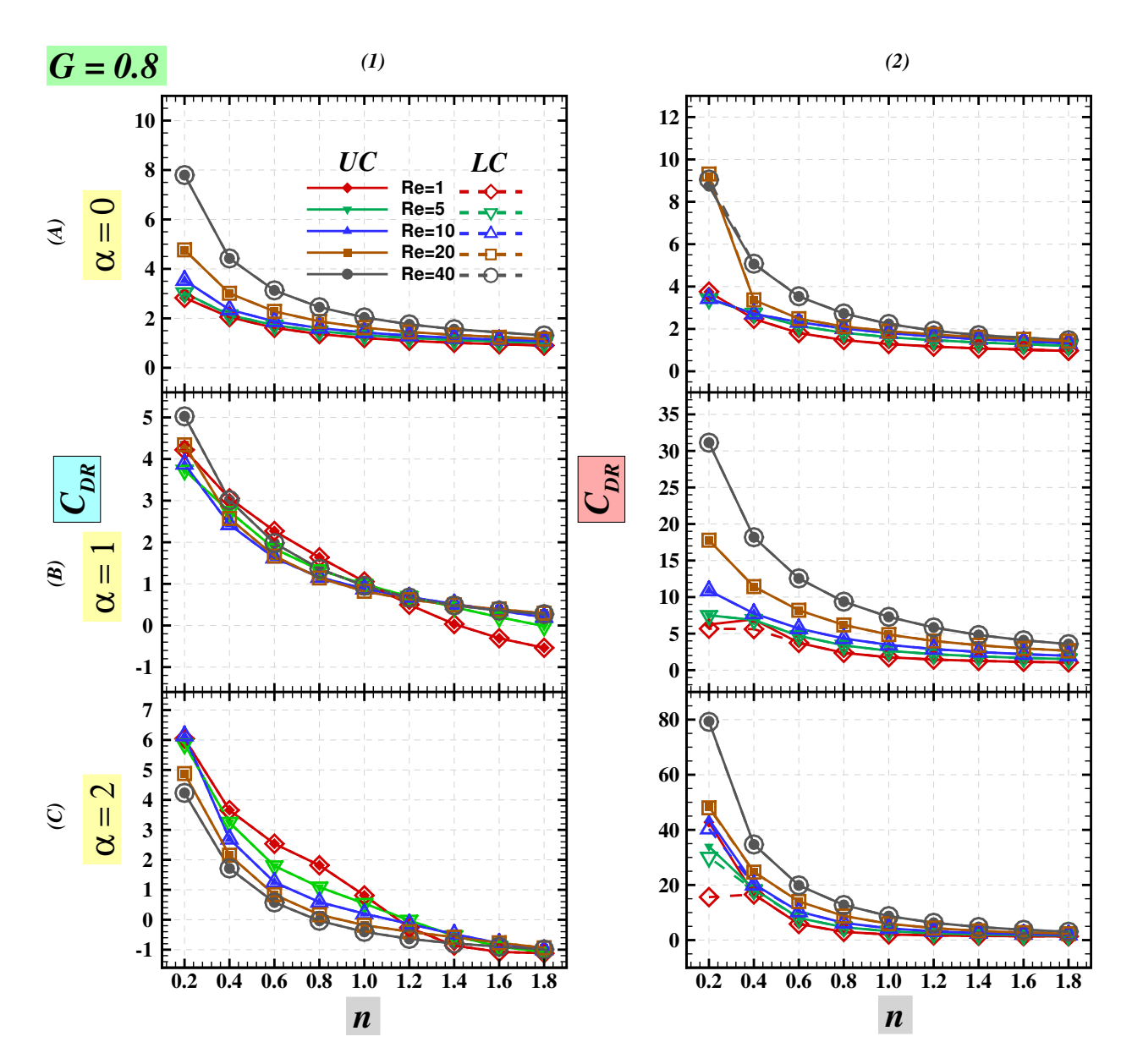


Figure J.4: Variation of drag and lift ratio (C_{DR} and C_{LR}) with n and Re for G=0.8.

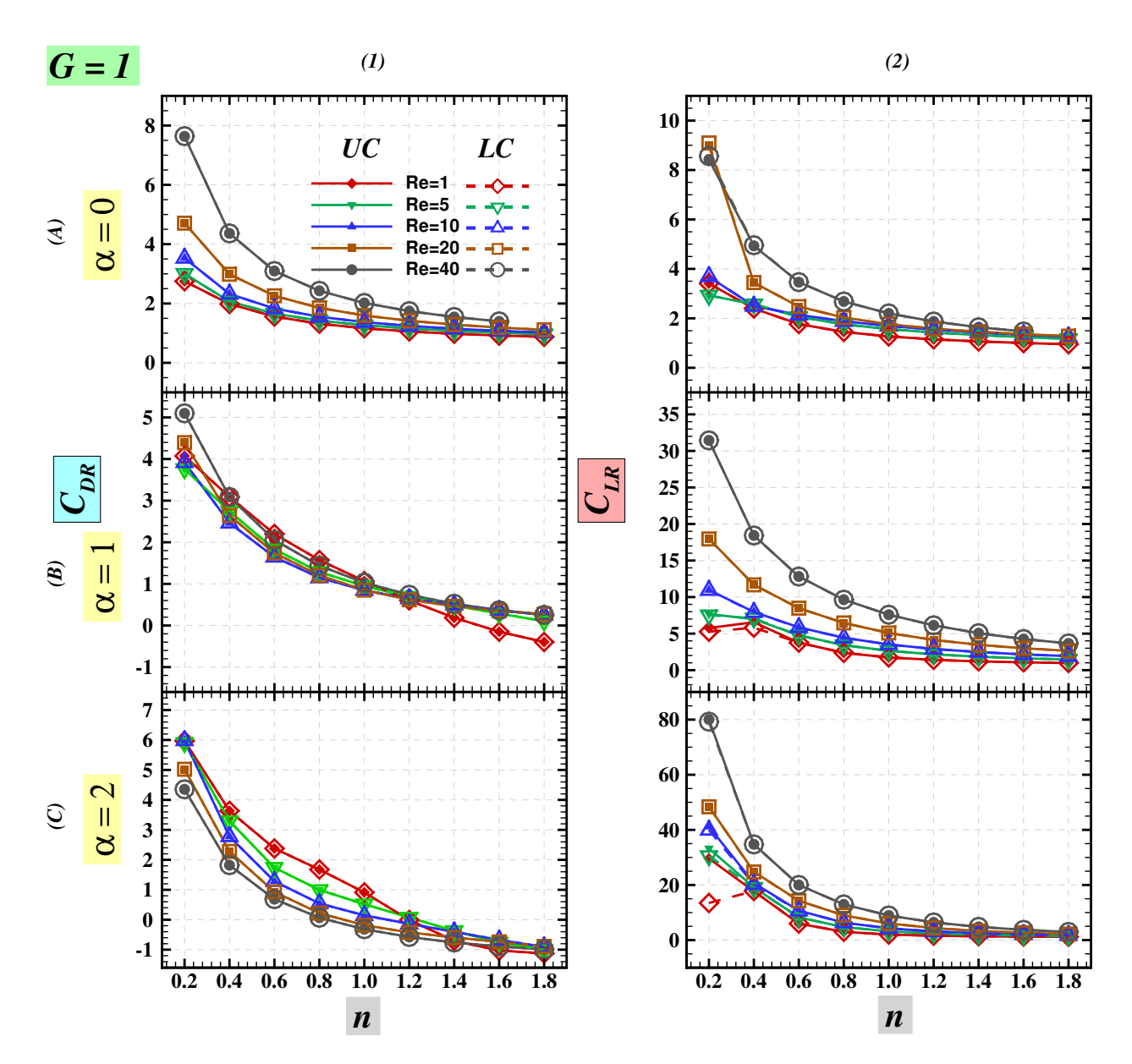


Figure J.5: Variation of drag and lift ratio $(C_{DR} \text{ and } C_{LR})$ with n and Re for G=1.